

Copyright  
by  
Yajai Promboon  
2000

# **ACOUSTIC EMISSION SOURCE LOCATION**

by

**Yajai Promboon, B. Eng., M.S.E.**

**Dissertation**

Presented to the Faculty of the Graduate School of

The University of Texas at Austin

of the requirements

for the Degree of

**Doctor of Philosophy**

The University of Texas at Austin

August, 2000

## **Dedication**

*To my parents, Seubsak and Yenchit Promboon, for their love and encouragement  
throughout my life*

## **Acknowledgements**

I would like to thank all the people who helped me with this dissertation and to the people who helped make my stay in Austin a pleasant one.

First of all, I would like to express my most sincere gratitude to my supervisor, Dr. Timothy Fowler for his technical and moral support throughout the project. Working under his supervision has been a great pleasure and a unique learning experience. I also would like to mention his wife, Mrs. Marie Fowler, for all her kindness and good hospitality. Next, I would like to thank Dr. Jose Reosset, who was my Master's supervisor as well as one of my committee members. I would also like to thank the rest of my committee, Dr. Michael Engelhardt, Dr. Karl Frank, and Dr. Anthony Bedford for their valuable guidance.

The financial support from Thomas N. Crump from E.I. du Pont de Nemours and Company, which made this research project possible, is greatly appreciated. Additional funding and specimen donation from Union Tank Car, Procar Limited, Rescar, Alltranstrk, L.L.C, PPG Industries, Transport Canada, and Allies Signal Corporation is also deeply appreciated. I also would like to thank Martin Peacock, Tom Delafosse, and Allan Giffin who provided great helps with the tank car tests.

I would like to thank Physical Acoustic Corporation (PAC), especially Dr. Sotirios Vahaviolos and Mark Carlos, who always provided all the help I needed. Thank you for lending us a wonderful DISP system for testing the tank car. I would not have finished this dissertation without their help.

I would like to mention my colleagues and friends who helped me with my work and made my time in Austin enjoyable. To Willy Ramirez, who helped me

with everything when I first started my Ph.D. program, thank you for helping me with my test, for helping me develop confidence, and for being such a great friend. To Charles Barnes for teaching me how to use the acoustic emission system. To Rani El Hajjar for being such a great co-worker. Rani made it a lot easier to test the tank car in Orange, TX. Special thanks to my wonderful friend and roommate, Anna Boenig who is always being such a great help and moral support. To all my friends at UT who made me enjoy my life in Austin.

My very special thank to Brian Tinkey. Thank you for helping me with testing, for the technical guidance, for proof reading my dissertation, for teaching me to have balance of work and play, for introducing many new things to my life, and especially for being such a great company. His unique sense of humor helped me go through all the difficult time with my work. I cannot credit him enough.

Finally, my most profound feelings of gratitude are devoted to the people I love the most in my life, my parents. They helped and supported me without expecting anything in return. They always provided all they had for the education and well being of their child. I cannot say enough for what they have done and I want them to know I really appreciate it and I miss them so much. Without them, I would not have made it this far.

Yajai Promboon

August, 2000

# Acoustic Emission Source Location

Publication No. \_\_\_\_\_

Yajai Promboon, Ph.D.

The University of Texas at Austin, 2000

Co-Supervisor: Timothy J. Fowler

Co-Supervisor: Michael D. Engelhardt

The objective of the research program was development of reliable source location techniques. The study comprised two phases. First, the research focused on development of source location methods for homogeneous plates. The specimens used in the program were steel railroad tank cars. Source location methods were developed and demonstrated for empty and water filled tanks. The second phase of the research was an exploratory study of source location method for fiber reinforced composites. Theoretical analysis and experimental measurement of wave propagation were carried out. This data provided the basis for development of a method using the intersection of the group velocity curves for the first three wave propagation modes. Simplex optimization was used to calculate the location of the source.

Additional source location methods have been investigated and critically examined. Emphasis has been placed on evaluating different methods for determining the time of arrival of a wave.

The behavior of wave in a water filled tank was studied and source location methods suitable for use in this situation have been examined through experiment and theory. Particular attention is paid to the problem caused by leaky Lamb waves

A preliminary study into the use of neural networks for source location in fiber reinforced composites was included in the research program. A preliminary neural network model and the results from training and testing data are reported.

## Table of Contents

List of Tables.....	xvi
List of Figures.....	xvii

### Chapter 1: Introduction and Overview

1.1 Introduction.....	1
1.2 Overview.....	1

### Chapter 2: Background and Literature Review

2.1 Acoustic Emission.....	5
2.1.1 Introduction.....	5
2.1.2 Instrumentation.....	7
2.1.3 Signal.....	9
2.2 Wave Propagation.....	11
2.2.1 Elastic Stress Waves in Bulk Material .....	12
2.2.2 Waves at Boundaries between Solids.....	16
2.2.3 Elastic Stress Waves in Plates .....	19
2.2.4 Attenuation of Waves.....	26
2.2.5 Leaky Lamb Waves.....	29
2.2.6 Lamb Wave Propagation in Composite Plates .....	32
2.3 Source Location Approach.....	35
2.3.1 The Method Based on the Arrival Time.....	36
2.3.1.1 Difference in Time-of-Arrival Approach... ..	37
2.3.1.2 Zonal Method.....	53
2.3.2 Waveform Based Approach.....	55



2.3.2.1	Cross Correlation Technique .....	55
2.3.2.2	Other Source Location Methods.....	56
2.4	Search Algorithms in Cylindrical Structures.....	59
2.5	Neural Network .....	63
2.5.1	Theory.....	63
2.5.2	Case Study of Acoustic Emission Neural Network.....	67

### **Chapter 3: Preliminary Study of Source Location on an Empty Tank Car**

3.1	Introduction.....	69
3.2	Artificial Sources.....	70
3.3	Source Location Study on a Tank Car with a 15/32 inch Thick Shell.....	71
3.3.1	Specimen Descriptions.....	71
3.3.2	Instruments.....	73
3.3.3	Attenuation Test.....	74
3.3.4	Currently Used Source Location Approaches.....	76
3.3.4.1	Zonal Method.....	76
3.3.4.1.1	Test Setup.....	76
3.3.4.1.2	Results.....	79
3.3.4.1.3	Conclusion.....	81
3.3.4.2	Difference in Time of Arrival Approach.....	84
3.3.4.2.1	Concept of the Approach.....	84
3.3.4.2.2	Theoretical Wave Velocity on the Tank car.....	85
3.3.4.2.3	Velocity Measurement.....	86
3.3.4.2.4	Conclusion.....	88
3.3.5	Improvement of Difference in Time of Arrival Approach.....	90
3.3.5.1	Dispersion Curve.....	90

3.3.5.2	Source Location with Simplex Optimization Approach.....	92
3.3.5.3	Velocity Measurement .....	94
3.3.5.4	Source Location Program.....	96
3.3.5.5	Results from Pencil Lead Break on the Tank Body.....	99
3.3.5.6	The Study of Wave Propagation on the Bolster Area .....	103
3.3.5.6.1	Test Setup.....	103
3.3.5.6.2	Results .....	105
3.3.5.6.3	Conclusion.....	112
3.3.5.7	Results from a Bar Bending Approach.....	113
3.4	Source Location Study Problem on a Tank Car with 13/16 inch thick Shell.....	126
3.4.1	Specimen Description.....	126
3.4.2	Instruments.....	127
3.4.3	Attenuation Test.....	128
3.4.4	Theoretical Group Velocity.....	129
3.4.5	Velocity Measurement.....	130
3.4.6	Source Location Methods.....	132
3.4.6.1	Difference in the Arrival Time of the First Two Modes.....	133
3.4.6.2	Source Location Based on the Intersection of the Group Velocity.....	138
3.4.7	Summary of Source Location Studies on the Orange Tank.....	141
3.5	Conclusion.....	142

#### **Chapter 4: Jacking and Twist Bar Tests on an Empty Tank Car**

4.1	Introduction.....	145
4.2	Instruments and Sensor Locations.....	146
4.2.1	Instruments.....	146

4.2.2	Sensor Locations.....	146
4.2.3	History of Tank and Sources of Emission.....	148
4.3	Source Location Approach.....	149
4.3.1	Concept of the Approach.....	149
4.3.2	Software Algorithm Developed for a Tank Car.....	149
4.3.3	Illustrative Test Results.....	154
4.4	Jacking Test.....	167
4.4.1	Test Procedure.....	167
4.4.2	Test Results.....	169
4.5	Jacking - Blocked Test.....	184
4.5.1	Test Procedure.....	184
4.5.2	Test Results.....	184
4.6	Twist Bar Test.....	192
4.6.1	Test Procedure.....	192
4.6.2	Test Results.....	193
4.7	Summary.....	200

## **Chapter 5: Preliminary Study of Source Location on a Water Filled Tank**

5.1	Introduction.....	203
5.2	Artificial Source.....	204
5.3	The Study of Source Location Problem on a Tank car with ½ inch thick wall.....	205
5.3.1	Instrument and Specimen.....	205
5.3.2	Attenuation Test.....	206
5.3.3	Source Location Approach Using Narrow Band Frequency at the Intersection of the Group Velocity of the First Three Wave Modes.....	208

5.3.4	Source Location Approach for a Water Filled Tank car using Non Leaky Waves.....	211
5.3.4.1	Background in Leaky/Non Leaky Lamb Waves.....	211
5.3.4.2	Source Location Approach Based on Non-Leaky Part.....	214
5.3.4.3	Velocity Measurement.....	217
5.3.4.4	Results from Bar bending.....	218
5.3.4.5	Conclusion.....	224
5.4	The Study of Source Location Problem on a Tank car with 13/16 inch thick wall.....	227
5.4.1	Introduction.....	227
5.4.2	Instrumentation.....	228
5.4.3	Attenuation Test.....	228
5.4.4	Source Location Analysis and Results from Bar Bending Approach...	229
5.4.5	A Study of Water Borne Waves.....	240
5.4.5.1	Water Borne Waves.....	241
5.4.5.2	Sound Waves at Interfaces with Oblique Incidence.....	248
5.4.5.3	Results from Water Borne Studies.....	250
5.4.5.4	Discussion of Water Borne Waves.....	255
5.5	Summary.....	256

## **Chapter 6: Internal Pressure Test of a Tank Car**

6.1	Introduction.....	258
6.2	Experimental Setup.....	258
6.2.1	Instrumentation and Sensor Location.....	258
6.2.2	Loading Sequence.....	260

6.3	Source Location Analysis.....	261
6.3.1	Source Location Method using Higher Frequency.....	261
6.3.2	Results from the Internal Pressure Test.....	261
6.3.3	Discussion of the Source Location Method and Results.....	280
6.4	Water Borne Wave Study.....	285
6.5	Summary.....	295

## **Chapter 7: Exploratory Source Location Studies in Composites**

7.1	Introduction.....	297
7.2	Specimen and Instruments.....	298
7.3	Preliminary Study of the Conventional Source Location with the Time of Arrival Method.....	299
7.3.1	Wave Velocity on Composites.....	299
7.3.2	Discussion.....	306
7.4	Source Location with a Neural Network Approach.....	308
7.4.1	Introduction to MLP Neural Network.....	308
7.4.2	Training Data.....	309
7.4.3	Network Model.....	310
7.4.4	Feature Extraction.....	311
7.4.5	Network Optimization.....	313
7.4.6	Results from the Final Network.....	313
7.5	Experimental Program.....	314
7.5.1	Introduction.....	314
7.5.2	Test Setup.....	315
7.5.3	Final Neural Network Model.....	316
7.5.4	Experimental Results.....	317

7.6 Summary and Future Research.....318

**Chapter 8: Conclusions and Research Needs**

8.1 Summary.....320

8.2 Conclusions .....321

    8.2.1 Source Location on an Empty Tank Car.....322

    8.2.2 Source Location on Water Filled Tank Car.....324

    8.2.3 Source Location on Fiber Reinforced Composites.....327

8.3 Future Research.....327

**Appendix A.....329**

**References.....333**

**Vita.....343**

## List of Tables

Table 3.1 - Calculated Distance from Sensor 1 to Sensors 3 and 4 for the Upper Part of the Bolster .....	107
Table 3.2 – Calculated Distance from Sensor 1 to Other Sensors for the Lower Part of the Bolster .....	110
Table 3.3 - Calculated Distance Results .....	112
Table 3.4 - Calculated Distance from the Trigger Sensor to Other Sensors.....	123
Table 4.4 – Results from Combinations of Three Sensors from Four Path.....	156
Table 4.5 – Results with Low Flag Values from Four Paths.....	158
Table 4.6 – Results with no Redundant Paths.....	160
Table 4.7 – Results from Sensors Which Group Locations in the same Area of the Shell.....	162
Table 4.8 – Results after Eliminating the Combinations that have Sensors in a Straight Line, do not Cover the Source, and Provide Out of Group Answers.....	164
Table 5.1 – Energy Transmitted through Air and Water Interfaces with Steel... ..	211
Table 6.1 – Measured Differences in the Arrival Time between $t_0$ and Sensors 13 and 15.....	287
Table 7.1 – Feature Extraction.....	312
Table 7.2 – Training and Testing Results.....	314
Table 7.2 – Training and Testing Results.....	318

## List of Figures

### Chapter 1: Introduction and Overview

Figure 1.1 – General Purpose Tank Car .....	3
Figure 1.2 – Hydrogen Fluoride Pressure Tank Car .....	3
Figure 1.3 – FiberReinforced Pipe.....	4

### Chapter 2: Background and Literature Review

Figure 2.1 – Schematic Diagram of Typical Acoustic Emission Sensor.....	8
Figure 2.2 – Frequency Spectrum of Wide Band and R6I Sensors.....	9
Figure 2.3 – Acoustic Emission Waveform.....	11
Figure 2.4 – Particle Displacements for Bulk Plane Waves.....	13
Figure 2.5 – Effect of Different Acoustic Velocities on the Waveform.....	15
Figure 2.6 – Rayleigh Waves.....	16
Figure 2.7 – Wave at an Interface between Two Media.....	16
Figure 2.8 – Relative Amplitudes for Transmitted and Reflected Waves at the Interface of Acrylic/Aluminum Generated by an Incident Compression Wave.....	19
Figure 2.9 – Particle Displacement for Plate Waves.....	21
Figure 2.10 – Phase and Group Velocities.....	22
Figure 2.11 – Dispersive Curve of Group Velocity for Steel.....	23
Figure 2.12 - Dispersive Curve for Phase Velocity.....	24
Figure 2.13 - Dispersive Curve for Group Velocity.....	24
Figure 2.14 – Attenuation of Various Frequencies in Gas Pressure Vessel Wall. ..	28
Figure 2.15 – Flexural Plate Wave Traveling in a Steel Plate Creating a Bulk Wave at a Characteristic Angl.....	30



Figure 2.16 – Linear Source Location.....	37
Figure 2.17 – Result of Source Location with Two Sensors on a Plane.....	40
Figure 2.18 – Three Sensor Array with Detection Sequence 1,2,3.....	40
Figure 2.19 – Series of Contiguous Triangle Sensor Arrangement.....	43
Figure 2.20 – Guarding Sensor Scheme.....	44
Figure 2.21 – First Hit Zone by Central Sensor.....	45
Figure 2.22 – Ying Array Configuration.....	46
Figure 2.23 – Four Sensor Array.....	48
Figure 2.24 – Equilateral Triangle Sensor Arrangement.....	49
Figure 2.25 – Dispersion Effect in a Thin Plate.....	51
Figure 2.26 – Zone Construction.....	54
Figure 2.27 – Multi-Element Sensors Used to Determine the Angle of the Source.....	57
Figure 2.28 – Source Location Using Inverse Ray Tracing.....	57
Figure 2.29 – Possible Wave Propagation Paths in a cylinder.....	59
Figure 2.30 – Waveform of Multiple Arrivals Due to Different Propagation Paths.....	60
Figure 2.31 – Flowchart for Simplex Optimization Source Location.....	62
Figure 2.32 – Example of Multi-layer Perceptron Network.....	64
Figure 2.33 – A Neuron Model.....	65

### Chapter 3: Preliminary Study of Source Location on Empty Tank CARRS

Figure 3.1 – Artificial Sources.....	71
Figure 3.2 – Wide Band Sensor Waveform 50' from Artificial Sources.....	72
Figure 3.3 – Tank Car Located in the Ferguson Laboratory.....	73
Figure 3.4 – MISTRAS System.....	74

Figure 3.5 – Attenuation Test Setup.....	75
Figure 3.6 – Attenuation Curve.....	75
Figure 3.7 – Area of Tank Car Used for Source Location Studies.....	76
Figure 3.8 – Sensor Arrangement.....	78
Figure 3.9 – Results from Zonal Method with Open Spaced Sensor Arrangement.....	79
Figure 3.10 – Results from Zonal Method with Close Spaced Sensor Arrangement.....	81
Figure 3.11 – Attenuation Effect on the Arrival Time.....	83
Figure 3.12 – The Triangulation Method.....	84
Figure 3.13 – Test Setup for Velocity Measurements.....	86
Figure 3.14 – Velocity Results.....	87
Figure 3.15 – Test Setup for the Attenuation Effect.....	89
Figure 3.16 – Waveform from Near Filed Source and Far Field Source.....	89
Figure 3.17 – Dispersive Curve for 15/32” Thick Steel Plate.....	91
Figure 3.18 – Filtered Signal at 145 – 155 kHz.....	92
Figure 3.19 – Velocity Results.....	95
Figure 3.20 – Group Velocity.....	96
Figure 3.21 – Flowchart for the Source Location Program.....	98
Figure 3.22 – Results from Pencil Lead breaks in Area with no Discontinuities.....	100
Figure 3.23 – Results from Pencil Lead Breaks in an Area with a Vertical Weld.....	100
Figure 3.24 – Results from Pencil Lead Breaks in Area with Welds .....	101
Figure 3.25 – Results from Area with no Discontinuity Using R15I Sensors.....	102

Figure 3.26 – Test Setup for a Wave Propagation Study on the Upper Part of the Bolster.....	104
Figure 3.27 – Test Setup for a Wave Propagation Study around the Bolster.....	105
Figure 3.28 – Distance from the Trigger Sensor to Sensors 3 and 4 for the Upper Part of the Bolster.....	106
Figure 3.29 – Measured Distance from the Trigger Sensor to Sensors 3 and 4 for the Lower Part of the Bolster.....	109
Figure 3.30 – Distance from the Trigger Sensor to Other Sensors.....	111
Figure 3.31 – Waveform Generated by Bar Bending Method.....	114
Figure 3.32 – Bar Bending Test Setup in the Area with no Discontinuities.....	115
Figure 3.33 – Results from Bar Bending in the Area with no Discontinuities.....	116
Figure 3.34 – Test Setup for Multiple Sources Study.....	117
Figure 3.35 – Results from Multiple Sources.....	118
Figure 3.36 – Results from Bar Bending in the Area Including Welds.....	119
Figure 3.37 – Bar Bending Test Set-up in the Bolster Area.....	120
Figure 3.38 – Results from Bar Bending in the Bolster Area.....	121
Figure 3.39 – Test Setup for a Bar Bending Test at the End of the Tank.....	122
Figure 3.40 – Hydrogen Fluoride Tank Car.....	126
Figure 3.42 – The DiSP System.....	127
Figure 3.42 – Attenuation Test Setup.....	128
Figure 4.43 – Attenuation Curve.....	129
Figure 3.44 – Dispersion Curve for a Tank car with 13/16 inches Wall Thickness.....	130
Figure 3.45 – Velocity Results.....	131
Figure 3.46 – Group Velocity at a 100 KHz.....	132
Figure 3.47 – Time Difference between Two modes with 145-155 kHz Signal...	134
Figure 3.48 – Difference in the arrival time between the first two modes.....	135

Figure 3.49 – Phase Velocity Dispersive Curve for 13/16” Thick Shell.....	137
Figure 3.50 – Phase Velocity Dispersive Curve for 0.55” Thick Shell.....	137
Figure 3.51 – Locations of Sensors and Lead Breaks.....	139
Figure 3.52 – Errors due to Different Value of Velocity.....	140
Figure 3.53 – Results from Lead Breaks.....	140

#### Chapter 4: Jacking and Twist Bar Tests on an Empty Tank Car

Figure 4.1 – DiSP system.....	146
Figure 4.2 – Sensor Locations on the Tank Body.....	147
Figure 4.3 – Four Possible Wave Propagation Paths.....	153
Figure 4.4 – Source Locations Listed in Table 4.4.....	157
Figure 4.5 – Source Locations Listed in Table 4.5.....	159
Figure 4.6 – Source Locations Listed in Table 4.6.....	161
Figure 4.7 – Source Locations Listed in Table 4.7.....	163
Figure 4.8 – Source Locations Listed in Table 4.8.....	165
Figure 4.9 – Final Results.....	165
Figure 4.10 – Results from Multiple Sources.....	167
Figure 4.11 – Jacking Test Setup.....	168
Figure 4.12 – Load Schedule for a Jacking Test.....	169
Figure 4.13 – Symbols Used for Each Bolster.....	170
Figure 4.14 – Results from Combinations of Three Sensors from the AL Jacking Test.....	172
Figure 4.15 – Final Results from the AL Jacking Test.....	173
Figure 4.16 – Results from Combinations of Three Sensors from BR Jacking Test.....	175
Figure 4.17 – Final Results from BR Jacking Test .....	176

Figure 4.18 – Example of Waveform from Jacking Test at BL...	178
Figure 4.19 – Results from Combination of Three Sensors from BL Jacking Test with the Tight Band Frequency Approach.....	179
Figure 4.20 – Results from Combination of Three Sensors from BL Jacking Test .....	181
Figure 4.21 – Final Results from BL Jacking Test.....	182
Figure 4.22 – Crack at A End Reinforcement Pad.....	183
Figure 4.23 – Position of Jacks.....	185
Figure 4.24 – Amplitude of Emissions.....	186
Figure 4.25 – Results from Combinations of Three Sensors for Blocked Jacking Test.....	188
Figure 4.26 – Final Results.....	189
Figure 4.27 – Ultrasonic Testing on Top of the A End.....	190
Figure 4.28 - Results from Ultrasonic.....	191
Figure 4.29 – Twist Bar Test.....	192
Figure 4.30 – Load Schedule for a Twist Bar Test.....	193
Figure 4.31 – Results from Combination of Three Sensors from the Twist Bar Test at BR.....	195
Figure 4.32 – Final Results from Twist Bar Test at BR.....	196
Figure 4.33 – Results from Combinations of Three Sensors from the Twist Bar Test.....	198
Figure 4.34 – Final Results from Twist Bar Test at BL and Jack at BR .....	199
Figure 4.35 – Locations of the Bar.....	200

## Chapter 5: Preliminary Study of Source Location on Water Filled Tank Cars

Figure 5.1 - Center Punch.....	204
--------------------------------	-----

Figure 5.2 - Waveform from Center Punch Captured by R15I Sensor.....	205
Figure 5.3 - Test Setup for Attenuation Test on Filled Tank.....	206
Figure 5.4 - Attenuation Curve for Water Filled Tank.....	207
Figure 5.5 – Waveform from Bar Bending.....	209
Figure 5.6 – Filtered Signal (145-155 kHz).....	210
Figure 5.7 - Phase Velocity Dispersive Curve [PolyModal, 1998].....	212
Figure 5.8 - Phase Velocity Dispersive Curve from 0 to 100 KHz Comparing Shell and Water Wave Velocity.....	213
Figure 5.9 – Group Velocity Dispersive Curve.....	215
Figure 5.10 – Signal from Bar Bending on the Full Tank.....	216
Figure 5.11 – Test Setup for Velocity.....	217
Figure 5.12 - Velocity Results of 15-25 KHz Signal on Water Filled Tank... ..	218
Figure 5.13 - Results from Bar Bending in a Small Area.....	219
Figure 5.14 - Results from Bar Bending in an Area with no Discontinuities.....	220
Figure 5.15 - Results from Bar Bending in an Area with a Vertical Weld.....	221
Figure 5.16 - Results from Bar Bending in an Area with Vertical and Horizontal Welds.....	222
Figure 5.17 - Results from Bar Bending in a Large Area.....	223
Figure 5.18 - Results from a Bar Bending in the Bolster Area.....	224
Figure 5.19 – Attenuation on a Water Filled Tank Car.....	229
Figure 5.20 – Group Velocity of 13/16” Thick Tank Car Shell.....	230
Figure 5.21 – Wave Propagation Time Through Shell and Water.....	231
Figure 5.22 - Locations of Sensors and Bars.....	234
Figure 5.23 - Results from a Bar Bending Test at Location-A.....	235
Figure 5.24 - Results from a Bar Bending Test at Location B .....	236
Figure 5.25 - Location Results from a Bar Bending Test at Location C.....	237
Figure 5.26 - Location Results from a Bar Bending Test at Location D.....	238

Figure 5.27 - Location Results from a Bar Bending Test at Location E.....	239
Figure 5.28 – Phase Velocity of 13/16” Thick Steel Plate.....	242
Figure 5.29 – Phase Velocity from 0 to 100 kHz of 13/16” Thick Steel Plate.....	242
Figure 5.30 – Leakage Angle of Different Frequencies Transmitted into the Water.....	244
Figure 5.31 – Leakage Waves for Three Frequency Components.....	245
Figure 5.32 – AE generated by Bar Bending on a Full Tank.....	246
Figure 5.33 – Possible Waves in a Tank Car.....	248
Figure 5.34 – Energy Transmitted at a Water/Steel Interface.....	249
Figure 5.35 – Bar A and Sensor Locations on the Tank Car.....	251
Figure 5.36 – Measured Wave Propagation Time between Sensors 9 and 21.....	252
Figure 5.37 – Propagation Path between source and Sensor 21 for Directly Transmitted Water Borne Wave.....	252
Figure 5.38 – Calculated Time for the Wave to Propagate from the Source to Sensor 21 Versus the Angle of the Incident Water Borne Wave.....	254

## Chapter 6: Internal Pressure Test of a Tank Car

Figure 6.1 – Sensor locations.....	259
Figure 6.2 – Load Sequence for the Pressure Test.....	260
Figure 6.3 – Results from Combinations of Three Sensors from the First Group.....	264
Figure 6.4 – Final Results for Data from the First Group.....	265
Figure 6.5 – Results from Combinations of Three Sensors from the Second Group.....	266
Figure 6.6 – Final Results for Data from the Second Group.....	267

Figure 6.7 – Results from Combinations of Three Sensors from the Third Group.....	268
Figure 6.8 – Final Results from the Third Group.....	269
Figure 6.9 – Results from Combinations of Three Sensors from the Fourth Group.....	270
Figure 6.10 – Final Results for Data from the Fourth Group.....	271
Figure 6.11 – Results from Combinations of Three Sensors from the Fifth Group.....	272
Figure 6.12 – Final Results for Data from the Fifth Group.....	273
Figure 6.13 – Results from Combinations of Three Sensors from the Sixth Group.....	274
Figure 6.14 – Final Results for Data from the Sixth Group.....	275
Figure 6.15 – Results from Combinations of Three Sensors from the Seventh Group.....	276
Figure 6.16 – Final Results for Data from the Seventh Group.....	277
Figure 6.17 – Results from Combinations of Three Sensors from the Last Group.....	278
Figure 6.18 – Final Results for Data from the Last Group.....	279
Figure 6.19 – Group Velocity of 13/16” Thick Tank Car Shell.....	281
Figure 6.20 – Group Velocity of 0.4” Thick Tank Car Shell.....	281
Figure 6.21 – Original Event 1321 Waveform.....	283
Figure 6.22 – Filtered Event 1321 Waveform at a 100 kHz.....	284
Figure 6.23 – Source Location Results for Event 1744 Including Water Borne Wave.....	286
Figure 6.24 – Event 1744 Final Results.....	288
Figure 6.25 – Top View of Shell Showing Position of Sensors Relative to Point on Shell (O) Directly Opposite Source.....	289



Figure 6.26 – Side View of the Tank Showing the Point the Incident Water Borne Wave Strikes on Line BC with Angle $\gamma_0$ .....	290
Figure 6.27 – Section AA Showing Wave Propagation Through Water with Incident Angle $\gamma_0$ .....	291
Figure 6.28 – Section A'A' Located X inches from Section AA Showing Wave Propagation Through Water with Incident Angle $\gamma_0$ .....	291
Figure 6.30 – Top View of the Tank Showing Incident Angle Contour Plots of 0, 7, and 15 Degrees.....	293
Figure 6.31 – Source Propagates through Water and Incident at Point A and Propagate along the Shell to Sensor 13.....	294
Figure 6.32 – Calculated Time for the Wave to Propagate from the Source to Sensor 15 Versus the Angle of the Incident Water Borne Wave .....	294

## Chapter 7: Exploratory Source Location Studies in Composites

Figure 7.1 – Glass Fiber Reinforced Epoxy Pipe.....	298
Figure 7.2 – Measurement of Velocity in Axial Direction.....	301
Figure 7.3 – Wave Velocity in Axial Direction.....	302
Figure 7.4 – Measurement of Velocity in Hoop Direction.....	303
Figure 7.5 – Wave Velocity in Hoop Direction.....	304
Figure 7.6 – Measurement of Velocity along Fiber Direction.....	304
Figure 7.7 – Wave Velocity along Fiber Direction.....	305
Figure 7.8 – Attenuation in Different Directions.....	306
Figure 7.9 – Possible Wave Paths.....	307
Figure 7.10 – MLP Neural Network.....	308
Figure 7.11 – Output Zones on the Pipe.....	310
Figure 7.12 – Output Zones.....	311

Figure 7.13 – Simulations of Hidden Units.....	313
Figure 7.14 – Impact Testing Frame.....	315
Figure 7.15 – Final Network.....	316
Figure 7.16 – Damage Location.....	317

# **CHAPTER 1**

## **INTRODUCTION AND OVERVIEW**

### **1.1 INTRODUCTION**

Acoustic Emission (AE) has been widely used to detect stress waves generated by internal stress changes such as local yielding, crack initiation and fracture. The technique is able to monitor an entire structure with a limited number of sensors. An additional advantage is the flexibility to monitor during a controlled overload or continuously during operation. In the last decade, AE has been widely used as a nondestructive test method for tank car and pressure vessel structures. Even though these structures are relatively large, they can be inspected with a single test.

Location of the source of the AE is particularly important when monitoring large structures and one of the limitations of the technology is the inability to accurately identify the position of emitting defects. The objective of this research is the development of reliable source location techniques for large structures such as railroad tank cars.

### **1.2 OVERVIEW**

The work focuses on developing a new concept of waveform processing and a reliable search algorithm. The effectiveness of conventional and new source location methods for composite materials was also studied.

Four specimens were used in the research program, two railroad tank cars and two fiber reinforced plastic pipes. Figure 1.1 is a picture of the first specimen, a general purpose tank car located in the University of Texas at Austin Ferguson Structural Laboratory. The tank was used mainly to study AE wave propagation and location of artificial sources. The second tank car is shown in Figure 1.2. This car is a hydrogen fluoride pressure tank car located at the Rescar facility in Orange, Texas. Follow-up inspection of this car with another nondestructive testing method found an area of severe corrosion and another area with cracks. The car had been permanently removed from service and was used as a test bed for this and other research projects. The last two specimens are 6” diameter filament wound fiber reinforced plastic pipes of the type shown in Figure 1.3.

The research started with wave propagation studies on a steel tank car using artificial sources. First, currently used approaches were explored to locate the known source and the causes of the error were studied. Then, an improved method was developed for both the empty and water filled tank cars. This is discussed in Chapter 3 and 5. Finally, the approach was applied to the car under jacking and pressure tests. The method was able to identify defect locations in these experiments and the results show good agreement with follow up ultrasonic inspection. The experiments on the cars are discussed in Chapter 4 and 6.

After obtaining an approach that yields good results on a homogeneous steel tank, the same approach was applied to fiber reinforced plastic pipes. As expected, the accuracy of the results was not very good. Therefore, a new source location technique using neural networks was studied and developed for the application. This work is discussed in Chapter 7.



Figure 1.1 - General Purpose Tank Car

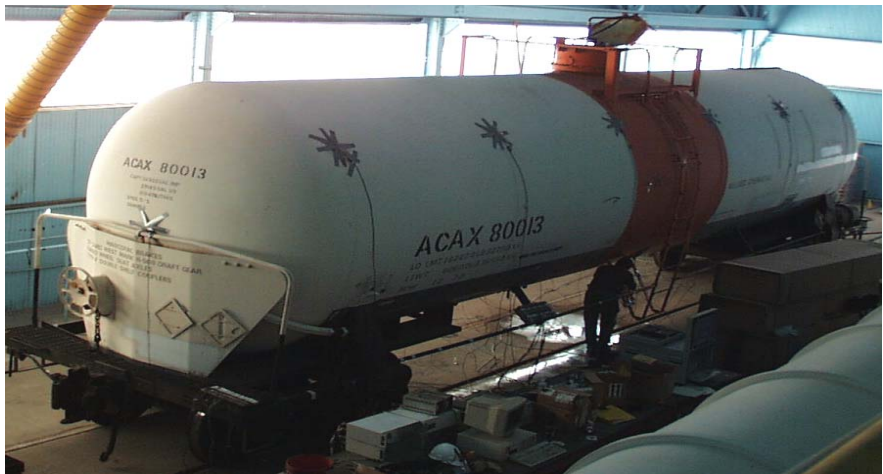


Figure 1.2 – Hydrogen Fluoride Pressure Tank Car



Figure 1.3 - Fiber Reinforced Plastic Pipe

## **CHAPTER 2**

### **BACKGROUND AND LITERATURE REVIEW**

#### **2.1 ACOUSTIC EMISSION**

##### **2.1.1 Introduction**

Acoustic Emission (AE) is defined as “the class of phenomenon whereby transient elastic waves are generated by the rapid release of energy from localized sources within a material, or the transient waves so generated” [ASTM E 1316]. For most nondestructive test applications, emission is monitored in the range of 10 kHz to 1 MHz. Emission can be from many different mechanisms including deformation and fracture. In metals, acoustic emission sources include yielding, corrosion and crack growth [Heiple and Carpenter 1987a, 1987b]. In composites, matrix cracking, fiber breakage, and fiber debonding are common sources of emission [Fowler, 1979].

In addition to internal acoustic emission sources, external noise such as mechanical rubbing, wind, air hoses and filling can create elastic waves, which interferes with the genuine data. These extraneous noises need to be prevented in the test or filtered out before the data is analyzed.

Acoustic emission is generated by the material itself. In contrast, other types of stress wave nondestructive testing methods such as impact echo and

ultrasonics need an external input source. An additional advantage of acoustic emission, compared to these other methods is that it is a global test. A global test covers a large area with one test, whereas the other methods cover a very limited area and are referred to as local tests. AE can also be used as a continuous monitoring system, which is important for many in-service structures. A drawback of acoustic emission is that it is dependent on the applied load. As a result, some discontinuities may not emit detectable AE under a particular load. The practical application of acoustic emission technology to field inspection of structures has advanced steadily over the past 25 years. Codes, standards, and recommended practices have been developed and the method has found wide acceptance as a method of nondestructive inspection [CARP, ASME sections V and X, AAR, ASTM, MONPAC]. There are four major areas where additional research is needed in order for the technology to reach its full potential.

- **Source Location:** The ability to determine the position of the emission sources in a large structure has important practical implications. In order to evaluate and, if appropriate, repair the source of emission it is necessary to be able to locate it without an extensive search. This area is the subject of the research reported in this dissertation.
- **Source Identification:** As presently practiced, an acoustic emission test detects the presence of an emission source but provides very little information about the type of defect, or external noise source giving rise to the emission. This area is often referred to as signature analysis. Limited guidance may be provided by the governing test procedure. Additional, complementary research has been carried out



in this area by C. A. Barnes at the University of Texas at Austin [Barnes 2000].

- **Defect Size and Orientation Determination:** In metals, fracture mechanics uses information about the size, orientation, and type of defect to calculate its structural significance. Acoustic emission provides an evaluation of the structural significance of a defect under the applied test load [MONPAC, CARP]. Accordingly, if the structural significance and type of a defect is known, its size and orientation may be less important. However, it would still be of value to determine this information from an AE test.
- **Probability of Detection (POD):** Conventional round robin methods for determining POD are not possible with AE because of the Kaiser effect. Accordingly, other methods based on theoretical studies with benchmark experimental testing have been proposed and incorporated into some of the test procedures [Fowler 1996, AAR].

### 2.1.2 Instrumentation

Acoustic Emission testing instrumentation is made up of three parts; sensors, preamplifiers, and signal analysis and recording unit. AE sensors are designed to attach to the surface of the specimen and come in two types, resonant and wide band. AE sensors usually use piezoelectric crystals that are acoustically coupled to the surface of the test item so that dynamic surface motion propagates into the piezoelectric element. The dynamic strain in the element generates a voltage time signal, which is the output from the sensor. Resonant sensors are

designed to sense a particular frequency range of interest. This is accomplished by choosing the appropriate dimensions of the piezoelectric element [Nondestructive Testing Handbook Vol. 5]. The benefit of the resonant sensor is that it has high sensitivity to the selected frequency range. The disadvantage is that it cannot be used for frequency analysis. The other type of sensor, a wide band sensor, is similar to a resonant sensor except that it is highly damped with damping material or backing added to the piezoelectric element. The purpose of the damping is to eliminate the preferential response of the sensor to particular frequencies. This results in a broad frequency response band. Unfortunately, the backing component makes the wide band sensor less sensitive. This is one of the major drawbacks of this type of sensor. Figure 2.1 shows schematic diagram of a typical acoustic emission sensor. The plots in Figure 2.2 show the calibration response of wide band (type S9208) and R6I sensors. The curve for the R6I includes 40 dB gain from the preamplifier. At the peak response frequency of 80-90 kHz the R6I has approximately 18 dB greater response than the wide band.

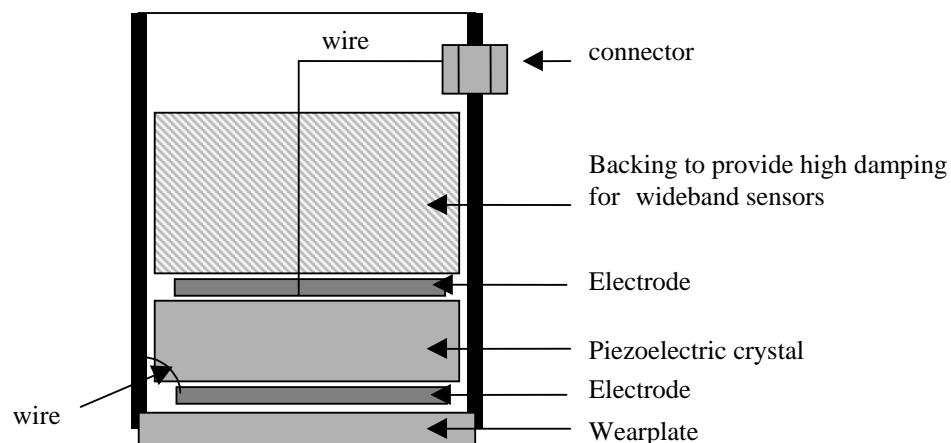


Figure 2.1 – Schematic Diagram of Typical Acoustic Emission Sensor [Nondestructive Testing Handbook, Vol. 5]

Some sensors are integrated with the preamplifier and some have the preamplifier as a separate unit. The purpose of the preamplifier is to increase the signal so that it can be transmitted to the signal analysis unit. Most preamplifier gains are in the range of 20 to 60 dB.

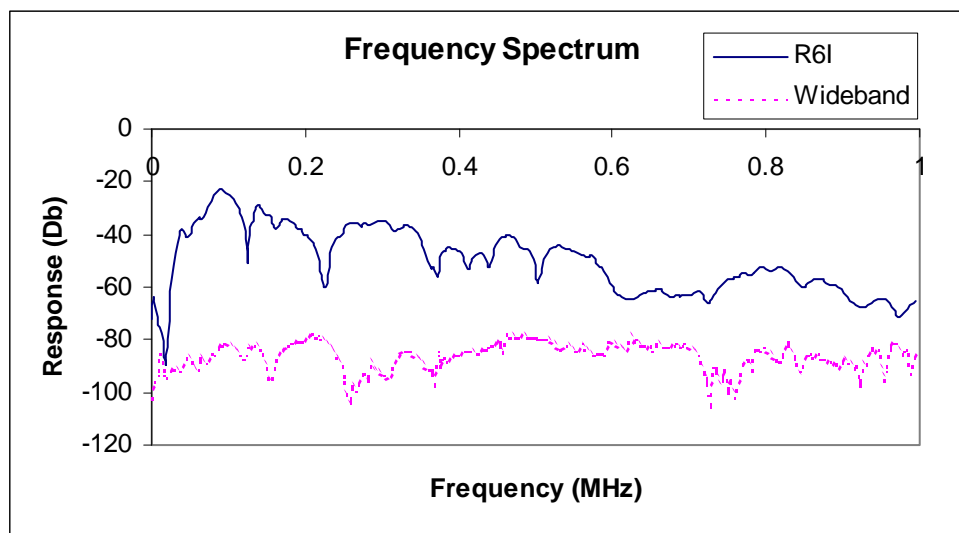


Figure 2.2 – Frequency Spectrum of Wide Band and R6I Sensors [PAC, 2000]

### 2.1.3 Signal

The acoustic emission instrument uses a preset threshold to detect the signal. Once the signal amplitude exceeds the threshold level, data acquisition is triggered and the system extracts features of the waveform such as arrival time, amplitude and duration. In order to eliminate background noise, the threshold value is just above the background noise level. A typical value is between 40 and 55 dB. The signal is monitored once its amplitude is above the threshold level

until it falls below the threshold for a certain value of time, which is called hit definition time. The typical value for hit definition time is 400  $\mu$ Sec.

Recently, the digital AE systems have been developed and this allows the waveform to be recorded for later processing. In order to capture a complete waveform, it is desirable to include a delay time or pre-trigger.

An example of an acoustic emission signal is shown in Figure 2.3. The signal was generated by a pencil lead break on a composite plate captured by a wide band sensor. It is important to note that the signal from the sensor is not the same as the wave in the material. The signal from the sensor is the response of the piezoelectric crystal to the impulse pressure. Pressure can be due to shear or flexure of the plate. The sensor will always ring, more so if it is resonant, and this gives rise to signals that are longer than the waves striking the face of the sensor.

In Figure 2.3 the wave obtained from the plate is a plate wave. The amplitude is defined as “ the peak voltage (measured in decibels) of the largest excursion attained by the signal waveform from an emission event” [CARP, 1999]. The first portion of the wave, which travels faster and arrives at the sensor first, is called an extensional mode. This mode has small energy and, as is the case with this wave, the amplitude is often below the threshold value. For this reason, the delay time is needed. Plate waves are described later in this chapter.

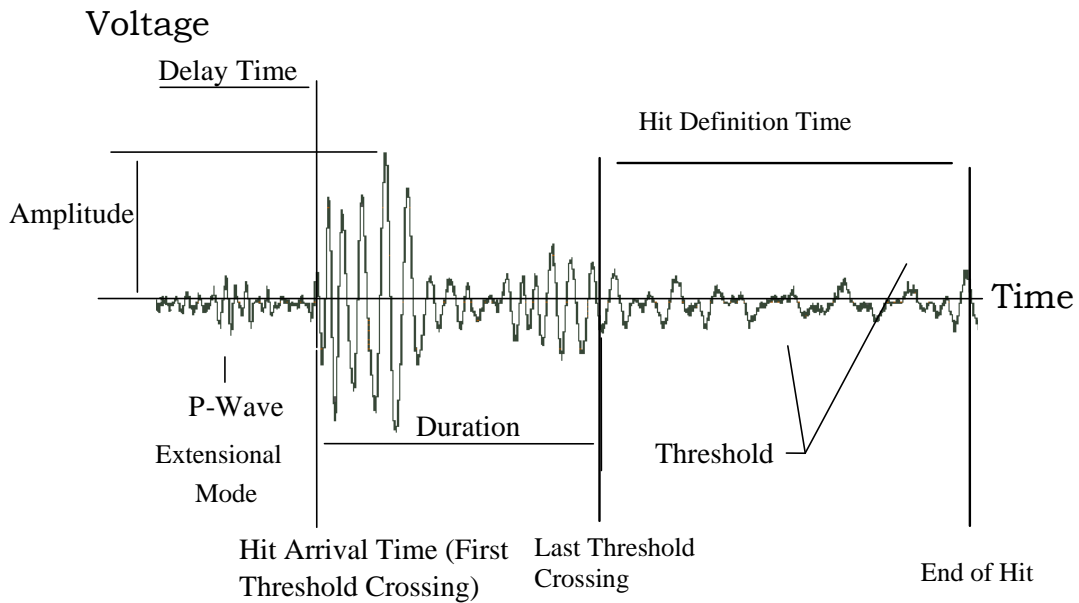


Figure 2.3 – Acoustic Emission Waveform

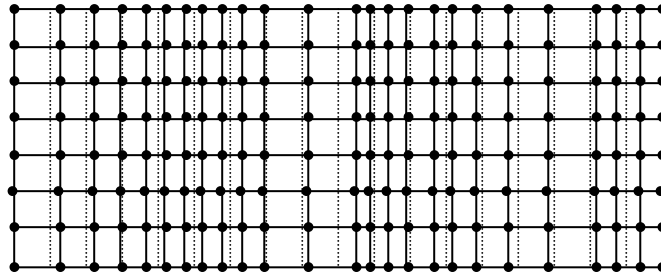
## 2.2 WAVE PROPAGATION

Generally, stress waves at the emission source are not the same as the acoustic emission waves detected by a sensor. A complex change in the stress waves occurs as they propagate through the medium. If a sudden push is applied to a solid, it is compressed. It resists the compression, and a wave analogous to a sound wave is started. Similarly, if a solid is distorted by pushing it sideways (called shearing), it tries to pull itself back and a shear wave starts to travel through the material. The speed of the waves is determined by the properties of the material, and the types of waves generated are governed by the geometry and

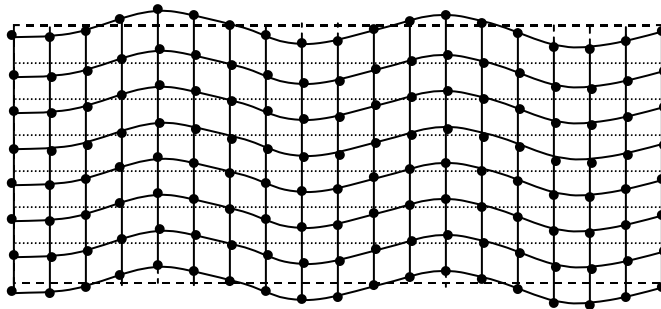
boundary condition of the structure. In order to develop source location techniques, it is necessary to understand the characteristics of stress waves. This section describes the phenomena of waves propagating in an elastic solid.

### **2.2.1 Elastic Stress Waves in Bulk Material**

Waves traveling through a medium whose dimensions are much larger than the wavelength are classified as bulk waves [Reese and Kawahara, 1993]. Two types of pure waves are usually generated in bulk material. They are called longitudinal (compression or P) and shear (transverse or S) waves. The type of wave is defined by the particle motion with respect to the direction of travel. Longitudinal waves are waves where the motion of a material particle is parallel to the direction of wave propagation and shear waves have the motion of a material particle perpendicular to the direction of wave propagation. Only longitudinal waves are present in an inviscid fluid. The two types of waves are illustrated in Figure 2.4



(a) Longitudinal Waves



(b) Transverse Waves

Figure 2.4 – Particle Displacements for Bulk Plane Waves

The shear component normally travels at slightly greater than half of the longitudinal velocity. The longitudinal velocity ( $\alpha$ ) and shear velocity ( $\beta$ ) are defined in Equations 2.1 and 2.2 as:

$$\alpha = \sqrt{\frac{\lambda + 2\mu}{\rho}} \dots\dots\dots(2.1)$$

$$\beta = \sqrt{\frac{\mu}{\rho}} \dots\dots\dots(2.2)$$

where  $\rho$  is the density of the material ,  $\lambda$  and  $\mu$  are Lamé' constants which are defined by:

$$\lambda = \frac{E\nu}{(1+\nu)(1-2\nu)} \dots\dots\dots(2.3)$$

$$\mu = \frac{E}{2(1+\nu)} = G \dots\dots\dots(2.4)$$

where E is Young's Modulus,  $\nu$  is the Poisson's ratio, and G is the shear modulus. From Equations 2.3 and 2.4, the longitudinal and shear velocities can be defined as:

$$\alpha = \sqrt{\frac{E(1-\nu)}{\rho(1+\nu)(1-2\nu)}} \dots\dots\dots(2.5)$$

$$\beta = \sqrt{\frac{G}{\rho}} \dots\dots\dots(2.6)$$

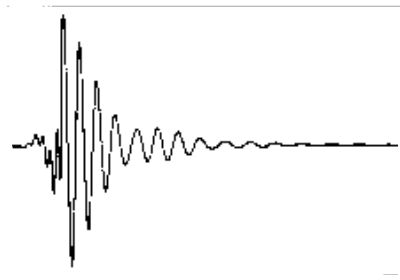
Waves can travel through the depth of material creating pure longitudinal and shear waves, or they can propagate on the surface of the material forming a surface wave. A surface wave has maximum amplitude at the surface boundary and the amplitude decreases with distance from the surface.

Since the two components travel at their own velocity, the result is different waveform shapes at different locations on the surface and in the body of the material. Figure 2.5 demonstrates the effect of different velocities on the

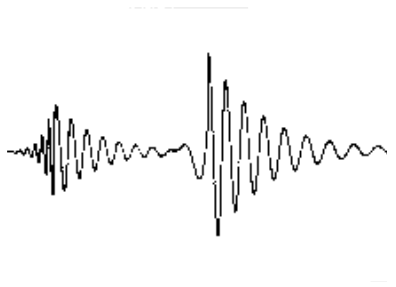


signal. Note that the effects of dispersion and attenuation (see Sections 2.2.3 and 2.2.4) are ignored in the figure.

Motions of the surface wave can be parallel and perpendicular to the surface. If the predominant motion is perpendicular to the surface, the wave is usually called a Rayleigh wave. The velocity of the Rayleigh waves is slightly lower than the shear velocity. Particle displacement of Rayleigh waves is illustrated in Figure 2.6. Note that this wave includes the predominant motion perpendicular to the surface, with some motion parallel to the surface.



a) Longitudinal Shear Waves Detected near Point of Origin



b) Longitudinal Shear Waves Detected Some Distance from the Point of Origin

Figure 2.5 – Effect of Different Acoustic Velocities on the Waveform  
[Handbook on Structural Testing, edited by Reese, R, T et al.]

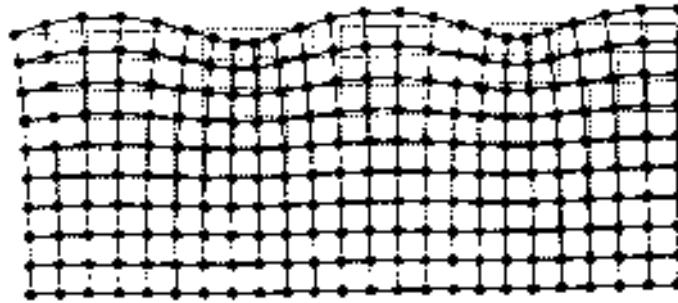


Figure 2.6 – Rayleigh Waves [Handbook on Structural Testing, edited by Reese, R, T et al.]

### 2.2.2 Waves at Boundaries between Solids

When an incident wave travels through a boundary between two media, part of the energy transmits through the boundary and the rest reflects back. This is shown in Figure 2.7.

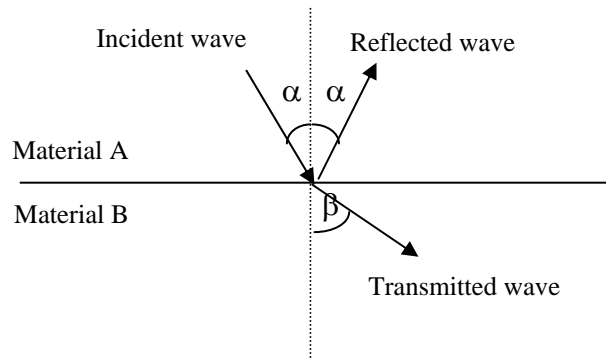


Figure 2.7 – Wave at an Interface between Two Media

The percentage of energy transmitted ( $E_T$ ) and reflected ( $E_R$ ) at the boundary is a function of acoustic impedance ( $Z$ ), which is defined for each material as:

$$Z = \rho V \dots\dots\dots(2.7)$$

$$E_T = \frac{4Z_1Z_2}{(Z_1 + Z_2)^2} * 100 \dots\dots\dots(2.8)$$

$$E_R = \left( \frac{Z_1 - Z_2}{Z_1 + Z_2} \right)^2 * 100 \dots\dots\dots(2.9)$$

where  $\rho$  is the density of the material and  $V$  is the velocity of the wave. The values of the amplitude transmitted and reflected are equal the square root of Equations 2.8 and 2.9, respectively.

Since acoustic impedance is a function of wave velocity, percentage of energy transmitted and reflected may be different for different type of waves. At the interface between the two materials, wave mode conversion may occur. An incident P or S wave arriving at the interface of two solid media can result in additional transmitted and reflected P and S waves. The angle of the reflected wave is always equal to the angle of the incident wave of the same type. The angle of the transmitted wave is a function of the angle of the incident wave. This is described by Snell's Law

$$\frac{\sin \alpha}{\sin \beta} = \frac{V_I}{V_T} \dots\dots\dots(2.10)$$

where  $V_I$  is the velocity of the incident wave,  $V_T$  is the velocity of the transmitted wave,  $\alpha$  is the incident angle, and  $\beta$  is the transmitted angle. The angle of the reflected wave of a different mode type is also given by Snell's Law:

$$\frac{\sin \alpha_I}{\sin \alpha_R} = \frac{V_I}{V_R} \dots\dots\dots(2.11)$$

where the subscript I stands for incident wave and R for reflected wave.

When a mode conversion occurs at the interface, the amount of energy transmitted and reflected in the new modes depends on the angle of the incident waves. The equations to calculate the energy of the mode conversions can be found in other references [Halmshaw, 1991 and Kraukramer, 1976], and will not be discussed in this section. An example of the relative amplitudes of compression and shear waves generated at an acrylic/aluminum interface by an incident compression wave striking at different angles is shown in Figure 2.8. Note that T denotes transmitted waves and R reflected waves.

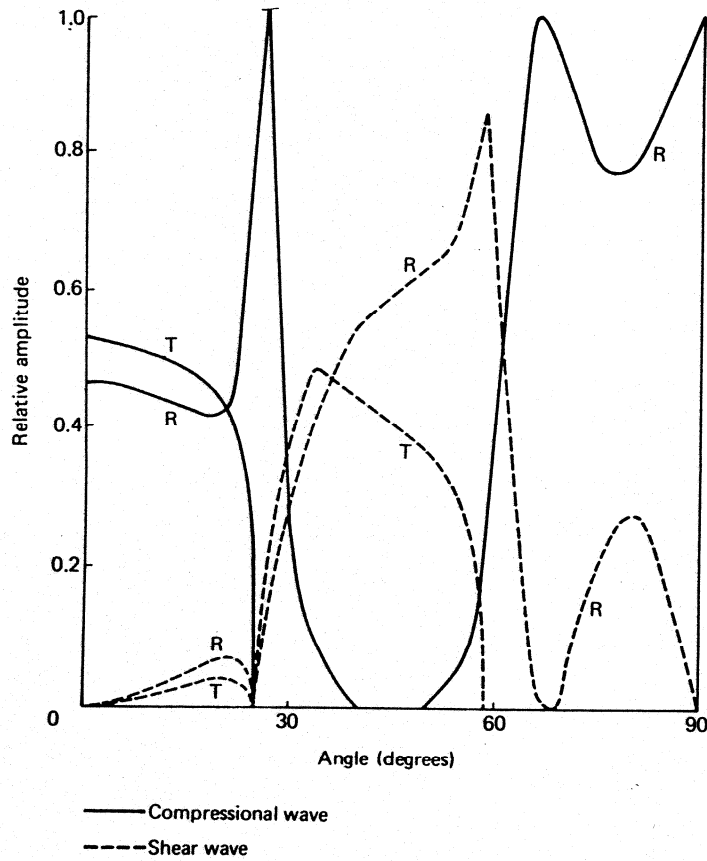
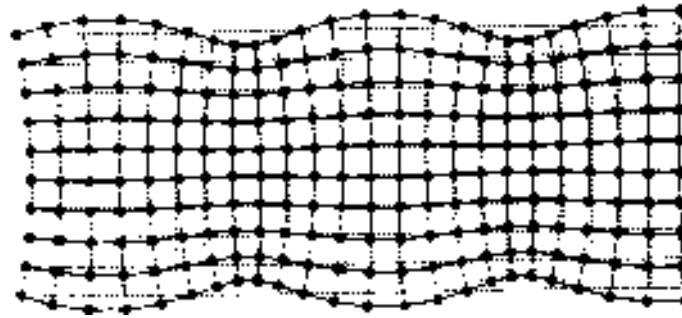


Figure 2.8 – Relative Amplitudes for Transmitted and Reflected Waves at the Interface of Acrylic/Aluminum Generated by an Incident Compression Wave [Halmshaw, 1991]

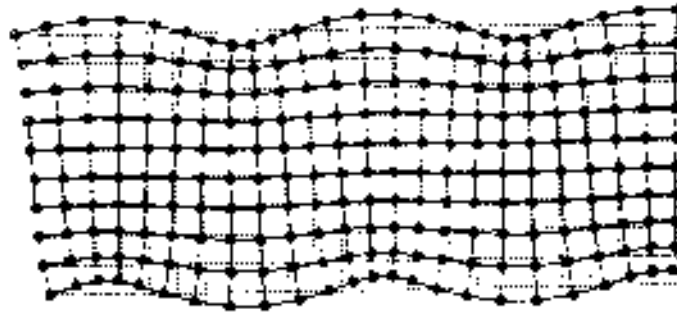
### 2.2.3 Elastic Stress Waves in Plates

When a solid is bounded by two surfaces to form a plate and the thickness of the plate is less than the acoustic wavelength, plate waves, sometime called guided waves or Lamb waves, can occur. The governing equations for the Lamb waves were first derived Professor Horace Lamb in 1917 [Lamb 1917]. A

comprehensive solution of Lamb waves was obtained by Mindlin [Mindlin 1960]. Later, Viktorov in his book dealt with the solution of Lamb waves in great detail [Viktorov 1967]. Most of the work on Lamb waves has been motivated by ultrasonic flaw detection in sheet material. These Lamb waves are the waves that are usually found in shell structures such as tank cars, pressure vessels, and thin pipes. Lamb waves can be considered as two surface waves propagating at the same time which can be synchronized either symmetrically or anti-symmetrically. Particle wave motions in plates are shown in Figure 2.9. The symmetric mode is also called the extensional mode [Gorman, 1991] or the breathing mode [Scruby et al. 1990]. “Flexural mode” is another name used for the anti-symmetric mode. The predominant particle displacement for the extensional mode is in the plane of the plate and the movement out of plane is caused by Poisson’s effect, while the predominant motion of the flexural mode is perpendicular to the plane of the plate [Prosser, 1996]. There are more than two modes of plate waves but in most cases the wave modes of particular interest are the lowest order symmetric mode and the lowest order anti-symmetric mode [Gorman, 1995].



(a)



(b)

Figure 2.9 – Particle Displacement for Plate Waves. (a) First Symmetric Mode; (b) First Antisymmetric Mode [Handbook on Structural Testing, edited by Reese, R, T et al.]

*Phase vs. Group Velocity*

Phase velocity ( $V_{ph}$ ) is the speed of movement of each phase point in the waves moves. The speed of the whole wave packet is called group velocity ( $V_g$ ). Figure 2.10 demonstrates the physical meaning of phase and group velocity.

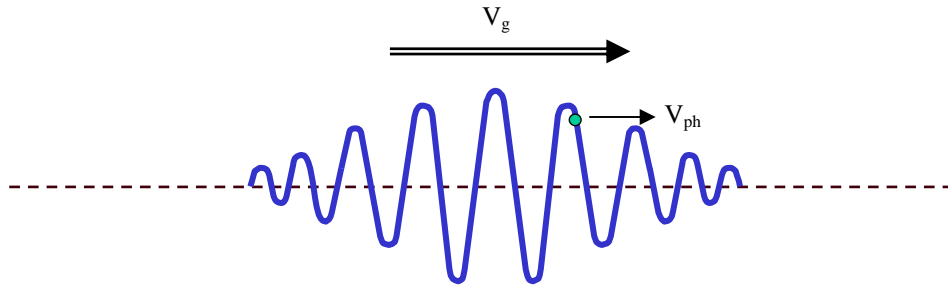


Figure 2.10 – Phase and Group Velocities

Phase velocity is a function of the angular frequency ( $\omega$ ) and wave number ( $k$ ) and is defined by:

$$V_{ph} = \frac{\omega}{k} \dots\dots\dots(2.12)$$

and group velocity is defined by:

$$V_g = \frac{d\omega}{dk} \dots\dots\dots(2.13)$$

Equations 2.8 and 2.9 show that phase and group velocities are dependent on the frequency. This characteristic is called dispersion. This phenomenon causes waves of different frequencies, initially moving together in phase, will drift apart as the packet propagates, making it broader in both space and time. Basically, dispersion causes waves to change shape as they propagate through a plate. Dispersion occurs when waves are propagating in any solid medium in which the wavelength is comparable to one or more dimensions of the medium. A dispersive curve is a plot showing different wave mode velocities as a function



of the wave frequency and the plate thickness. Sometimes the dispersive plot is also called the Krautkramer diagram [Krautkramer, 1976]. Figure 2.11 shows the dispersive curve of group velocity for steel. It is seen that group velocity is a function of plate thickness and frequency.

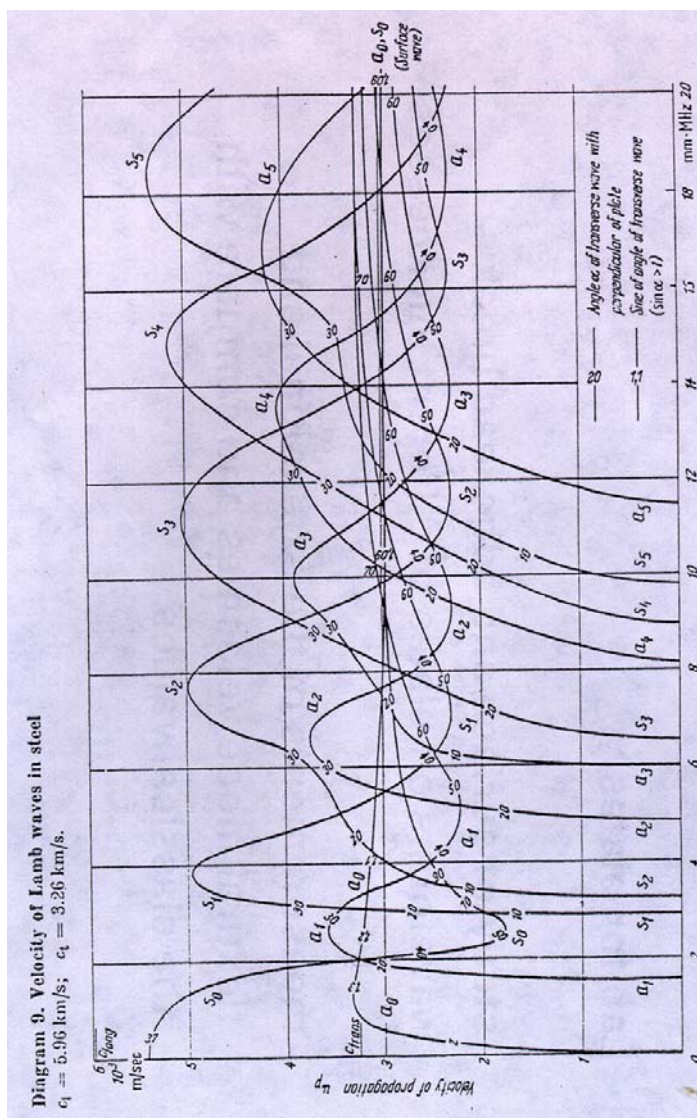


Figure 2.11 – Dispersive Curve of Group Velocity for Steel [Krautkramer, 1976]

Examples of dispersive curves for phase velocity and group velocity for a 15/32" steel plate are shown in Figures 2.12 and 2.13. The dispersive plots were generated by PolyModal Software written by Physical Acoustics Corporation [PAC, 1999].

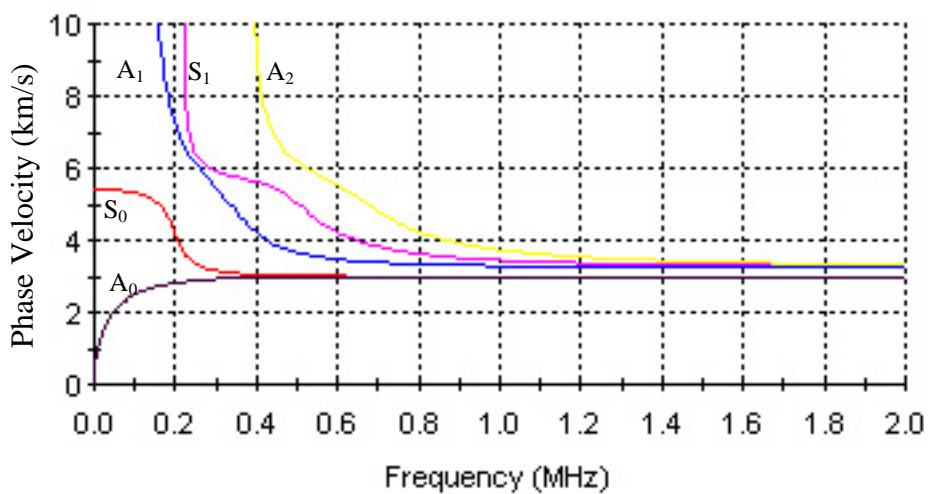


Figure 2.12 - Dispersive Curve for Phase Velocity [PAC, 1999]

The first three modes have the same group velocity at 150 KHz

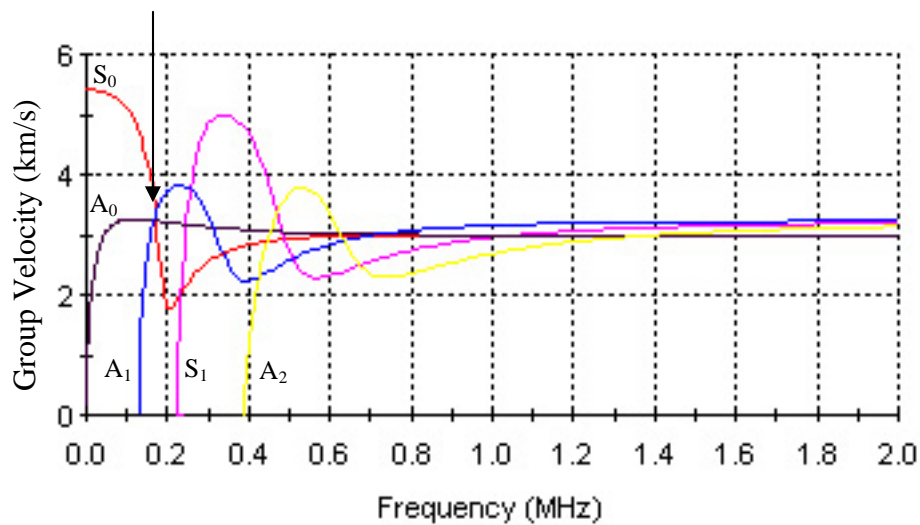


Figure 2.13 - Dispersive Curve for Group Velocity [PAC, 1999]

In Figures 2.12 and 2.13 each line represents a wave mode and the first five wave modes are displayed on the plots. The lowest order symmetric mode is called the extensional mode ( $S_0$ ), while the lowest order anti-symmetric mode is called the flexural mode ( $A_0$ ). From the group velocity plots in Figure 2.13, it is interesting to notice that for a 15/32" steel plate, the first three modes travel at the same group velocity of 3.2 km/sec or 125,000 inch/sec at 150 KHz. For a thicker plate, the position of the intersection point of the first three modes shifts to a lower frequency. A thinner plate has an intersection point of the first three modes at a higher frequency. Although the intersection point shifts in frequency, the value of the group velocity stays constant at 3.2 km/sec or 125,000 in/sec for the same material.

For a low frequency range, the phase velocity of the lowest order symmetric mode ( $C_e$ ) is given in Equation 2.14. The velocity of the lowest order anti-symmetric mode ( $C_f$ ) is defined in Equation 2.15.

$$C_e = \sqrt{\frac{E}{\rho(1-\nu^2)}} \dots\dots\dots(2.14)$$

$$C_f = \left(\frac{D}{h\rho}\right)^{1/4} \sqrt{\omega} \dots\dots\dots(2.15)$$

where  $D = \frac{Eh^3}{12(1-\nu^2)}$ ,  $\omega$  is the circular frequency ( $2\pi f$ ) of a component wave in rad/sec, and h is the thickness of material.

#### 2.2.4 Attenuation of Waves

Attenuation means the decrease in amplitude as a wave travels through a medium [NDT Handbook, Vol. 5]. There are several mechanisms causing this decrease of amplitude which are discussed in this section.

- *Geometric Attenuation*

Geometric attenuation is the phenomenon that a wave loses its energy due to spread (or propagation) over a larger spherical surface. Once the wave is generated, it propagates outwards in all directions from the source. The wavefront is a spherical surface. In order for the energy to remain constant, the amplitude of the wave must decrease with increasing distance from the source.

For body waves in bulk material, if the wave is sufficiently far from the source, the amplitude of the wave will decrease inversely as the distance from the source ( $1/r$ ) where  $r$  is the distance from the source. For surface waves and plate waves, the amplitude decreases as  $1/r^{1/2}$  if the wave is far from the source [NDT Handbook, vol 5].

- *Attenuation from Dispersion*

Dispersion is caused by the frequency dependence of the wave speed as discussed in Section 2.2.3. Since the wave speed is a function of its frequency, a wave made up of various frequency components will change in form as the components propagate along the medium. This is because each component travels at a different speed. The result is a longer duration waveform. In order to maintain a constant energy, the amplitude of the wave must decrease.

- *Attenuation from Scattering and Diffraction*

Scattering of the waves occurs when the waves encounter complex geometric boundaries and discontinuities in the medium and are reflected or partially reflected. Diffraction is a phenomenon that occurs when a wave encounters a sharp edge, such as a crack, and is reflected from the discontinuity. Both scattering and diffraction lead to a decrease (or an increase in some case) in wave amplitude. This phenomenon can cause attenuation.

- *Attenuation due to Energy Loss Mechanisms*

In all the mechanisms discussed earlier, the total energy remains constant if the solid is an elastic medium. However, wave propagation in real media is not conservative. Losses of energy can be from (1) viscoelastic material behavior prevalent in plastics; (2) friction between surfaces that slip; (3) incompletely bonded inclusions, or fibers in composite materials. This loss of energy causes the amplitude of the wave to decrease as the wave propagates through the medium.

Figure 2.15 shows attenuation of various frequencies as a function of distance traveled in a 5 inches thick gas pressure vessel wall [NDT Handbook Vol. 5]. The relative amplitudes are plotted as attenuation in decibels equal to  $20\log_{10}(A/A_0)$  where  $A$  is the measured amplitude at the distance ( $r$ ) and  $A_0$  is the amplitude at  $r = 0$ . A series of plots have been displayed to show the attenuation variations as a function of the frequency component. The measured data are shown by the circles and the solid lines are an approximation of the linear

variations of the data for the near and far field. The dotted lines are a linear value based on the amplitude at  $r = 0$  and  $r = 7.5$  meters.

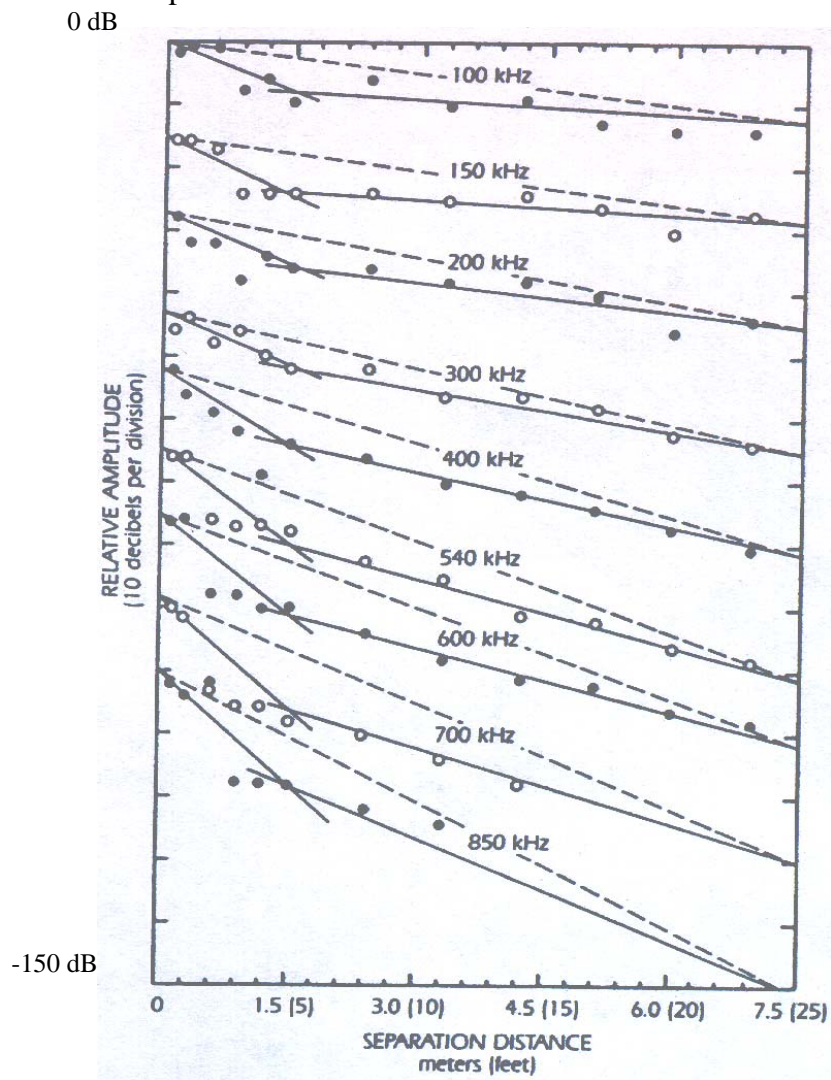


Figure 2.14 – Attenuation of Various Frequencies in Gas Pressure Vessel Wall [NDT Handbook, vol. 5]

In Figure 2.14, it is seen that the attenuation increases dramatically within the first 1.5 m. (5 ft.). Much of this is caused by geometric attenuation as the

waves spread outward from the source. At distances greater than 1.5 m. (5 ft.), the attenuation decreases but is still present. Most of this is caused by energy loss mechanisms with a smaller component caused by dispersion. It is also seen that higher frequency waves tend to attenuate faster than lower frequency ones.

- *Attenuation due to Surface Condition or Coatings*

A plate with a very rough surface, such as may occur in a corroded area will have higher attenuation than a similar plate with a smooth surface. The rough surface causes scattering and diffraction of the type discussed above. With a severely corroded plate the attenuation effect can be very significant. Certain types of surface coatings, such as thick layers of paint, a bituminous coating, or bonded insulation can also result in an increase in the attenuation

- *Attenuation due to Energy Loss into Adjacent Media*

This loss can be by direct transmission as discussed in Section 2.2.2, or by leaky Lamb waves. These waves are discussed in the following Section.

### **2.2.5 Leaky Lamb Waves**

When a plate is in contact with other media, energy can radiate from the plate into the surrounding air, liquid, or solid. This is known as a leaky Lamb wave. Osborne and Hart [1945] dealt with the problem of waves generated in a steel plate immersed under water. Numerous papers have been presented on this subject [Bao et al. 1998, Pavlakovic 1998, Zhu et al. 1991, Schmidt et al. 1985, Queheillalt et al. 1997, Sawaguchi et al. 1993, Motegi et al. 1999, Kinra et al.

1995, Cheeke et al. 1998, Diachok 1973, Pareige et al. 1992, and Kettani et al. 1996]. All Lamb waves are leaky unless the plate specimen is in a vacuum. For an AE stress wave, the amount of leakage is important as it affects the attenuation of the wave. Once the energy leaks from the plate, it is free to propagate in the form of bulk waves traveling in the other medium as shown in Figure 2.15.

Figure 2.15 shows a flexural wave in a steel plate bounded by water on one side.  $\lambda$  is the wavelength and is a function of wave velocity ( $V$ ) and frequency ( $f$ ) as defined in the following equation:

$$\lambda = \frac{V}{f} \dots\dots\dots(2.16)$$

In addition to the frequency and phase velocity, the attenuation must be determined for each mode at each frequency.

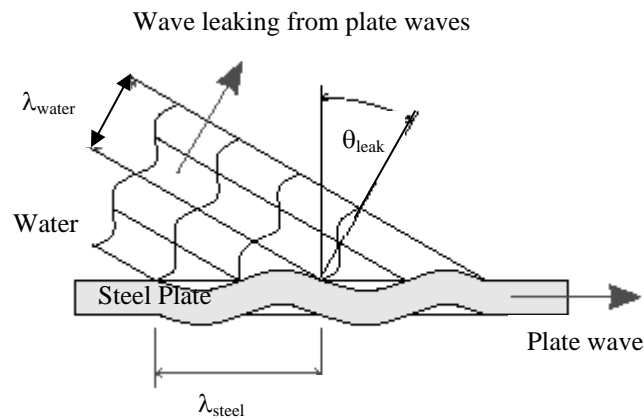


Figure 2.15 – Flexural Plate Wave Traveling in a Steel Plate Creating a Bulk Wave at a Characteristic Angle



As shown in Figure 2.15, as a plate wave travel along the specimen, the radial displacements at the surface of the plate couple energy into the surrounding fluid creating a bulk wave in the fluid. This decreases the energy in the plate. The waves travel at one speed in water, 60,000 in/sec.

The wave frequency in water is the same as the plate wave. Therefore, from Equation 2.16, the wavelength of the water wave can be computed. The wavelength of the plate wave can be calculated from the dispersive curves. From Snell's Law in Equation 2.10 for the plate wave traveling at 90°, the leakage angle ( $\theta_{leak}$ ) can be calculated by:

$$\theta_{leak} = \sin^{-1}\left(\frac{V_{water}}{V_{ph}}\right) = \sin^{-1}\left(\frac{\lambda_{water}}{\lambda_{plate}}\right) \dots\dots\dots(2.17)$$

where  $\lambda_{water}$  is the wavelength in the water,  $\lambda_{plate}$  is the wavelength in the plate,  $V_{water}$  is the bulk velocity of the longitudinal wave in water,  $V_{ph}$  is the phase velocity of the plate wave. In Equation 2.17, if the phase velocity ( $V_{ph}$ ) is less than the bulk velocity in the surrounding medium, the leakage angle will be imaginary. The physical meaning of the imaginary angle is that instead of wave propagation away from the plate, the displacement dies away exponentially and the energy is trapped against the plate creating another type of wave propagating along the interface between the water and the plate [Bao et al. 1998]. This wave is called Scholte-Stoneley wave. Therefore, if the phase velocity is less than the bulk velocity of the waves existing in the surrounding liquid, this part of the energy does not propagate into the water. This phenomenon also is known as the coincidence principle or the phase matching condition [Pavlakovic, 1998].

## **2.2.6 Lamb Wave Propagation in Composite Plates**

Composite materials have the unique properties of high strength, low weight, and anisotropic properties that can be manipulated to place the greatest strength in the most demanding direction. The overall properties of a laminated composite structure depend on the fiber directions and their stacking sequence. In composite plates, the anisotropic properties further complicate the already complex wave propagation caused by the dispersion characteristics.

From the acoustic emission point of view, attenuation can be relatively high due to absorption of energy by the matrix. High frequencies can be selectively absorbed by the matrix and scattered by the filaments and other small discontinuities [Handbook of Nondestructive Testing vol. 5]. Also, long term loading on the composite, and environmental effects over a period of time, will cause changes in attenuation and dispersion [Handbook of Nondestructive Testing vol. 5]. All of the factors mentioned above result in a much different behavior of guided waves in fiber reinforced plastic plates than in metal plates.

As discussed in Section 2.2.3, for plate waves in an isotropic material the variation of the phase velocity with the frequency is known as dispersion. Dispersion is a function of the frequency multiplied by the thickness, whereas dispersion in an anisotropic material is also dependent on the orientation of the wave front relative to the material symmetry [Sullivan et al. 1996].

Studies of wave mode propagation in composite plates have been performed by numerous researchers and it is still an ongoing research topic [Sullivan et al. 1996, Gorman et al. 1994, Prosser et al. 1994, and Prosser et al. 1992]. Gorman and Ziola demonstrated that simulated AE signals in flat composite plates consist of the lowest order of plate modes [Gorman et al. 1994]. The lowest order symmetrical mode is called the extensional mode, while the

lowest order anti-symmetric mode is called the flexural mode. Gorman and Prosser [1994] studied the behavior of the first two wave modes (extensional and flexural) generated by pencil lead breaks in thin composite plates. In their studies, Gorman and Prosser measured the velocities of the first two wave modes in three directions of propagation. The directions are along the two principal axes in the plane of the plate (0 and 90 degree) and at an angle of 45 degrees. The specimen used has four different composite lamina. The ply layups for the laminate were  $[0_{16}]$ ,  $[0_4, 90_4]$ ,  $[0, 90]_{4s}$ , and  $[0, 45, -45, 90]_{2s}$ . The equations to calculate the wave mode velocities are basically the same as those presented as Equations 2.14 and 2.15 in Section 2.2.3. The difference is that each mode does not propagate at the same velocity since the properties are different in different directions.

In an anisotropic composite material, the extensional velocity is dependent on the stiffness coefficients  $A_{ij}$ , where  $i$  and  $j$  are the directions 1 to 6. The  $A_{ij}$  are defined as:

$$A_{ij} = \int_{-h/2}^{h/2} Q_{ij}^k dz \dots\dots\dots(2.18)$$

where  $h$  is the thickness of the laminate,  $z$  is the distance in the thickness direction from the mid plane of the laminate, and  $Q_{ij}^k$  are lamina stiffness coefficients for the  $k^{\text{th}}$  lamina of the composite. For propagation along the  $x$  axis or 0 degree direction, the extensional mode is a pure mode wave with a velocity of

$$C_{ex} = \sqrt{\frac{A_{11}}{\rho h}} \dots\dots\dots(2.19)$$

where  $\rho$  is the density.

In the y direction or 90 degree, the extensional mode is also a pure mode and its velocity is defined by:

$$C_{ey} = \sqrt{\frac{A_{22}}{\rho h}} \dots\dots\dots(2.20)$$

For propagation at 45 degrees to the x and y axes, the solution yields a quasi-extensional mode with a velocity given by:

$$C_{exy} = \sqrt{\frac{A_{11} + A_{22} + 2A_{66} + \sqrt{R}}{4\rho h}} \dots\dots\dots(2.21)$$

where  $R = (A_{11} + 2A_{66} + A_{22})^2 - 4(A_{11} + A_{66})(A_{22} + A_{66}) + 4(A_{12} + A_{66})^2$

Note that these velocities are valid only for low frequencies.

The flexural velocity is a function of the bending stiffness coefficients ( $D_{ij}$ ). These are defined as:

$$D_{ij} = \int_{-h/2}^{h/2} Q_{ij}^k z^2 dz \dots\dots\dots(2.22)$$

The velocity is dispersive and is dependent on the propagation direction. The flexural velocities in x, y, and 45 degree directions (or xy) are defined by Equations 2.23, 2.24, and 2.25; respectively.

$$C_{fx} = 4\sqrt{\frac{D_{11}}{\rho h}}\sqrt{\omega} \dots\dots\dots(2.23)$$

$$C_{fy} = 4\sqrt{\frac{D_{22}}{\rho h}}\sqrt{\omega} \dots\dots\dots(2.24)$$

$$C_{fxy} = 4\sqrt{\frac{\frac{1}{4}(D_{11} + 4D_{16} + 2(D_{12} + 2D_{66}) + 4D_{26} + D_{22})}{\rho h}}\sqrt{\omega} \dots\dots\dots(2.25)$$

where  $\omega$  is circular frequency.

From Equations 2.23 to 2.25, the velocity is predicted to increase as the square root of the frequency.

### 2.3 SOURCE LOCATION METHODS

The ability to accurately locate the position of a defect is one of the most important functions in any nondestructive testing method. With the method of recording data described in Section 2.1.3 (the threshold crossing technique), it is difficult to perform accurate source location due to inaccuracies in measuring the arrival time, or even detecting the signal at enough sensors due to the dispersive and attenuation characteristics of the specimen. This problem will be discussed later in Section 2.3.1.1.

Over the last ten years, digital AE monitoring systems have been developed and are now finding their way into general use. A digital system detects the AE signal in the same way as an analog system by using the preset

threshold technique. However, instead of recording just the extracted parameters of the waveform, a complete waveform is recorded for later processing. In addition, once one channel is triggered, adjacent channels can be set to record the waveform even if the threshold is not exceeded on these channels.

The following section provides a literature review of source location approaches including the conventional methods based upon parametric time-of-arrival, and the recently developed methods using waveform processing.

### **2.3.1 Methods Based on the Arrival Time**

There are two main source location techniques that are based on arrival time. Both of them have the same basic assumption that all the sensors receive the emission from the same source.

The first one calculates the difference between the arrival times of a stress wave at each sensor in an array of sensors. This method is referred to as the “difference in time-of-arrival” method, “time-of-arrival” method, or “triangulation” method. The time-of-arrival method allows the location of the AE source to be determined as calculated coordinates.

The second approach is called the zonal method. This approach uses the sensor that first detects the signal to indicate the primary zone of the source. Additional sensor hits are used to refine the primary zone and reduce its area. Zonal location results in a less precise definition of the location but is more robust and less prone to error than the time-of-arrival method [Fowler, 1984].

### 2.3.1.1 Difference in Time-of-Arrival Approach

- *Linear Source Location*

In concept, the time-of-arrival method allows the defect to be pinpointed in the structure. Unfortunately, for a number of reasons that will be discussed later, this is not the case in practice. Location accuracy with this method can vary from very good to extremely bad.

If the diameter of a cylindrical test object, such as a pipe, is much less than the sensor spacing, linear source location using two sensors is the most appropriate method. Linear source location performs in one dimension. The concept of the method is illustrated in Figure 2.16.

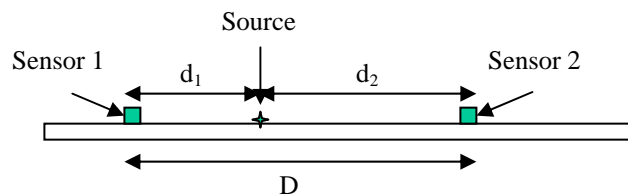


Figure 2.16 – Linear Source Location

Two sensors are placed at a known distance apart ( $D$ ). These two sensors are referred to as an array. The stress waves are generated from the source at time  $t_0$  and travel at a known velocity ( $V$ ). The stress waves reach sensor 1 at arrival time  $t_1$  and sensor 2 at  $t_2$ . Simple equations can be formed to calculate the distances  $d_1$  and  $d_2$ . These equations are shown as 2.26, 2.27 and 2.28.

$$d_1 = V(t_1 - t_0) \dots\dots\dots(2.26)$$

$$d_2 = V(t_2 - t_0) \dots\dots\dots(2.27)$$

$$d_2 + d_1 = D \dots\dots\dots(2.28)$$

Equations 2.26 and 2.27 can be reduced to

$$d_2 - d_1 = V(t_2 - t_1) \dots\dots\dots(2.29)$$

From Equations 2.28 and 2.29, the distances  $d_1$  and  $d_2$  can be calculated and are given by:

$$d_1 = \frac{D - V(t_2 - t_1)}{2} \dots\dots\dots(2.30)$$

$$d_2 = \frac{D + V(t_2 - t_1)}{2} \dots\dots\dots(2.31)$$

In general the time  $t_0$  is not known and the hit arrival time of the first hit sensor is taken as zero. The equation shows that the value  $t_2-t_1$  is needed. This is the difference in time of arrival between the two sensors,  $\Delta t$ , that is measured. If the source is outside the two sensors, linear source location will place the source at one of the sensors.

- *Source Location in Two Dimensions*

If two sensors are used in a plane as shown in Figure 2.17, a relation between velocity and time can be formed in Equation 2.32.

$$\Delta tV = r_2 - r_1 \dots\dots\dots(2.32)$$



where  $\Delta t$  is the difference in the arrival times between the two sensors,  $r_1$  is the distance from the source to sensor 1, and  $r_2$  is the distance from the source to sensor 2. In Figure 2.17, a geometric relationship can be shown in Equations 2.33 and 2.34.

$$z = r_1 \sin(\theta) \dots\dots\dots(2.33)$$

$$z^2 = r_2^2 - (D - r_1 \cos \theta)^2 \dots\dots\dots(2.34)$$

where  $D$  is the distance between from the two sensors,  $z$  is the distance from the source position perpendicular to line  $D$  and  $\theta$  is the angle between line  $r_1$  and  $D$ . Equations 2.33 and 2.34 yield:

$$r_1^2 \sin^2 \theta = r_2^2 - (D - r_1 \cos \theta)^2 \dots\dots\dots(2.35)$$

Moving the term  $r_1^2 \cos^2 \theta$  to the left hand side leads to:

$$r_1^2 = r_2^2 - D^2 + 2Dr_1 \cos \theta \dots\dots\dots(2.36)$$

Substituting  $r_2 = \Delta tV + r_1$  from Equation 2.32 yields:

$$r_1 = \frac{1}{2} \frac{D^2 - \Delta t^2 V^2}{\Delta tV + D \cos \theta} \dots\dots\dots(2.37)$$

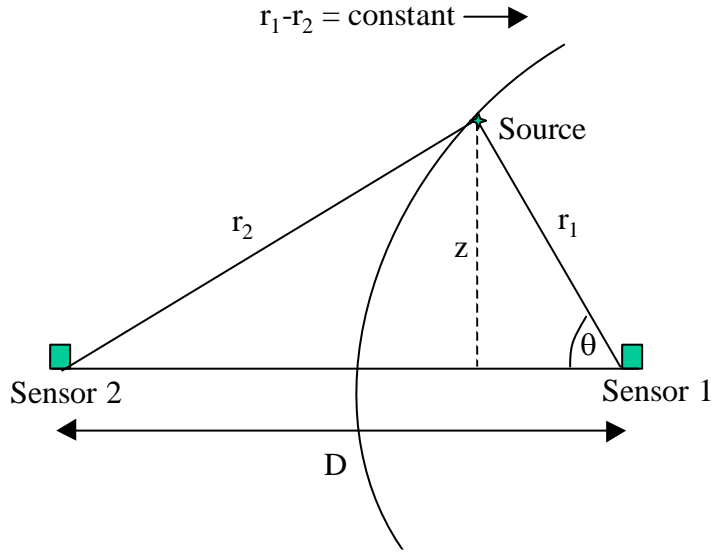


Figure 2.17 – Result of Source Location with Two Sensors on a Plane

In two dimensions, an array with a minimum of three sensors is needed to pinpoint the source position. The concept of the two dimensional source location is similar to the linear approach and is shown in Figure 2.18.

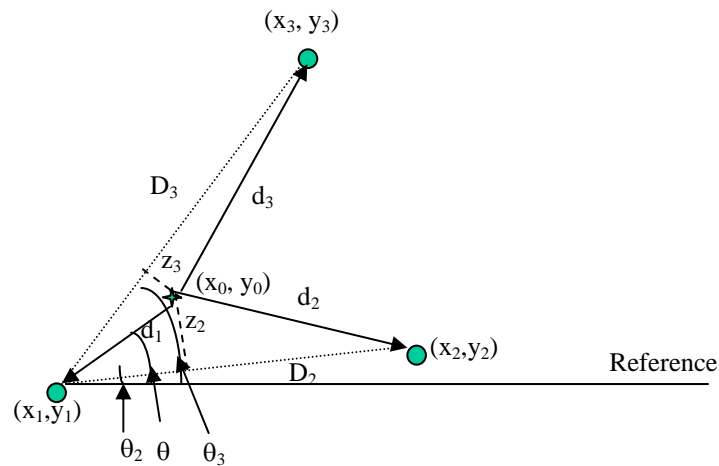


Figure 2.18 – Three Sensor Array with Detection Sequence 1,2,3

In Figure 2.18,  $x_0$  and  $y_0$  is the location of the source,  $x_i$  and  $y_i$  is the location of sensor  $i$ ,  $d_i$  is the distance between the source and sensor  $i$ .  $D_2$  and  $D_3$  are the distance between sensor 1 and sensors 2 and between sensor 2 and sensor 3. Simple equations can be formed based on the arrival time at each sensor:

$$V(t_2 - t_1) = d_2 - d_1 \dots\dots\dots(2.38)$$

$$V(t_3 - t_1) = d_3 - d_1 \dots\dots\dots(2.39)$$

The geometric relationships can be given by:

$$z_2 = d_1 \sin(\theta - \theta_2) \dots\dots\dots(2.40)$$

$$z_2^2 = d_2^2 - (D_2 - d_1 \cos(\theta - \theta_2))^2 \dots\dots\dots(2.41)$$

$$z_3 = d_1 \sin(\theta_3 - \theta) \dots\dots\dots(2.42)$$

$$z_3^2 = d_3^2 - (D_3 - d_1 \cos(\theta_3 - \theta))^2 \dots\dots\dots(2.43)$$

Using the geometric relationships from Equations 2.40 to 2.43 leads to

$$d_1 = \frac{D_2^2 - (t_2 - t_1)^2 V^2}{2[(t_2 - t_1)V + D_2 \cos(\theta - \theta_2)]} \dots\dots\dots(2.44)$$

and

$$d_1 = \frac{D_3^2 - (t_3 - t_1)^2 V^2}{2[(t_3 - t_1)V + D_3 \cos(\theta_3 - \theta)]} \dots\dots\dots(2.45)$$

The location of a source in two dimensions can be obtained by solving Equations 2.44 and 2.45 simultaneously for  $d_1$  and  $\theta$ .

- *Limitation of the method*

In the time-of-arrival method with three sensors, the results are only valid for sources within the area bounded by the triangle. Note that the solutions in Equations 2.44 and 2.45 were developed without a limitation on the sensor placement. A way to identify that the hit is in the bounded area needs to be incorporated before applying the equations. There are three methods used to determine if the source is in the area bounded by the sensors.

The most widely used method to determine which sensors bound the source is to arrange the sensors so that they form a series of contiguous triangles. An example is shown in Figure 2.19. An assumption is made that the source lies within the area bounded by the first three sensors that receive hits from an event. In Figure 2.19, if the first three sensors hit are 1, 2, and 3 it is assumed that the source is within the triangle 1, 2, 3. In many situations, the assumption is incorrect and the source is not within the triangle. There are many reasons why this can occur including:

- The arrangement of sensors may be such that the three closest sensors do not enclose the source. In general, sensor spacing is governed by the geometry of the part being monitored. sensor spacing in the horizontal and vertical directions may be different, or a sensor may have to be moved

out of the regular layout pattern because an attachment, nozzle, or reinforcement pad is in that position.

- Local shielding due to a nozzle or attachment may prevent the wave from reaching one of the sensors.
- Attenuation may be much greater in one area of the plate than another. The high attenuation could be caused by a poor plate weld, local corrosion, bonded insulation, liquid in a partially full tank, or a coating.
- Two sensors may be hit by waves transmitted through the shell, and the third sensor may be hit by a wave that has traveled as a water borne wave through the tank.

Most modern field test systems use this approach and in some cases, good source location results are obtained. Unfortunately, in other situations the source location calculations give erroneous results.

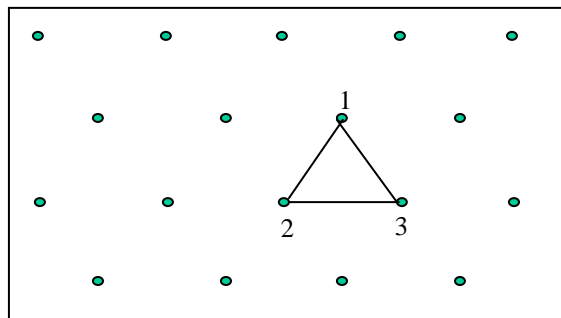


Figure 2.19 – Series of Contiguous Triangle Sensor Arrangement

The second technique is to use guard sensors as shown in Figure 2.20. In this approach, each active sensor is paired with a guard sensor. If its guard sensor received the signal before the active sensor, the source is not in the effective area and the data should not be processed. Note that guard sensors are used to reject data. They are not used to calculate the position of the source.

In practice, this method is usually the method of last resort because it doubles the number of sensors and channels needed for a test and greatly increases the cost of the instrument, setup time, and data processing. Even if the guard sensors are near the sensors they are guarding, a significant area lies outside of the area bounded by the sensors and this can lead to ambiguous results.

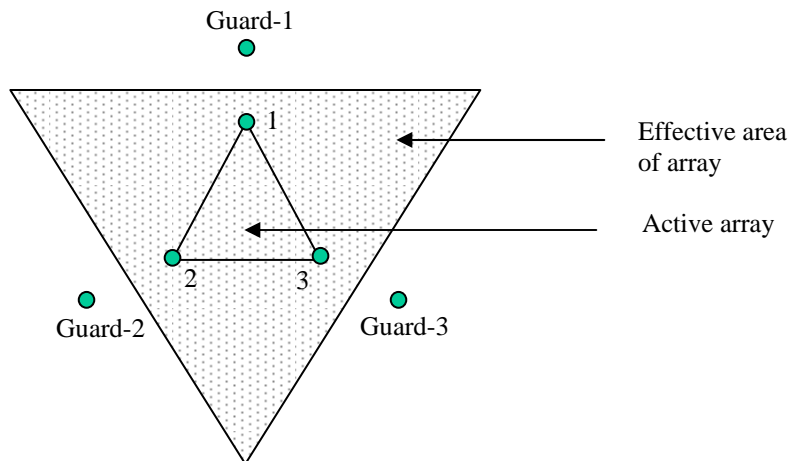


Figure 2.20 – Guarding Sensor Scheme

The third approach uses four sensors and the arrangement of the sensors is shown in Figure 2.21. In Figure 2.21, the shaded area shows the effective zone. The active zone is defined by rejecting all the emission unless the central sensor (or sensor 1) is hit first.

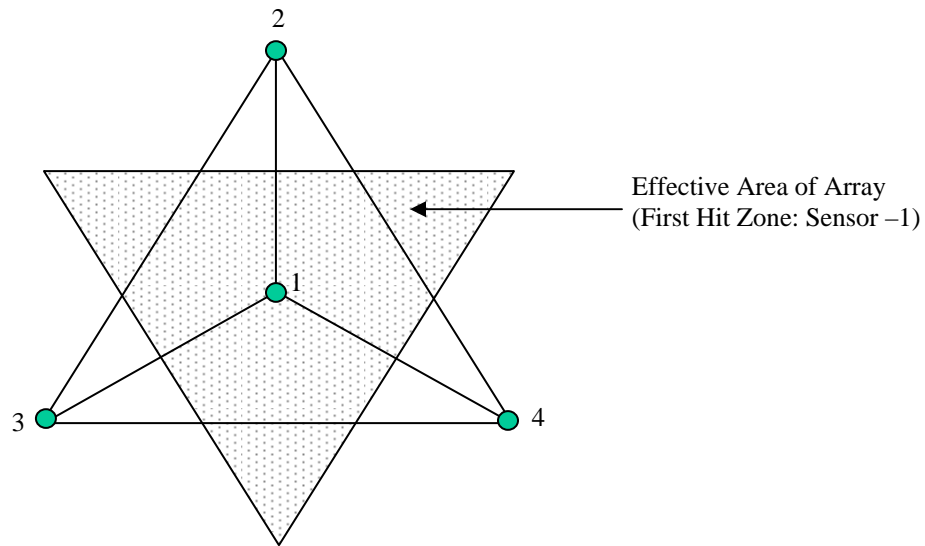


Figure 2.21 – First Hit Zone by Central Sensor

Although this method uses less sensors than the first method, some parts of the effective area are still out of the area bounded by the sensors leading to ambiguous results.

- *Four Sensor Array Configurations*

Ying et al. [1974] suggested using a four sensor array of the type used in source location of seismic events. The sensors are located at  $(X,0)$ ,  $(-X,0)$ ,  $(0,Y)$ , and  $(0,-Y)$  as illustrated in Figure 2.22.

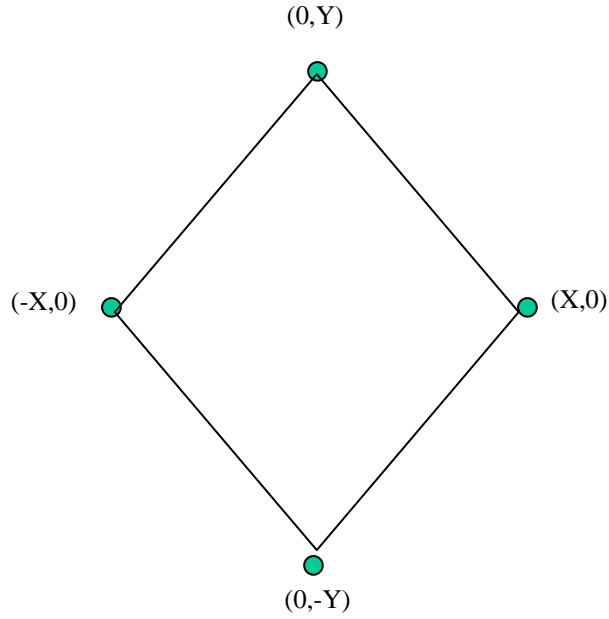


Figure 2.22 – Ying Array Configuration

Instead of measuring the first, second and third hit, the two  $\Delta t$  measurements are taken between the pair of X sensors and the pairs of Y sensors. The location of source is given by:

$$X = aB \sqrt{\frac{b^2 + A^2}{b^2 B^2 - a^2 A^2}} \dots\dots\dots(2.46)$$

and

$$Y = Ab \sqrt{\frac{a^2 + B^2}{b^2 B^2 - a^2 A^2}} \dots\dots\dots(2.47)$$

where



$$a = \frac{\Delta t_x V}{2}$$

$$b = \frac{\Delta t_y V}{2}$$

$$A = \sqrt{X^2 - a^2}$$

$$B = \sqrt{Y^2 - b^2}$$

$$V = \text{WaveVelocity}$$

The solutions in Equations 2.46 and 2.47 contain the square root form, therefore the quadrant the source lies in is not clear. Fortunately, measuring the first hit X sensor and Y sensor can solve this ambiguity.

Four sensors can be used to uniquely define the position of the source, even if it is outside the area bounded by the sensors. Hsu (1975) derived the basic formulas for triangulation with four sensors and the formulas for the special case of an equilateral triangle configuration.

In the first case, four sensors can be located anywhere at (0,0) for sensor 0, (x<sub>1</sub>, y<sub>1</sub>) for sensor 1, (x<sub>2</sub>, y<sub>2</sub>) for sensor 2, and (x<sub>3</sub>, y<sub>3</sub>) for sensor 3. The source is located at (x, y) which is an unknown location as shown in Figure 2.23. Note that the locations of sensors do not have to form a rectangular shape with the source. They can be anywhere on the plane.

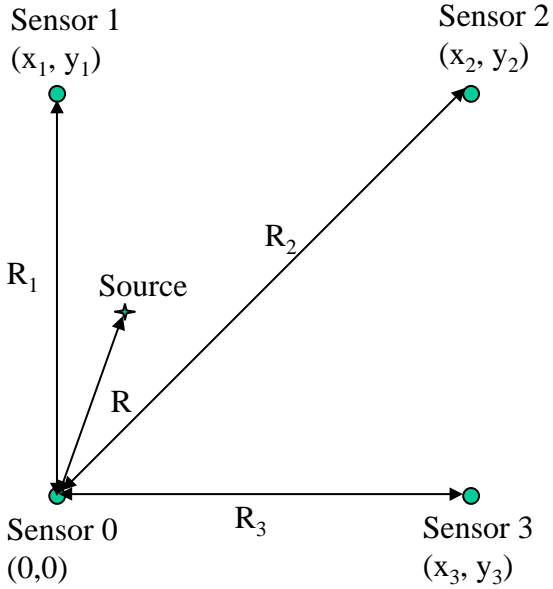


Figure 2.23 – Four Sensor Array

The derivations of the formulas are presented in Appendix A. The final equations to locate  $x$ ,  $y$ , and  $R$  are given by:

$$x = \frac{[(R_1^2 - V^2 t_1^2)(y_2 t_3 - y_3 t_2) + (R_2^2 - V^2 t_2^2)(y_3 t_1 - y_1 t_3) + (R_3^2 - V^2 t_3^2)(y_1 t_2 - y_2 t_1)]}{2[(t_1(x_2 y_3 - x_3 y_2) + t_2(x_3 y_1 - x_1 y_3) + t_3(x_1 y_2 - x_2 y_1)]V} \dots\dots\dots(2.48)$$

$$y = \frac{[(R_1^2 - V^2 t_1^2)(x_3 t_2 - x_2 t_3) + (R_2^2 - V^2 t_2^2)(x_1 t_3 - x_3 t_1) + (R_3^2 - V^2 t_3^2)(x_2 t_1 - x_1 t_2)]}{2[(t_1(x_2 y_3 - x_3 y_2) + t_2(x_3 y_1 - x_1 y_3) + t_3(x_1 y_2 - x_2 y_1)]V} \dots\dots\dots(2.49)$$

$$R = \frac{[(R_1^2 - V^2 t_1^2)(x_2 y_3 - x_3 y_2) + (R_2^2 - V^2 t_2^2)(x_3 y_1 - x_1 y_3) + (R_3^2 - V^2 t_3^2)(x_1 y_2 - x_2 y_1)]}{2[(t_1(x_2 y_3 - x_3 y_2) + t_2(x_3 y_1 - x_1 y_3) + t_3(x_1 y_2 - x_2 y_1)]V} \dots\dots\dots(2.50)$$

where  $R$  is the distance from the source to sensor 0,  $R_i$  is the distance from the source to sensor  $i$ ; where  $i$  is 1 to 3,  $V$  is the speed of AE pulse, and the time durations required for the stress wave to travel from the source to sensor 0, 1, 2, and 3 are  $t$ ,  $t+t_1$ ,  $t+t_2$ , and  $t+t_3$ , respectively.

The solutions from the four-sensor scheme can be used independently to check the validity of the data. The condition is that the solution  $x$ ,  $y$ , and  $R$  obtained must satisfy the relation:

$$x^2 + y^2 = R^2 \dots\dots\dots(2.51)$$

As mentioned earlier, Hsu (1975) also derived solutions for the case of an equilateral triangle sensor configuration. This configuration is shown in Figure 2.24.

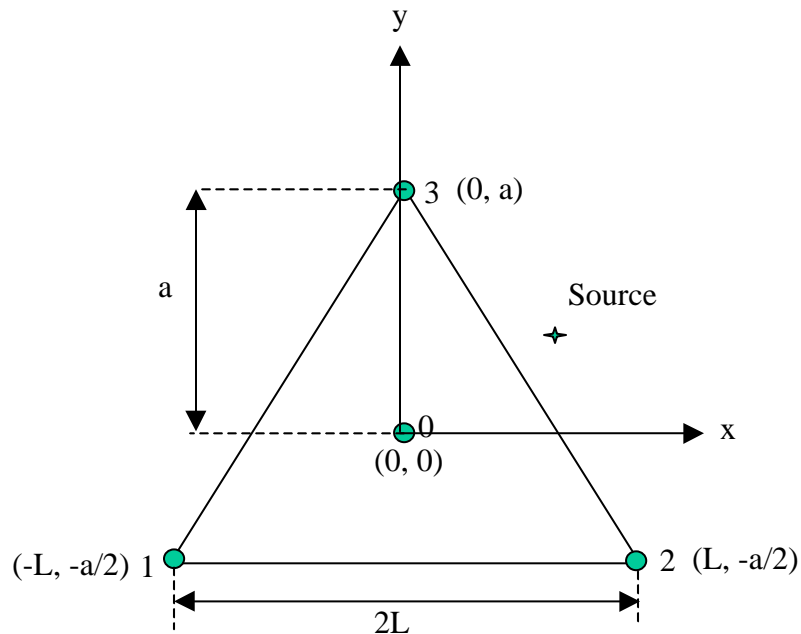


Figure 2.24 – Equilateral Triangle Sensor Arrangement

After substituting the variables in Equations 2.48, 2.49, and 2.50, the solutions for x, y, and R in the equilateral triangular arrangement case are shown below:

$$x = \frac{(t_1 - t_2)[4L^2 + V^2(t_1t_3 + 2t_1t_2 + t_2t_3 - t_3^2)]}{4L(t_1 + t_2 + t_3)} \dots\dots\dots(2.52)$$

$$y = \frac{V^2[(t_1^2 + t_2^2)t_3 - (t_1 + t_2)t_3^2] - \frac{4}{3}L^2[2t_3 - (t_1 + t_2)]}{\frac{4L(t_1 + t_2 + t_3)}{\sqrt{3}}} \dots\dots\dots(2.53)$$

$$R = \frac{4L^2 - V^2(t_1^2 + t_2^2 + t_3^2)}{2V(t_1 + t_2 + t_3)} \dots\dots\dots(2.54)$$

With this four-sensor arrangement, the solutions are not restricted to the area bounded by the sensors [Hsu, 1975].

- *Problems of the method*

In practice, the time-of-arrival method often yields very poor source location results. The problems with source location are such that in a number of test procedures [AAR, CARP, MONPAC], source location is treated as a secondary issue and not an essential component of the procedure. When it is used, the primary method is zonal (see Section 2.3.1.2 which follows) and time-of-arrival is relegated to use “if it can help”. Sources of error in the triangulation method come mainly from the dispersion effect and attenuation effect.

### Dispersion Effect

An assumption that waves travel at a constant speed is included in the solutions for the triangulation method. This is not true in the case of plate waves. The speed of propagation depends on the mode and frequency of the wave. This is the dispersion effect discussed in Section 2.2.3.

The dispersion also results in a changing shape of the waveform as it travels. This can cause major errors in defining the arrival time. The dispersion effect makes it difficult to define the arrival time at the same point on the signal from different sensors.

Figure 2.25 illustrates the dispersion effect on the waves propagating in a thin shell. The distances from the point of crack initiation to each sensor are different resulting in a different shape of waveform captured at each sensor. Inaccurate measurement of the arrival time can result in major errors in location of the source.

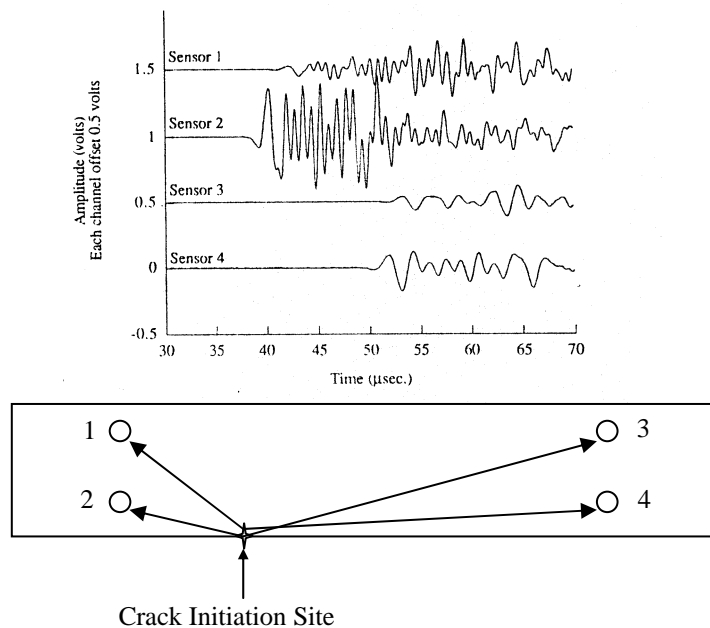


Figure 2.25 – Dispersion Effect in a Thin Plate [Prosser et al., 1994]

### Attenuation Effect

Once the waves travel, the energy or amplitude of the waves decrease. This effect, which is known as attenuation, is discussed in Section 2.2.4. Attenuation has a similar effect to dispersion. When the first threshold crossing technique is used to define the arrival time of the signal, the arrival times at different sensors are not at the same point on the signal. Attenuation makes it very difficult to define the arrival times with consistency from sensor to sensor. Another problem with the triangulation method is that not enough sensors can detect the stress waves to locate many of the events due to attenuation of the stress wave as it travels in the specimen [Fowler 1984].

### Other Sources of Error

Aside from the dispersion and attenuation effects, more factors can deviate the accuracy of the method. Complex geometry requires special calculations and setup. Examples are the head to shell junction of a vessel, and shell openings.

Multiple sources also contribute to errors in source location. The arrival of signals at four sensors may not be from a single source. This can lead to an incorrect location [Hsu, 1976]. Currently used software is not able to treat the multiple source problem.

Another source of error is caused by waves traveling from a third dimension. For example, this can be from the water inside the vessel or from background noise or a dip pipe. The problem of water borne noise is also currently being studied by Physical Acoustic Cooperation [PAC, 1999]

### 2.3.1.2 Zonal Method

- *Basic Concept*

A zone is defined as the area surrounding a sensor from which acoustic emission can be detected and from which acoustic emission will strike the sensor before striking any other sensors [AAR 1999]. This method is used in real time testing to approximate the locations of the source of the events [Fowler 1984]. A refinement of the zonal method is sometime called the Jolly-Stuart method and based on the hit sequence of a number of sensors. The method was originally proposed by Jolly [Hutton, Jolly, and Vetrano, 1973] and refined by Fowler [Fowler, 1984]. The approach uses the first hit to define the zone of the source. If multiple sensor hits are used, the zone can be refined. In general, the zonal method has the reputation of being robust to errors in sensor placement.

- *Jolly-Stuart Method*

There are two steps to locate the zone of the source in the Jolly-Stuart method. The first step is called “hit identification”. The process groups the hits into events in orders them based on the arrival time at each sensor.

The second step is to define a zone of each sensor. The zone of sensor  $i$  is the set of all points in the specimen closer to sensor  $i$  than any other sensors. With this zone definition, it is important to confirm that all sensors have approximately the same sensitivity. To refine the zone of interest, multiple sensors detecting the same event are included. If sensor  $i$  detects the emission first and then sensor  $j$ , which is one of the sensors adjacent to sensor  $i$ , detects the hit the second, the source must be in the portion of zone- $i$  closer to sensor  $j$  than

any other sensors. The zone i-j can be further subdivided by additional hits on other sensors. The concept is illustrated in Figure 2.26.

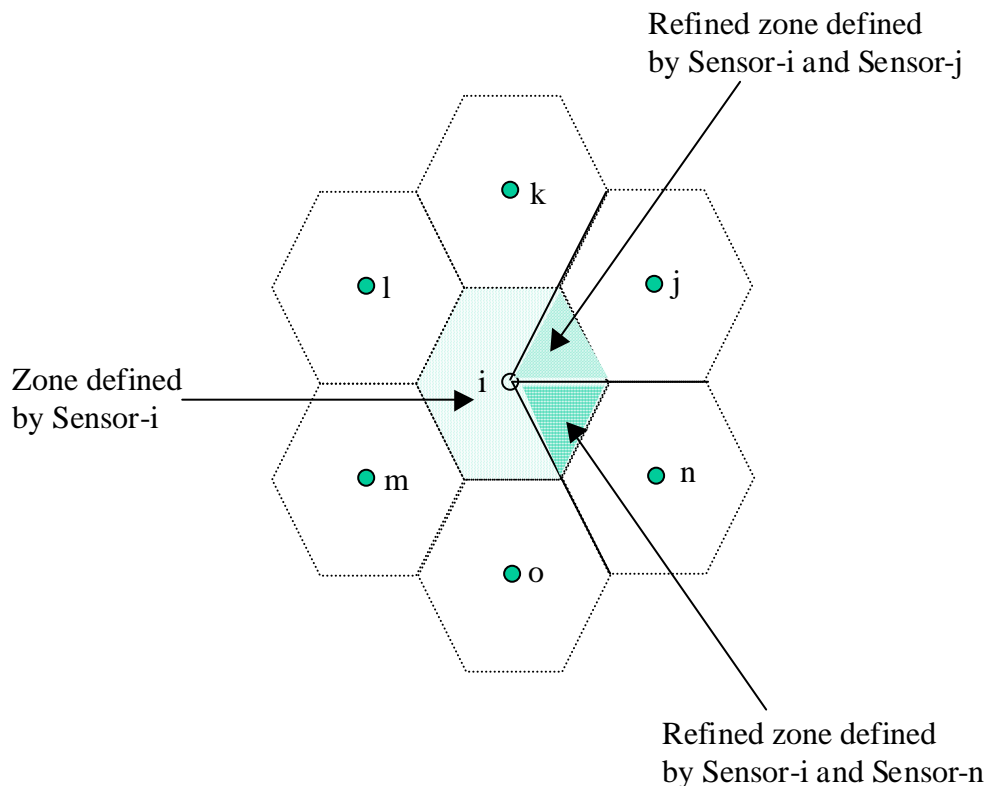


Figure 2.26 – Zone Construction

- *Limitation of the Method*

In order to subdivide the zones by equidistance, it is important that the sensitivities of the sensors are the same. Differences in sensor sensitivity do not have a major effect on the primary zone but can be critical when the zone is refined by multiple sensors.



## 2.3.2 Waveform Based Methods

Digital acoustic emission systems offer the possibility of a significant improvement in source location. Improved methods to measure the time of arrival are made possible by the capturing the entire waveform. In addition, it is possible to use waveforms that do not cross the threshold. Source location techniques using waveform processing are discussed in this section.

### 2.3.2.1 Cross Correlation Technique

In order to improve the accuracy of conventional time of arrival source location, Ziola and Gorman [1991] published a technique to locate and use corresponding phase points on the sensor outputs to determine arrival times. This technique is called the cross correlation method and is performed by cross correlating the sensor outputs with a single frequency cosine wave modulated by a Gaussian pulse.

The studies were performed on a thin plate, with two wave modes (extensional and flexural modes) present. The researchers first tried to use the extensional mode, which is non-dispersive, to perform source location. It was discovered that the extensional mode is highly attenuated since it has a large high frequency component. The method provided poor results.

As a result of the problems with the extension mode, the source location studies focused on the flexural mode, which attenuates much less and propagates a greater distance. Cross correlation is defined as the time average of the product of two functions, where one function has been delayed relative to the other as shown in Equation 2.55.

$$R_{xy}(\tau) = \lim_{T \rightarrow \infty} \frac{1}{2T} \int_{-T}^T x(t)y(t+\tau)dt \dots\dots\dots(2.55)$$

The idea of the method is that if a single frequency in the output waveform from each transducer can be isolated, then the time differences due to the propagation of that frequency component can be used for the source location analysis. The velocity of this frequency component could be either calculated from theory or experimentally determined. In the dispersive systems, since the pulse changes shape as it propagates, it is impossible to receive a useful result from cross correlating waveforms from any two transducers. Therefore, a single frequency cosine wave modulated by a Gaussian pulse was used to cross-correlate with the output from the transducer. From this, the correct time differences needed for the source location can be obtained.

The experiments were performed by breaking pencil leads on a thin aluminum plate (2 ft x 2 ft). Three wide band sensors were used with a low gain preamplifier (60 db) and high gain (80 db) preamplifier. The location results from the cross-correlation method were very poor for the data captured by sensors with low gain preamplifiers. The results from the data taken by sensors with high gain preamplifiers show good accuracy.

### 2.3.2.2 Other Source Location Methods

- *Reverse Ray Tracing Method*

The reverse ray tracing method was developed by Horn [1995]. The method uses special receivers with multi-elements inside. Each element responds independently and sequentially to a stress wave. The order of elements detecting

the stress wave can be used to determine the azimuth approach angle as shown in Figure 2.27. With two sensors, the area of the source can be determined by inverse tracing of the rays as illustrated in Figure 2.28.

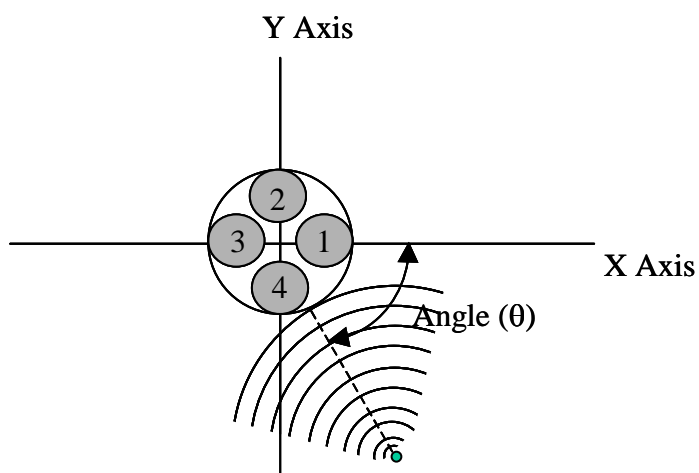


Figure 2.27 – Multi-Element Sensors Used to Determine the Angle of the Source

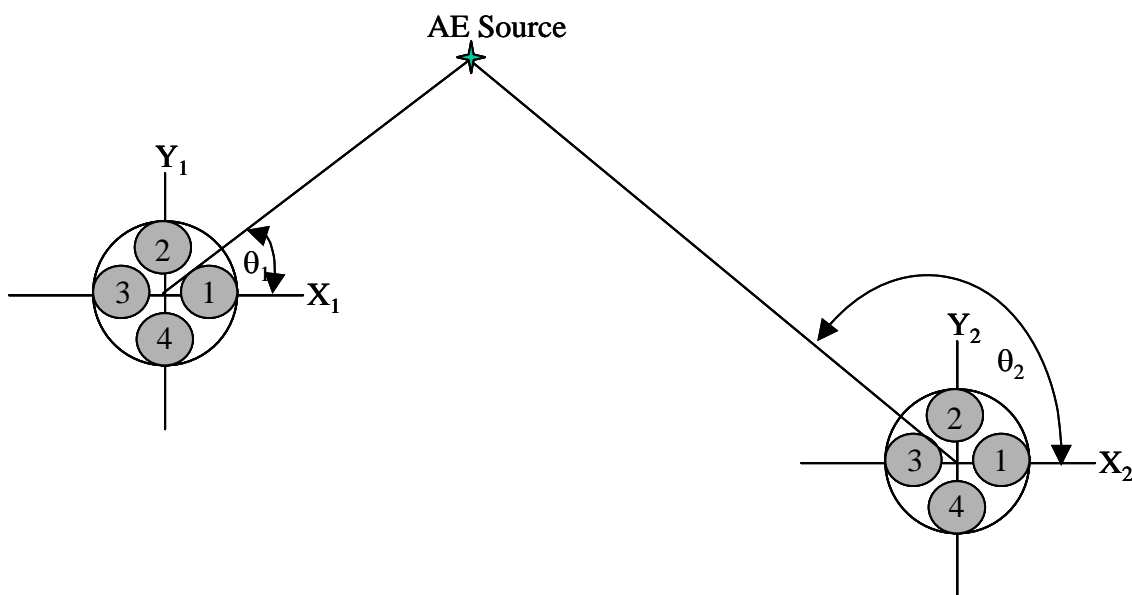


Figure 2.28 – Source Location Using Inverse Ray Tracing

- *Moment Tensor Analysis*

A number of studies have been performed using the moment tensor method to determine crack orientation and direction of growth and location. This section focuses on the source location part using Moment Tensor Analysis. Moment tensor analysis is based on the change in stress geometry that occurs at the source of the acoustic emission. The name is based on the fact that this change is described in terms of both direction, which is related to tensor, and magnitude, which is related to moment.

The moment tensor method performs source location on the beginning of the fastest wave mode. This is the longitudinal wave in the case of wave propagation in a bulk material and the lowest order symmetrical Lamb wave in the case of plates. The major problem with moment tensor analysis is that 6 clear fastest wave modes need to be recorded for the each event. Due to attenuation, the beginning of the fastest wave mode blends with the background noise making the arrival time difficult to determine. During one study, 1024 sets of waveforms were recorded and only 19 sets were found to be useable [Yuyama et al., 1995]. Other studies confirm that the method can give accurate location but that most of the data recorded is not useable for analysis [Yepez, 1997, Shiotani et al., 1995].

## 2.4 SEARCH ALGORITHMS IN CYLINDRICAL STRUCTURES

Computer programming is often used to implement a source location approach. In programming, search algorithms play an important role in the efficiency and accuracy of the source location method. The term “search algorithm” means the step or procedure the programming routine uses to search for the correct answer for the location of the source. With a simple geometry, such as a rectangular plate, the wave propagation paths are not complicated. Accordingly, three sensors can be used to locate a point in a triangle. This was discussed previously in Section 2.3.1.1. In a cylindrical structure such as a tank car, the wave propagation paths are more complicated since the geometry is a closed loop structure. As shown in Figure 2.29, possible paths include direct and spiral routes. In addition, there will be a liquid bypass route if liquid is present inside the structure. This will further complicate the search algorithm.

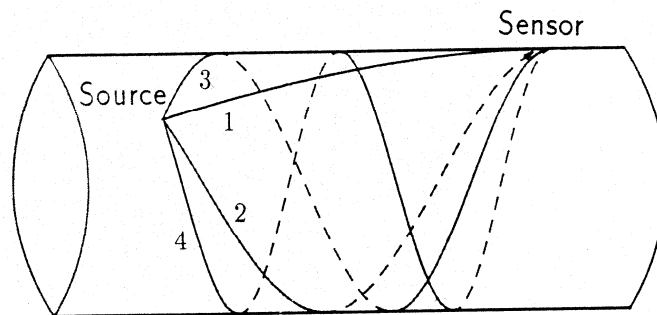


Figure 2.29 – Possible Wave Propagation Paths in a cylinder  
[Yoon et al., 1990]

With a filament wound fiber reinforced plastic pipe this can become a very complex problem because the wave will propagate around the pipe better in the direction of the fibers than in a direction across the fibers. In addition, the velocity along the fibers will be much greater than across the fibers. The direct path wave may not reach the sensor, even though one of the spiral waves may do so.

Yoon et al. [1990] used different propagation paths to help in source location by capturing a long hit length. This enabled them to cover the possible routes as shown in Figure 2.30. In the Figure,  $t_i$  is the arrival time from the path  $i$  where  $i$  is referred to the path in Figure 2.29. With this approach, the time difference between routes can be used to track back to the source. As a result, the number of sensors used in the test can be minimized.



Figure 2.30 – Waveform of Multiple Arrivals Due to Different Propagation Paths [Yoon et al., 1990]

When liquid is involved in the test, more complication arises. Aside from the fact that liquid inside the tank adds more wave propagation paths with different wave speeds, liquid can attenuate the signal propagating in the structural shell. An ongoing research program using water borne waves for source location is being carried out by Physical Acoustics Corporation [PAC, 1998].

The computational model used to calculate the location can influence the efficiency of the source location approach. Newton's Least Squares (NLS) method has been used to model the triangulation method [Redfern et al. 1982]. This method is discussed earlier in Section 2.3.1.1. The major drawback of this approach is that if large errors are present in the arrival time, the NLS algorithm will often fail to converge.

An alternative method of solving the problem used a simplex algorithm instead. The simplex optimization is a well known method for sequentially optimizing multivariate experimental system. In the source location problem, variables which are modified during the optimization are the location of the source in terms of the x, y, and z spatial coordinates. In simplex optimization, these variables, which are sometimes called vertices, are selected randomly in order to minimize the error from the arrival time. The simplex is constrained at all times to fall within the physical bounds of the structure. The procedure of simplex optimization is illustrated in the flowchart in Figure 2.31.

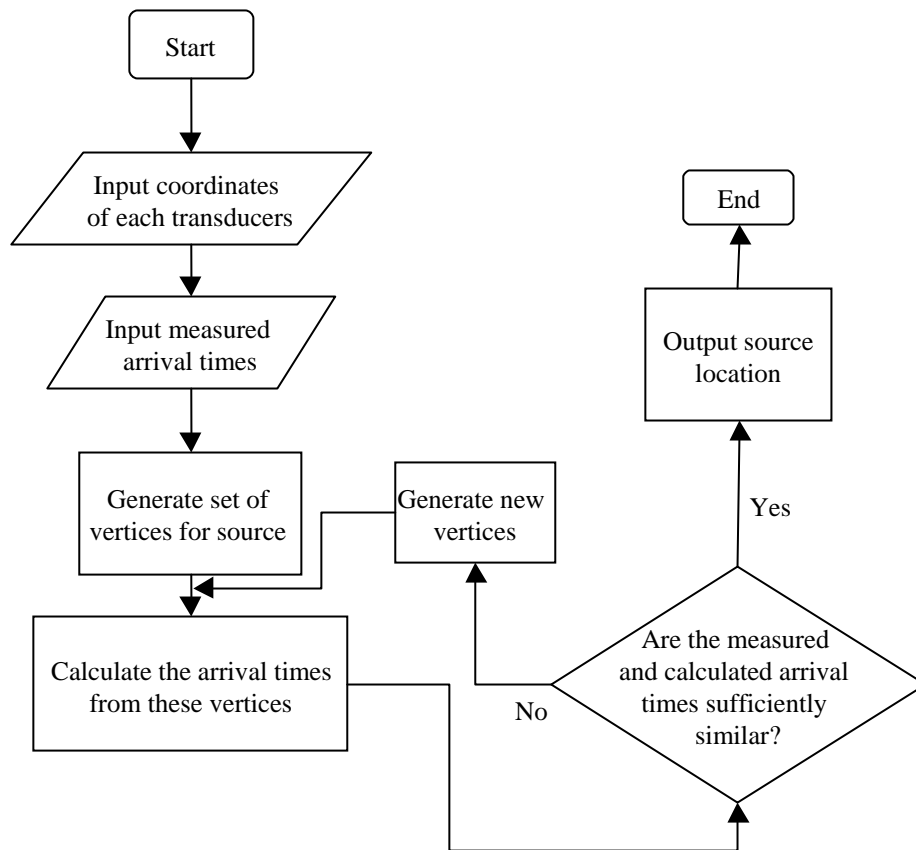


Figure 2.31 – Flowchart for Simplex Optimization Source Location



## **2.5 NEURAL NETWORK**

### **2.5.1 Theory**

A neural network is defined by a network of many simple processors or units with a small amount of local memory. The units are connected by communication channels, which usually carry encoded numeric data. Each unit operates only on its local data and on the inputs received via the connections. The inspiration for neural networks came from the desire to mimic the human brain. Most neural networks have training rules and a learning process. Inter-processor connection strengths, known as synaptic weights, are used to store the knowledge. This process is similar to that used by the human nervous system.

Neural networks are used for feature extraction, association, optimization, function fitting, and modeling. The following are among the wide range of applications:

- Finance and banking: firm failure prediction, bond rating, credit and fraud prevention, stock price prediction.
- Manufacturing: quality control, mechanical equipment fault diagnosis.
- Marketing: customer purchasing behavior and merchandising, hotel room pricing.
- Medicine: analysis of electrocardiogram, RNA & DNA sequencing in proteins.
- Pattern recognition: signature validation.

Recently, neural networks have been used in civil engineering and engineering mechanics areas to predict the failure load of a structure and in nondestructive testing applications [Barga et al. 1991].

### Multi-Layer Perceptron (MLP)

There are many types of neural networks. Each type fits a particular range of applications. This section discusses one of the popular neural networks which is used for pattern recognition. This type of network is known as the multi-layer perceptron (MLP) neural network.

In general, a neural network is analogous to a mathematic model and the multi-layer network is equivalent to a nonlinear mathematical model. A multi-layer perceptron network comprises a number of active nodes known as ‘neurons’, which are connected together to form a network. The network is made up of at least three layers. A basic network structure is shown in Figure 2.32.

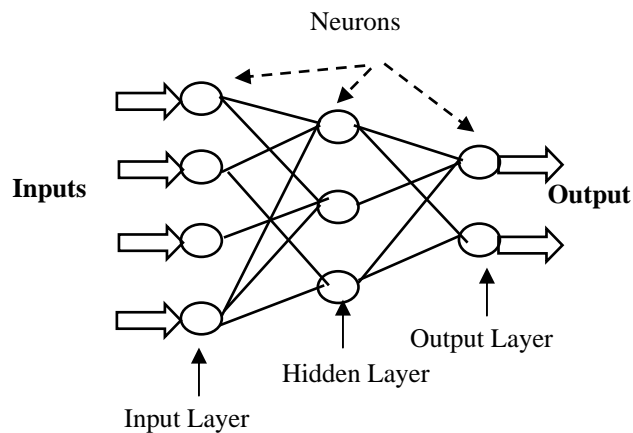


Figure 2.32 – Example of Multi-layer Perceptron Network

In Figure 2.33, the network is composed of one input layer, one hidden layer, and one output layer. A hidden layer is a group of nodes between the input and output layers. A hidden layer increases the ability of the network to memorize the data. In an MLP network, more than one hidden layer can exist. The necessity for more layers depends on the complexity of the problem.

The basic element of the network is called the neuron or node. Each neuron consists of a set of weights, one for each input, and a transfer function. The neuron calculates the weighted sum of the inputs and passes this value to a transfer function, which generates an output. The mathematical model of a neuron is illustrated in Figure 2.33.

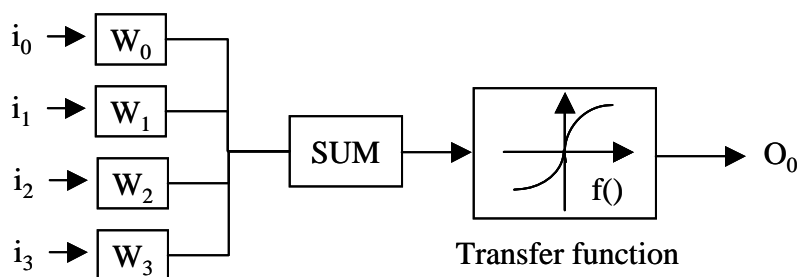


Figure 2.33 – A Neuron Model

In Figure 2.33,  $W_i$  is the weight vector,  $i_i$  is the corresponding input and  $O$  is an output. A transfer function can be a sigmoid function as shown in Figure 2.33 or it can be just a simple threshold function. The selection of the transfer function is also dependent on the complexity of the problem.

Implementation of the neural network can be done by either hardware or software. Electronic circuits are used to mimic neurons in a hardware

implementation. With software, linkages, nodes, inputs, and outputs can be programmed.

A neural network uses trial and error as a method of learning. The network tries to find pattern association inputs and outputs using a large set of training data. The inputs and outputs of these data are known. The network initially begins with random weights and corrects mistakes by modifying the weight that it has given each input.

In the learning process, there is a trade off between training speed and weight quality. If the learning process is too fast, weights may not be effective for new data. On the other hand, if the process is too slow, the network may memorize the data and not predict well for new data. The latter case is called over training. There are many rules for learning and these rules are based in biology and psychology such as:

- Hebb's rule: change in synaptic strengths are proportional to neuron activation
- Grossberg learning: self training and self organization allow the net to adapt to changes in input data over time

In general, there are two ways for network learning: unsupervised learning and supervised learning. In unsupervised learning, nets are self learning without training data. Weight adjustments are not from comparison with known values. The whole learning is based on the input pattern. Examples of the applications that use the unsupervised learning process are spell checker, and voice recognition, etc.

In supervised learning, the network gradually trains weights to meet desired outputs. The corrections are based on the difference between actual and

desired output which is computed for each training cycle. The training process stops when the average error is within a specified tolerance. After finishing the training, the weights are locked in and the network is ready to use. The way the network adjust the weights based on the desired output in a multi layer network is called a back propagation process. The procedure of back propagation training is listed below:

1. Randomly initialize the weights
2. Produce outputs from presented inputs
3. Compute the difference between actual and desired outputs
4. Adjust output layer weights using differences between desired outputs and actual outputs
5. Adjust the hidden layer weights
6. Adjust input layer weights
7. Repeat from step 2 to 6 until the accuracy is acceptable

The advantage of this method is the ability to learn any arbitrary complex nonlinear mapping. Unfortunately the procedure is long.

### **2.5.2 Case Study of Acoustic Emission Neural Network**

Neural network have been used widely for many applications including non-destructive testing. An example application of a neural network in the AE area was developed by Battelle Pacific Northwest Laboratory [Barga et al. 1991] The example includes source location. The objective of the research was to apply a neural network monitoring system for continuous surveillance of the NASA Space Station Freedom in order to detect and locate atmospheric leakage.

The network used in the work is a multilayered perceptron. It was trained using back propagation learning. Two networks were used in the work. The first network was trained for the feature extraction (automatically discovering features) and the second network was for source location. The two networks were combined into a four-layer network. The input layer was composed of 512 elements of waveform data from two sensors (total of 1024 elements). The output layer had 40 elements whose components have values between 0 and 1. The prediction location for the leak is identified by the output element with the largest value.

The results from the tests showed that the neural network system for leak location is moderately accurate when presented with leaks that are from locations for which the network has been trained. For the locations where the network has not been trained, the accuracy of the results was disappointingly low.

## **CHAPTER 3**

### **PRELIMINARY STUDY OF SOURCE LOCATION ON EMPTY TANK CARS**

#### **3.1 INTRODUCTION**

This chapter focuses on source location of two empty steel tank cars. The objective of this chapter is to present a preliminary study of wave propagation and a proposed source location approach.

The study was performed on two types of tank cars. The first one is a general purpose tank car located in the Ferguson Structural Engineering Laboratory at the University of Texas at Austin. The second tank car used in the study is a pressure car with a thicker shell located at the Rescar plant in Orange, Texas. The second tank is in a worse condition than the first one due to severe internal corrosion and blistering.

In the preliminary study on the tank car located in the Ferguson Laboratory, a 6 channel digital wave detecting system with wide-band sensors was used to capture waveforms. All sensors were attached to the tank by magnetic holddowns. Vacuum grease was used as a couplant between the sensor face and metal surface of the tank car. Two types of artificial sources were used; a pencil lead break and a bar bending method. These artificial sources are explained in more detail in Section 3.2.

The source location method developed for an empty tank car and the results from the wave propagation study on the thinner tank are presented in Section 3.3. Studies of source location problems on the thicker tank and the results are presented in Section 3.4. Finally, Section 3.5 presents the conclusion from the studies.

### **3.2 ARTIFICIAL SOURCES**

Two types of artificial sources were used for the preliminary wave propagation study on the tank car shell. The first one is a pencil lead break as shown in Figure 3.1a Pentel 0.3 mm, 2H leads [Hsu, 1977 and ASTM vol. 03.03 designation E976-94] were used to simulate emission on the tank car shell. The signal produced by this type of source has about the same frequency content and amplitude as a genuine AE signal but shorter duration [Hsu, 1977].

The other type of artificial source used in the program was generated by a bar bending method. A rectangular steel bar was tack welded to the tank car shell, then a force was applied at the end of the bar to yield and finally fracture the weld. The welds were designed for weld failure before the base material yields. The signal generated by this type of source has high energy. This is ideal for a preliminary study of wave propagation on a tank car filled with liquid because of the attenuation problem. Figure 3.1b shows an example of the bar bending test setup on a steel plate. Examples of signals generated by a lead break and a bar bending approach on the tank car located in the Ferguson Laboratory are depicted in Figure 3.2. Both waveforms were captured by a wide band sensor and the sources were 50 inches from the sensor.





a) Pencil Lead Break



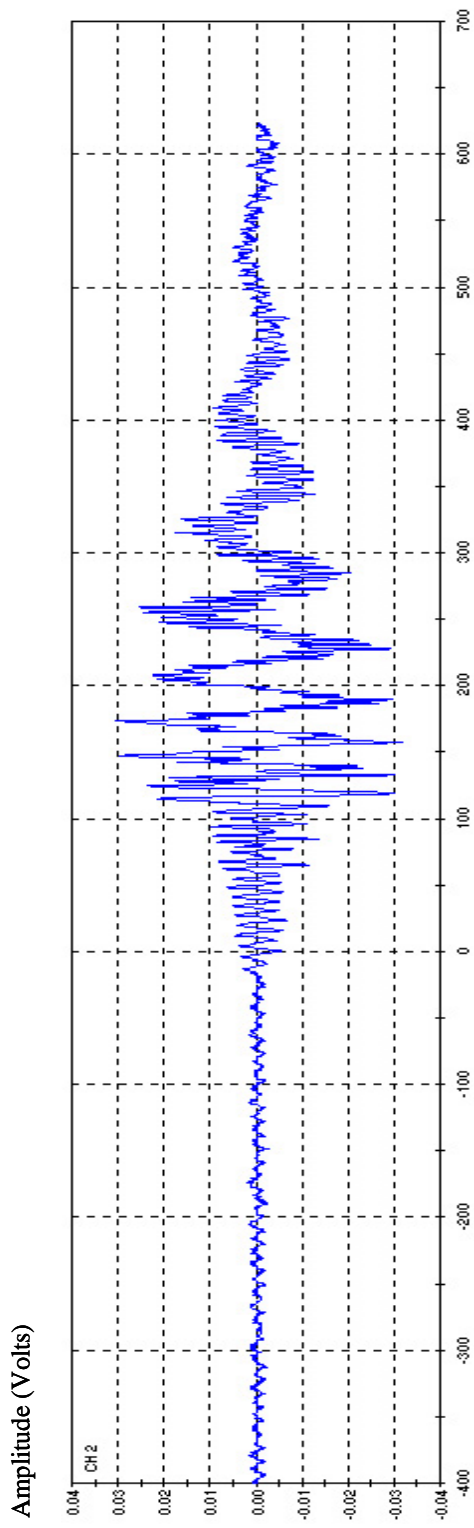
b) Bar bending on a steel plate

Figure 3.1 - Artificial Sources

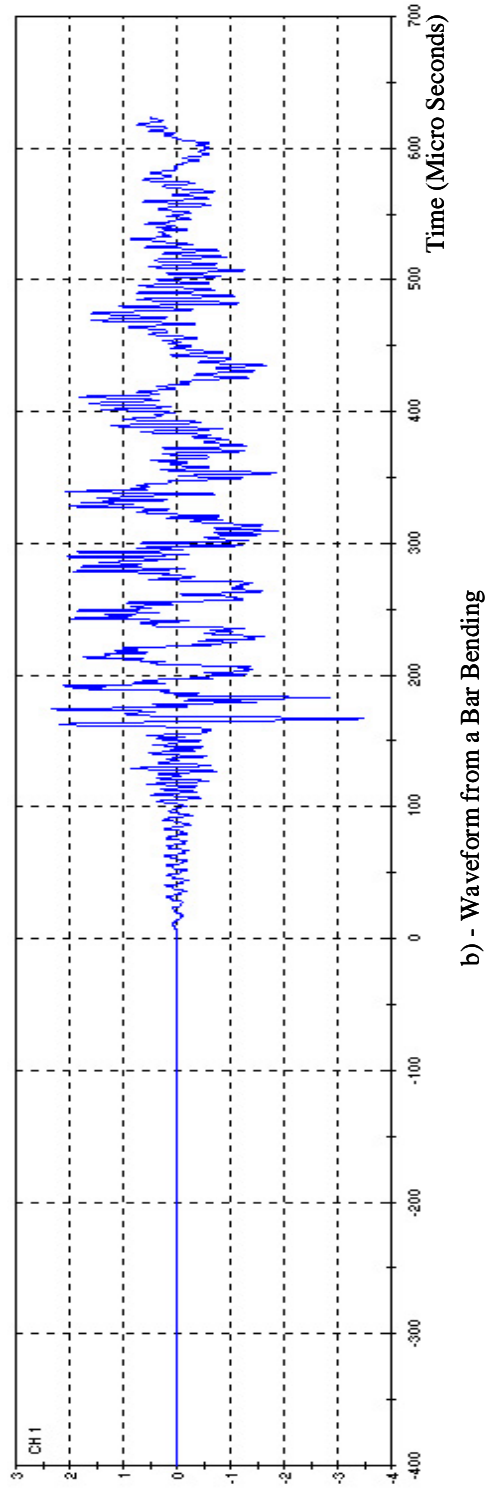
### **3.3 SOURCE LOCATION STUDY ON A TANK CAR WITH A 15/32 INCH THICK SHELL**

#### **3.3.1 Specimen Descriptions**

The first specimen used to study the source location problem is a general-purpose steel railroad tank car located in the Ferguson Laboratory. The tank car is a U.S Department of Transportation specification 111A100-W1, ASTM A-515 grade 70 steel, built in 1969. It is a 36 feet long with an outside diameter of 114 inches and a thickness of 15/32 inch. The thickness of the head of the tank is 1/2". The tank had been used to transport mainly non-hazardous products carried at low pressure such as liquid detergent and corn syrup. The tank car (UTLX 48696) is non-jacketed and was donated to the University of Texas by Union Tank Car company in 1996. In general, the tank is in good condition. A picture of the tank car is shown in Figure 3.3.



a) Waveform from a lead break



b) - Waveform from a Bar Bending

Figure 3.2 – Wide Band Sensor Waveform 50” from Artificial Sources



Figure 3.3 – Tank Car Located in the Ferguson Laboratory

### **3.3.2 Instruments**

The equipment used in the study was a 6 channel digital system named MISTRAS. The system is shown in Figure 3.4. The MISTRAS is manufactured by Physical Acoustic Corporation, Princeton NJ. The sensors used in the tests are wide band sensors (model 9208) and R15I sensors. Preamplifiers with a gain of 40 db were used with wide band sensors. An R15I sensor is resonant at 150 khz with an integral 40 dB preamplifier.



Figure 3.4 – MISTRAS System

### 3.3.3 Attenuation Test

An attenuation test is necessary to ensure that sensor spacing will not exceed the sensor spacing distance. The test requires experimental determination of the zone radius. The zone radius is “the distance at which the average of five 0.3 mm (2H) pencil lead breaks give an amplitude equal to the spacing amplitude” [AAR]. For an empty tank the spacing amplitude is 48db and 42 dB for a full tank. In this case, the spacing amplitude of 48 dB was used.

To obtain the value of zone radius, an attenuation test was performed on the tank car. For the uninsulated tank, 0.3 mm. (2H) pencil lead breaks were performed at every 2 feet along a straight line from the sensor. The test setup is shown in Figure 3.5. The amplitude was recorded as the average amplitude of five lead breaks at each point. This attenuation test was performed for both the wide band and R15I sensors and the results are plotted in Figure 3.6. From the graph, it can be seen that a R15I sensor is approximately 12 dB more sensitive

than a wide band sensor. For this tank, the zone radius is 32 feet for R15I sensors and 17.5 feet for wide band sensors.

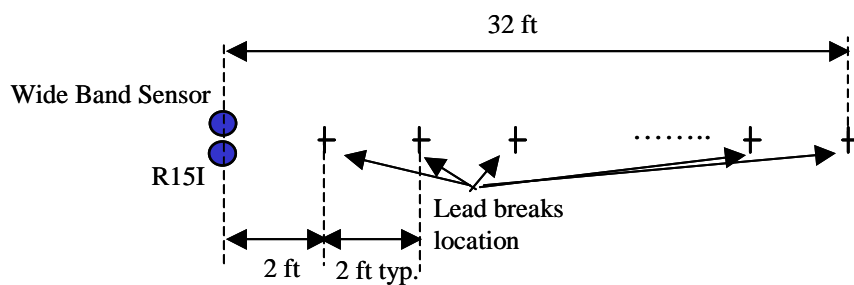


Figure 3.5 – Attenuation Test Setup

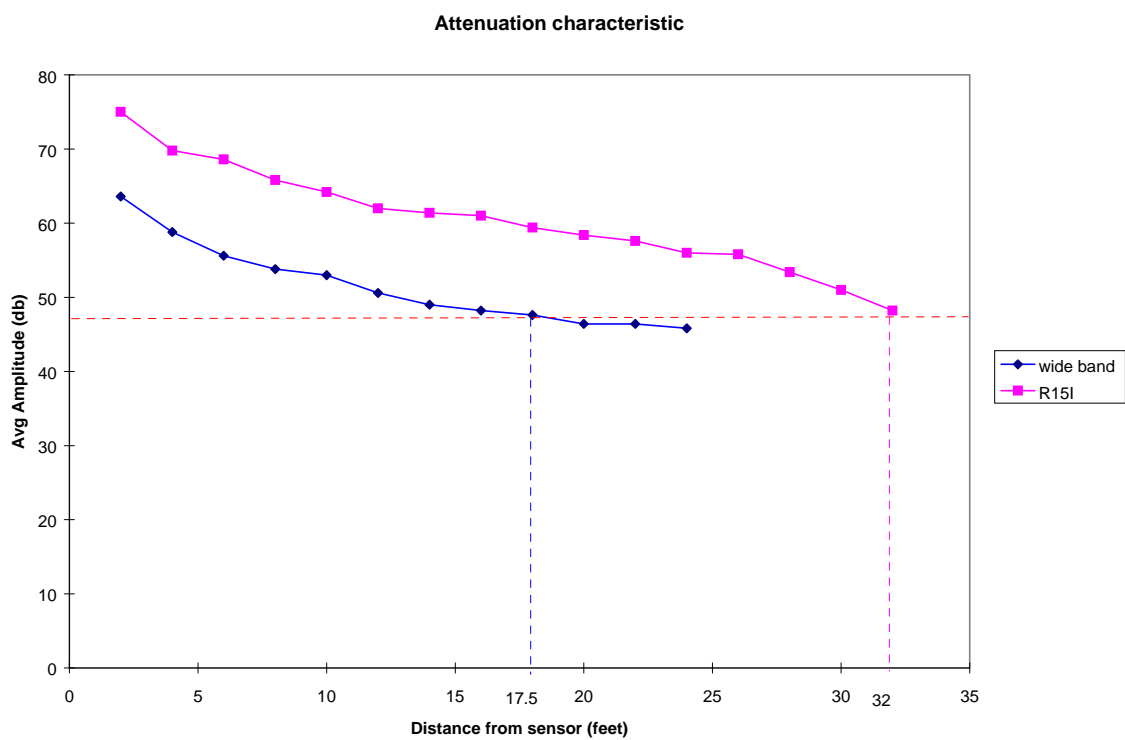


Figure 3.6 – Attenuation Curve

### **3.3.4 Currently Used Source Location Approaches**

Currently used conventional source location methods such as the zonal method and the difference in time of arrival technique are explored in this section. The purpose of this section is to find the errors from these methods and lay a foundation for the improvements discussed in the next section.

#### ***3.3.4.1 Zonal Method***

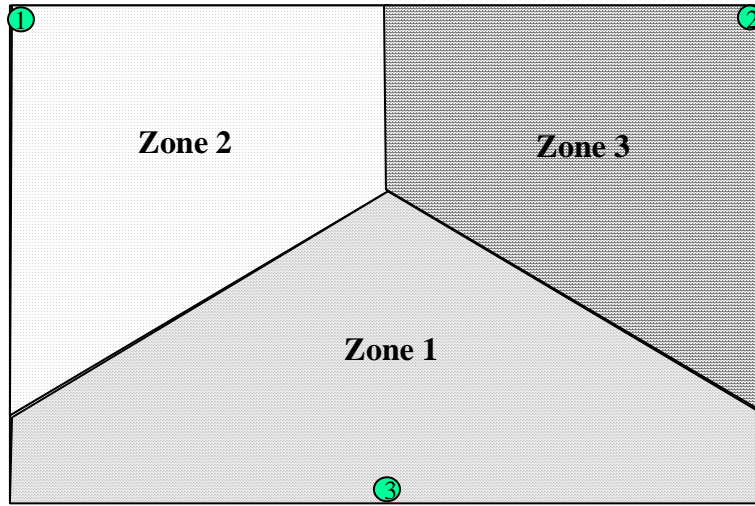
##### *3.3.4.1.1 Test Setup*

For the zonal method, pencil lead breaks were used as an artificial source of emission on the tank car shell. The area of concentration is half of one side of the tank as shown by the rectangle frame in Figure 3.7. The white dots, 9 inches apart in each direction, on the tank car are marks for the location of the lead breaks. Lead breaks were performed three times at each mark.

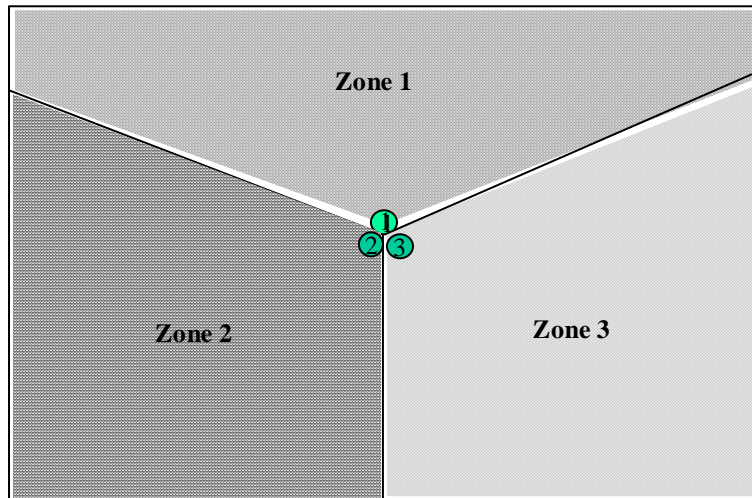


Figure 3.7 – Area of Tank Car Used for Source Location Studies

Two sensor arrangements were explored in the test: open spaced and close spaced arrangements. The open spaced arrangement places the sensors far apart from each other. An example of the open spaced sensor arrangement is presented in Figure 3.8a. The close sensor arrangement places the sensors close to each other as shown in Figure 3.8b. The open spaced sensor arrangement is the typical sensor setup used for AE testing of tank cars. The close spaced sensor setup was for the purpose of testing the multi-element sensor method discussed in Section 2.3.2.2.



a) Open Spaced Sensors



b) Close Spaced Sensors

Figure 3.8 – Sensor Arrangement



#### *3.3.4.1.2 Results*

In this section, all the results were computed based on the first threshold crossing technique with a threshold set at 40 db. The results from the conventional zonal approach based on the open spaced sensor arrangement are shown in Figure 3.9. The marks are 9 inches apart in each direction except for rows 3 and 4 and columns M and N which are 1 inch apart due to longitudinal and horizontal welds. In Figure 3.9, the black lines separate three zones, the black dotted lines represent the weld on the tank car, the red dots are results representing zone 1, the green dots are the results for zone 2, and the blue dots are the ones for zone 3. Most of the results are located in the correct zone except the results in the dashed ellipses.

The results from the close spaced sensor arrangement are shown in Figure 3.10. The symbolic colors which represent the zones are the same as Figure 3.9, except for the yellow dots which represent inconsistent results from three lead breaks. The black dots are locations where lead breaks were not performed. The errors of the results from this sensor arrangement are considerably more than for the open spaced arrangement. Sensor 3 seemed to be more sensitive than the others and therefore received the first hit from almost everywhere.

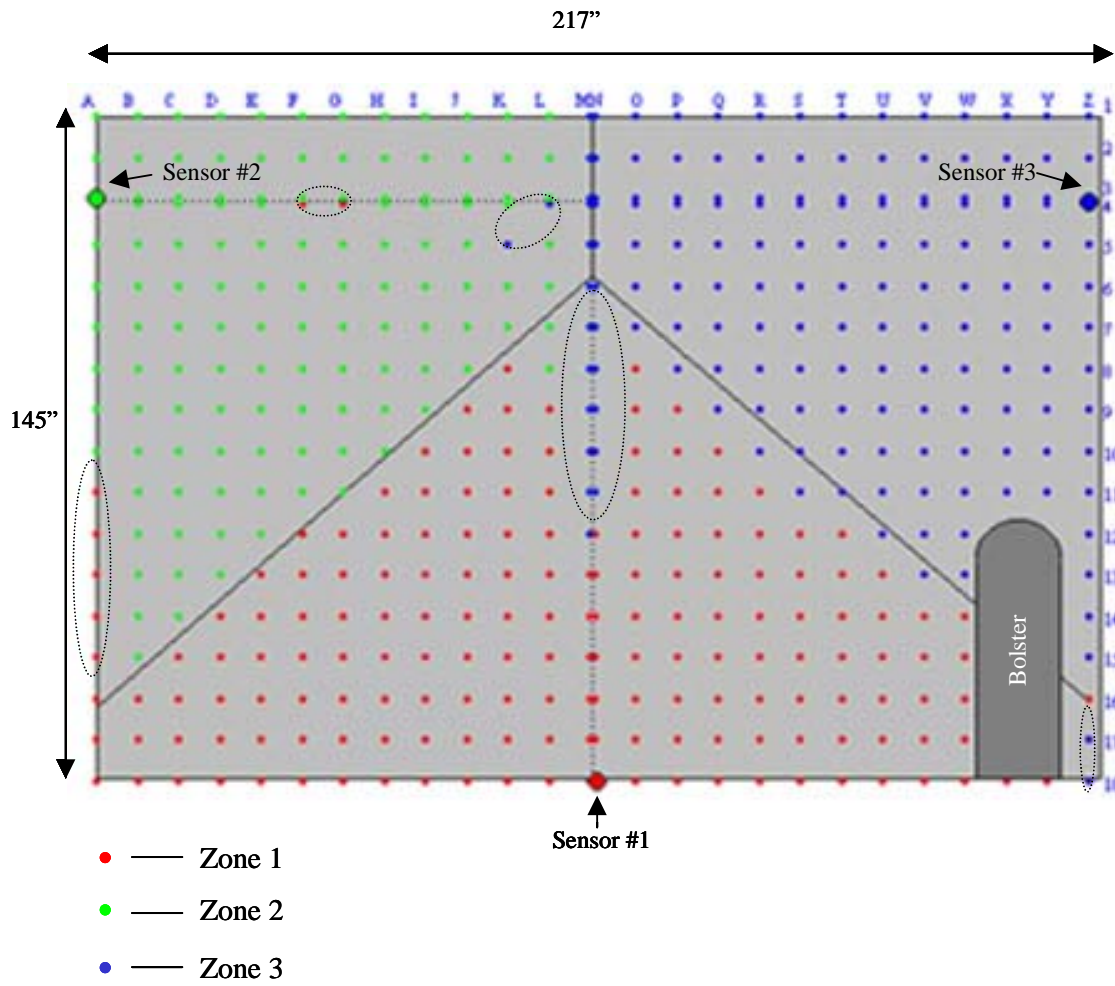


Figure 3.9 – Results from Zonal Method with Open Spaced Sensor Arrangement

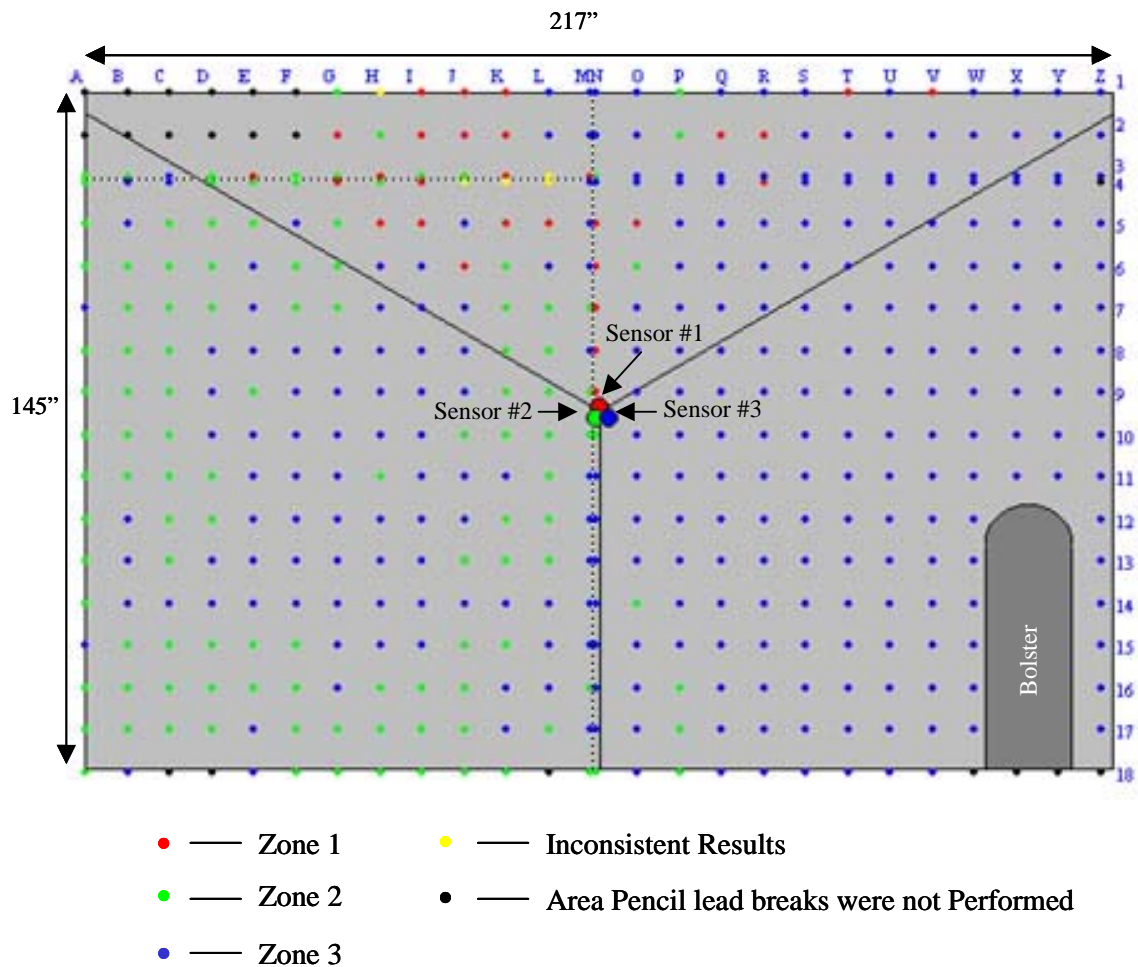


Figure 3.10 – Results from Zonal Method with Close Spaced Sensor Arrangement

### 3.3.4.1.3 Conclusion

Results from the open spaced sensor arrangement (Figure 3.9) show that most of the results were located in the correct zone. Since all sensors were located far apart and with the first threshold crossing technique to detect the

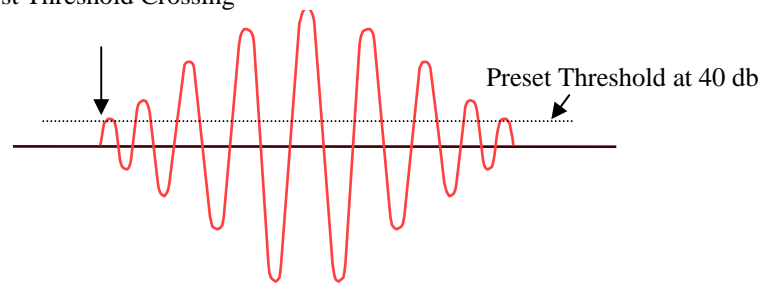
arrival time, all three sensors detected time of arrival at a different phase point of the signal due to the attenuation effect. Although, the signal was known to be attenuated, it does not hurt the method, but instead improves the accuracy. Figure 3.11 illustrates the attenuation of the signal that improves the accuracy in the zonal method.

Figure 3.11 shows that the arrival time defined from the first threshold crossing technique does not give the arrival time at the same phase point for the near and far sensor. The difference is due to the decrease of signal amplitude. However, this does not hurt the results for the zonal approach because the near sensor detects the signal before the far sensor does. The far sensor detects the signal later and the attenuation increases the  $\Delta t$  and makes the method more robust. Therefore the zone is located correctly. Although, the results from the zonal method with the open spaced sensor arrangement yields good accuracy, a method to pinpoint the defect locations is required.

With the close spaced sensor arrangement, all three sensors were placed close together, thus all three sensors were subject to the same attenuation effect and detected the waveform at approximately the same point. Therefore, attenuation was not a problem in this case. However, with the close space arrangement, small differences in the sensitivity of the sensors become more significant. From the calibration data, sensor 3 reads three dB higher than the other sensors. This is the probable reason why sensor 3 received the signal first from almost everywhere.

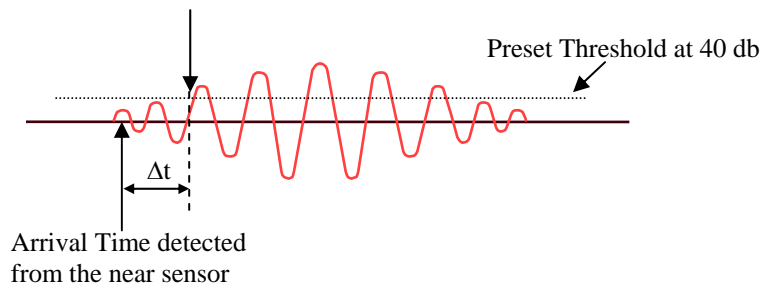
In a practical field test, particularly at low amplitude, it is almost impossible for any two sensors to have exactly the same sensitivity. For the concept of multi-element sensors to work all crystals inside the sensors need to be calibrated for the exact same sensitivity. This means that recalibration would be needed often.

Arrival Time defined by  
the 1st Threshold Crossing



a) Waveform Detected by a Near Sensor

Arrival Time defined by  
the 1st Threshold Crossing



b) Waveform Detected by a Far Sensor

Figure 3.11 - Attenuation Effect on the Arrival Time

### 3.3.4.2 Difference in Time of Arrival Approach

#### 3.3.4.2.1 Concept of the Approach

The difference in time of arrival approach, sometimes called the triangulation method is an approach used to pinpoint the location of defects. The approach which is discussed in Section 2.3.1.1 uses the signal from at least three sensors. This is illustrated in the sensor setup in Figure 3.12.

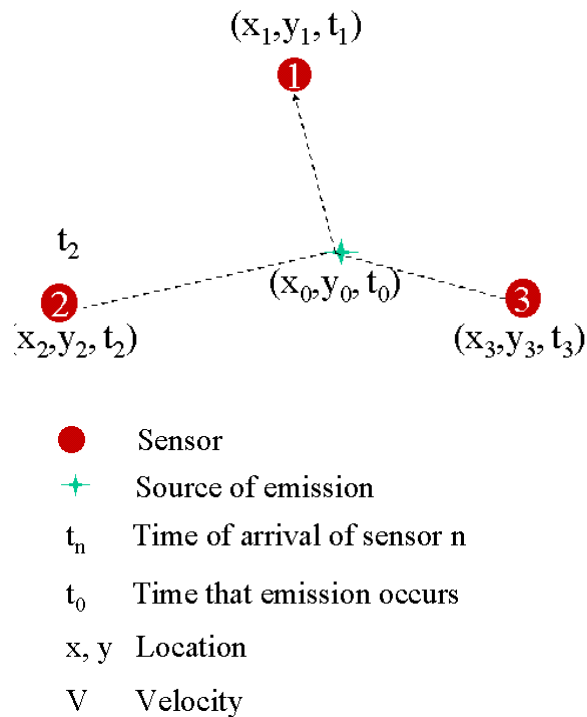


Figure 3.12 – The Triangulation Method

The goal of triangulation is to calculate the location of the source  $x_0$  and  $y_0$ , from known parameters. The location and time of arrival of the stress wave at each sensor are the known parameters. The time  $t_0$  is not included in the calculation. The equations used to calculate the location of the source are:

$$\sqrt{(x_1 - x_0)^2 + (y_1 - y_0)^2} - \sqrt{(x_2 - x_0)^2 + (y_2 - y_0)^2} = V(t_1 - t_2) \dots\dots\dots(3.1)$$

$$\sqrt{(x_1 - x_0)^2 + (y_1 - y_0)^2} - \sqrt{(x_3 - x_0)^2 + (y_3 - y_0)^2} = V(t_1 - t_3) \dots\dots\dots(3.2)$$

In this approach, the main factors used in the calculation are velocity and arrival time at each sensor.

*3.3.4.2.2 Theoretical Wave Velocity on the Tank car*

The key to source location using the difference in time of arrival approach is the wave velocity. The thickness of the tank car wall is 15/32” and waves traveling in the shell are classified as plate waves as discussed in Chapter 2. The velocity of the lowest symmetric mode is faster than the lowest anti-symmetric mode. As the frequency approaches zero (or in the low frequency range), the lowest symmetric mode is a non-dispersive mode traveling at a constant speed as defined in:

$$C_e = \sqrt{\frac{E}{\rho(1-\nu^2)}} \dots\dots\dots(3.3)$$

Where  $C_e$  = plate wave velocity,  $E$  = Young's Modulus,  $\nu$  = Poisson Ratio, and  $\rho_0$  = Density

Typical values for steel are:  $E = 29,000,000$  psi.,  $\nu = 0.3$ , and  $\rho_0 = 0.000733$  lb-sec<sup>2</sup>/in<sup>4</sup>. Therefore, the fastest portion of the lowest order symmetric mode traveling in the steel tank car shell is 212,074 in/sec.

### 3.3.4.2.3 Velocity Measurement

A simple test was performed on the tank car to experimentally measure wave velocity. Two wide band sensors were placed 4.5 inches apart and lead breaks were performed every one-inch for 48 inches. The first break was two inches from the center of the nearest sensor. The test setup is shown in Figure 3.13.

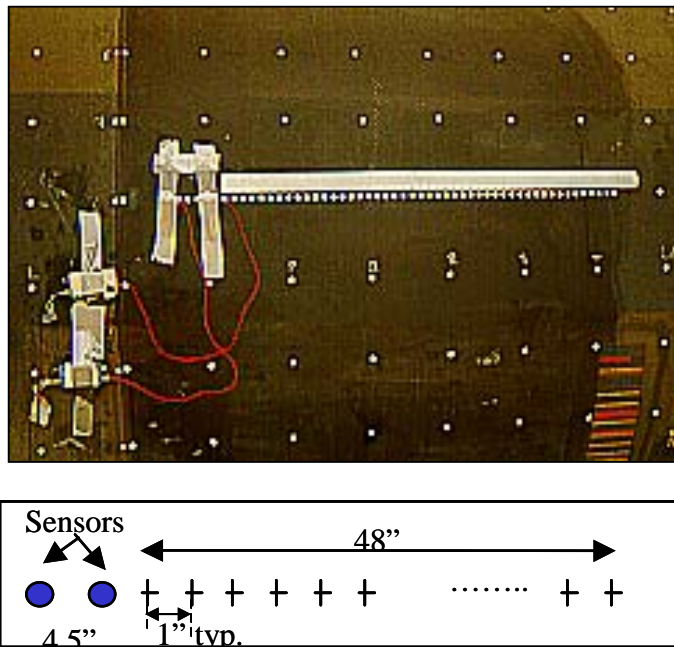


Figure 3.13 - Test Setup for Velocity Measurements



In the calculation of wave velocity, the first threshold crossing of the wave at each sensor was used as the criteria to detect time of arrival. Distances between the two sensors are known values and therefore, wave velocity can be easily calculated. The velocity results compared to the theoretical results are plotted in Figure 3.14. For the results from the first 12 inches, the theoretical and experimental velocity values show good agreement. It is seen that the results from the experiment do not match the theoretical value very well once the source is far (more than 12 inches) from the sensors and the results are inconsistent.

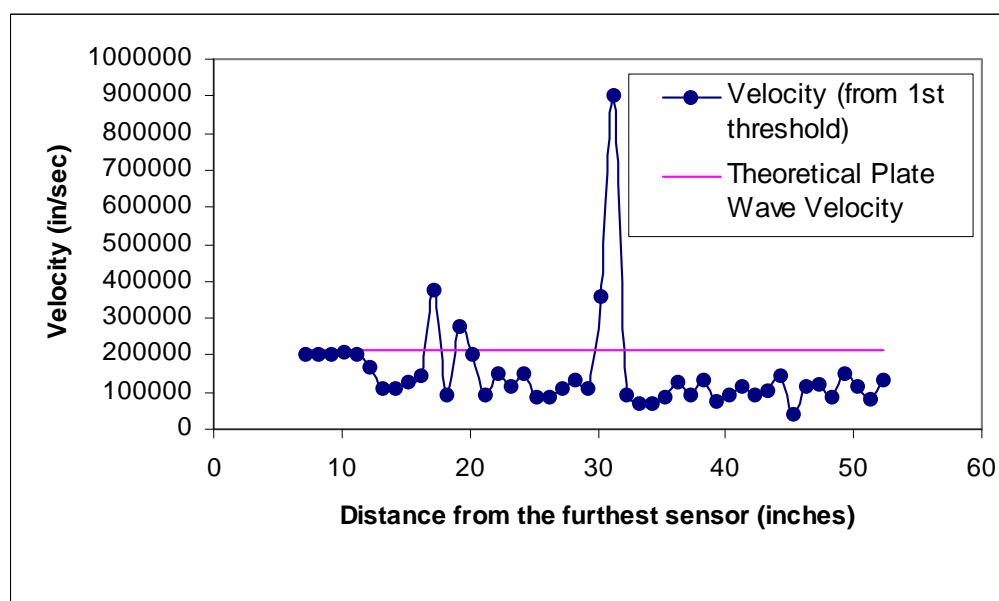


Figure 3.14 - Velocity Results

#### 3.3.4.2.4 Conclusion

From the velocity results in Figure 3.14, when the sources are close to the sensors, the first threshold crossing technique is able to define the arrival time of the beginning of the lowest order symmetric mode, leading to a consistent and correct value of the velocity results.

The velocity results obtained from the sources that are further from the sensors are inconsistent and the value does not match the theoretical velocity. The main reason for the scatter of the velocity results is the attenuation. As the signal travels further, the amplitude of the signal will decrease, which results in the lowest order symmetric mode falling below the threshold. As a result at greater distances from the source, the velocity of the lowest order anti-symmetric mode will be read instead. This is illustrated below. As discussed in Section 3.3.4.1.3 for zonal location, the first threshold crossing technique detects the arrival time of the signal at a different phase point for each sensor. This variation, in the velocity leads to bad source location results.

Figure 3.15 shows a test setup demonstrating the attenuation effect. Two R15I sensors were placed 26 inches apart. Pencil lead break was performed 2 inches from sensor 1. Figure 3.16 demonstrates near field and far field waveforms. The near field signal was detected by a sensor that is close to the source (2 inches) and the far field signal was captured from the sensor that is further away from the source (24 inches).

For the near field signal in Figure 3.16 a, the amplitude of the signal is 0.2V. When the signal has traveled 22 inches further, the amplitude of the signal has dropped to less than 0.05 V as shown in Figure 3.16b. Due to the dispersive characteristic, the lowest order symmetric mode travels faster and separates from the lowest order anti-symmetric mode. The attenuation causes the amplitude of

the lowest order symmetric mode to stay below the threshold. Therefore, the arrival times from two signals were detected at different points. The near sensor defines the arrival time of the lowest order symmetric mode, while the far sensor defines the arrival time at the lowest order anti-symmetric mode.

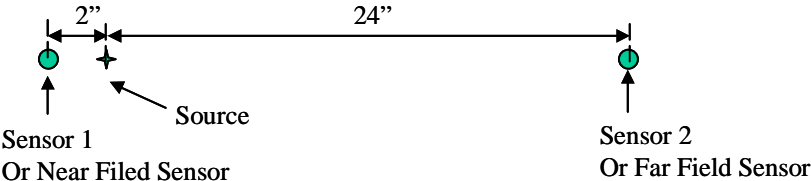
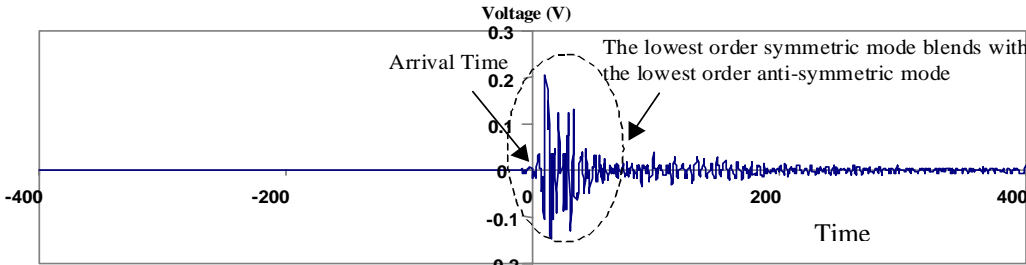
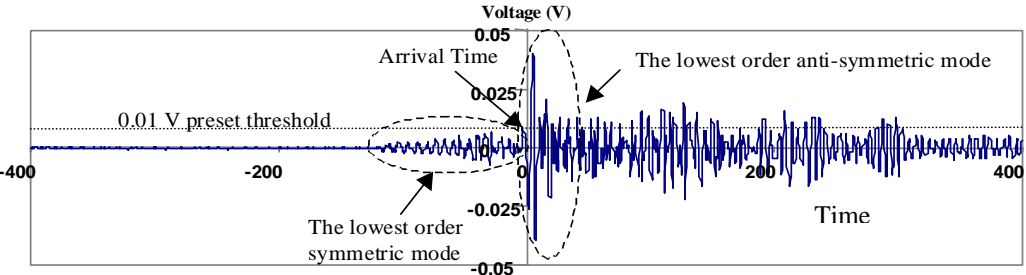


Figure 3.15 – Test Setup for the Attenuation Effect



a) Near Field Wave form



b) Far Field Waveform

Figure 3.16 – Waveform from Near Field Source and Far Field

Attenuation is one of the main reasons the difference in time of arrival technique does not work very well. In order to improve the technique, a new approach to define the arrival time is required. Aside from the attenuation effect, there are problems due to the dispersive characteristic and multiple modes of the plate wave. These factors will complicate the source location task even more. This issue is addressed in the next section.

### **3.3.5 Improvement of Difference in Time of Arrival Approach**

#### ***3.3.5.1 Dispersion Curve***

The thickness of the tank car shell is 15/32", therefore, waves traveling in the shell are plate waves. The main characteristic of plate waves is their dispersive character. Dispersive means that waves do not travel at a constant velocity, rather each frequency travels at a different speed. The dispersion curve of waves traveling in a 15/32" thick tank car shell is shown in Figure 3.17.

In the dispersion curve in Figure 3.17, each line represents a different mode as discussed in Chapter 2. It is seen that waves do not travel at a constant speed and that the velocity depends on their frequency content. In addition, there can be more than one mode traveling at the same time depending on the level of energy exciting the structure. These factors complicate the source location problem.

The energy content of stress waves generated by genuine and artificial sources will be mostly in the first three modes with very little energy in the higher modes [Gorman, 1991]. Fortunately, the first three modes have an intersection at approximately 150 kHz, which means that at about 150 kHz, all three modes travel at the same speed. This speed is 3.2 km/sec or 125,984 in/sec. It is noted

that the intersection of the group velocity is 150 kHz for a 15/32” steel plate. For other thicknesses and types of material, the intersection point will be at a different frequency. The intersection group velocity will be at a higher frequency for a thinner material and for materials with higher modulus of elasticity.

Since at approximately 150 kHz the first three modes travel at the same velocity, source location on an empty tank car can be performed at this frequency. Therefore, all the signals were filtered with a Bessel band-pass filter at the range of 145–155 kHz. Then a triangulation method using simplex optimization, which will be explained in detail in the next section, was performed to pinpoint the location of the source.

At 150 kHz,  $V = 3.2 \text{ km/sec}$  (125,984 in/sec)

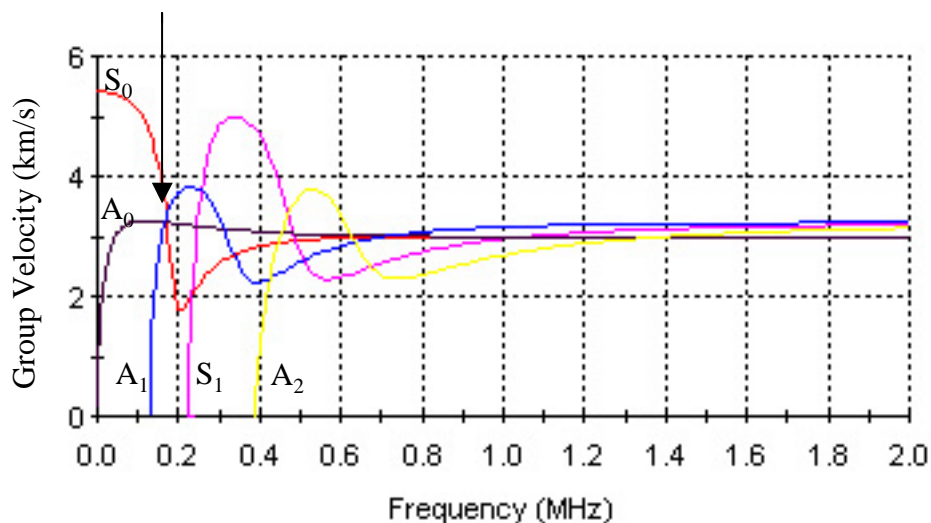


Figure 3.17 – Dispersive Curve for 15/32” Thick Steel Plate

### 3.3.5.2 Source Location with Simplex Optimization Approach

To pinpoint the location of a source, there are two main factors; velocity and time of arrival. The first factor (velocity) is obtained from the dispersion curve at the place where the first three modes intersect at the group velocity. The original signal is filtered in a tight band range at the intersection of the group velocity, which is 150 kHz in this case. Figure 3.18 presents an example of the signal after being band-pass filtered at 145-155 kHz. As for time of arrival, there are a number of ways to define the arrival time. What is important is to ensure that approximately the same phase point is selected on the signal at each sensor. The arrival time can be defined from either the peak of the rectified signal, the negative peak or the positive peak. For the analysis described in this section, the mean time of the negative and positive peaks was used to define time of arrival. This is shown in Figure 3.18.

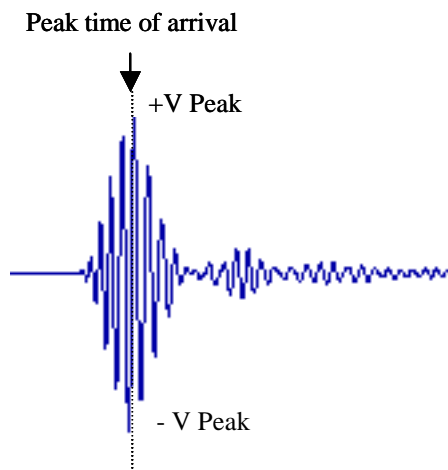


Figure 3.18 - Filtered Signal at 145 – 155 kHz

The algorithm used to calculate source location in this work is the reverse procedure of the regular triangulation technique discussed earlier in Section 3.3.4.2.1. The method is known as simplex optimization. In this method,  $t_0$  will be included as an unknown in the calculation. The procedure starts with the formation of the simple distance calculation equation between each sensor and the source:

$$\sqrt{(x_a - x_0)^2 + (y_a - y_0)^2} = V(t_a - t_0) \dots\dots\dots(3.4)$$

where  $a = 1, 2, 3, \dots, n$   
and  $n =$  number of sensors

The procedure begins by selecting an arbitrary location  $x_0$  and  $y_0$  and calculating  $t_0$ . The values of  $x_0$  and  $y_0$  are adjusted and the procedure repeated to find the location that minimizes the difference in  $t_0$  among the equations. This value will be referred as the Flag value in the dissertation. The formula to calculate the Flag value is given by:

$$Flag = \sum_{a=1}^{n-1} (\sum_{b=1}^{n-a} (\sqrt{(t_{0(a)} - t_{0(a+1)})^2})) \dots\dots\dots(3.5)$$

where  $t_{0(a)}$  is the  $t_0$  of sensor a

Since this method does not use the difference in arrival time between two sensors, no special provisions are needed to locate a source equidistance from the sensors.

There are two different ways to perform the procedure of seeking the best location. The first method uses a predetermined procedure to select analysis locations. Each location is a small increment or decrement in the x and y direction from the previous location. In this manner, the analysis steps through the structure. Location accuracy is determined by the size of the increment. The value that yields the least error in  $t_0$  among all sensors is reported as the location. This algorithm is easy to model and it ensures that the best location is obtained. On the other hand, it is a time consuming when the structure is large and a small stepped value is selected.

The second method is to divide the structure into zones and select the location in the middle of each zone and calculate the best answer among those positions. Then, the zone of interest is subdivided and the procedure repeated to find the sub-zone that yields the best answer. The algorithm repeats until the zone is smaller than the allowable error. This approach takes a lot less time to process but it is possible that the true location will not be in the zone with the least error at the middle.

In this work, a source location application using Microsoft C++ running on a Windows environment programmed by the author uses the first approach to ensure that none of the locations were missed in the calculation. A stepped value of one inch increment was chosen.

### ***3.3.5.3 Velocity Measurement***

From the dispersion curve in Figure 3.17, the theoretical group velocity at the intersection of the first three modes of the plate wave traveling in 15/32" of steel plate is 125,984 in/sec. In this section, the group velocity was measured experimentally to compare with the theoretical one. Data from the same velocity



test presented in Section 3.3.4.2.3 was used. This time, all the signals were band-pass filtered in the range of 145-155 kHz and the median of the negative and positive peaks was used for the arrival time. Figure 3.19 shows the comparison of all velocity results. It shows that the measured group velocity obtained from a 145-155 kHz signal shows a good agreement with the theoretical group velocity. Figure 3.20 shows the comparison of the theoretical and measured group velocity at a smaller scale. The average velocity used in the analysis is 125,000 in/sec.

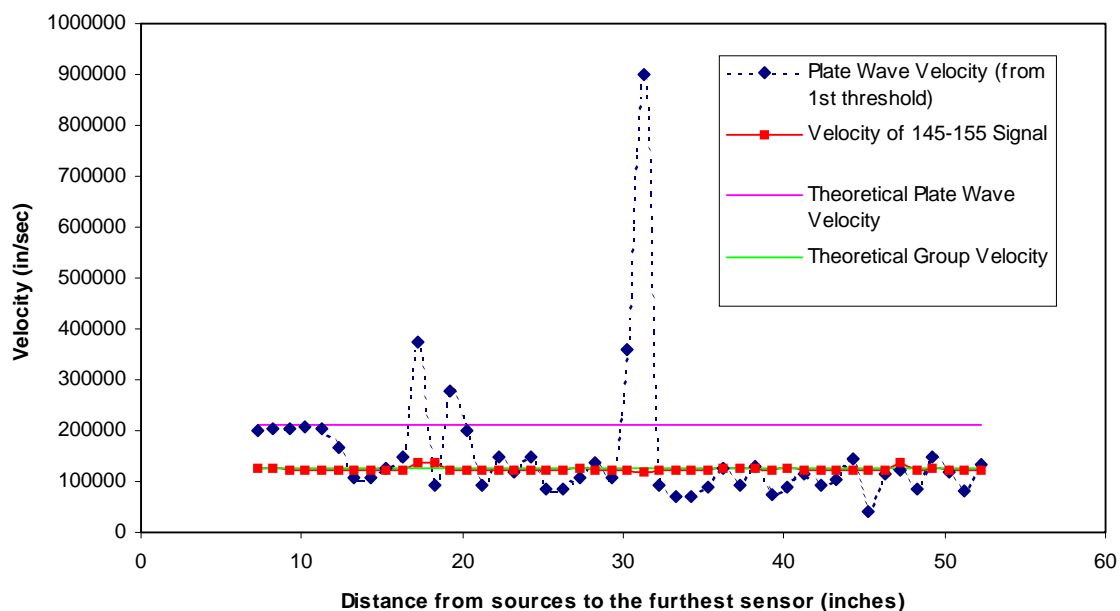


Figure 3.19 - Velocity Results

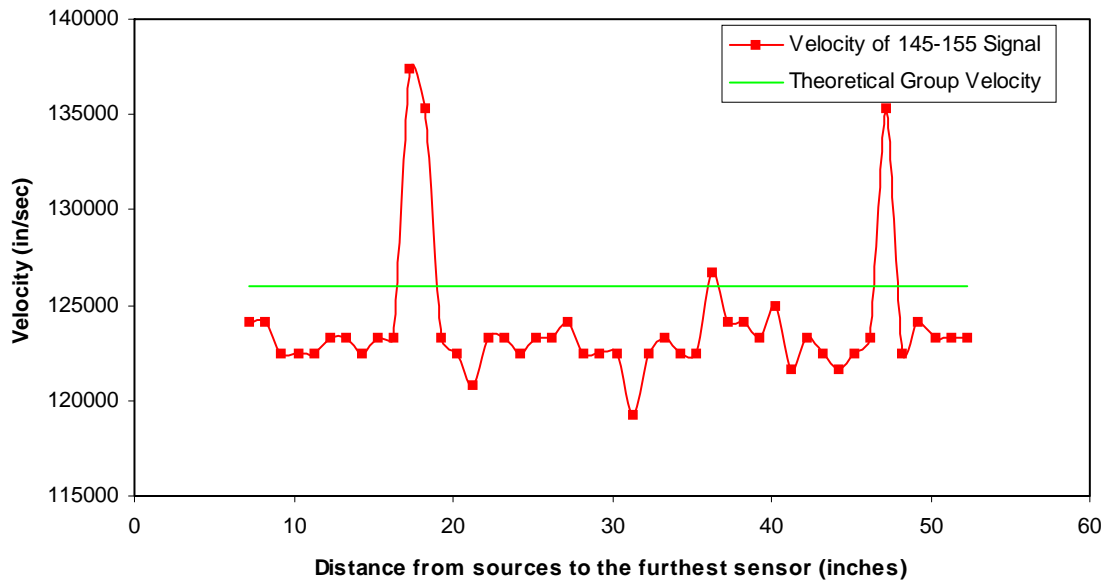


Figure 3.20 - Group Velocity

#### 3.3.5.4 Source Location Program

A source location program using the concept of a tight band-pass filter was developed by the author. The application was programmed with Microsoft C++ running in a Windows environment. The algorithm of the program is shown in Figure 3.21.

The program reads the filtered waveform information from the PolyModal program [PAC, 1999] and arranges the hits in time order based on the arrival time from the first threshold crossing.

From the time ordered hits, the program separates events. In this process, if the next hit is 0.003 milliseconds later than the previous hit, the next hit belongs

to a new event. The 0.003 milliseconds came from the maximum time the waves travel in the tank. This number also covers the case of water borne waves.

The program displays the waveforms in a group for each event and allow the user to define the arrival time of each waveform manually by a mouse click. The program also allows the user to select the signal for source location analysis in the case that more than three sensors pick up the signal and some signal cannot be defined for the arrival time. After the arrival time has been defined, source location analysis was performed using the simplex optimization method with a predefined step value. The location results are recorded in an output file.

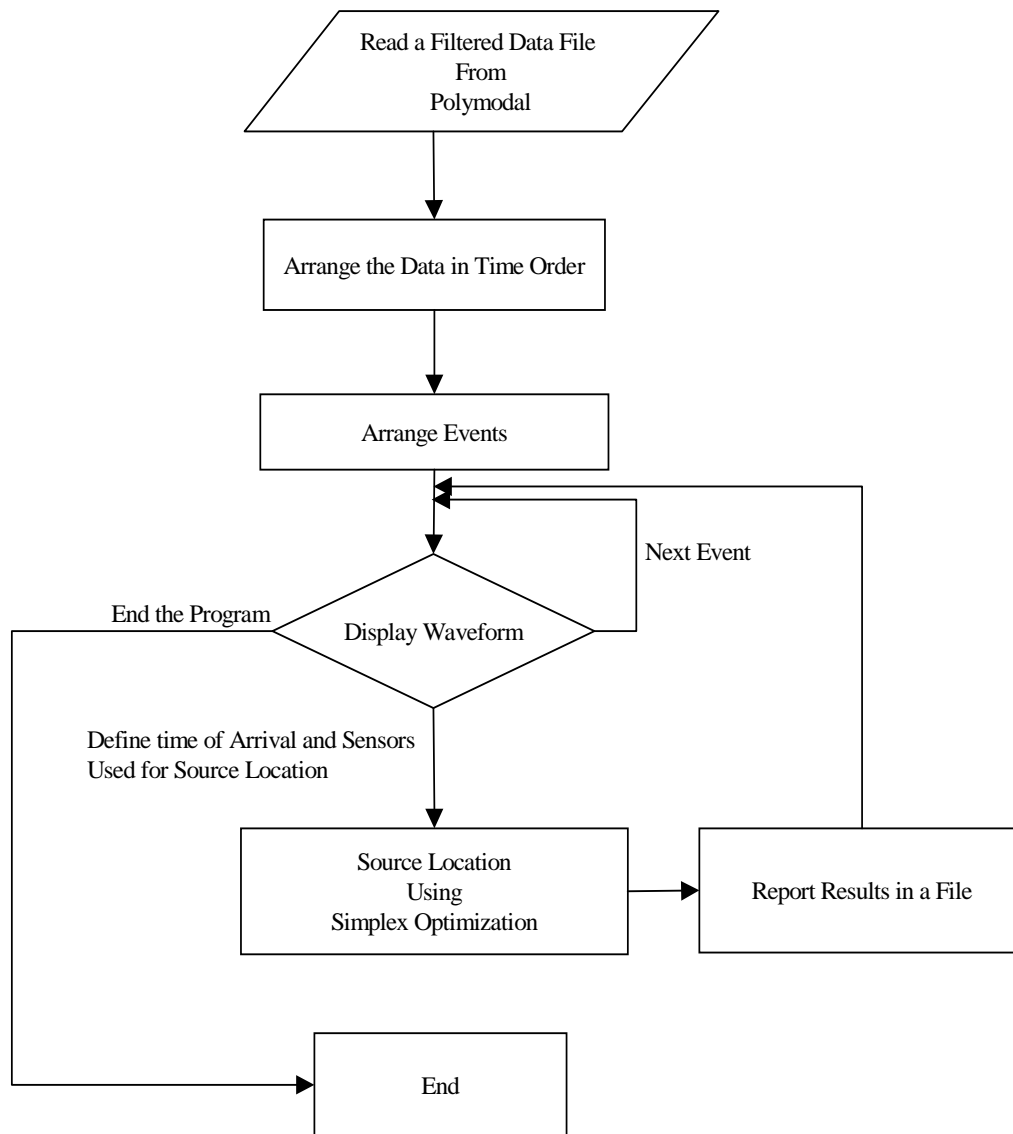


Figure 3.21 - Flowchart for the Source Location Program

### ***3.3.5.5 Results from Pencil Lead Break on the Tank Body***

Pencil lead was first used as an artificial source to study wave propagation in an empty tank car. Lead breaks were performed every 9 inches apart in the horizontal and vertical direction on the tank car wall, and four wide band sensors were used to capture the waveforms. First, the lead breaks were performed on an area with no discontinuities. An area of 36 ft<sup>2</sup> (6 ft x 6ft) was covered with four wide band sensors. The results are plotted to scale in Figure 3.22, where 85% of the results (62 out of 77 breaks) are located exactly at the source. The maximum error of the other hits is 1 inch which is the accuracy of the simplex optimization approach which used one-inch steps in the x and y directions. The starting point for calculating  $t_0$  was chosen as the real location of the lead breaks.

A similar test was performed in an area including a vertical weld. The area the sensors covered was 41 ft<sup>2</sup> (6 ft x 6.83 ft). The source location results in the area with the weld discontinuity are shown in Figure 3.23. The dotted line in the picture represents the vertical weld in the tank. The width of the weld is approximately one inch and the weld is thicker than the tank shell. Forty seven percent of the results were located correctly. The calculation did not consider mode conversion and local changes in the wave velocity at the weld. This is the likely reason for the lower accuracy of the results. The maximum error from this test is 2 inches.

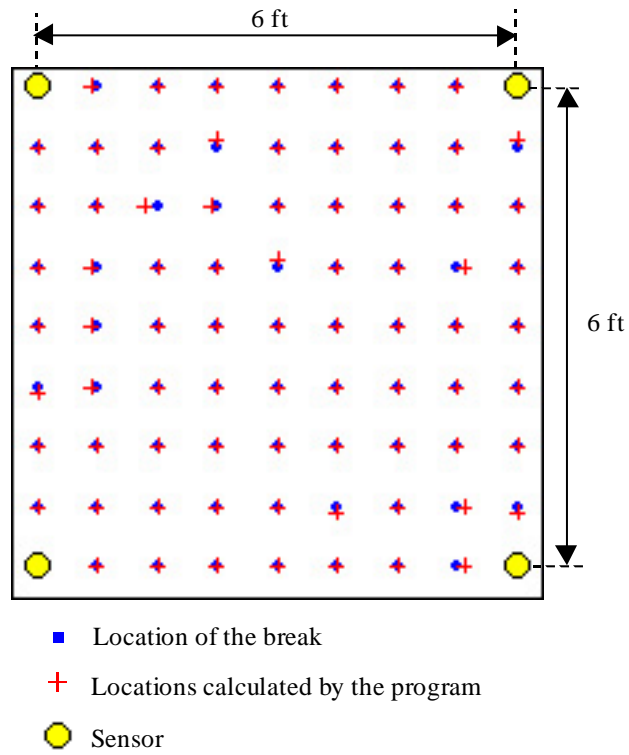


Figure 3.22 – Results from Pencil Lead breaks in Area with no Discontinuities

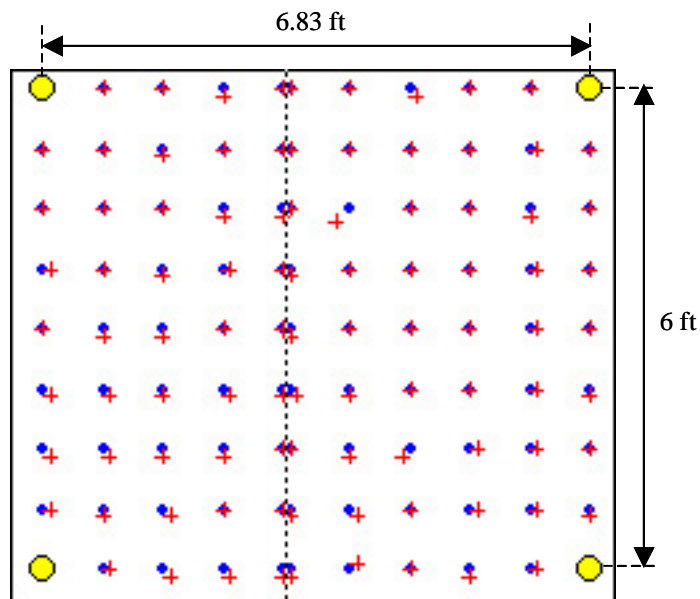


Figure 3.23 - Results from Pencil Lead Breaks in an Area with a Vertical Weld

Another lead break test was performed in an area including a vertical and horizontal weld in the tank car. The sensors covered an area of 51 ft<sup>2</sup> (7.5 ft x 6.83 ft). The source location results from the test are shown in Figure 3.24. The dotted lines in the picture represents the vertical and horizontal welds in the tank. The width of both welds is approximately one inch and the weld is thicker than the tank shell. Forty eight percent of the results were located exactly. Again the calculation did not consider the discontinuity between the welds and the tank car shell. The maximum error from this test is 2 inches.

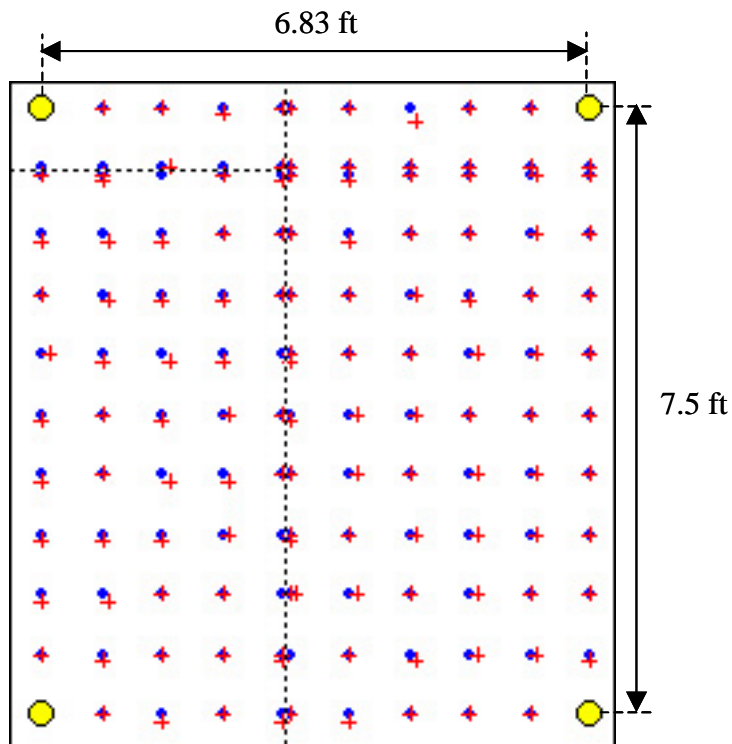


Figure 3.24 - Results from Pencil Lead Breaks in Area with Welds

Since the source location analysis for the empty tank was performed based on the frequency at the intersection of the group velocity of the first three modes and in this case the working frequency is in the range of 145-155 kHz, another lead break test was performed on the area with no discontinuity using four 150 kHz resonant sensors (R15I). The benefit of the resonant sensors over the wide band sensors is the increased sensitivity. The source location results from the test are shown in Figure 3.25. Seventy two percent of the results were located correctly. The maximum error is two inches.

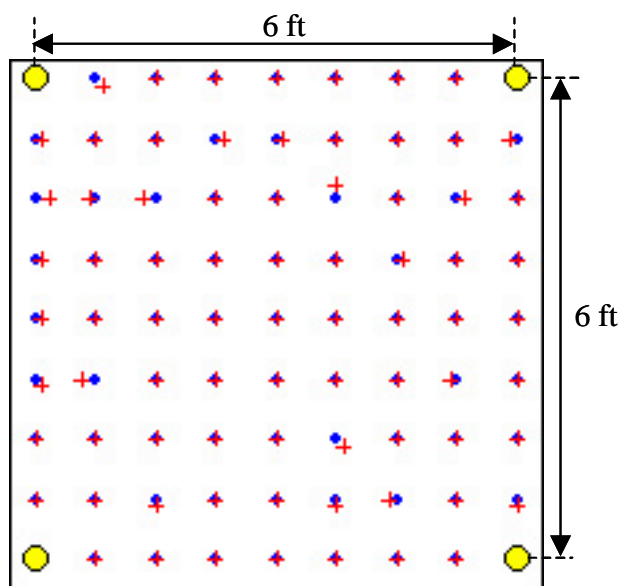


Figure 3.25 - Results from Area with no Discontinuity Using R15I Sensors

The results shown in Figure 3.25 show that the accuracy of the source location approach using wide band and R15I sensors is comparable. The advantage of using R15I sensors is that they allow a larger area to be covered with the same number of sensors. Note that for different thicknesses, the frequency of



the resonant sensors must be chosen to correspond to the intersection of the group velocity for that thickness.

### ***3.3.5.6 Study of Wave Propagation on the Bolster Area***

Bolsters create a discontinuity on the tank car. They function as supports for the tank by transferring forces to the wheels. The bolster consists of a one-inch thick steel pad welded to the tank shell. A bolster leg is welded to the pad forming a support for the tank. In this study, four wide band sensors were used with pencil lead breaks as artificial AE sources. In all tests, sensor 1 was mounted next to the source and was used as to capture a signal. Accordingly, sensor 1 is referred as the trigger ( $t_0$ ).

#### ***3.3.5.6.1 Test Setup***

Two testing setups were arranged to study the signal traveling through the bolster area. The first test was conducted to study the signal propagating through the upper part of the bolster, not including the leg. This test setup is shown in Figure 3.26. Locations of the lead breaks are marked by white dots surrounding sensor 1 which was attached with duct tape. The other sensors were attached with magnetic holdowns. The second setup was performed to study the signal traveling through the lower part of the bolster where the leg of the bolster is involved. The test setup is similar to the setup for the upper part of the bolster and is presented in Figure 3.27.

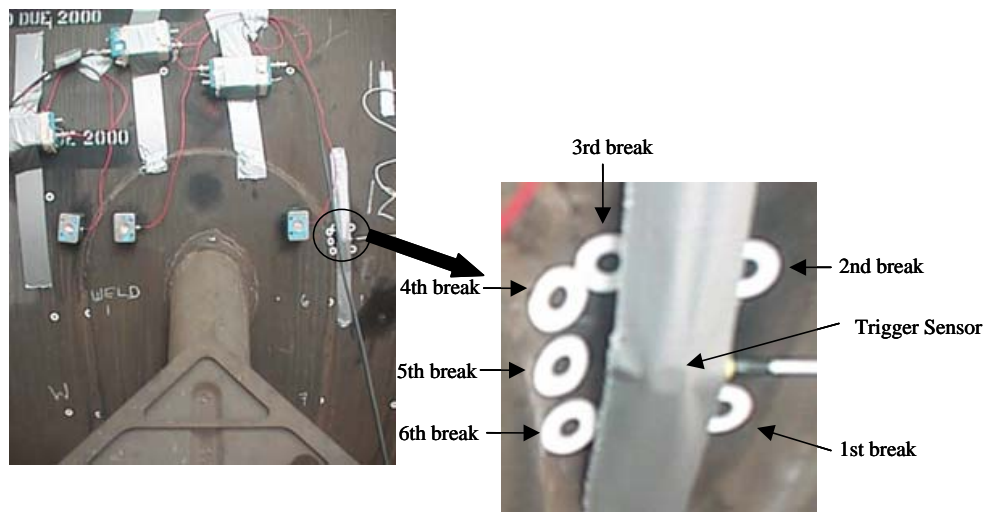


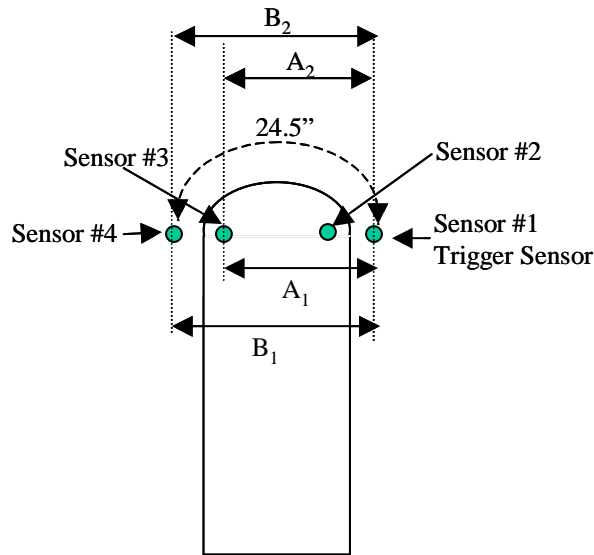
Figure 3.26 – Test Setup for a Wave Propagation Study on the Upper Part of the Bolster



Figure 3.27 – Test Setup for a Wave Propagation Study around the Bolster

#### 3.3.5.6.2 Results

The distances between the trigger sensor and the sensors 3 and 4 for the test through the upper part of the bolster are shown in Figure 3.26. In the test, data from sensor 2 was not used in the analysis.



$A_1 = 16''$  through pad  
 $A_2 = 15''$  direct distance  
 $B_1 = 20.125''$  through pad  
 $B_2 = 18''$  direct distance

Figure 3.28 – Distance from the Trigger Sensor to Sensors 3 and 4 for the Upper Part of the Bolster

The objective of the analysis is to find the path of the signal through the bolster. Possible paths include the bolster pad, the tank car shell underneath the pad, or an indirect route around the bolster pad. The dispersion curves for these paths were then studied in order to obtain a correct group velocity for each path. For the one-inch thick pad, the group velocity occurs at a frequency of 85 kHz, whereas for the tank shell (15/32" thickness) it occurs at the frequency of 150 kHz. At these two frequencies the signals travel at the same velocity of 125,000 in/sec.

Based on the assumption above, the signals were filtered twice, once in the range of 145-155 kHz and, once in the range of 90-80 kHz. The mean of the

negative and positive peak of the filtered signal was then used to define the arrival time which was subsequently used to calculate the distance from the source (or sensor 1) to the other sensors. Pencil lead breaks were performed at six different locations with the last three breaks carried out directly on the weld. All of the breaks were close to sensor 1 (less than 1 inch) and therefore the mean of the peak of the signal from sensor 1 was used as the trigger time, or  $t_0$ . Note that errors are expected from each break since the breaks surrounded the sensor and were up to one inch away. Knowing the difference in time between the two sensors and the velocity, the distance the waves travel from the source to other sensors can be calculated. The calculated distance between the sensors from the test are presented in Table 3.1. In Table 3.1, note that Dist1-4 and Dist1-3 are distances from sensor 1 to sensor 4, and distance from sensor 1 to sensor 3.

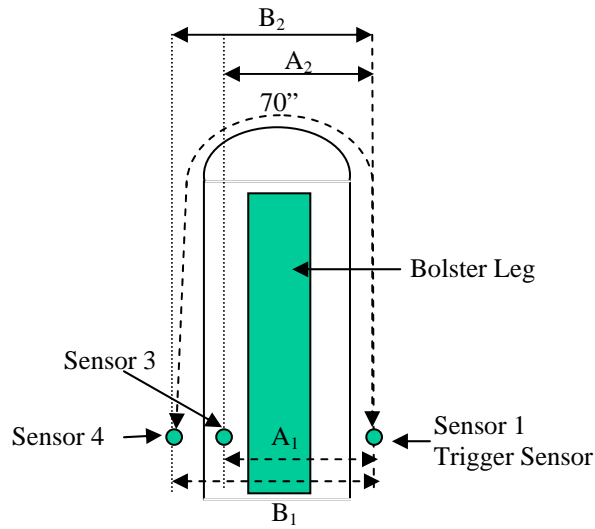
Break #	145-155 kHz Signal		80-90 kHz Signal	
	Dist1-4(inches)	Dist1-3 (inches)	Dist1-4 (inches)	Dist1-3 (inches)
1 <sup>st</sup> break	20.16	19.12	18.89	19.37
2 <sup>nd</sup> break	18.45	17.67	18.21	13.64
3 <sup>rd</sup> break	17.51	16.60	16.92	10.80
4 <sup>th</sup> break	16.41	12.75	15.65	9.98
5 <sup>th</sup> break	16.09	16.25	16.72	11.21
6 <sup>th</sup> break	21.51	17.61	19.37	18.61
<b>Avg.</b>	<b>18.35</b>	<b>16.67</b>	<b>17.63</b>	<b>13.93</b>
<b>Measured Distance</b>	<b>18.00</b>	<b>15.00</b>	<b>20.13</b>	<b>16.00</b>

Table 3.1 - Calculated Distance from Sensor 1 to Sensors 3 and 4 for the Upper Part of the Bolster

As mentioned before, an error is expected from each break because the break is not exactly at the trigger sensor. They were off by up to one inch either to the right or left. The distance calculated from each break is not expected to be consistent, but the average value from the results should be reliable.

Based on the assumption that the signal travels through the thicker pad, the average calculated distance from the sources to sensor 4 is 17.63 inches, whereas the measured distance of the route is 20.125 inches. For the indirect path around the top of the bolster pad on the tank shell, the average calculated result is 18.35 inches which should be compared to the measured distance of 24.5 inches. For the direct path through the tank shell underneath the pad, the average calculated distance of 18.35 inches closely matches the measured distance of 18 inches. Therefore, from the test it is seen that the most likely path is that the signal propagates through the tank shell underneath the bolster pad.

The second test studied the signal propagation through the lower area of the bolster including the bolster leg. The measured distance between the trigger sensor and sensors 3 and 4 are shown in Figure 3.29. The calculated distances from the trigger sensor to other sensors, based on the velocity, are presented in Table 3.2. This time not every sensor received all of the hits. When the breaks were performed on the tank shell (the 1<sup>st</sup>, 2<sup>nd</sup>, and 3<sup>rd</sup> breaks), sensor 3, which is on the bolster pad did not receive the signal. This indicates that the signal does not travel through the bolster pad. When the break was on the weld (the 4<sup>th</sup> and 6<sup>th</sup> breaks), sensor 3 received the signals.



$A_1 = 16''$  through pad  
 $A_2 = 15''$  direct distance

$B_1 = 20.125''$  through pad  
 $B_2 = 18''$  direct distance

Figure 3.29 – Measured Distance from the Trigger Sensor to Sensors 3 and 4 for the Lower Part of the Bolster

Based on the assumption that the signal travels through the indirect path around the top of the bolster pad, the average calculated distance from the sources to sensor 4 is 18.89 inches compared to the measured distance of 70 inches. For the route through the bolster pad, an average result of 19.06 inches was obtained compared to the measured distance of 20.125 inches. For the direct path through the tank shell underneath the pad, the average calculated distance is 18.89 inches; which shows agreement with the measured distance of 18 inches.

The results obtained from these two tests show the correct path of the signal is directly through the tank shell underneath the bolster pad. The assumption that the signal made an indirect path around the bolster pad was

obviously incorrect due to the large difference between the calculated and measured distances. The assumption that the signal travels through the bolster pad is not correct either because the sensor on the bolster pad in the second test did not receive the signal when the source came from the shell of the tank. Rather, the sensor only detected a stress wave when the source was on the weld. The only explanation for these events is that the signal actually made two separate paths. One went right through the tank shell under the bolster pad, the other went on the pad. The reason why the sensor on the pad did not receive the signal on the test with the leg of the bolster included, is that the signal travels through 2 more welds. These welds act as a shield to the signal. Also, a thicker material tends to have a higher attenuation rate.

Break #	145-155 kHz Signal		80-90 kHz Signal	
	Dist1-4(inches)	Dist1-3 (inches)	Dist1-4 (inches)	Dist1-3 (inches)
1 <sup>st</sup> break	19.65	N/A	17.37	N/A
2 <sup>nd</sup> break	19.65	N/A	20.03	N/A
3 <sup>rd</sup> break	17.98	N/A	19.75	N/A
4 <sup>th</sup> break	18.99	16.78	20.00	16.9
5 <sup>th</sup> break	18.30	N/A	18.80	N/A
6 <sup>th</sup> break	18.77	15.31	18.39	16.95
<b>Avg.</b>	<b>18.89</b>	<b>16.05</b>	<b>19.06</b>	<b>16.93</b>
Measured Distance	<b>18.00</b>	<b>16.00</b>	<b>20.13</b>	<b>15.00</b>

Table 3.2 – Calculated Distance from Sensor 1 to Other Sensors for the Lower Part of the Bolster



A final test was performed to confirm the results from the analysis above. The test setup using three sensors is shown in Figure 3.30. This time, three lead breaks were performed at the same place right next to sensor 1. The calculated distances from the trigger sensor to the other sensors are listed in Table 3.3.

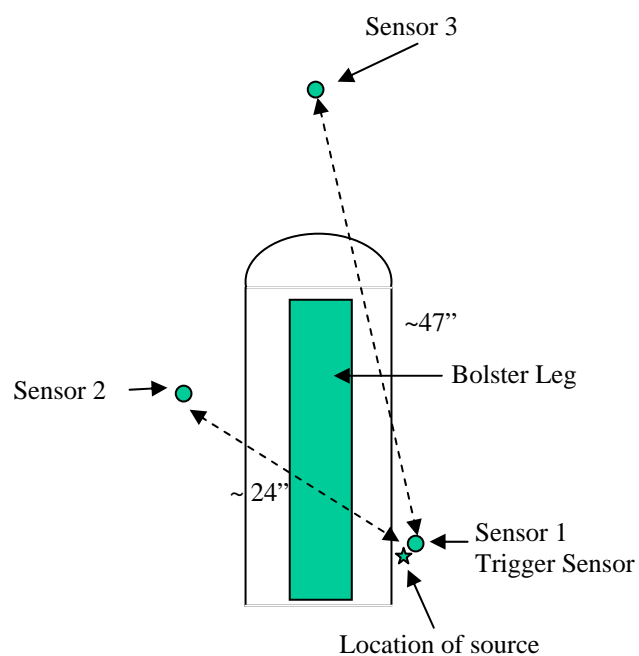


Figure 3.30 – Distance from the Trigger Sensor to Other Sensors

Break #	145 – 155 kHz Signal	
	Dist1-2 (inches)	Dis1-3 (inches)
1 <sup>st</sup> break	23.68	47.06
2 <sup>nd</sup> break	24.31	47.47
3 <sup>rd</sup> break	23.78	47.12
<b>Avg.</b>	<b>23.91</b>	<b>47.22</b>
<b>Measured Distance</b>	<b>~24</b>	<b>~47</b>

Table 3.3 - Calculated Distance Results

From the results, the average calculated distance from the trigger sensor to sensor 2 is 23.91 inches compared to the measured length of approximately 24 inches and the average calculated result from the trigger sensor to sensor 3 is 47.22 inches comparing to the measured distance of approximately 47 inches. The results obviously show that the signal took a path through the tank shell under the bolster pad.

### 3.3.5.6.3 Conclusion

To study wave propagation paths in the bolster area, three tests were performed with pencil lead breaks. The first test demonstrates the wave propagation route through the upper part of the bolster. The second test shows the wave propagation path through the lower part of the bolster. In this test, the bolster leg is attached to the bolster pad between the source and the sensors. The last test was to confirm the routes concluded from the first two tests.

From the first two tests, it is seen that the calculated distances from the source to sensors 3 and 4 have vary with each lead break. This is because lead breaks were not performed right at the location of the trigger sensor. Instead, they surrounded the trigger sensor.

The results for the first test on the upper part of the bolster from sensor 1 to sensor 4 show that the waves propagate through the tank car shell underneath the bolster pad. The results from sensor 3 are not conclusive from this test.

From the second test on the lower part of the bolster, the results from sensor 1 to sensor 4 also show that the signals propagate through the tank car shell. In this test, sensor 3, which was placed on the bolster pad, sometimes did not detect the signal while sensor 4 detected the signal. This shows that the signal propagates separately in two paths, one through the tank car shell and the other on the pad.

The distance results from the last test were calculated based on the assumption that the source propagates through the tank car shell. All sensors were placed on the shell and the calculated results show good agreement with the measured distances.

### ***3.3.5.7 Results from a Bar Bending Approach***

After obtaining promising results from the lead break tests in Section 3.3.4.4, the bar bending method was used as a source to confirm the accuracy of the source location method. In these tests, a rectangular steel bar was welded to the tank car shell, then a force was applied at the end of the bar to yield and finally fracture the weld. The benefit of the bar bending approach is that the signal generated by this type of source has high energy. More importantly, the method stimulates real source mechanisms (yielding and cracking), which is very

useful for source location studies. In the calculation for locating the source, the simplex optimization was used with a step value of 0.1”.

In this section, five bar bending tests were performed on the tank car. Four bar bending tests were performed on the tank car body and one was done on the head of the tank. The tests were performed in the laboratory where, because of the controlled environment, external noise was minimized. Therefore, the threshold was set to the low value of 35 dB. Figure 3.31 shows an example of the waveform from a bar bending test captured by a wide band sensor.

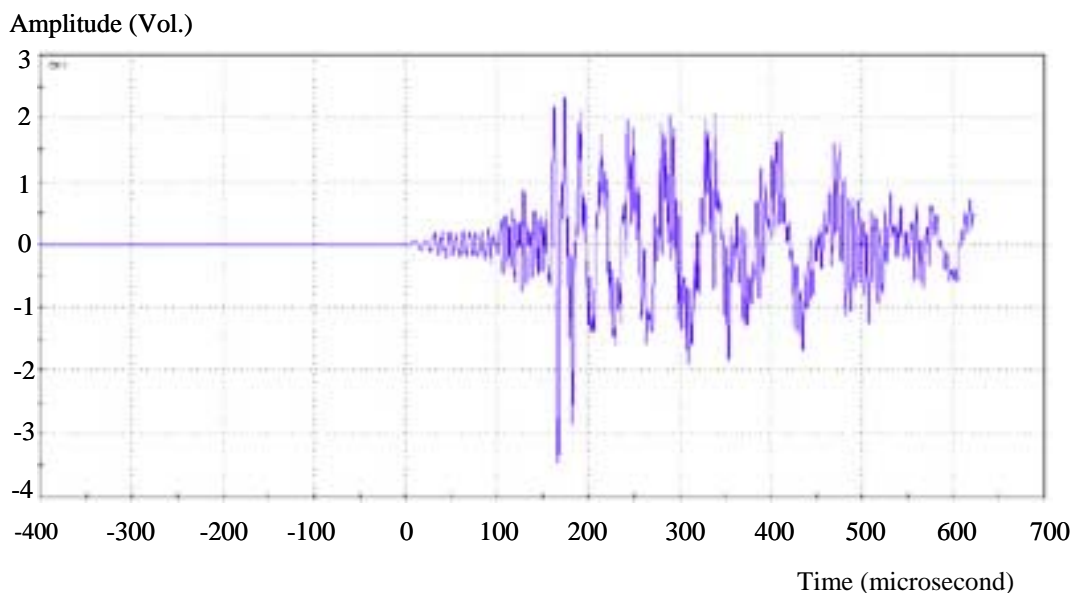


Figure 3.31 - Waveform Generated by Bar Bending Method

In the tests, parametric information and waveforms are recorded. Since the process of recording the waveform information takes longer than saving the parametric information, the waveform was only recorded for some hits.

- *Bar Bending Test in an Area with no Discontinuities*

The first bar bending was performed in an area with no discontinuities on the tank car. An area of 36 ft<sup>2</sup> (6 ft x 6ft) was covered with four wide band sensors. The test setup is shown in Figure 3.32. Note that the white marks in the picture have no bearing on the test.

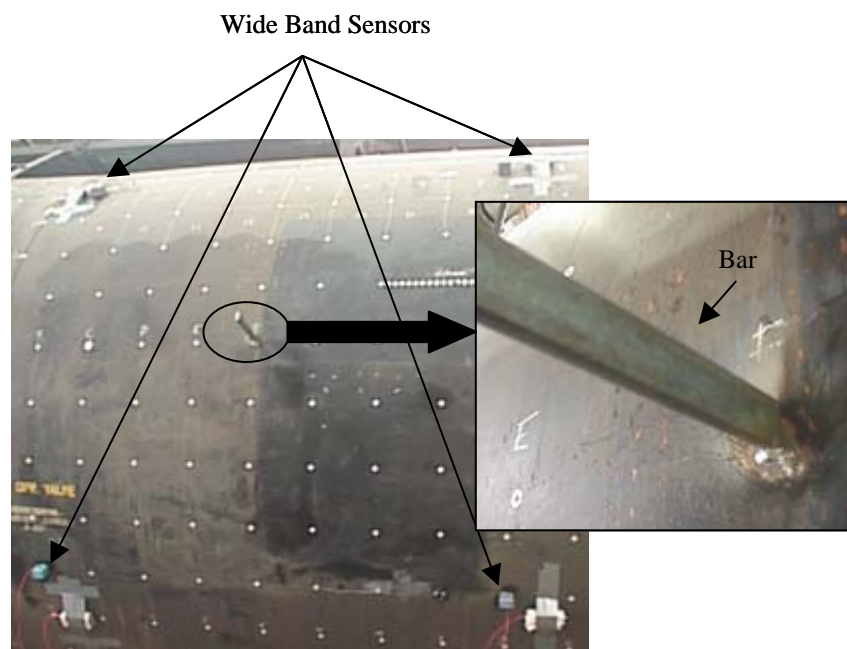


Figure 3.32 – Bar Bending Test Setup in the Area with no Discontinuities

In this test, a sampling rate of 4 MHz was used to acquire the data and a total of 1 millisecond time duration was monitored. The delay time was set for 400 microseconds.

The bar was welded in the middle of the four sensors. Therefore, the attenuation and dispersion affects all four sensors the same. A total of 875 hits

were created from the bar but only 422 waveforms were recorded. These waveforms were grouped as 175 events of which only 20 events (11.4%) locatable. Locatable events mean at least three sensors detected the signal for that event. The amplitudes of the hits range from 35 to 97 dB. The location results of all locatable events are plotted in Figure 3.33. It is seen that, the results were located close to the known source. The average error was 1.5” and the maximum error was 3.5”.

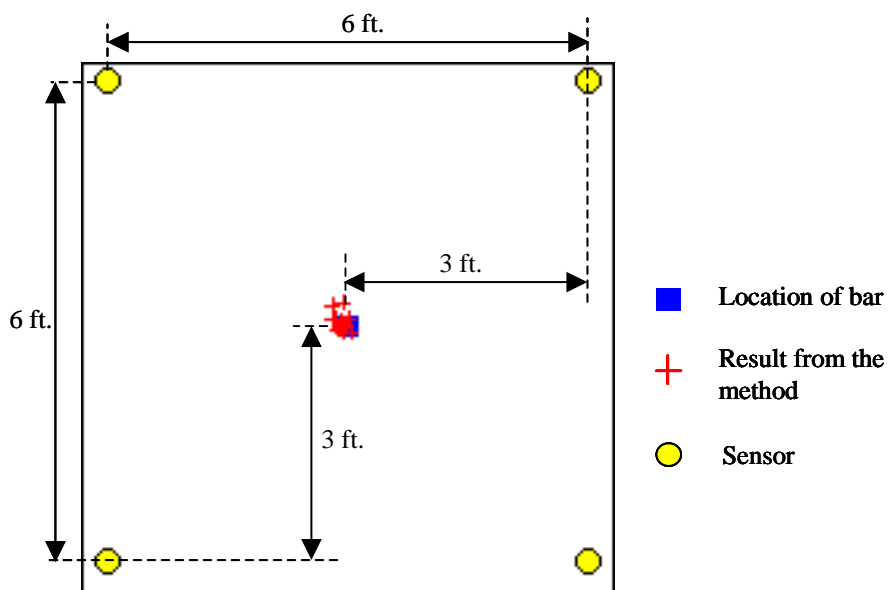


Figure 3.33 - Results from Bar Bending in the Area with no Discontinuities

- *Multiple Sources with Two Bars*

Interference of multiple sources was studied by bending two bars at the same time in the same area as in the previous test. Two bars were located 54

inches apart as shown in Figure 3.34. The white marks have no meaning for this test.



Figure 3.34 - Test Setup for Multiple Sources Study

In this test, two persons bent the bars at the same time. The right bar was fractured right away after bending, while the left one demonstrated some ductility during bending.

Since the rate of updating the waveform is a lot slower than recording the parametric information of the hits, the sampling rate was decreased to 1 MHz in this test. A total of 392 hits were created from the bar and all 392 waveforms were recorded. The hits were grouped as 125 events with only 24 events (19.2%) locatable. In the 24 events, 6 events have very low energy (the amplitude is lower than 40 dB) and it is difficult to define the arrival time from the peak of the signal. Therefore, source location was not performed for these 6 events.

Results of locatable events for which the arrival time can be defined are plotted in Figure 3.35. Two out of 18 events were located at the right bar area and 16 were located in the left bar area. The results show good accuracy. An average error of 0.9" and maximum error of 1.7" were obtained in the test.

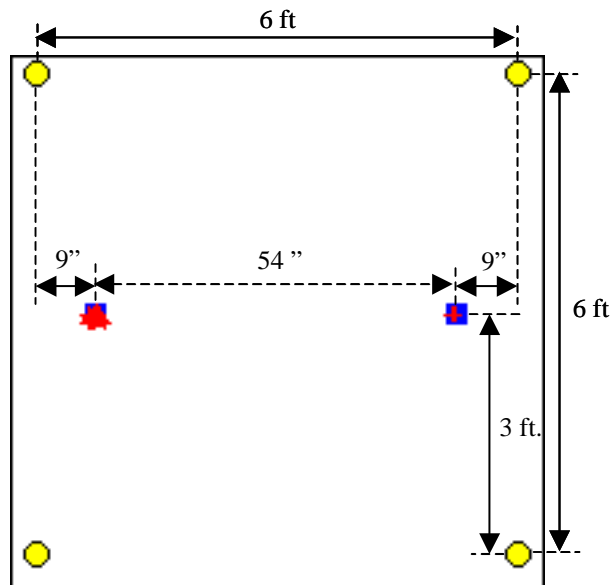


Figure 3.35 - Results from Multiple Sources

- *Bar Bending Test in the Area with Discontinuities*

A bar bending test was conducted on the area with vertical and horizontal welds in the tank. The area covered by four wide band sensors is 51 ft<sup>2</sup> (7.5 ft x 6.83 ft). In this test, a sampling rate of 1 MHz was used to acquire the data and a total of 1 millisecond time duration was monitored.



A total of 256 hits were created from the bar and all 256 waveforms were recorded. With 256 waveforms, the hits were grouped as 64 events with only 7 events (10.9%) locatable. Figure 3.36 shows locatable results from the test. An average error of 0.7" and maximum error of 1.8" were obtained.

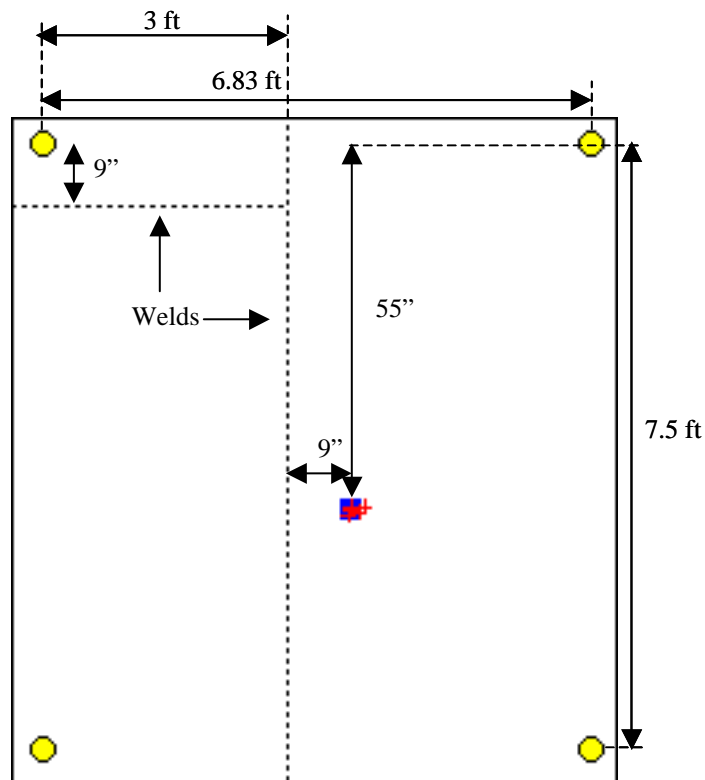


Figure 3.36 - Results from Bar Bending in the Area Including Welds

- *Bar Bending Test in the Bolster Area*

Another bar bending test was performed in the bolster area. A bar was welded close to the bolster pad as shown in Figure 3.37. The area covered by the

four wide band sensors is  $3.75 \times 5.25 \text{ ft}^2$ . The welds on the bolster serve as a very strong shield for the AE signal. This is why the monitored area is smaller.

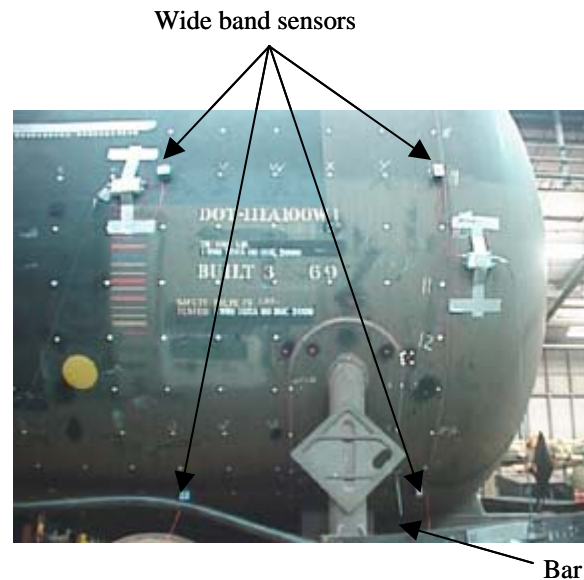


Figure 3.37 - Bar Bending Test Set-up in the Bolster Area

Based on the pencil lead break tests discussed in Section 3.3.4.5, the calculation was performed based on the assumption that waves propagate through the tank car shell under the bolster pad.

In the test, a total of 96 hits were created from the bar and all 96 waveforms were recorded. The 96 hits were grouped as 25 events with only 4 events locatable. The locatable results from the test are plotted in Figure 3.38. The method yielded a maximum error of 3.6" and an average error of 3.1" in this test.

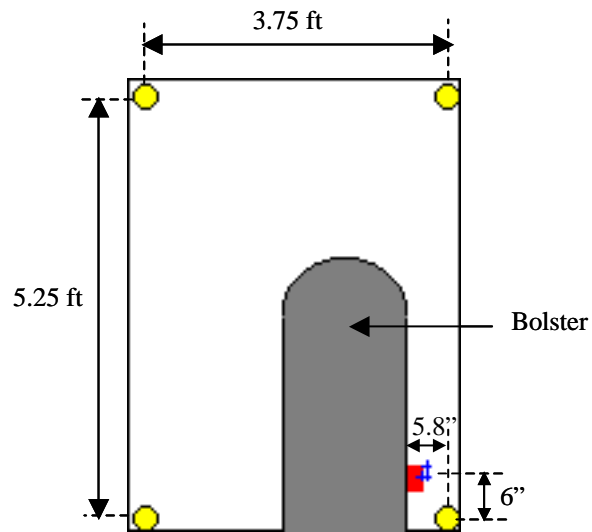


Figure 3.38 - Results from Bar Bending in the Bolster Area

- *Bar Bending Test on the Head of the Tank Car*

The last bar bending test was performed on the head of the tank car. The thickness of the shell at the end is a little bit thicker than the tank body but there is no significant change on the frequency at the intersection of the group velocity. Therefore, the analysis was performed on the same range of frequency, 145-155 kHz. In the test, a bar was welded off the middle of the end and four wide band sensors were used. The test set up is shown in Figure 3.39. In the test, sensor 1 was placed next to the bar location, therefore, the signal from sensor 1 is considered as the signal at the source.

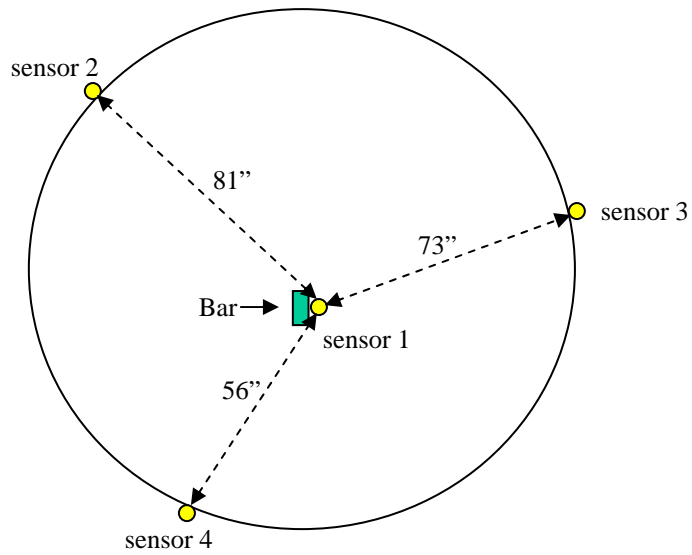


Figure 3.39 - Test Setup for a Bar Bending Test at the End of the Tank

A total of 260 hits were recorded from the test. The 260 hits were grouped as 119 events. Of these events, only 13 events were useful. Table 2.4 lists the distance results from the trigger sensor (at the bar location) to other sensors. The average calculated distance from the trigger sensor to sensor 2, sensor 3, and sensor 4 is 80.38, 73.41, and 55.89 inches, which can be compared to the measured distance of 81, 73, and 56 inches respectively. This is good considering that the trigger sensor is not exactly at the source.

Event #	Distance 1-2 (inches)	Distance 1-3 (inches)	Distance 1-4 (inches)
1	80.45	72.92	54.81
2	80.83	72.92	54.72
3	80.39	72.95	54.84
4	79.75	73.58	56.82
5	80.32	Not Detected	57.77
6	77.01	70.75	53.83
7	Not Detected	Not Detected	54.68
8	81.30	73.96	57.71
9	81.05	74.18	56.23
10	81.17	74.49	56.44
11	N/A	N/A	57.14
12	80.26	73.46	55.25
13	81.64	74.87	56.38
<b>Avg.</b>	<b>80.38</b>	<b>73.41</b>	<b>55.89</b>
<b>Measured distance</b>	<b>81</b>	<b>73</b>	<b>56</b>

Table 3.4 - Calculated Distance from the Trigger Sensor to Other Sensors

- *Discussion of Results from Bar Bending Tests*

In the first bar bending test, a bar was placed in the area with no discontinuity. The bar was welded in the middle among four sensors so the attenuation and dispersion problem are minimized. The results show that only 11.4% of the events are locatable. The locatable events (Figure 3.33) were

located in the area where the bar was welded. The average error was 1.5” and the maximum error was 3.5”.

The second bar bending test simulated the multiple source problem. Two bars were placed 54” apart and bent at the same time. The results show that 19.2% of the events are locatable. Among the locatable results, it is difficult to define the arrival time for the signal that has low energy (less than 40 db) since the signal did not have a clear by defined peak. The results from the test do not show interference between waves from the two sources. This might be because the right bar fractured right away creating a lot less emission while the left one showed ductility when bending. It was a lot harder and took much longer to fracture the left bar. Therefore, there is less chance for interference of the signals. The results in Figure 3.35 are located in the area where the bars were welded. The average error was 0.9” and the maximum error was 1.5”.

The third bar bending test was performed in the area with vertical and horizontal welds. The results show that 10.9 % of the events are locatable. The monitored area is larger than the one in the first two tests. The results in Figure 3.36 are located in the area the bar was welded. The average error was 0.7” and the maximum error was 1.8”. The results show that the welds do not affect the accuracy of the source location approach.

The fourth bar bending test was performed in the bolster area. The monitored area is smaller compared to the previous tests. This is because of the attenuation problem from the bolster leg. In this test, a lot fewer events were detected. This is because of the attenuation problem. It is seen from the results in Figure 3.38 that all of the locatable results were located in the correct area.

From the first four tests, it can be concluded that the source location approach using a tight band-pass filter at the intersection of the group velocity of the first three wave modes can be used with good accuracy as long as enough

sensors detect the signal and the signal does not have too low energy (less than 40). It is interesting to see that the accuracy of the results from the first test when the bar was placed in the middle is worse than other tests. This shows that the analysis method does not suffer from the attenuation and dispersion effect.

For the last bar bending test on the head of the tank car, source location was not performed since the geometry of the head is difficult to model. Instead, the distances between the source and the sensors were calculated using the trigger sensor. The results in Table 3.4 shows good accuracy. This confirms that the concept of group velocity can apply to the head as well.

Since the geometry of the head makes it difficult to use triangulation, alternative methods using a look-up table or a neural network are suggested. A specific look up table or a neural network would need to be developed for this geometry. The input to the network or table would be the difference in time of arrival between sensor 2 and 3 ( $\Delta t_{23}$ ), sensor 2 and 4 ( $\Delta t_{24}$ ), and sensor 3 and 4 ( $\Delta t_{34}$ ). Training data from artificial sources would be obtained using either the bar bending approach or pencil lead breaks at different places on the head. Analysis of this type is not included in this dissertation. However, an example of source location using a neural network was performed on a reinforced plastic pipe. This is reported in Chapter 7.

### 3.4 SOURCE LOCATION STUDY PROBLEM ON A TANK CAR WITH 13/16 INCH THICK SHELL

#### 3.4.1 Specimen Description

The second specimen used in the program is also a steel railroad tank car but with a thicker shell. The normal thickness was 13/16". However due to corrosion the thickness was less in many areas. This tank car (ACAX 80013) is a US. Department of Transportation specification 112S400W car built in 1970 by ACF industries. It is non-jacketed and was located at the Rescar maintenance facility in Orange, Texas.



Figure 3.40 – Hydrogen Fluoride Tank Car



A picture of the car is shown in Figure 3.40. The tank car had been used to transport hydrogen fluoride, which is a very corrosive chemical. This tank car is no longer in use because of a severe internal corrosion and blistering of the tank car wall and cracks at the welds attaching the bottom plate and the tank body. The tank car was donated to this test program by Allied Signal Corporation.

### 3.4.2 Instruments

The equipment used in the study was a 24 channel digital system (DISP) as shown in Figure 3.41. The system is manufactured by Physical Acoustics Corporation and was lent by them to the University of Texas for full scale testing of the tank car. R6I resonant sensors were used to capture the AE signal. The calibration response of an R6I sensor is shown in Chapter 2. The sensors were attached to the tank car with duct tape. Vacuum grease was used as a couplant between the sensor and the surface of the tank.

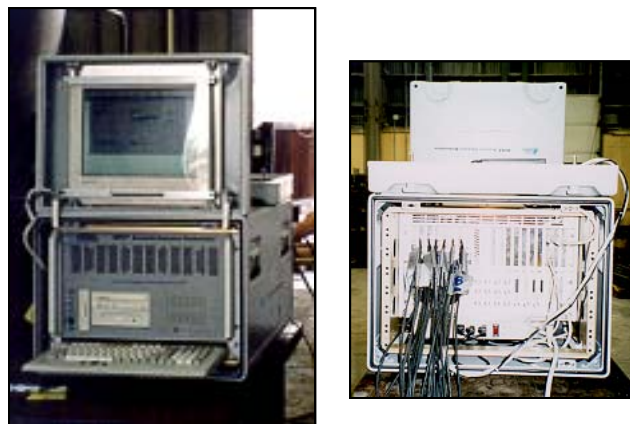


Figure 3.41 – The DiSP System

### 3.4.3 Attenuation Test

Two R6I sensors were placed 10 inches apart and lead breaks were performed 4" away and every 9" away from the second sensor for 135 inches. The test setup is shown in Figure 3.42. The purpose of the test is to measure the attenuation of the wave traveling on the tank car shell and to measure the wave velocity, which will be presented in Section 3.4.4.

In the attenuation test, amplitudes of the signal were plotted against the distance of the source from the second sensor. The results are plotted in Figure 3.43. From the attenuation results, it is seen that the zone radius for this tank car is more than 135 inches.

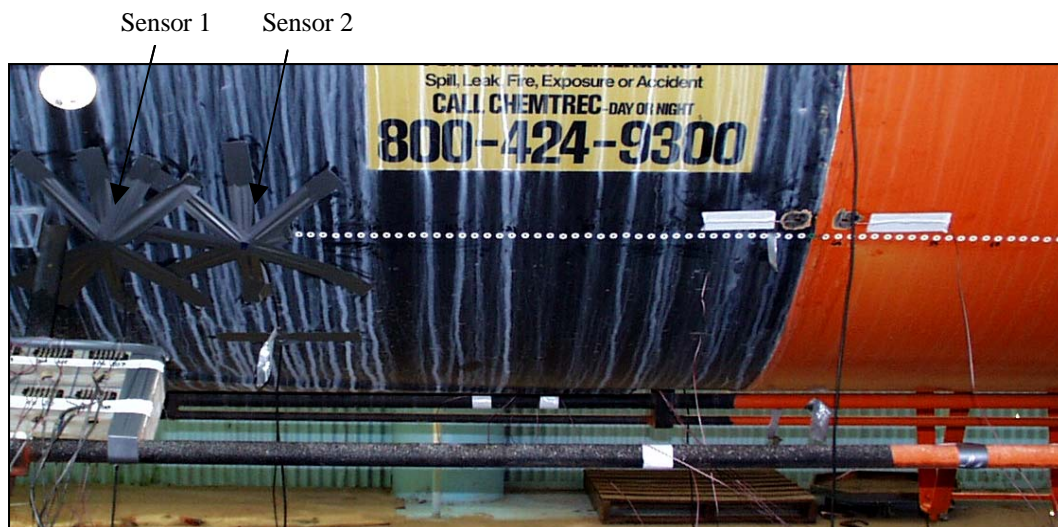


Figure 3.42 - Attenuation Test Setup

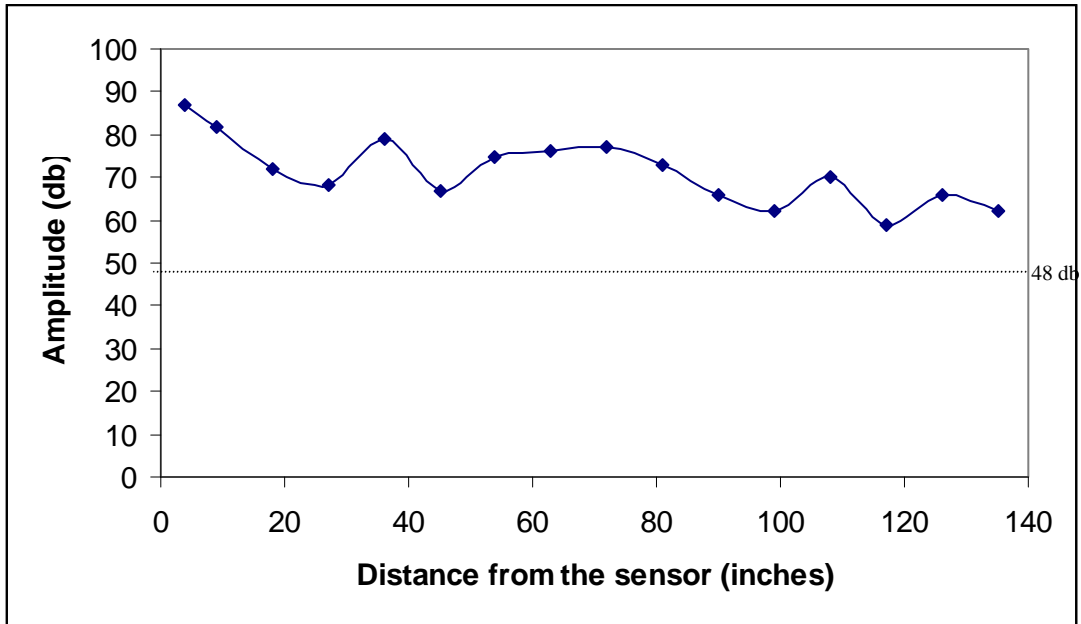


Figure 4.43 – Attenuation Curve

### 3.4.4 Theoretical Group Velocity

Since the tank car shell is thicker than the previous specimen, the group velocity occurs at a lower frequency. The dispersion curve for the steel plate with a thickness of 13/16 inches is illustrated in Figure 3.44. In this case, the intersection of the group velocity of the first three modes occurs at approximately 100 kHz and travels with a speed of 125,984 inches/sec or 3.2 km/sec.

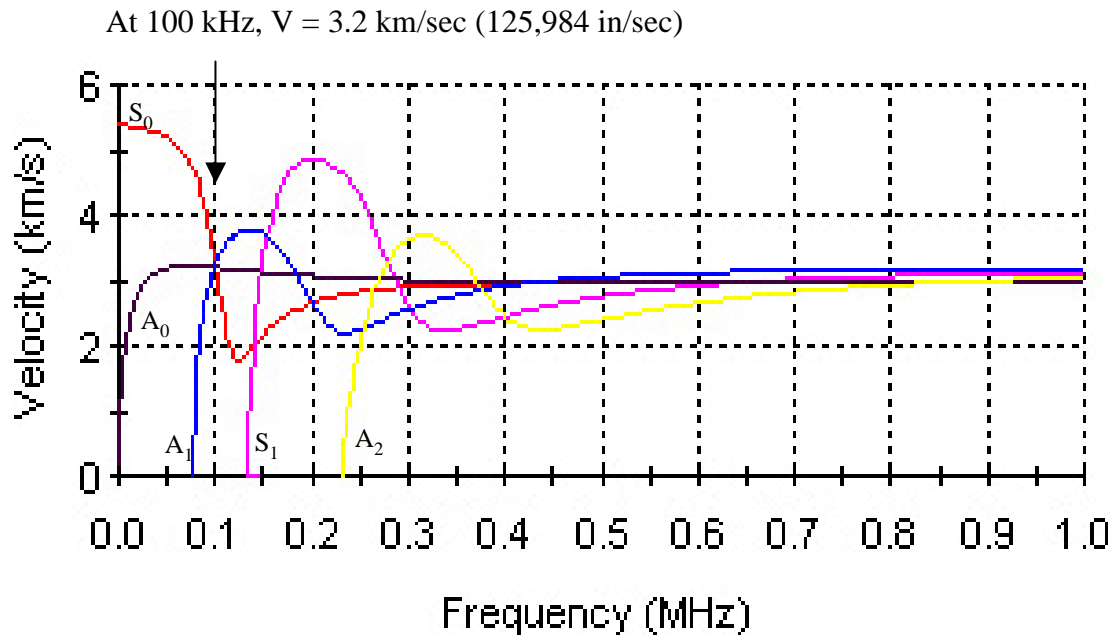


Figure 3.44 - Dispersion Curve for a Tank car with 13/16 inches Wall Thickness

### 3.4.5 Velocity Measurement

Data from pencil lead breaks using the attenuation test setup in Section 3.4.3 were used to calculate the velocity of the wave. Pencil breaks were performed every inch away from the second sensor. The distance between the two sensors is 10 inches. Knowing the distance, the velocity can be calculated from the measured arrival time.

Figure 3.45 shows the velocity results of the plate wave based on the first threshold crossing technique, and the intersection of the group velocity at a 100 kHz. In the group velocity, the method described in Section 3.3.5 was used. All of the signals were band-pass filtered in the range of 95-105 kHz and the median

of the negative and positive peaks was used to identify the arrival time. The average of the group velocity is 108,213 in/sec, which is less than the theoretical value of 125,984 in/sec. In the graph, it is seen that the velocity obtained from the first threshold crossing technique yields a more consistent result than was obtained with the wide band sensors in the previous specimen. This is because the R6I has a better sensitivity than the wide band sensor and suffers less from the attenuation.

In order to view the variation of the velocity values, the group velocity results were plotted again in an expanded scale shown in Figure 3.46. It is interesting to see that the group velocity obtained from the Orange tank is a lot less consistent than the results obtained from the thin shell tank studied earlier. This variation will be discussed further in Section 3.4.6.2.

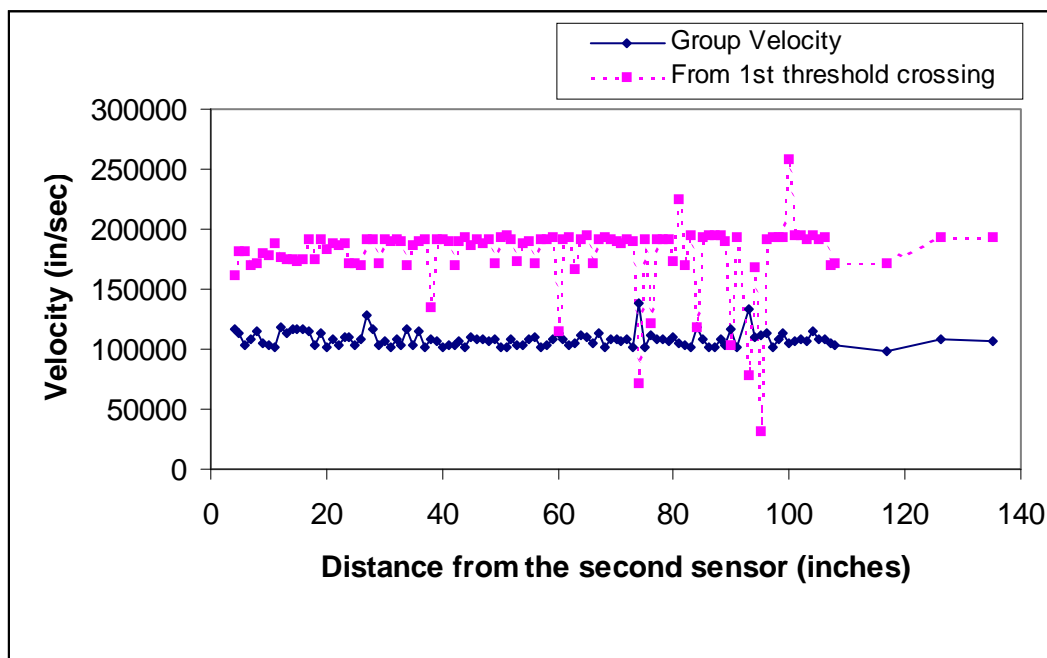


Figure 3.45 - Velocity Results

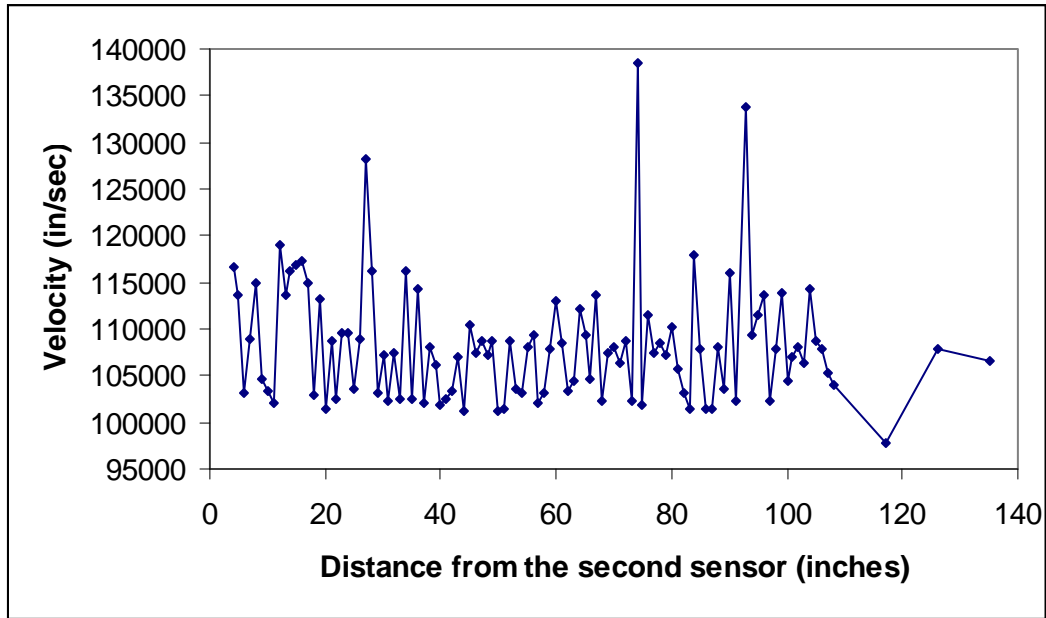


Figure 3.46 - Group Velocity at a 100 KHz

### 3.4.6 Source Location Methods

Two source location methods are explored in this section. The first one uses the difference in the velocities between two wave modes to calculate the distance of the source to the sensor. The second method uses a tight band frequency wave that travels at a constant group velocity to pinpoint the location of source with the simplex optimization approach.

### ***3.4.6.1 Difference in the Arrival Time of the First Two Modes***

- *Concept of the Method*

Sometimes only one sensor detects the signal from the source and it is impossible to use the triangulation method to pinpoint the location. In view of this, a new approach using the difference in velocities between the first two modes is explored in this section. From the dispersion curve in Figure 3.40 it can be seen that different wave modes normally travel at different wave speeds. The exception is at a 100 kHz where the first three modes travel at the same speed for this tank car. Due to the difference in velocity between the lowest order symmetric and anti-symmetric modes, the distance from the source to the sensor can be determined. The benefit of the approach is that it requires data from only one sensor to determine the distance from the source and two sensors can be used to locate.

The concept is based on the use of a tight band frequency signal, which can be in any range except the range of the intersection of the group velocity, which is 100 kHz in this case. In this work, a frequency range of 145-155 kHz was selected. Since the two modes travel at different velocities and the extensional mode travels faster, it therefore arrives at the sensor first and is followed by the second mode or the lowest anti-symmetric mode. The first step was to band-pass filter all the signals in the frequency range of 145-155 kHz. Based on this data, the difference in the arrival time of the two modes was calculated. The concept of the work is demonstrated in Figure 3.47. The arrival time of the two modes were defined by the beginning of the mode. In this work, this process was performed manually. This approach has the disadvantage of

being subjective and dependent on the inspector. The waveform in Figure 3.47 is the 145-150 kHz signal of a lead break 48 inches from the sensor.

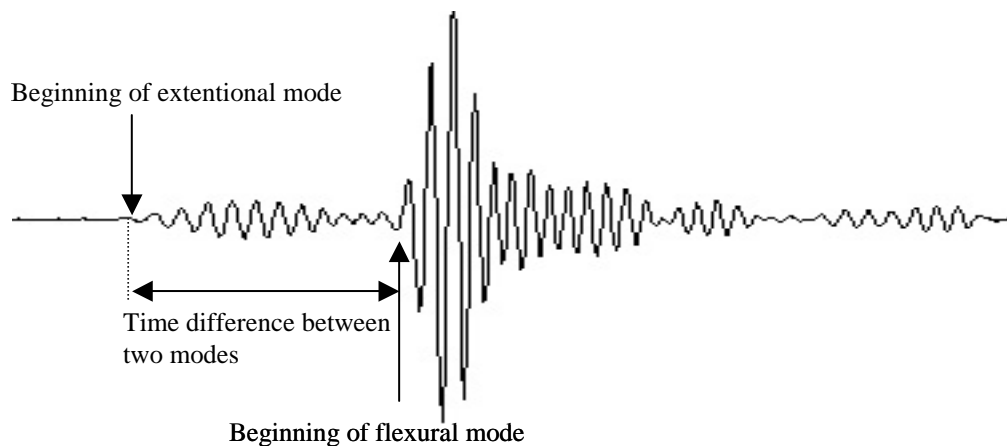


Figure 3.47 – Time Difference between Two modes with 145-155 kHz Signal

- *Experimental Results*

The data from the pencil lead breaks used for the attenuation test in Section 3.4.3 was again used to calculate the difference between the arrival time of the two modes and is plotted in Figure 3.48. Data from sensor 2 was used in this work. It is noted that once the source is further away from the sensor (after 70 inches), it is quite difficult to pick the beginning of the wave modes and the results are very dependent on the discretion of the analyzer.

In Figure 3.48, the solid line is the plot of the raw data and the dashed line is the trend line. The equation of the trend line is  $y = 3.385x$ , in which  $y$  is the difference in the arrival time of the first two modes and  $x$  is the distance between



the source and the sensor. The  $R^2$  value from the trend line is very close to one, which indicates that the group of data fits the curve very well. The units of time and distance are in microseconds and inches. From the trend line equation, the slope 3.385, which means the difference in the velocity between the two modes is 295,421 in/sec.

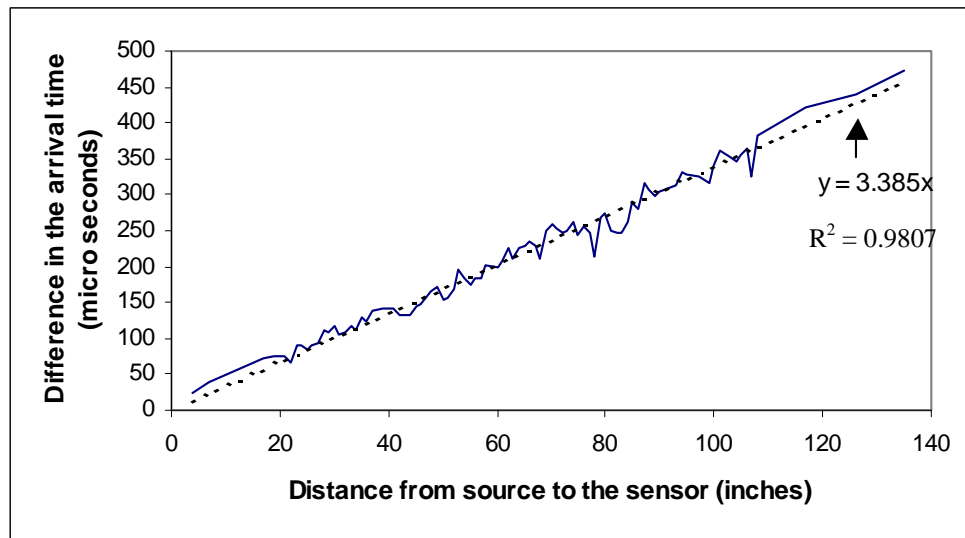


Figure 3.48 - Difference in the arrival time between the first two modes

- *Discussion*

The plot in Figure 3.48 is linear. The  $R^2$  value is close to 1 meaning the results can be represented with the trend line. The measured difference of velocities between the two modes is 295,421 in/sec.

The way to define the arrival time of two modes is based on the beginning of the mode. With this way, the fastest phase point was selected. Although the

wave package of the filtered signal moves at the group velocity, the individual point travels with the phase velocity. Defining the arrival time based on the beginning of the mode means defining the arrival time from the fastest phase point. The dispersion phase velocity for this tank with a nominal thickness of 13/16" is shown in Figure 3.49. At 145 to 150 kHz, the difference of the velocities between the  $S_0$  and  $A_0$  is 0.45 km/sec which is 11,716 inch/sec. The number is too low when compared to the experimental result. At the same frequency, the difference of the velocities between the  $S_1$  and  $A_0$  is 3.5 km/sec, which is 137,795 inch/sec. The number is higher but still not close to the experimental result. That means the first mode reaching the sensor first is the  $S_1$ .

As mentioned before, the tank has severe corrosion and blistering. An ultrasonic test was performed on the tank and it was found that the actual thickness of the tank ranged between 0.4" to 0.81". The dispersion phase velocity for the thickness of 0.55" is shown in Figure 3.50. The difference of the velocities between the  $S_1$  and  $A_0$  is 7.6 km/sec, which is 299,212 inch/sec. The number is close to the experimental result of 295,421 in/sec.

These results illustrate a severe disadvantage to using the difference in the arrival time of the first two modes for source location. The results are extremely sensitive to small changes in the thickness of the plate. In practical applications, plate thicknesses will vary due to many reasons including initial manufacture, plate forming, and corrosion.

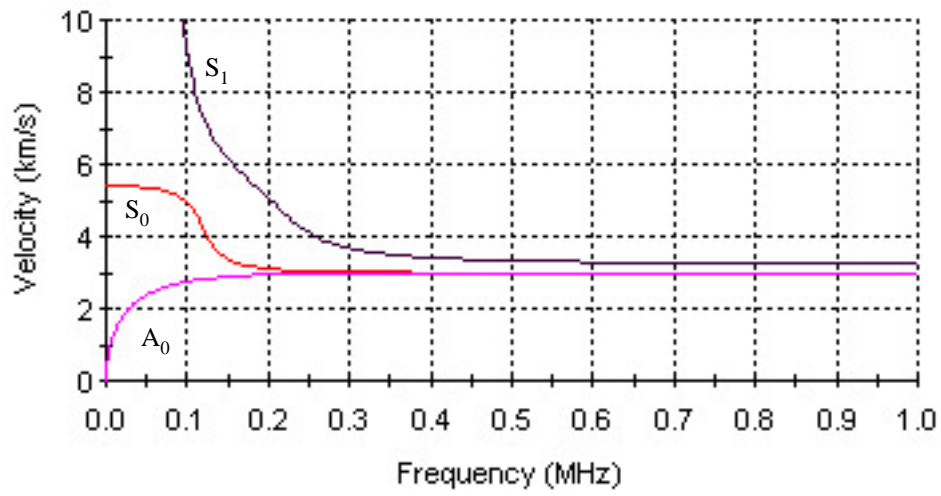


Figure 3.49 - Phase Velocity Dispersive Curve for 13/16" Thick Shell

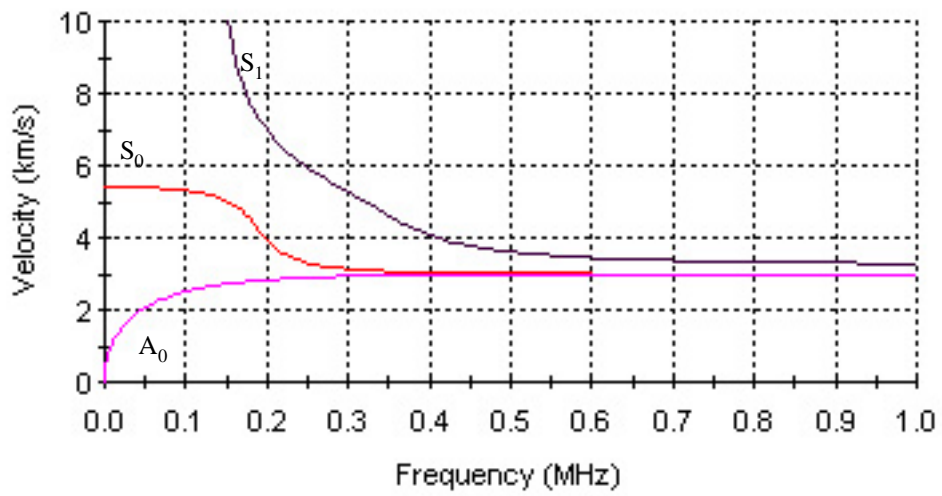


Figure 3.50 - Phase Velocity Dispersive Curve for 0.55" Thick Shell

### ***3.4.6.2 Source Location Based on Group Velocity***

In this section, a tight band frequency source location approach using the intersection of the group velocity was used. This method was developed earlier in the study (see Section 3.3.5) and was applied to the lead break data. The calculation for the location was performed by the simplex optimization with a stepped value of 1 inch. Seven R6I sensors were used to capture the signals. locations and the lead break positions are shown in Figure 3.51. The first four sensors detecting the signal were used for source location.

Numbers in parentheses underneath the sensors are locations in the x (along the length of the tank car), and y (along the circumference) directions and are shown in inches. A total of 16 lead breaks were applied. The first break was at 4 inches away from sensor 8. Subsequent ones were spaced at 9 inch intervals from the sensor.

As mentioned earlier, a 100 kHz signal was selected because this range is the first intersection of the group velocity resulting in a constant speed of travel. The velocity results from Section 3.4.5 are not consistent. This is because the tank car wall has severe corrosion and blistering leading to variations in the thickness of the shell. Blistering is quite severe and this acts like sections of a thinner tank. Since the plate wave velocity is a function of the thickness of the plate, variation in the thickness results in variation in velocity.

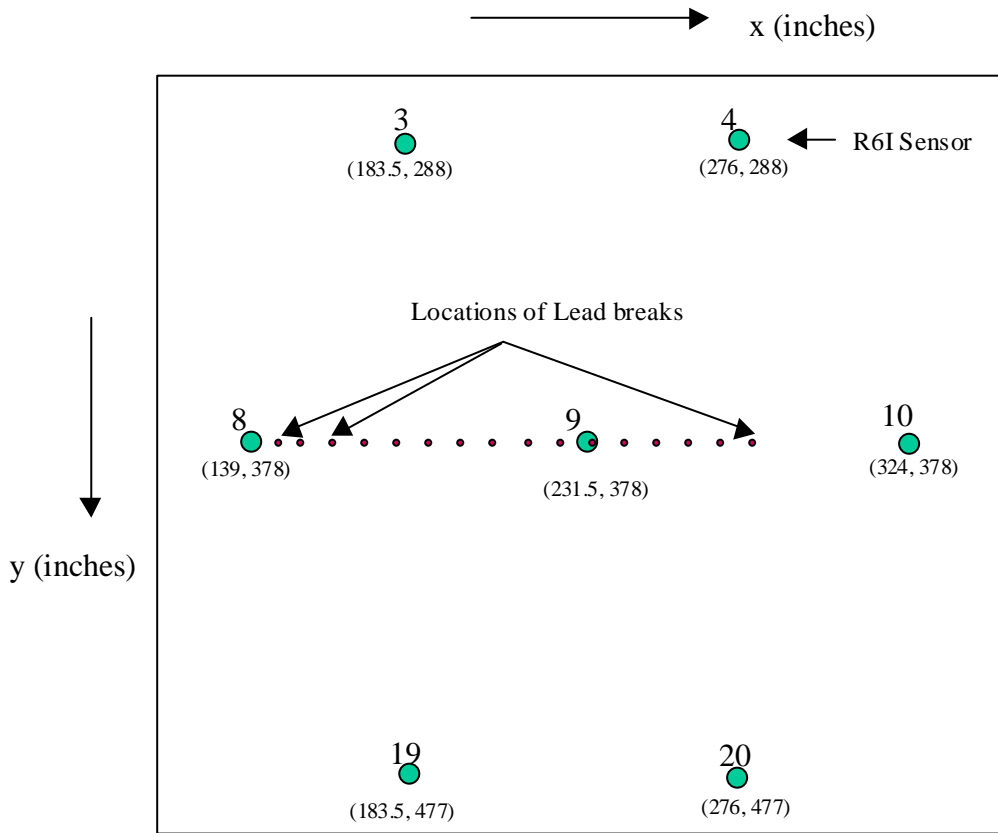


Figure 3.51 - Locations of Sensors and Lead Breaks

Since the velocity results in Figure 3.46 are not very consistent, source locations were performed based on 5 different values of velocity, 100,000, 110,000, 120,000, 125,000 and 130,000 in/sec and the errors from the results are plotted in Figure 3.52. From the calibration, it is seen that the velocity of 125,000 in/sec provides the least error with the average error for this case of 2.1 inches. With the group velocity of 125,000 in/sec, the location results are shown in Figure 3.53. The maximum error in this test is 4.5 inches.

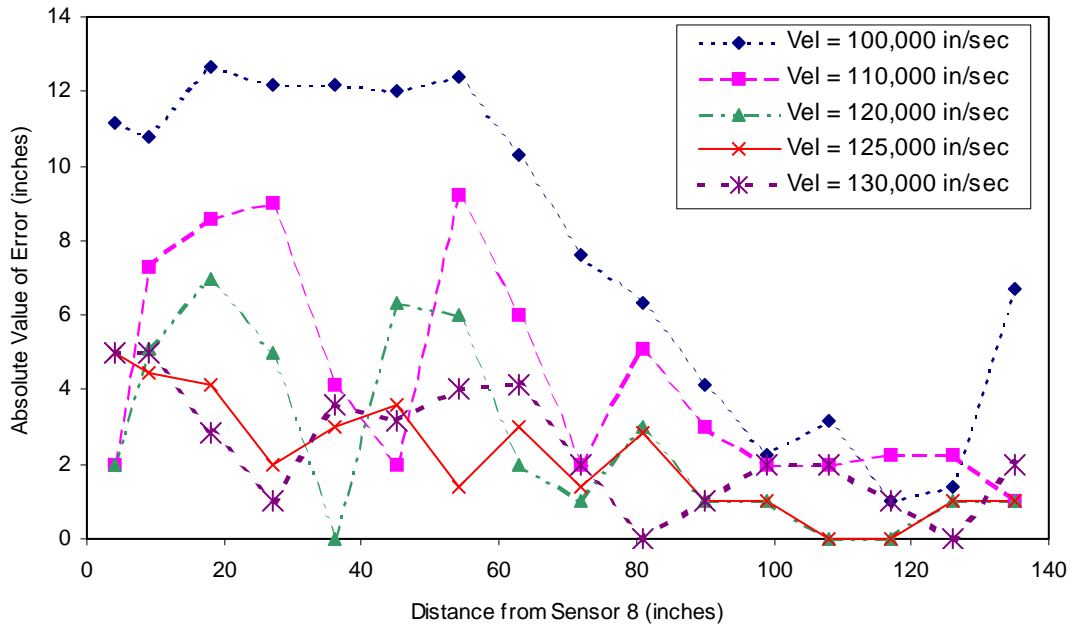


Figure 3.52 - Errors due to Different Value of Velocity

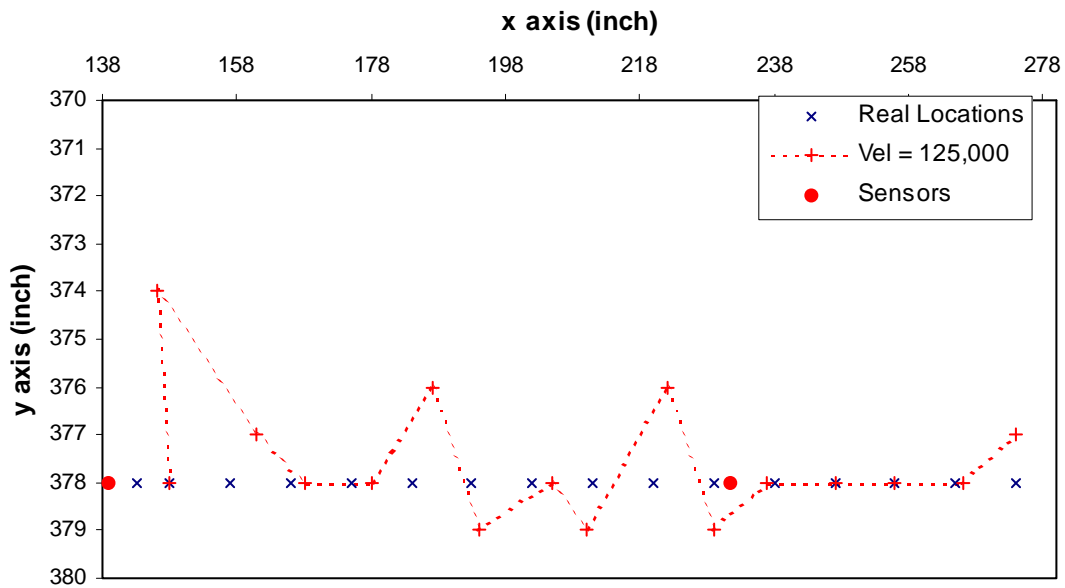


Figure 3.53 - Results from Lead Breaks

### **3.4.7 Summary of Source Location Studies on the Orange Tank**

Two source location approaches were explored in this Section. The first one uses the difference in velocities between the first two wave modes. The method is useful when only one sensor detects the signal, however it is only able to tell the distance from a defect to the sensor. If two sensors detect the signal, the source can be located. Note that for the approach to work, the sensor has to detect the beginning of the first mode clearly. That means if the source is far away, the signal suffers from attenuation and it is difficult to define the beginning of the first mode because it blends with the background noise.

The second approach studied is the source location method using a narrow band frequency in the range that travels with a group velocity. In this case, the group velocity occurs at a 100 kHz signal. The theoretical group velocity from the dispersion curve (Figure 3.44) is 3.2 km/sec or 125,984 inches/sec. Nevertheless, the measured velocity from Figure 3.46 yields inconsistent results and the average measured group velocity is 108,213 in/sec, which is less than the theoretical value. Therefore, a calibration for a correct group velocity was performed and the velocity of 125,000 in/sec provided the least error in the location results.

In this tank car, there is a lot of variation in the velocity results and the location errors are greater than the results obtained from the previous test on a thinner shell tank car in Ferguson Lab. This is because the thickness of the tank car shell is not consistent due to severe corrosion and blistering of the tank wall. An ultrasonic test was performed later to measure the thickness of the shell and it was found that the thickness of the wall varies from 0.40 to 0.81 inches. This is probably the main source of the error.

### 3.5 CONCLUSION

Currently used source location approaches have been studied. The first method is the zonal approach. Two sensor arrangements were studied; the open spaced and close spaced arrangements. The results from the open spaced arrangement show good accuracy. With this type of sensor arrangement, attenuation occurs when the waves travel but the attenuation makes the method more robust and increases the accuracy.

With the close spaced sensor arrangement, although the attenuation does not have an effect on the method because all the sensors see the same waveform, the sensitivity of the sensor becomes important. In order for the method to give good accuracy, the sensitivity of the sensors must be the same. In practice, this is very difficult to achieve.

The second source location approach is an improvement of the triangulation technique using a tight band-pass filter at the intersection of the group velocity of the first three modes. With this approach, the dispersive problem is minimized. A new way to define the arrival time is introduced by using peaks of the filtered signal. With this way, the attenuation does not affect the defined arrival time.

The approach was applied to two tank cars. The first one has a thinner wall (15/32") and is in a good condition, while the second tank car has a thicker wall (13/16") and has severe corrosion on the inside of the shell.

For the good specimen, the source location approach based on the group velocity at 150 kHz has provided very promising results on an empty tank car. From the tests that used pencil lead breaks as artificial sources, the error of the location results is less than 2 inches in the area with discontinuities. The location results from the bar bending yields good accuracy with an error less than 3.6



inches. The maximum error occurred from the test in the bolster area. Note that the size of the bar is significant relative to the error.

The simplex optimization method is a trial and error algorithm to perform triangulation source location. This algorithm makes a use of  $t_0$  (time that the source occurs). The procedure selects an arbitrary location ( $x_0$  and  $y_0$ ) and calculates  $t_0$  based on data from each sensor. The location that yields the least differences in  $t_0$  among the sensors is the answer. This procedure minimizes the total error from each sensor and gives the best result. The simplex method provides a benefit over the exact solution when more than three sensors are used.

For the severely corroded specimen with a thicker wall, the technique was performed at a group velocity frequency of 100 kHz. However, the measured group velocity at a 100 kHz does not yield a consistent result and the value varies from less than 100,000 in/sec to almost 140,000 in/sec. From a velocity measurement in a local area on the tank car shell, the average velocity of 108,213 in/sec was obtained. However, a calibration using the correct position of the source provides a higher velocity value, which is 125,000 in/sec. This value is close to the theoretical group velocity.

The error in the location results is greater in the corroded tank car than in the tank car in good condition. This is expected due to the variation in the thickness of the tank car wall.

The third source location approach explored in this chapter is the use the difference of velocities of two wave modes. This method was applied to the data from the Orange tank car only. The method is useful when not enough sensors detect the signal. If only one sensor detects the signal, the distance from the source to the sensor can be calculated. With this method, the source will be located with only two sensors. However, the method is sensitive to variations in thickness. One limitation of the method is that the beginning of the first mode has

to be detected clearly. When the wave travels from a far distance, it attenuates. It is difficult to define the beginning of the first mode because it blends with the background noise.

## **CHAPTER 4**

### **JACKING AND TWIST BAR TESTS ON AN EMPTY TANK CAR**

#### **4.1 INTRODUCTION**

This chapter focuses on applying the source location approach developed in Chapter 3 to a practical field test on an empty tank car. Two types of testing were performed; jacking and twist bar tests [AAR]. The specimen used in the test is the thicker shell tank car located at the Rescar facility at Orange, Texas. In this chapter, the instrumentation used and sensor locations are presented in Section 4.2. Section 4.3 summarizes the concept of the source location approach used for the analysis, including a new algorithm for source location developed specifically for a large cylindrical structure. Test results from conventional jacking tests on an empty tank car and the test setup are reported in Section 4.4. Results from a research program to evaluate alternative procedures are described in Section 4.5. Twist bar tests were conducted at one end of the tank car and the results are presented in Section 4.6. It should be noted that each of these tests loads the car in a different manner and may stimulate emission from different area. For example, a jacking test will stimulate emission from the bolster area and the end of the cylindrical portion of the tank. In contrast a twist bar test is designed to stimulate emission from the sill, headblock, their attachment welds, the bolster and the lower portion of the tank. Finally, Section 4.7 summarizes the method used and discusses the results obtained from the tests.

## 4.2 INSTRUMENTS AND SENSOR LOCATIONS

### 4.2.1 Instruments

A 24 channels digital system (DiSP) was used for AE monitoring of the jacking and twist bar tests. The system was manufactured by Physical Acoustic Corporation, Princeton, NJ and was loaned to the University of Texas at Austin for these tests. The system is shown in Figure 4.1. 24 R6I sensors were used in the tests. 22 sensors were mounted on the tank body and one was placed on each head. All sensors were attached to the tank with duct tape. Vacuum grease provided coupling between the tank and the sensor.

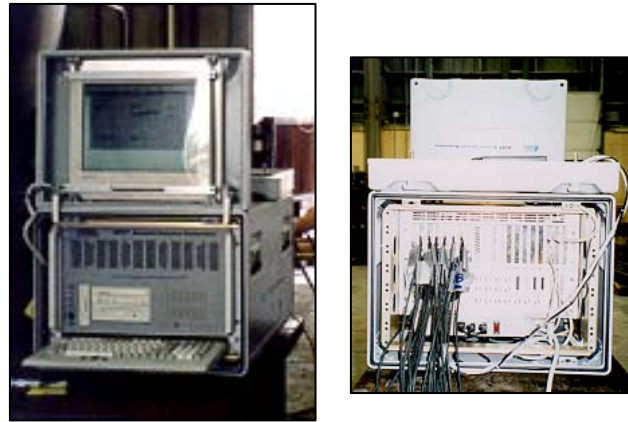


Figure 4.1 – DiSP system

### 4.2.2 Sensor Locations

Sensor locations on the tank body are shown in Figure 4.2. The figure is a developed view of the tank car shell looking from the top with the shell opened up

as if cut along the bottom. The units are in inches. The dashed line represents the center line on the top of the tank car. Circles represent sensors and numbers below are coordinates of the sensors along the length and circumference. The x axis runs from the B end to the A end and the y axis runs from top of Figure 4.2 to the bottom of the figure. The coordinate of the center line is (0, 234) at the B-end and (462, 234) at the A-end.

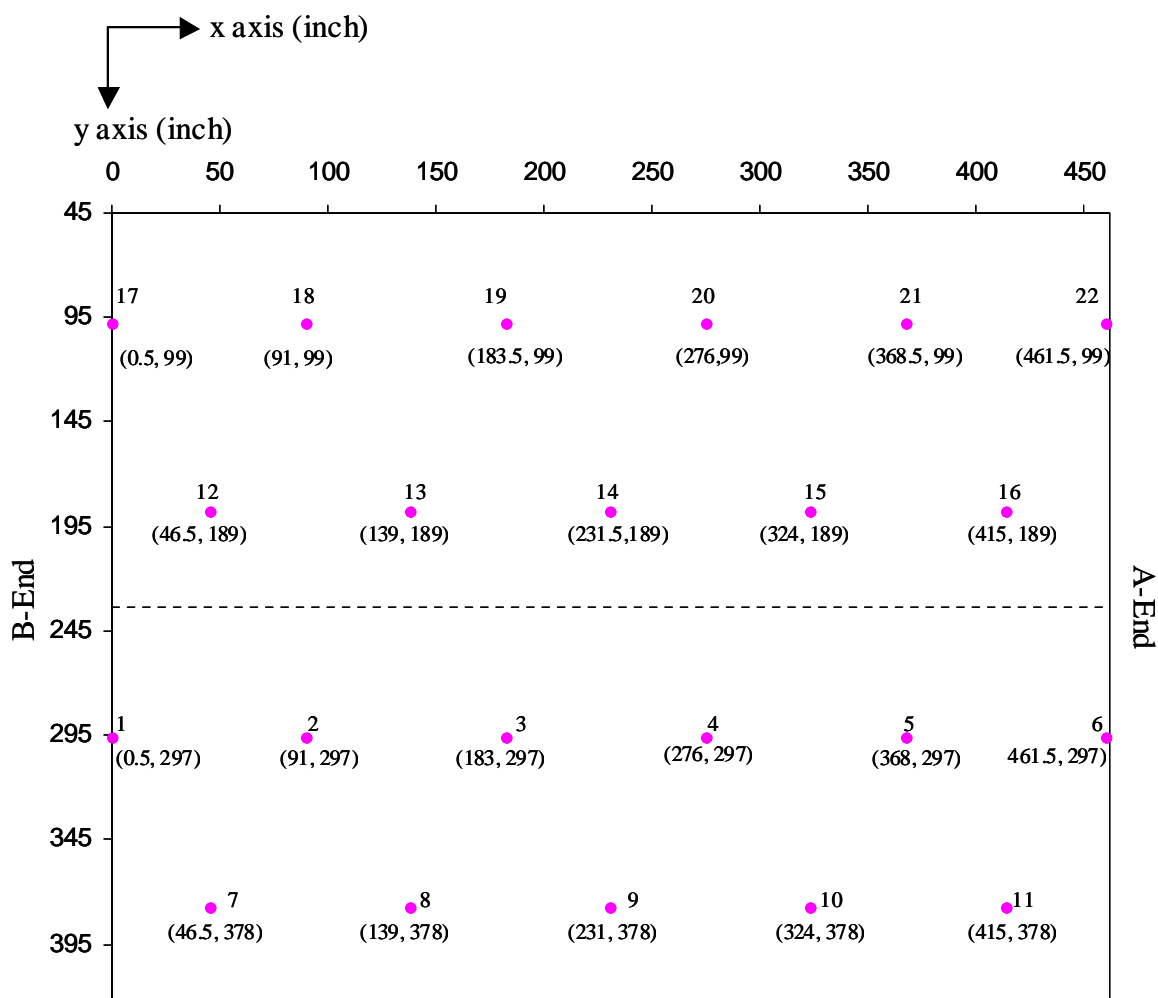


Figure 4.2 – Sensor Locations on the Tank Body

### 4.2.3 History of Tank and Sources of Emission

This tank car was one of a series that was removed from service because of severe widespread blistering. The blisters, or delaminations, are caused by hydrogen fluoride and are common in cars used to transport this chemical. The car was chosen for this test program because it was known that the internal blistering should give multiple sources of emission.

To confirm specific emission sources follow inspection was performed at the A end of the car

- A crack at the junction of the tank and sill was confirmed by dye penetrant. This is discussed in the section describing the BL jacking test.
- Severe delamination or loss of thickness (believed to be evidence of blistering) was confirmed by external ultrasonic inspection. This is discussed in the section describing the blocked jacking test at AL.
- Emissions detected during the BL twist bar test were found to be from a region of fractured weld where a bar bending test had been carried out
- A source at the bottom of the car near the middle showed up on a number of tests including the AL jacking, BR jacking, BR twist, and BI twist tests.
- Other sources along the top of the car are believed to be due to blistering. Blistering frequently occurs in this region.

## **4.3 SOURCE LOCATION APPROACH**

### **4.3.1 Concept of the Approach**

A source location approach using a tight band-pass filter at the intersection of the group velocity of the first three wave modes was developed earlier in Chapter 3 for an empty tank car. The method was used with the simplex optimization approach to triangulate the source. The method is used to locate defects from the jacking and twist bar tests reported in this chapter.

The tank car used in the test is the 13/16" thick car and the group velocity occurs at approximately 100 kHz, therefore, a band-pass filter with a frequency range of 95-105 kHz was applied to the signal. A group velocity of 125,000 in/sec was used in the analysis. To define the arrival time, the mean value of the negative and positive peak was selected. The simplex optimization algorithm, which is also known as the reverse procedure of the triangular method, was applied with a step value of 1 inch.

### **4.3.2 Software Algorithm Developed for a Tank Car**

- *Possible Wave Propagation Routes*

For a large cylindrical tank car structure, there are a number of complications in the analysis. Many sensors are used and symmetrical geometry might become a problem. One of the difficulties is that signals reach the sensor from different directions. Due to shielding, attenuation and discontinuities, the

shortest path may not be the route that the stress wave takes to strike the sensor. The algorithm developed in this section covers this complication by including a number of possible paths and calculates the best location. Based on the sensor locations shown in Figure 4.2, four possible paths were considered for a signal to propagate. This is illustrated in Figure 4.3.

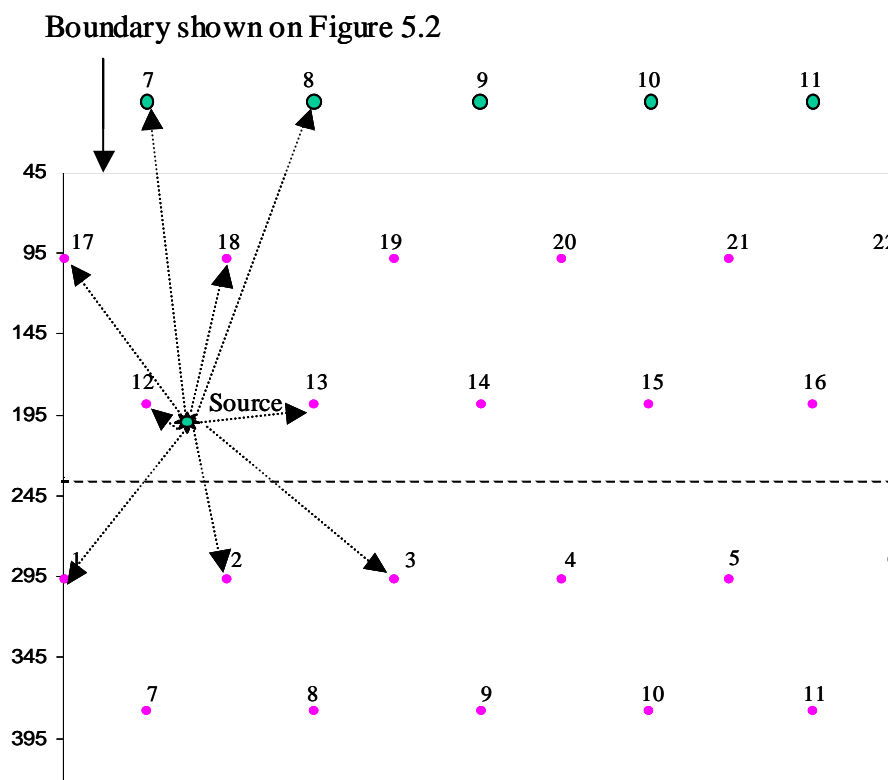


Figure 4.3a – First Possible Path



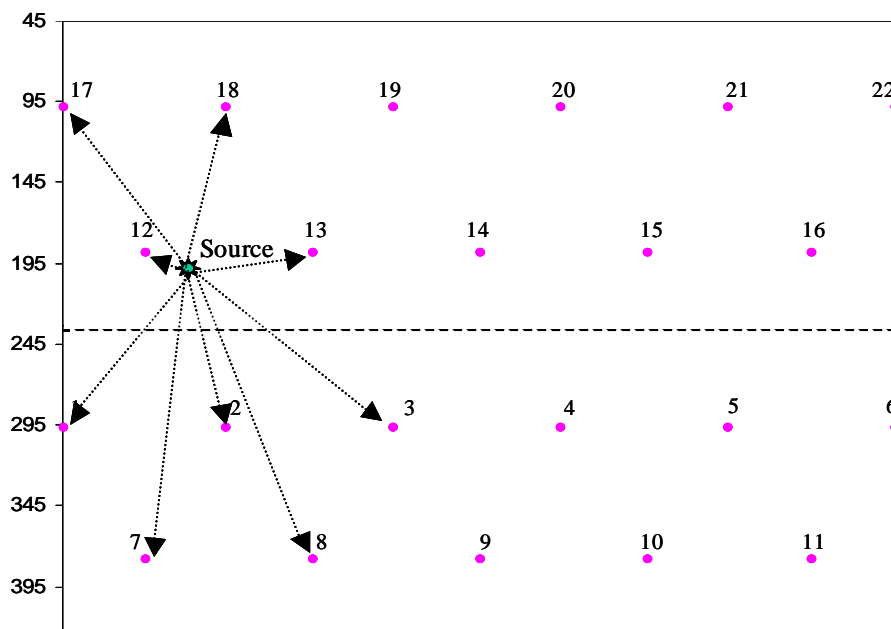


Figure 4.3b – Second Possible Path

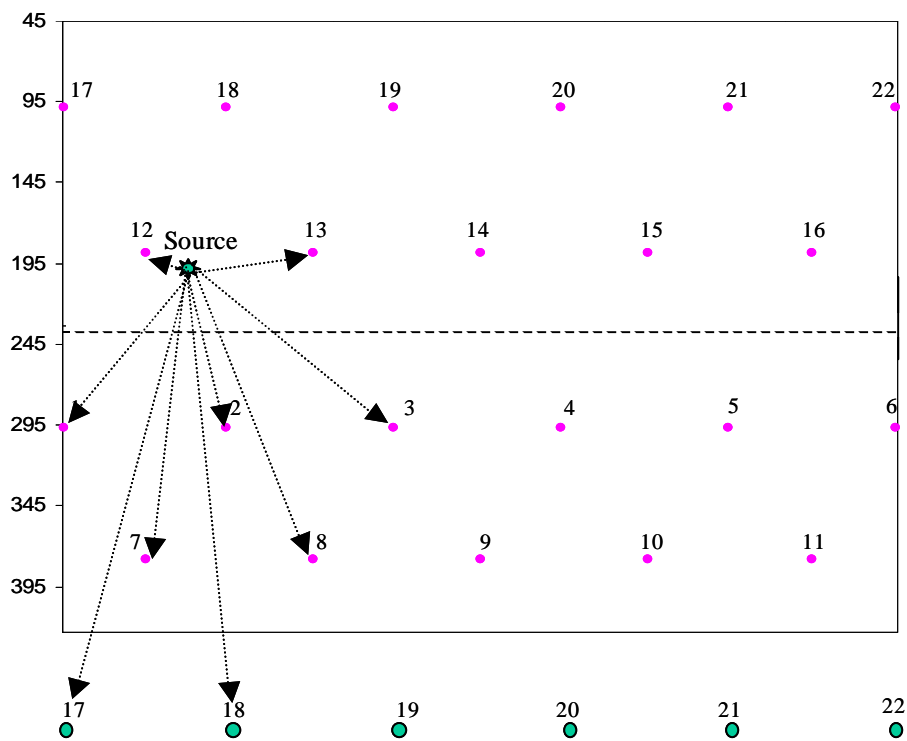


Figure 4.3c – The Third Possible Path

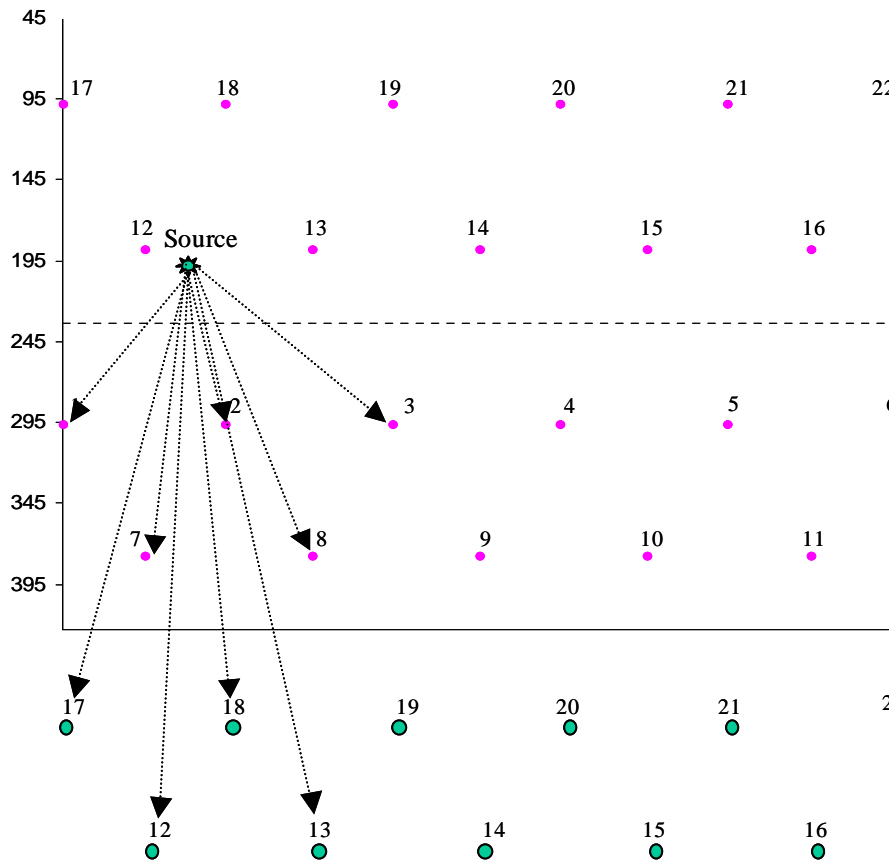


Figure 4.3d – Last Possible Route

Figure 4.3 – Four Possible Wave Propagation Paths

In Figure 4.3, it is seen that the most probable route is either the first path shown in Figure 4.3a, or the second route as shown in Figure 4.3b. However, it was found by examination of the test data that the signal does not always travel through the shortest path since discontinuities can shield or attenuate the signal. The last route is shown in Figure 4.3d. It is the least likely to be the correct path since the source is out of the sensor area. The fifth possible path that was not

included is all sensors with the y values less than the y value of the center line along the top of the tank car. As with the route shown in Figure 4.3d, this is the least likely to be the correct path. However, the analysis always included all four different routes.

- *Number of Sensors Included in the Analysis*

Another issue arises when more than three sensors detect the signals. It is necessary to decide how many sensors should be included in the calculation. Generally, the more sensors used in the analysis the better the accuracy of the results obtained. However, all sensors included in the analysis must receive signals from the same source. The problem is that it is difficult to tell if a sensor detects a signal from a different source that happens at the same time. If the sensor detecting the signal from a different source is included in the calculation, an error in the calculated location will occur. This is often referred to as the multiple-source problem.

To minimize the multiple-source problem, a new algorithm using combinations of three sensors was developed. The concept of the approach is to apply simplex optimization to sets of three sensors that detect the signals. The number of analysis sets can be calculated by:

$$n = \frac{N!}{(N-3)!3!} \dots\dots\dots(5.1)$$

where n is the number of analysis sets and N is the number of sensors detecting the signal.

If the sensors included in each analysis set detect the signal from the same location, the results from each analysis will provide a grouping. Combinations that include a sensor hit from another source will yield locations that are significantly different from others in the group.

The combination of three sensors method calculates every possible combination with three sensors. The analysis does not consider the limitation of the triangulation technique. For example, the results obtained from the sensors aligned in a straight line can be ambiguous. The results from the three sensors that do not cover the area of the source can give more than one solution. Therefore, the results from some combinations are eliminated if they fit the categories and yield results out of the group.

### **4.3.3 Illustrative Test Results**

- *Example 1*

This section gives a step by step illustration of the combination of three sensors algorithm. The data used in this section is from one of the events generated by the jacking test at the A-end on the left side with the other bolsters restrained.

In this case, six sensors received data. They are Sensors 6, 11, 15, 16, 21, and 22. With 6 sensors included, the possible combination of three sensors is 20 sets. The simplex optimization approach was used for the analysis with a step value of 1". Tables 5.4 to 5.8 illustrate the analysis procedure step by step. The results listed in the table are corresponding to the plots in Figure 4.4 to Figure 4.8.

The results from every analysis set from four possible paths are listed in Table 4.4. The results from Table 4.4 are plotted shown in Figure 4.4. It is seen

from the plot that the results are very scattered. Note that x and y are in inches and the Flag is in microseconds.

The next step is to eliminate the results with a Flag value higher than a 100 microseconds. The results of this are shown in Table 4.5 and Figure 4.5. The limit of the Flag value was set at a 100 microsecond because this value yields allowable error in the location. As mentioned in Chapter 3 that the Flag value is the total error in the difference of  $t_0$  among three sensors. Therefore, the average error is  $\text{Flag}/3$ . That means the maximum error allowed in the calculation is 33.33 microseconds. With the wave velocity of 125,000 in/sec, the allowable error in distance is approximately 4”.

Redundant paths that provide the same results are taken away and the results are shown in Table 4.6 and Figure 4.6. In this case, redundant path mean two or more paths that yield the same route for three sensors in the combination. Redundant paths will yield the same results.

Then, there are three paths providing results with low Flags. Since every combination in the second route yields answers in the same range, and the analysis sets from the first and third path give very scattered results, all the answers in the first and third route are also eliminated. The results from all combinations from the correct path are shown in Table 4.7 and Figure 4.7.

The next step is to manually eliminate some combinations that provide errors in the results. These are highlighted in Table 4.7. As mentioned previously, the combination that has three sensors arranged in the straight line yields ambiguous results. In this case, the combination of sensor 6, 16, and 21 yields result that is out of the group. This combination is eliminated because three sensors are arranged in the straight line. Also, the results from the combinations where all sensors do not cover the source can provide more than one solution. The results show that some combinations that fit this category give

wrong answers and some yield results out of the group. The combinations that yield the results out of group are also eliminated. The results are shown in Table 4.8 and Figure 4.8.

The final step is to take the average of all the results from each combination and The final result is presented in Figure 4.9.

Sensor	1st Route			2nd Route			3rd Route			4th Route		
	X	Y	Flag1	X	Y	Flag2	X	Y	Flag3	X	Y	Flag4
6:11:15;	461	179	4401	428	249	27	428	249	27	324	346	15004
6:11:16;	461	179	7676	427	248	39	427	248	39	461	86	15367
6:11:21;	461	200	9323	427	246	59	324	185	5387	324	185	5387
6:11:22;	324	235	7508	427	245	28	461	321	6317	461	321	6317
6:15:16;	429	247	76	429	247	76	429	247	76	461	47	1270
6:15:21;	433	243	17	433	243	17	396	305	47	324	302	11987
6:15:22;	432	244	37	432	244	37	391	310	63	324	394	6286
6:16:21;	415	234	11	415	234	11	389	278	38	461	399	15028
6:16:22;	438	243	45	438	243	45	339	293	22	324	376	13006
6:21:22;	431	244	15	431	244	15	431	331	29	431	331	29
11:15:16;	430	130	64	430	248	64	430	248	64	430	130	64
11:15:21;	461	198	8521	436	245	39	324	312	3031	461	198	8521
11:15:22;	325	79	49	433	246	47	461	261	7029	325	79	49
11:16:21;	461	145	7735	415	248	37	324	259	4498	461	145	7735
11:16:22;	324	190	4915	438	247	23	461	245	6995	324	190	4915
11:21:22;	422	47	79	431	246	59	422	47	79	422	47	79
15:16:21;	411	220	22	411	220	22	461	290	163	411	220	22
15:16:22;	440	200	14	440	200	14	400	283	53	400	182	109
15:21:22;	430	239	27	430	239	27	434	297	50	427	232	234
16:21:22;	431	339	36	431	239	36	454	299	87	430	222	107

Table 4.4 – Results from Combinations of Three Sensors from Four Path

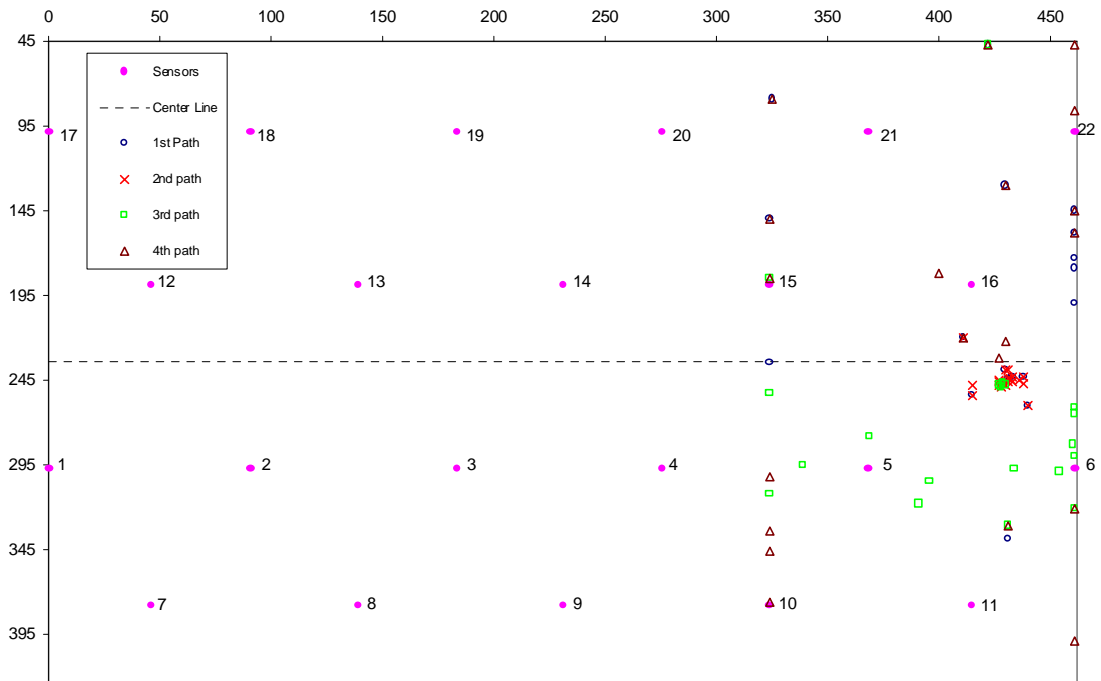


Figure 4.4 – Source Locations Listed in Table 4.4

	X1	Y1	Flag1	X2	Y2	Flag2	X3	Y3	Flag3	X4	Y4	Flag4
<b>Sensors</b>												
6:1:15:				428	249	27	428	249	27			
6:1:16:				427	248	39	427	248	39			
6:1:21:				427	246	59						
6:1:22:				427	245	28						
6:15:16:	429	247	76	429	247	76	429	247	76			
6:15:21:	433	243	17	433	243	17	396	305	47			
6:15:22:	432	244	37	432	244	37	391	318	63			
6:16:21:	415	234	11	415	234	11	389	278	38			
6:16:22:	438	243	45	438	243	45	339	295	22			
6:21:22:	431	244	15	431	244	15	431	331	29	431	331	29
11:15:16:	430	130	64	430	248	64	430	248	64	430	130	64
11:15:21:				436	245	39						
11:15:22:	325	79	49	433	246	47				325	79	49
11:16:21:				415	248	37						
11:16:22:				438	247	23						
11:21:22:	422	47	79	431	246	59	422	47	79	422	47	79
15:16:21:	411	220	22	411	220	22				411	220	22
15:16:22:	440	280	14	440	280	14	480	283	53			
15:21:22:	430	239	27	430	239	27	434	297	50			
16:21:22:	431	139	36	431	239	36	454	299	87			

Table 4.5 – Results with Low Flag Values from Four Paths



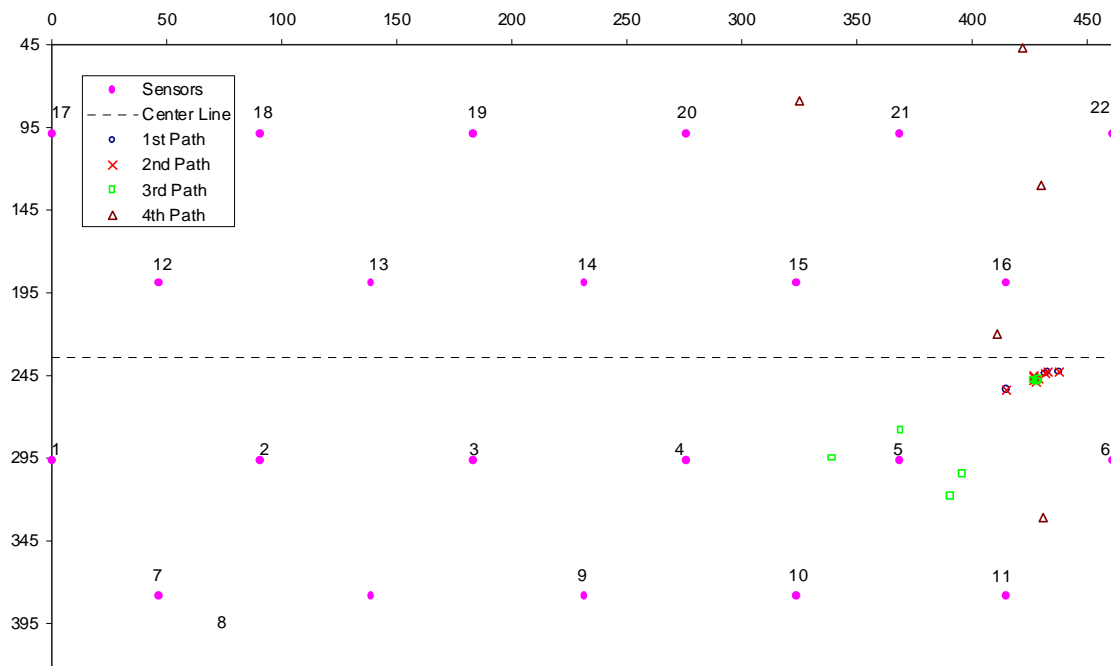


Figure 4.5 – Source Locations Listed in Table 4.5

	X1	Y1	Flag1	X2	Y2	Flag2	X3	Y3	Flag3	X4	Y4	Flag4
Sensors												
6;11;15;			64	428	249	27			47			63
6;11;16;				427	248	39						
6;11;21;				427	246	59						
6;11;22;				427	245	28						
6;15;16;				429	247	76						
6;15;21;				433	243	17	396	305				
6;15;22;				432	244	37	391	318				
6;16;21;				415	254	11	369	278				
6;16;22;				438	243	45	339	295				
6;21;22;				431	244	15	431	331				
11;15;16;	430	130		64	430	248	64					
11;15;21;				436	245	39						
11;15;22;	325	79		49	433	246	47					
11;16;21;				415	248	37						
11;16;22;				438	247	23						
11;21;22;	422	47		79	431	246	59					
15;16;21;				411	220	22						
15;16;22;				440	260	14	460	283				
15;21;22;				430	239	27	434	297				
16;21;22;			431	239	36	454	299					

Table 4.6 – Results with no Redundant Paths

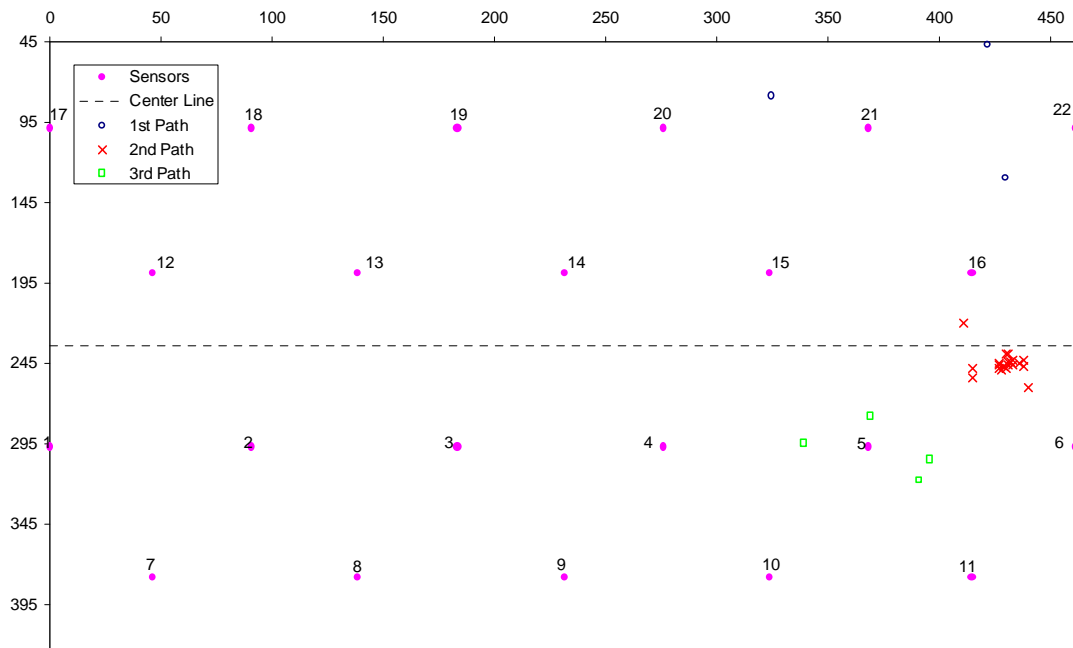


Figure 4.6 – Source Locations Listed in Table 4.6

	X1	Y1	Flag1	X2	Y2	Flag2	X3	Y3	Flag3	X4	Y4	Flag4
Sensors												
6;11;15;				428	249	27						
6;11;16;				427	248	39						
6;11;21;				427	246	59						
6;11;22;				427	245	28						
6;15;16;				429	247	76						
6;15;21;				433	243	17						
6;15;22;				432	244	37						
6;16;21;				415	254	11						
6;16;22;				438	243	45						
6;21;22;				431	244	15						
11;15;16;				430	248	64						
11;15;21;				436	245	39						
11;15;22;				433	246	47						
11;16;21;				415	248	37						
11;16;22;				438	247	23						
11;21;22;				431	246	59						
15;16;21;				411	220	22						
15;16;22;				440	260	14						
15;21;22;				430	239	27						
16;21;22;				431	239	36						

Table 4.7 – Results from Sensors Which Group Locations in the same Area of the Shell

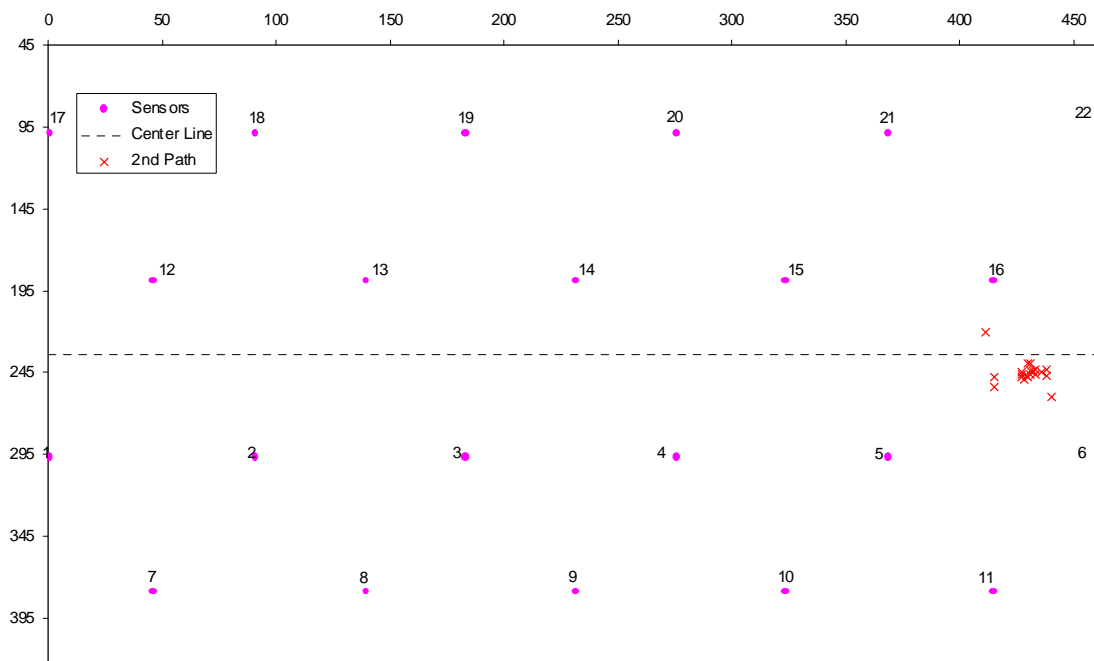


Figure 4.7 – Source Locations Listed in Table 4.7

	X1	Y1	Flag1	X2	Y2	Flag2	X3	Y3	Flag3	X4	Y4	Flag4
Sensors												
6;11;15;				428	249	27						
6;11;16;				427	248	39						
6;11;21;				427	246	59						
6;11;22;				427	245	28						
6;15;16;				429	247	76						
6;15;21;				433	243	17						
6;15;22;				432	244	37						
6;16;21;												
6;16;22;				438	243	45						
6;21;22;				431	244	15						
11;15;16;				430	248	64						
11;15;21;				436	245	39						
11;15;22;				433	246	47						
11;16;21;												
11;16;22;				438	247	23						
11;21;22;				431	246	59						
15;16;21;												
15;16;22;												
15;21;22;				430	239	27						
16;21;22;				431	239	36						

Table 4.8 – Results after Eliminating the Combinations that have Sensors in a Straight Line, do not Cover the Source, and Provide Out of Group Answers

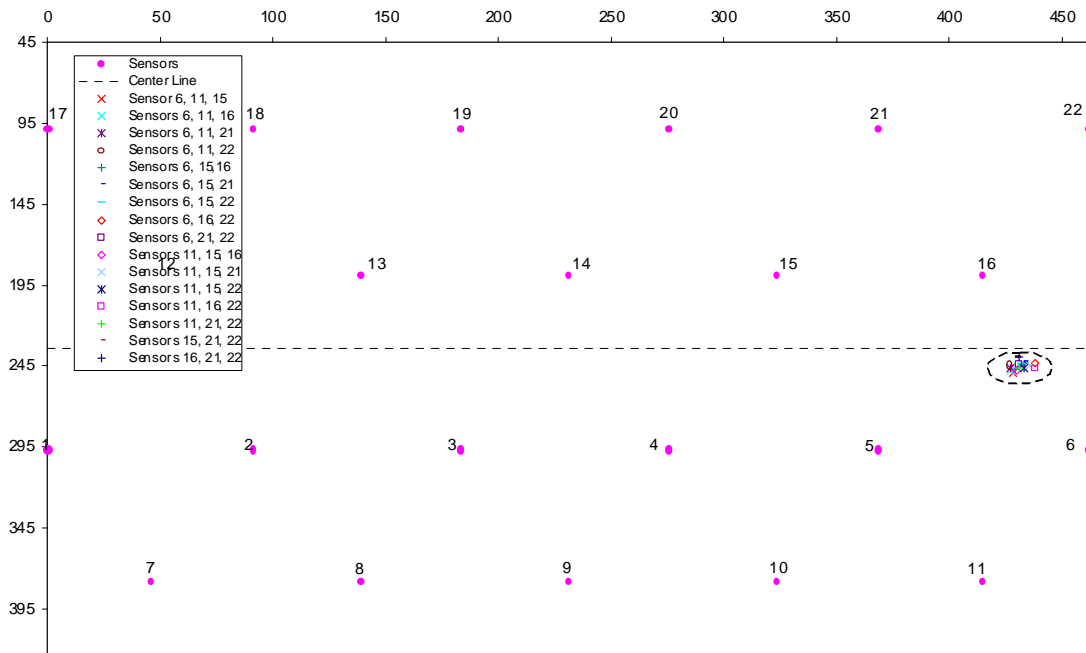


Figure 4.8 – Source Locations Listed in Table 4.8

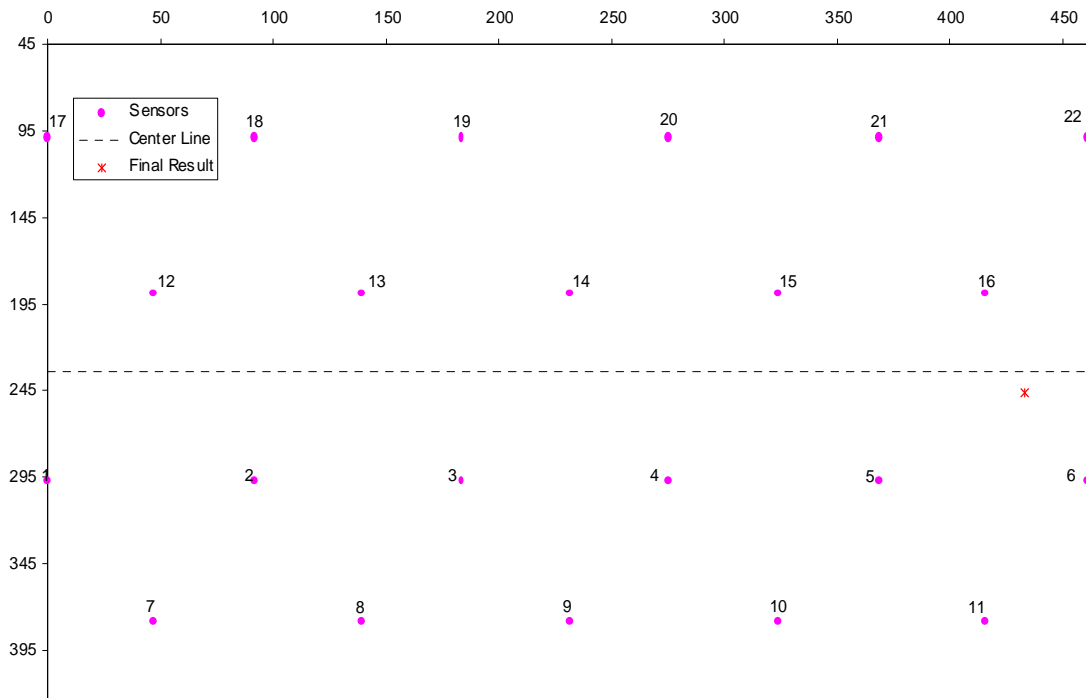


Figure 4.9 – Final Results

- *Example #2*

As mentioned earlier, the technique described in Example #1 is also able to minimize the multiple source problem. This section illustrates the procedure of minimizing the multiple-source problem. The data used in this section was from one of the events in the data from the jacking test at the A-end on the left side with other bolsters restrained. The simplex optimization approach was used for the analysis with a step value of 1”.

In this case, five sensors received data. They are Sensors 6, 10, 15, 16, and 22. With 5 sensors included, the possible combination of three sensors is 10 sets. The result from the combination of Sensor 6, 16, 22 was eliminated earlier because the Flag value is too high.

The results of the combinations of the right path are presented in Figure 4.10. It is seen that the combinations including sensor 6 yield scattered results indicating that sensor 6 detected the hit from another source that happened at the same time. The combination sensors of 10,15,16, and 22 yielded results in the same area as circled by the dashed line.



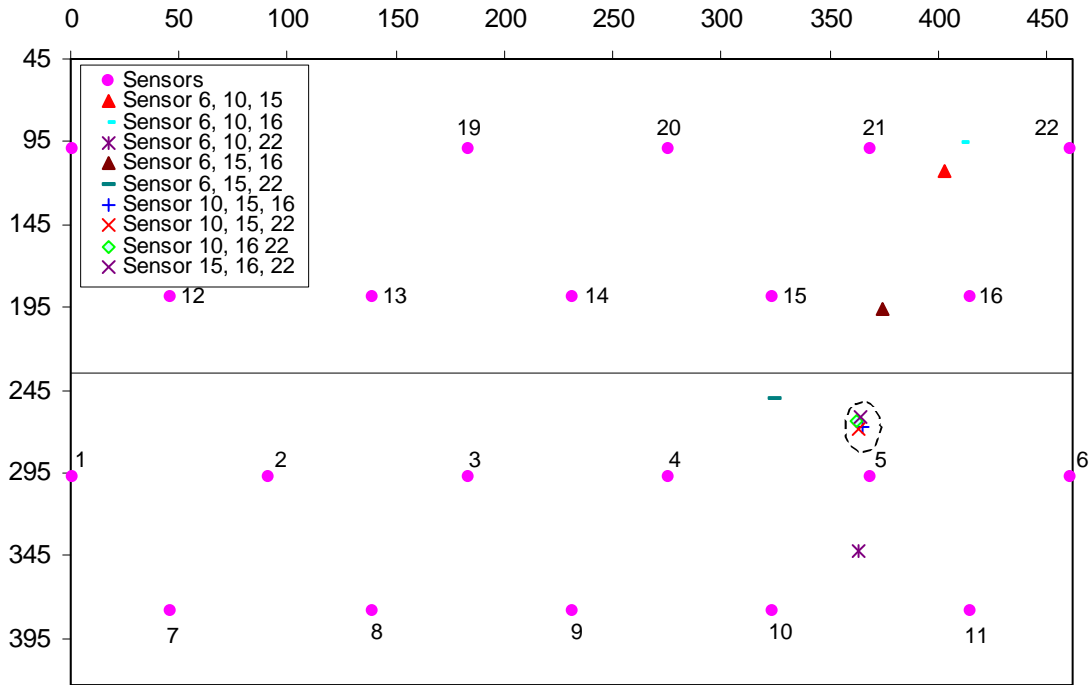


Figure 4.10 – Results from Multiple Sources

## 4.4 JACKING TEST

### 4.4.1 Test Procedure

The objective of the jacking test is to apply torsional loads with a single jack positioned underneath the bolster so that the car body is twisted by lifting the bolster [AAR]. The test setup is depicted in Figure 4.11. To evaluate the condition of the tank with AE, two jacking tests are required, one lift at each end. Both of these lifts need to be at the same side of the tank car. This type of loading detects cracks, corrosion, and other defects in the bottom area of the tank car including the sill, tank cradle pad, bolsters, and in the end of the cylindrical tank.



Figure 4.11 – Jacking Test Setup

The specified loading sequence for a jacking test is shown in Figure 4.12. At the beginning of the test, the tank is monitored without load for 10 minutes to ensure that there is no background noise to interfere with genuine AE signals. Then, the tank is lifted by a jack placed underneath the bolster up to the deflection of 1 inch for a full tank and 2 inches for an empty tank. The load is held for 10 minutes to monitor significant emission from the structure. It is not possible to monitor the car while loading because of the excessive mechanical noise that occurs. The noise is so copious that it masks any genuine emissions. For this reason, the AAR procedure specifies that only the load hold is monitored.

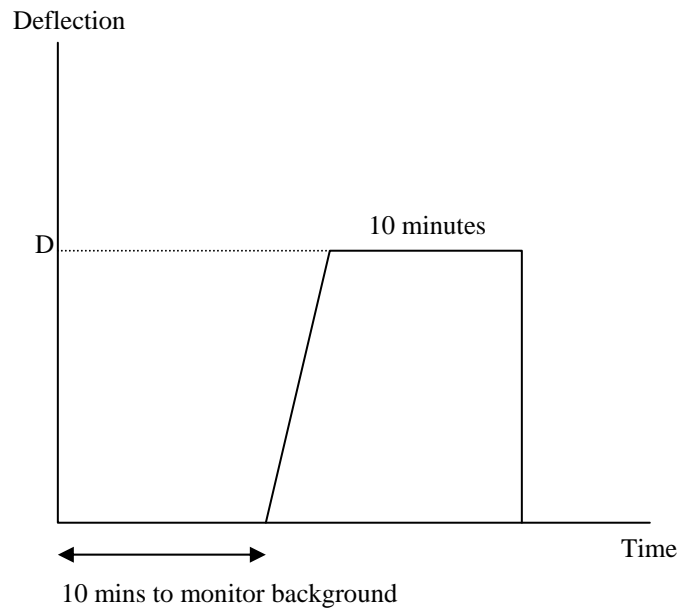


Figure 4.12 – Load Schedule for a Jacking Test [AAR]

The purpose of the jacking test described in this chapter is not to evaluate the tank car condition, since it is known that the tank is in a bad condition and has been removed from service. Instead, the objective of the test is to obtain emission from flaws for source location analysis. Therefore, all four bolsters were lifted instead of the two required by the AAR procedure. In addition, they were jacked more than the specified two inches and the load hold periods were sometimes more than the required 10 minutes.

#### 4.4.2 Test Results

In this part, four conventional jacking tests were performed on an empty tank car. One jack was used in the test to raise the bolster. Figure 4.13 presents

the top view of the tank showing the character symbols used to identify each bolster. In Figure 4.13, there are two heads on the tank car, one with the brake handwheel and one without. The end with the brake handwheel is called B end and the other end is called A end. The left and right sides of the tank car are determined by facing the tank car at the B end.

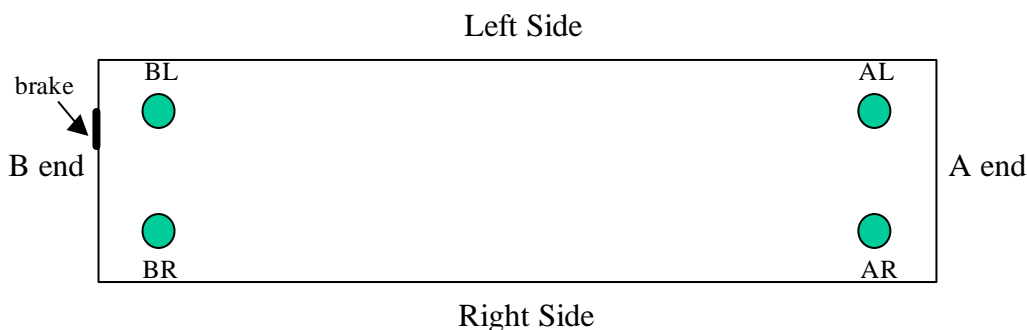


Figure 4.13 – Symbols Used for Each Bolster

In these tests, AE monitoring was performed only when the displacement of the bolster was being held constant to avoid interference from mechanical noise. Although jacking tests were performed on all four bolsters, only the results from three tests, jacking at AL, BL, and BR, are discussed in this section. Results from the AR jacking test did not provide any significant emissions and source location analysis was not possible.

- *Jacking at AL*

In this test, a jack underneath the AL bolster was raised to 1.5 inches and the deformation was held for 5 minutes. The jack height was then increased to 2.8 inches and held for 5 more minutes.

A total emission of 88 hits were obtained from the test and three sources were found from the data. The location results using the method described previously with combinations of three sensors are presented in Figure 4.14. Figure 4.15 presents the final results from the test. Note that the final results are from the average results from the data in each group. The first source was located at the bottom of the A end, the second source was located at the bottom in approximately the middle of the car, and the third source was located next to Sensor 12.

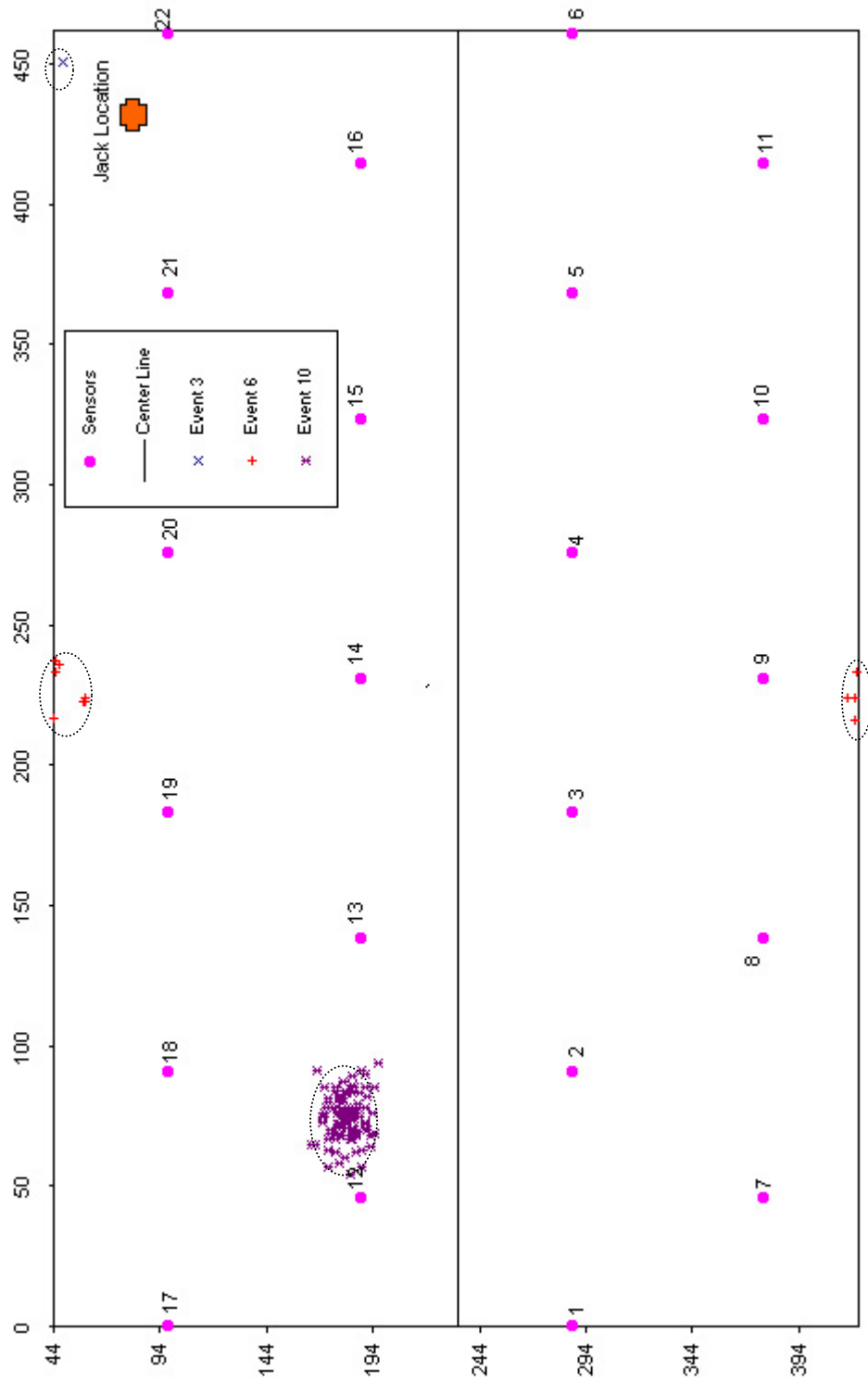


Figure 4.14 - Results from Combinations of Three Sensors from the AL Jacking Test

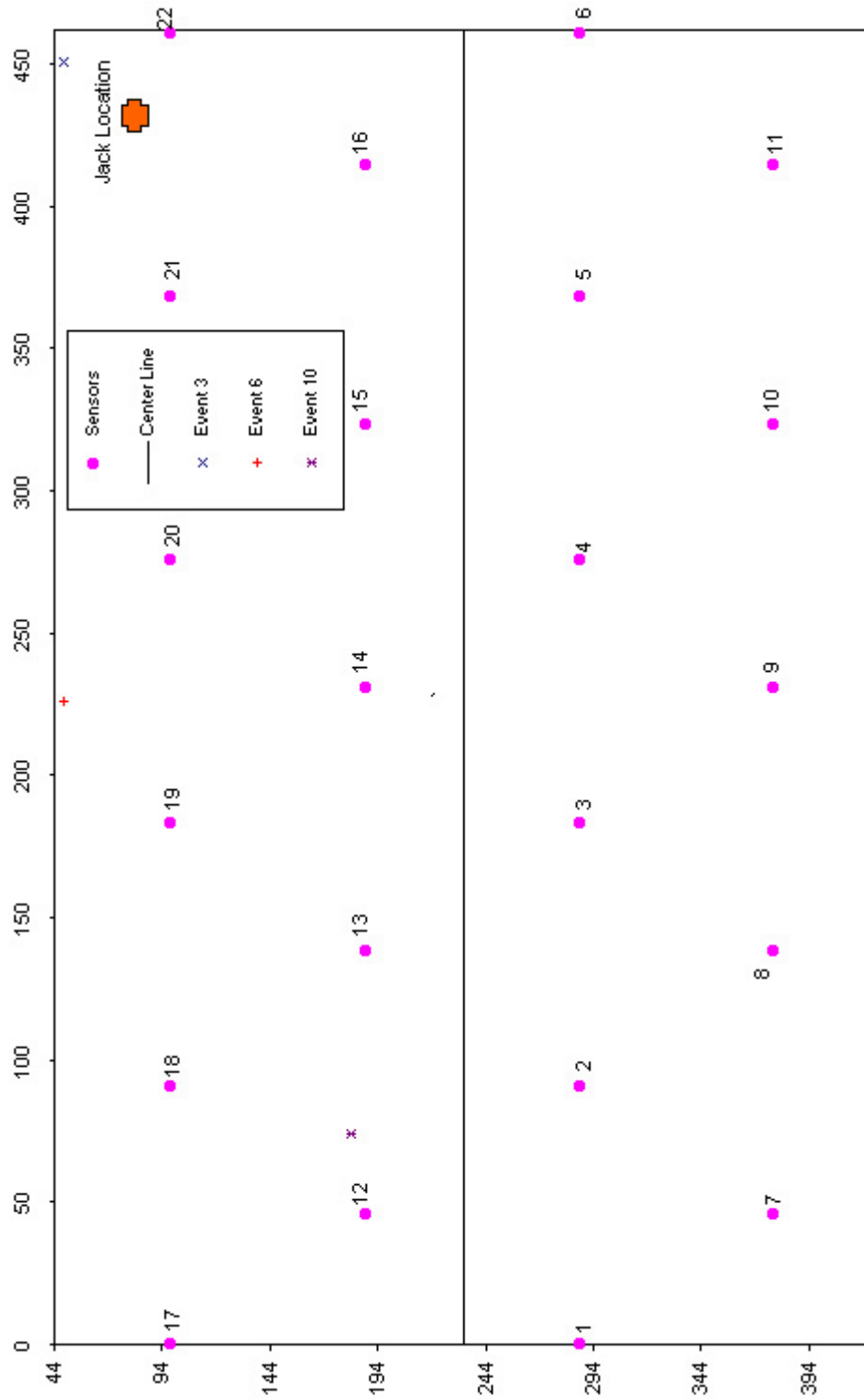


Figure 4.15 - Final Results from the AL Jacking Test

## **Jacking at BR**

In this test, a jack positioned underneath the BR bolster was raised to 2 inches and the load was held for 5 minutes. The location results using the method described previously with combinations of three sensors are presented in Figure 4.16. Figure 4.17 presents the final results from the test. Two areas were identified with possible defects. The first source was located at the bottom and in approximately the middle of the car, and the second and the third events were located beneath Sensor 3.



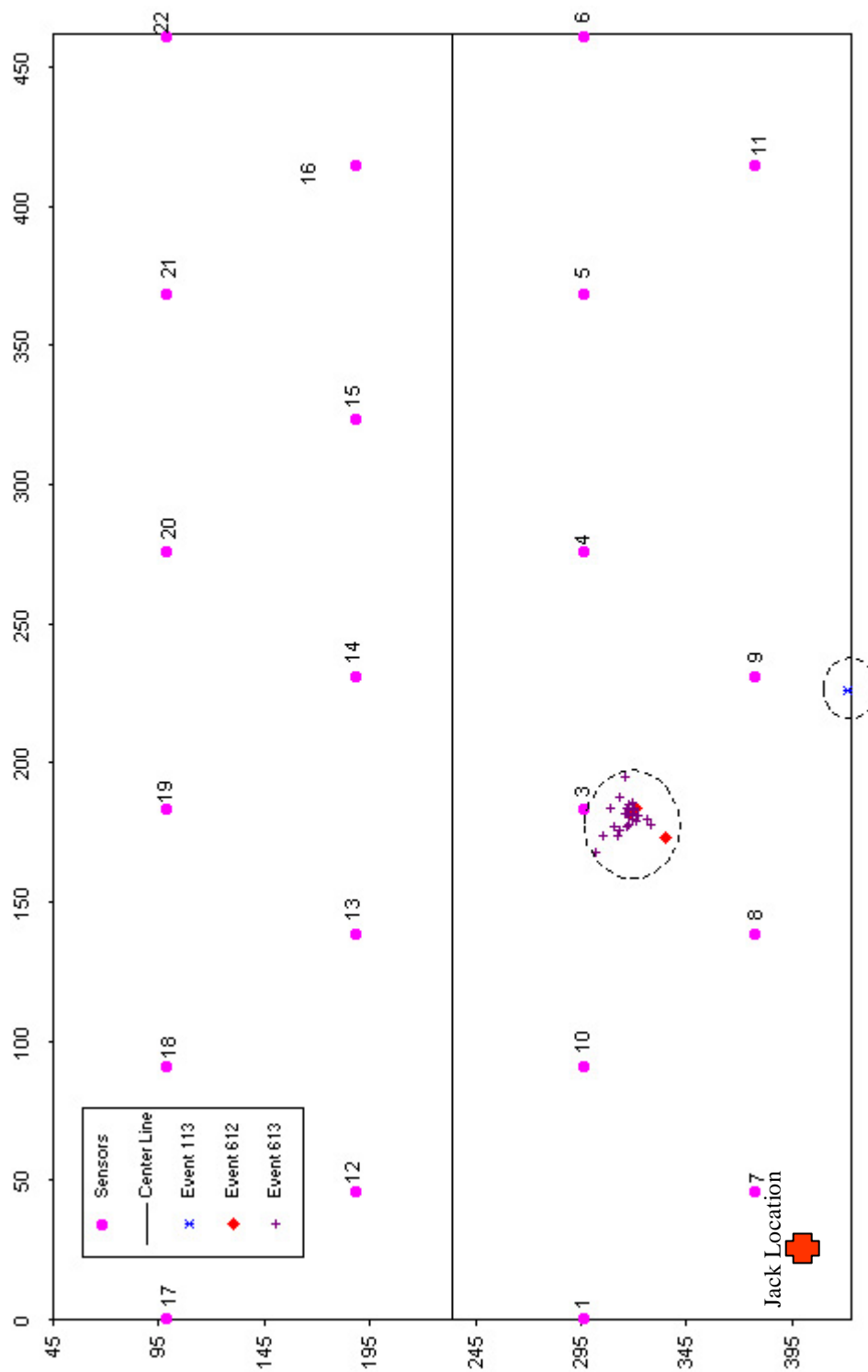


Figure 4.16 - Results from Combinations of Three Sensors from BR Jacking Test

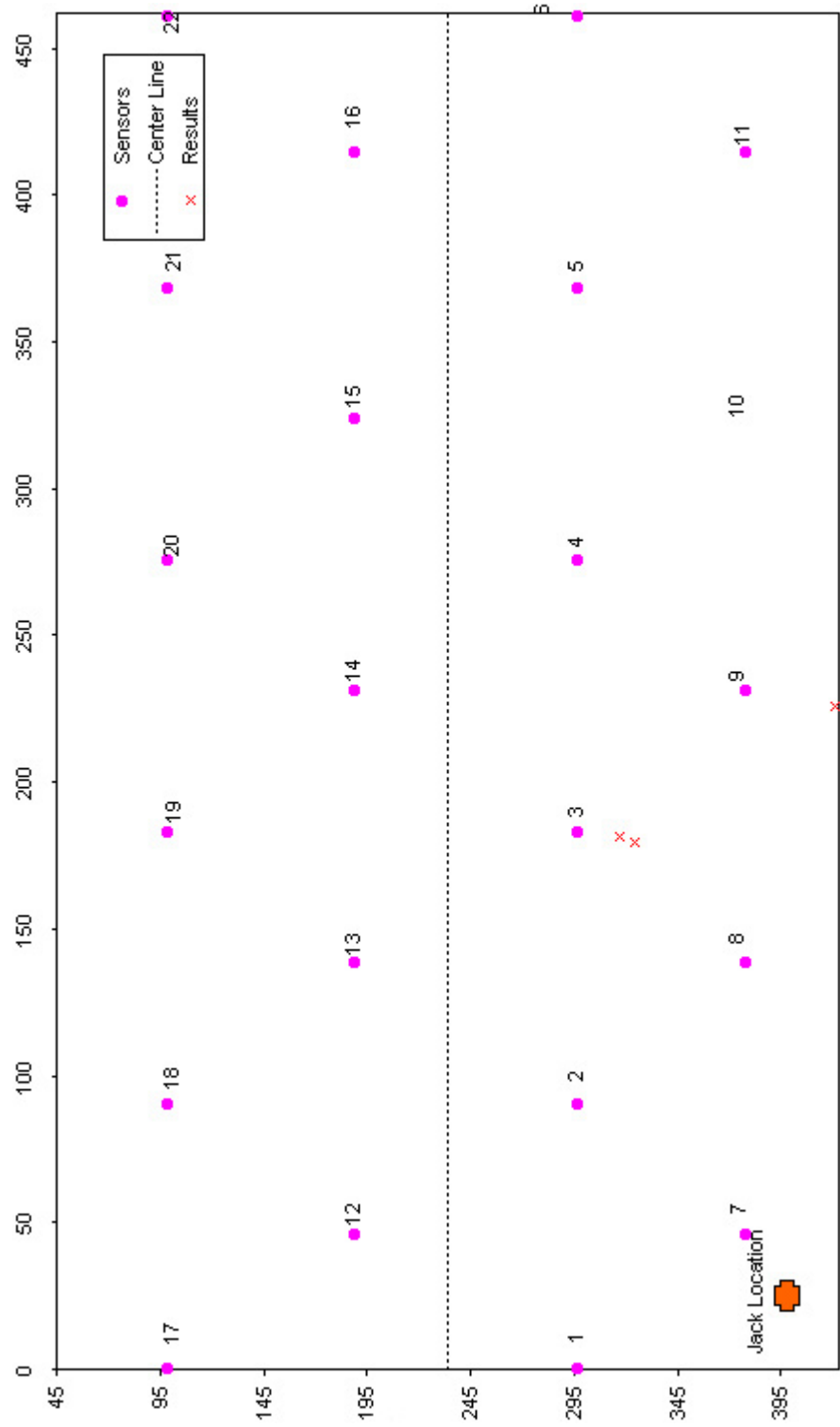


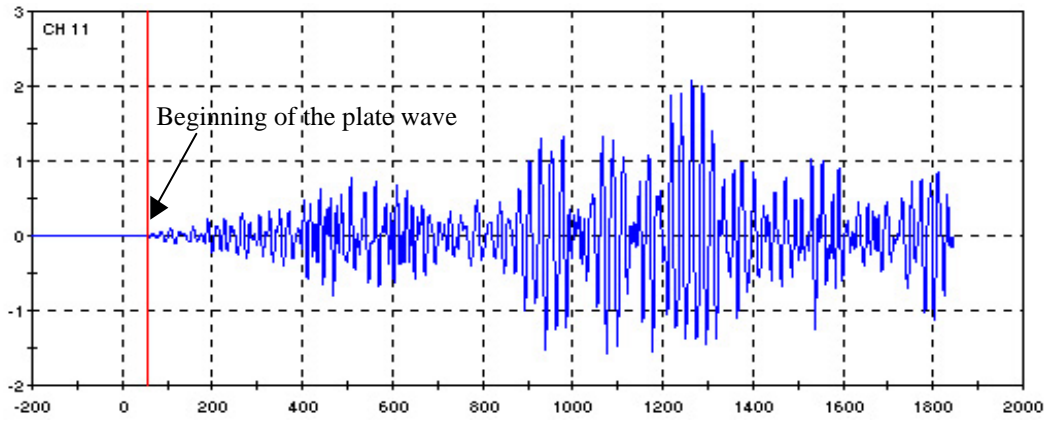
Figure 4.17 - Final Results from BR Jacking Test

## **Jacking at BL**

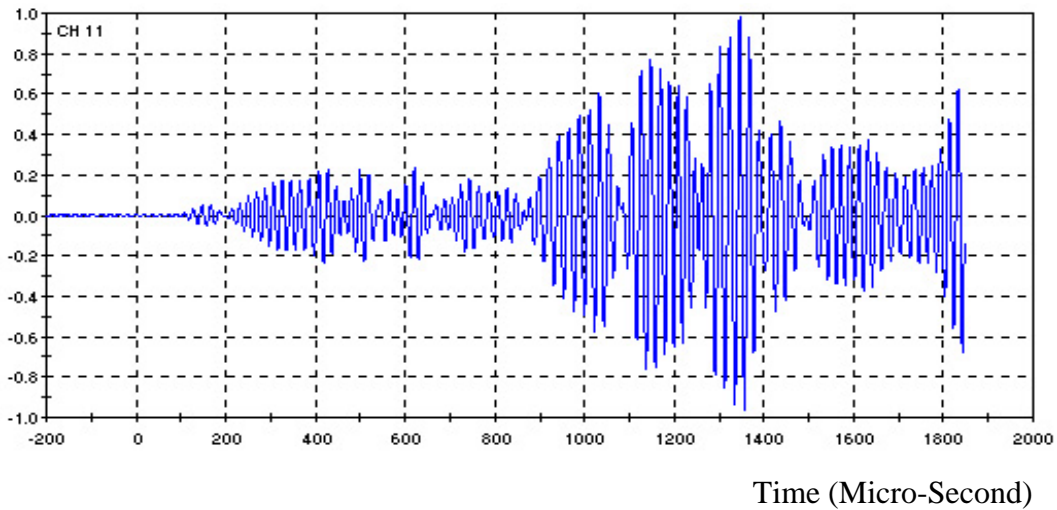
In this test, a jack positioned underneath the BL bolster was lifted to 2 inches and the deformation was held for 5 minutes. During the load hold, a major event created very high amplitude hits (more than 80 db). The method used to analyze source location was different from the approach developed in Chapter 3. More discussion about the data is provided in this section.

Source location analysis was first approached by the method described in Chapter 3. The waveforms were band-passed filtered in the range of 95-105 kHz. However, it was difficult to define the arrival time from the peak since there were many peaks in the waveform package. Examples of the original signal and filtered signal are shown in Figure 4.18. The results from the applying source location approach used for the other jacking tests are shown in Figure 4.19. It is seen that the results are scattered. Some combinations yield the results with a high Flag value. The cause of this error is the inability to define the arrival time corresponding to the right wave mode.

Amplitude (V)



a) Original Waveform



b) Filtered Waveform (95-105 KHz)

Figure 4.18 – Example of Waveform from Jacking Test at BL

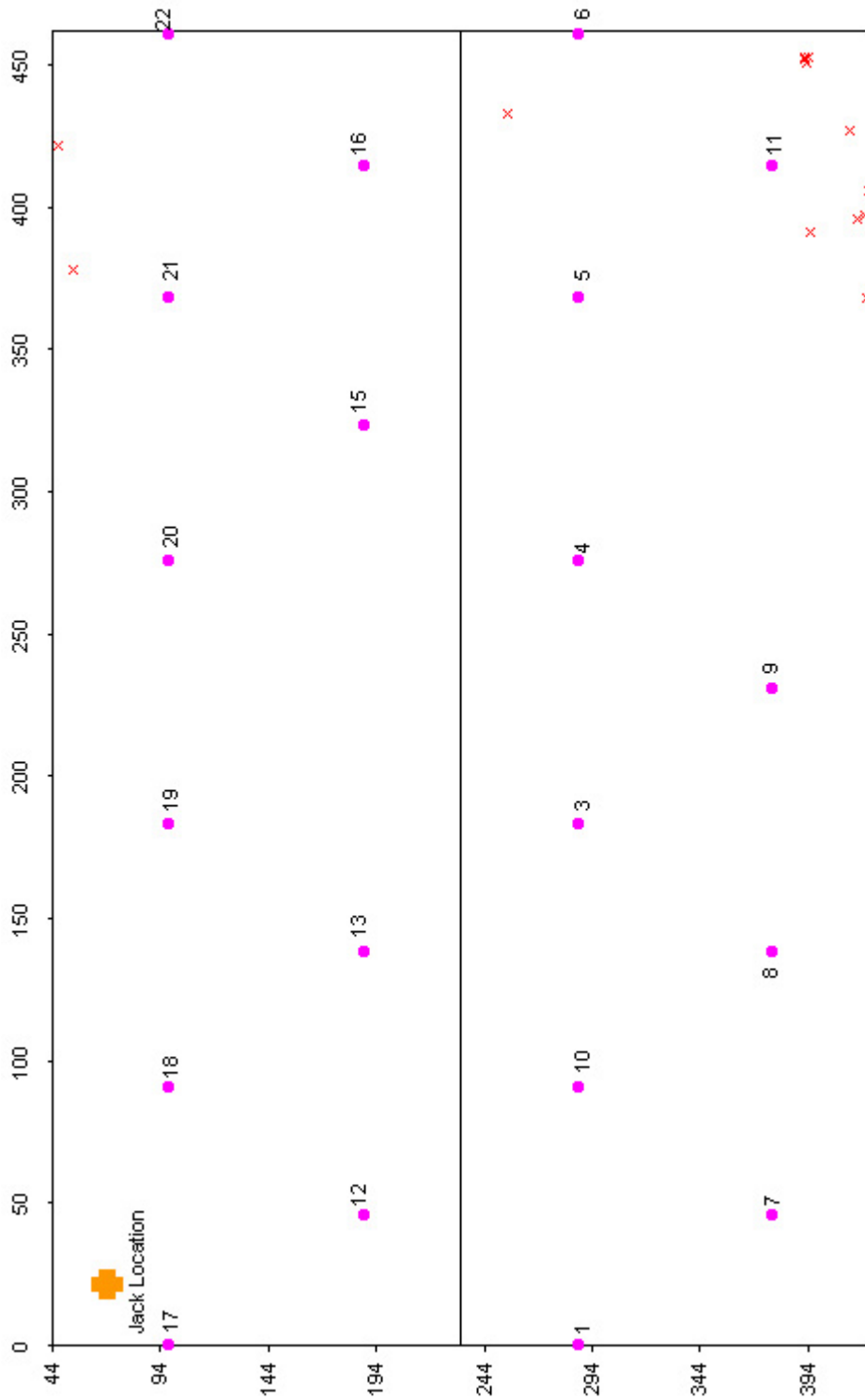


Figure 4.19 - Results from Combination of Three Sensors from BL Jacking Test with the Tight Band Frequency Approach

Since the results in Figure 4.19 are not grouped in the same area, a new way to define the arrival time is needed. For this test, the analysis went back to the traditional way of defining the arrival time by the beginning of the unfiltered waveform. Note that this method does not work well if the beginning of the waveform blends with the background noise and is difficult to define. In this case, the signals have high amplitude and the beginning of the waveforms did not blend with the background noise. As a result the beginning of the waveforms were able to be picked up by visual inspection.

Arrival time is now defined as the beginning of the wave. Accordingly, the wave speed used in the analysis should be the fastest wave mode, which is the lowest order symmetric mode. There are two way of defining this velocity. The first way is to use the concept of combination of three sensors to calibrate for the correct velocity. The analysis started by using combinations of three sensors that received the signals and varying the velocity from 100,000 to 500,000 inch/sec. The correct velocity should yield less scattered location results. From the analysis, the plate wave velocity of 210,000 inch/sec was chosen as it provided the best grouping of the results.

The second way to define the velocity is to calculate the theoretical wave speed for the lowest order symmetric mode. The formula to calculate the fastest speed of the lowest order symmetric mode was defined in Equation 3.3 in Chapter 3. In this case, the wave speed is 212,074 in/sec, which matches the value obtained from the calibration.

Source location was performed using the fastest mode, which is the lowest order symmetric mode. The results from combinations of three sensors are plotted in Figure 4.20 and the final result is shown in Figure 4.21.

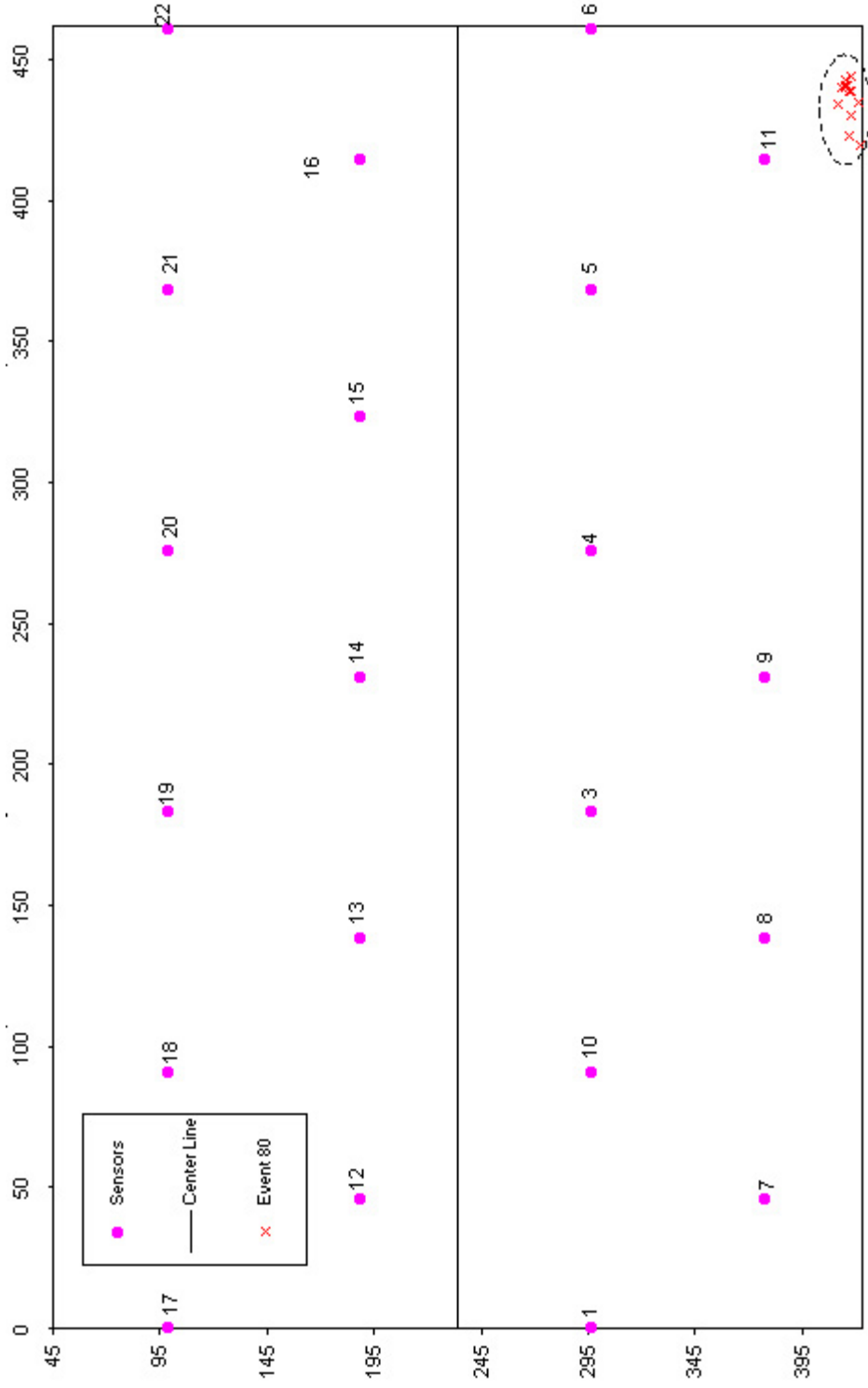


Figure 4.20 - Results from Combination of Three Sensors from BL Jacking Test

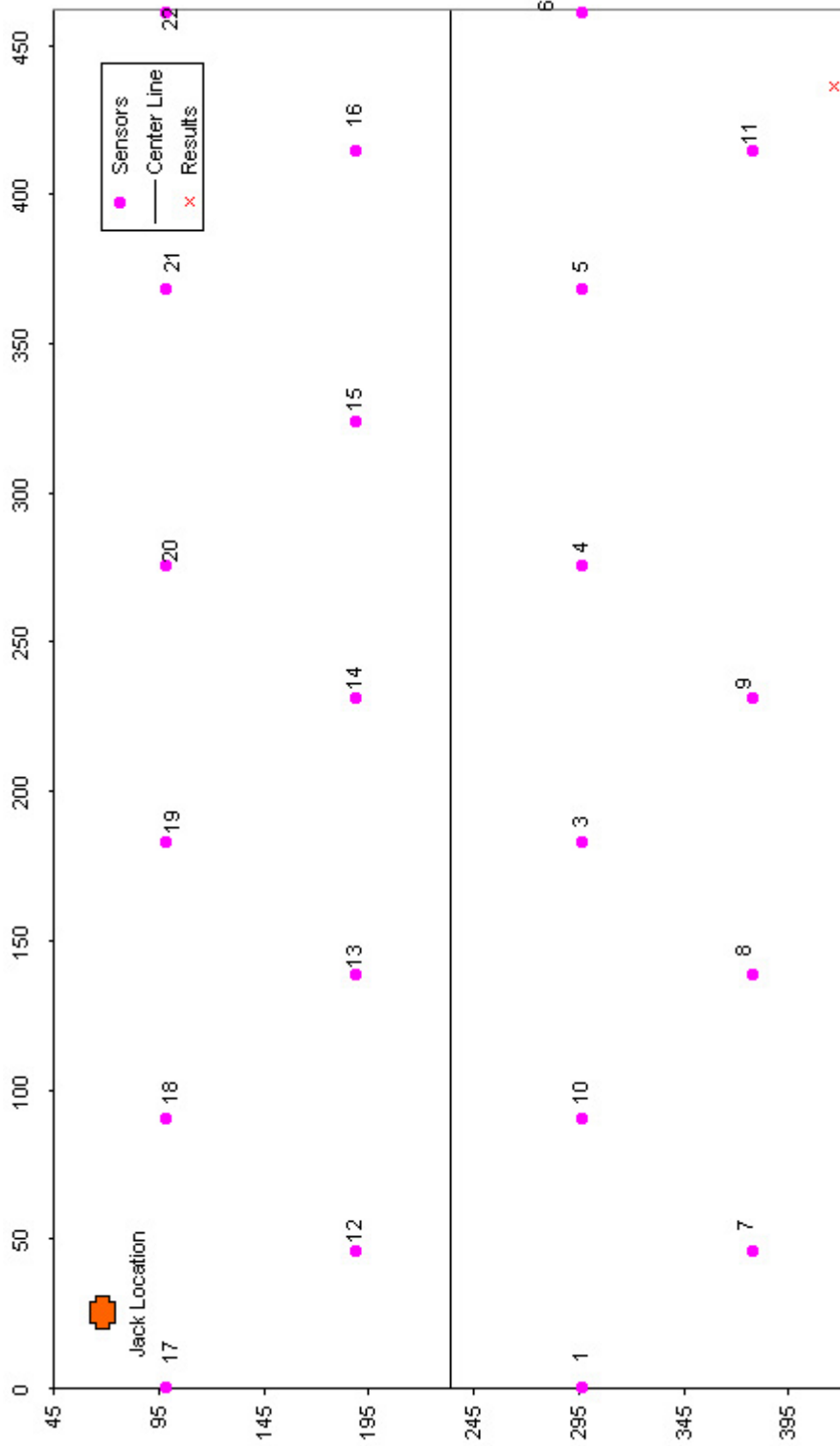


Figure 4.21 - Final Results from BL Jacking Test



The results shown in Figure 4.21 correspond well to the position of a crack in the weld between the reinforcement pad and the bottom of the tank at the A end. This is shown in Figure 4.22. Therefore, the emissions obtained from the test are probably from the crack growth. It is interesting to see that emission generated by crack growth has a high energy in the extensional mode since the movement of the particles could be both parallel and perpendicular direction to the motion of wave propagation. It is also interesting to note that emission from this type of source includes hits of long duration. Inspection of the waveform suggests that multiple hits were registered as the same hit. This makes it difficult to define time of arrival with the tight band frequency method and causes poor location results of the type shown in Figure 4.19.

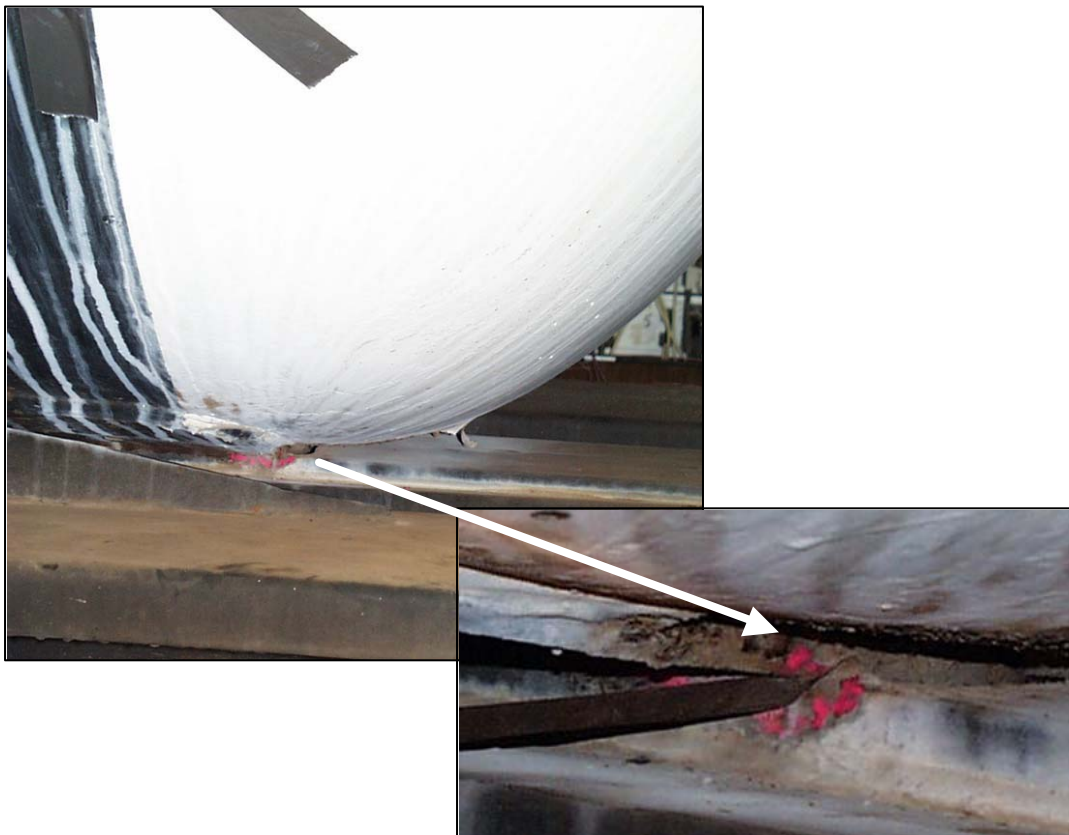


Figure 4.22 – Crack at A End Reinforcement Pad

## **4.5 JACKING - BLOCKED TEST**

### **4.5.1 Test Procedure**

In theory, the jacking test described in the previous section should detect defects in the bottom area of the tank car, but the test sometimes misses flaws in this area. Therefore, one of the current research programs at Ferguson Laboratory is focussing on development of a testing procedure that applies adequate stress on the bottom area of the tank car [El Hajjar, 2000]. One of the approaches that was investigated was a jacking test with the bolsters on the other side of the car restrained from the movement. Three jacks were used in the blocked jacking tests. One bolster was lifted and the bolsters on the other side were supported on jacks which blocked them from movement. One of the blocked jacking tests provided interesting source location results, which are discussed in the following section.

### **4.5.2 Test Results**

- *Jacking at AL and the bolsters on the other side blocked (AL Jack Blocked)*

In this test, a jack was positioned underneath the bolster at the A end on the left hand side and two jacks were located underneath the bolsters on the other side. The jacks on the right hand side restrained the movement as illustrated in Figure 4.23. This figure is a view from the top of the tank.

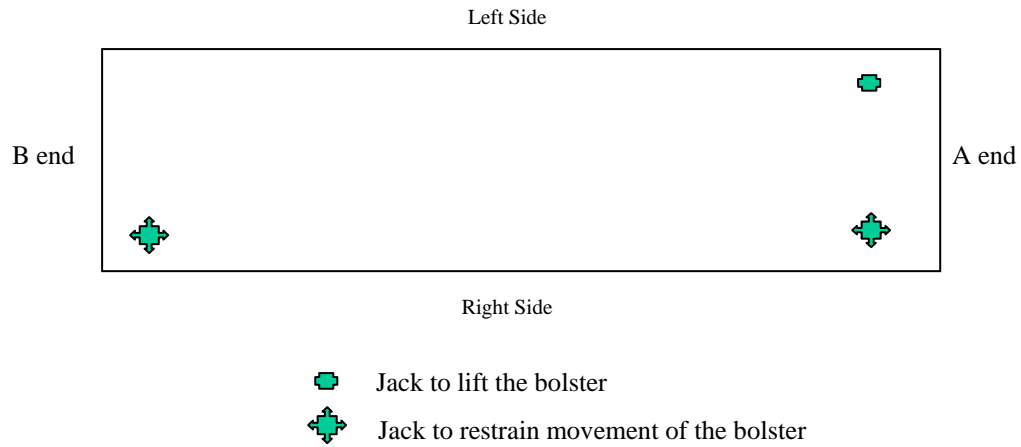


Figure 4.23 – Position of Jacks

In the test, the jack at AL was raised one inch and the load was held for 5 minutes, then the deformation was increased to two inches and the load was held. Significant emission was obtained periodically during the load hold. AE was not monitored during loading due to the mechanical noise. The load schedule and amplitude of emissions versus time is presented in Figure 4.24. The threshold was set at 40 db and it is seen that the amplitudes vary from 40 db to 60 db, which are not high amplitude events.

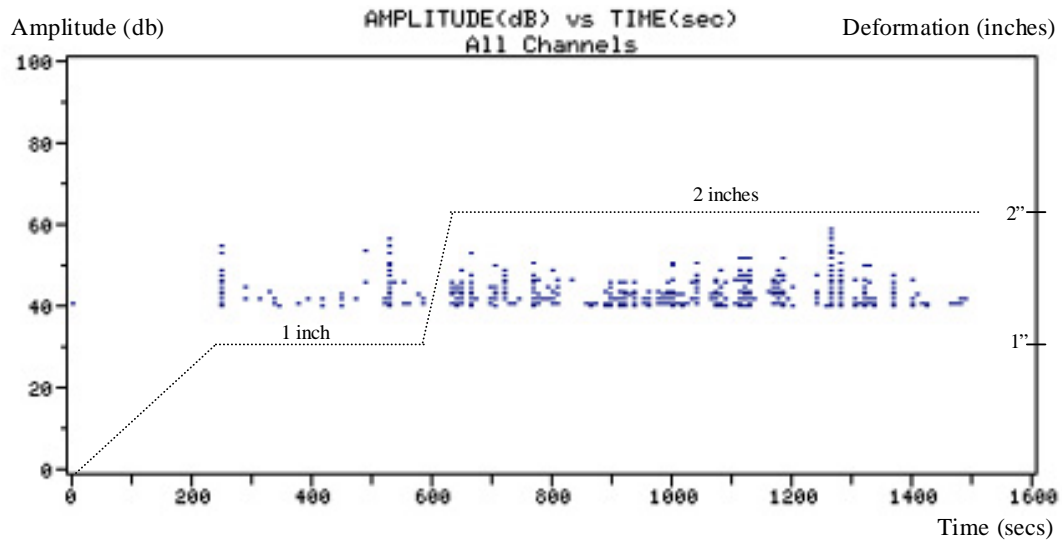


Figure 4.24 – Amplitude of Emissions

For the events where more than three sensors received the signals, source location analysis was performed based on the algorithm discussed in Section 4.3. The results from combinations of three sensors from the correct path for each event are illustrated in Figure 4.25. The figure shows locations of all grouped locatable events. This plot is similar to the data shown in Figure 4.8. Figure 4.26 presents the final results and is similar to Figure 4.9. Note that each result in Figure 4.26 was calculated from the average results from the combinations of three sensors for a particular event. The results in Figure 4.25 and 5.26 show that there are significant flaws on the top of the tank at the A end. The events do not appear to be from a single flaw, but seem to be from a number of flaws distributed over a fairly large area. To verify the results, ultrasonic testing was performed to measure the thickness in the area depicted in Figure 4.27. It was found that there are delaminations, major internal pits, and loss of thickness due to corrosion. The

thickness of the shell has been reduced by approximately half in some areas. The ultrasonic results are presented in Figure 4.28.

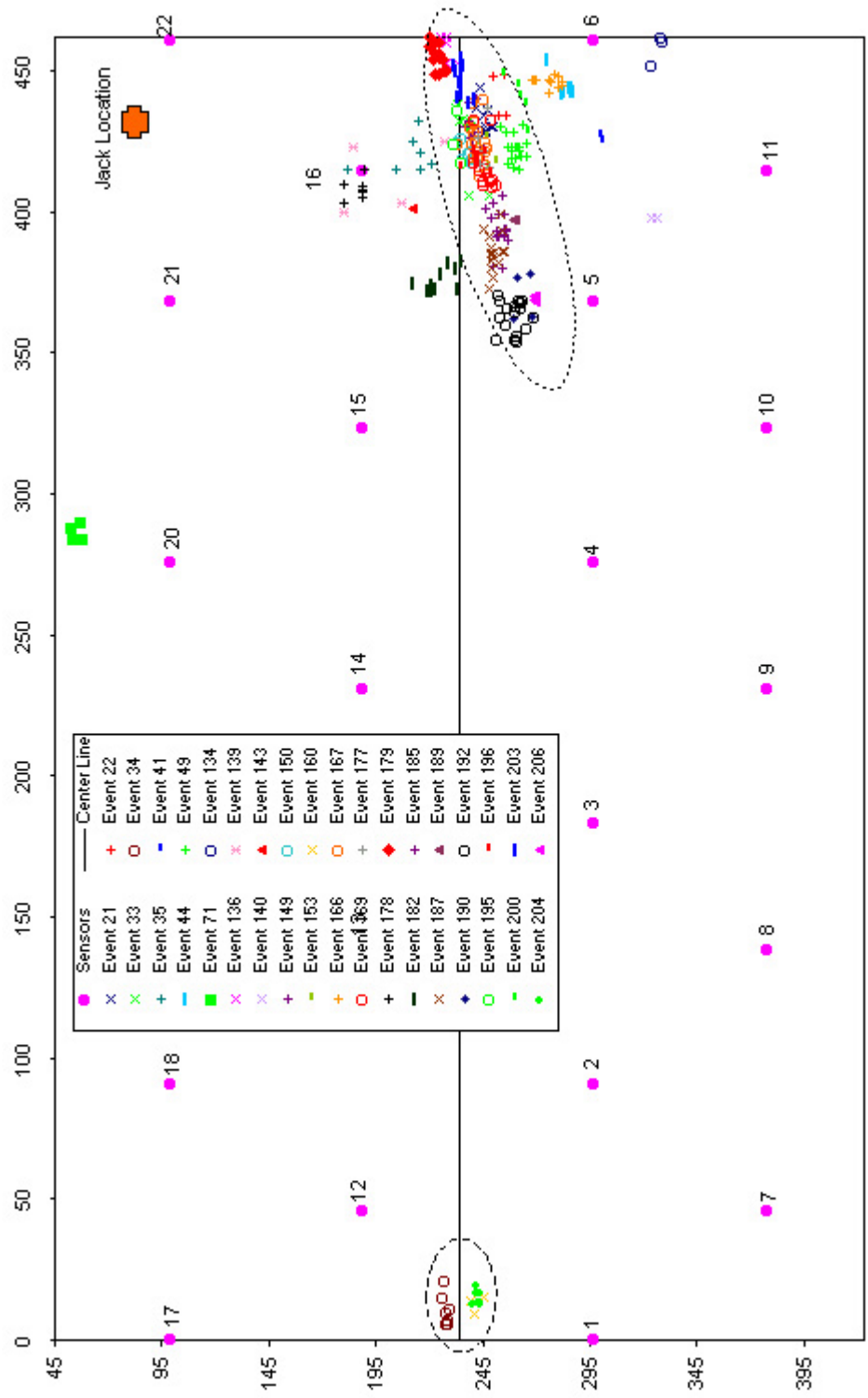


Figure 4.25 - Results from Combinations of Three Sensors for Blocked Jacking Test

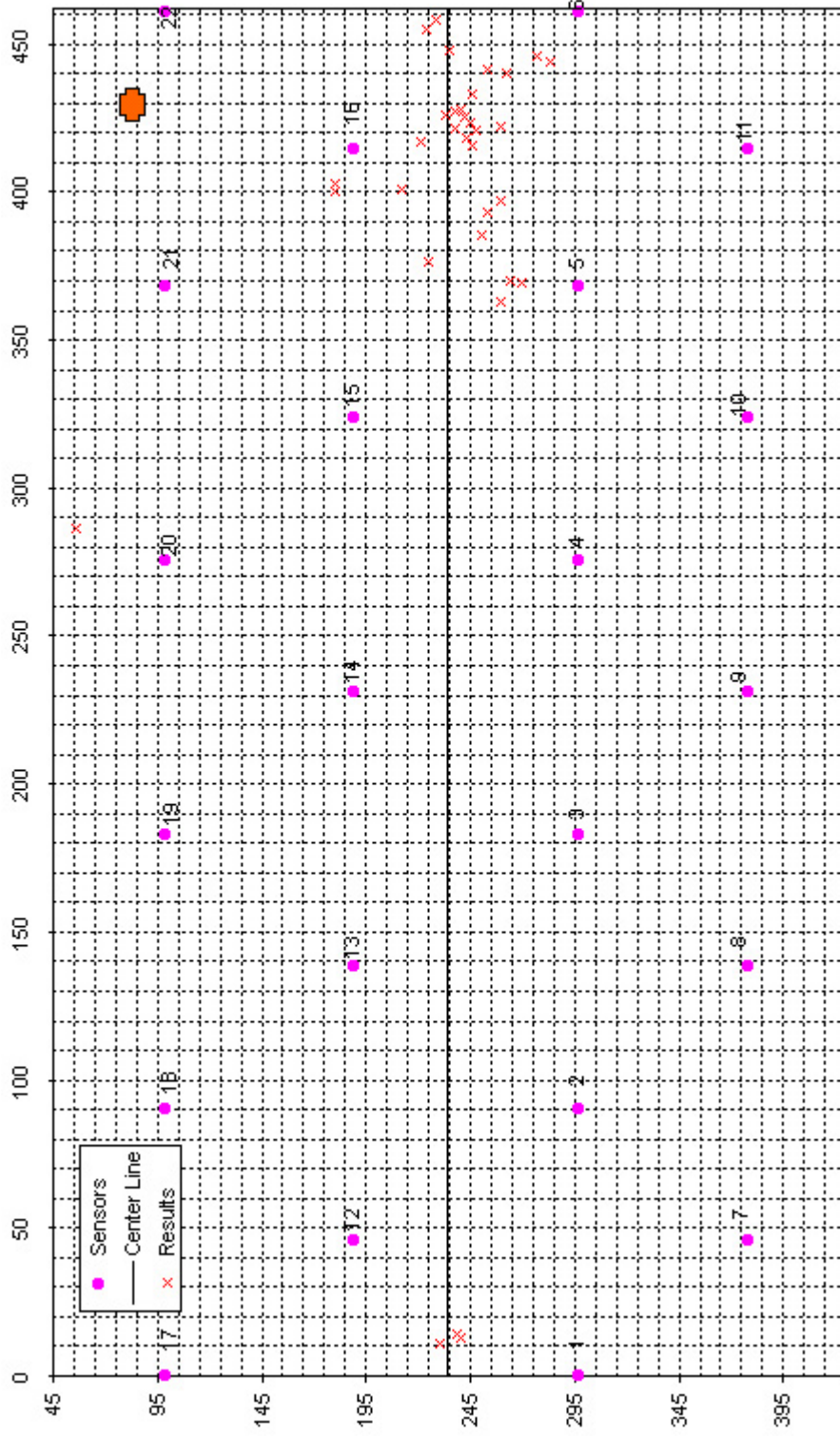
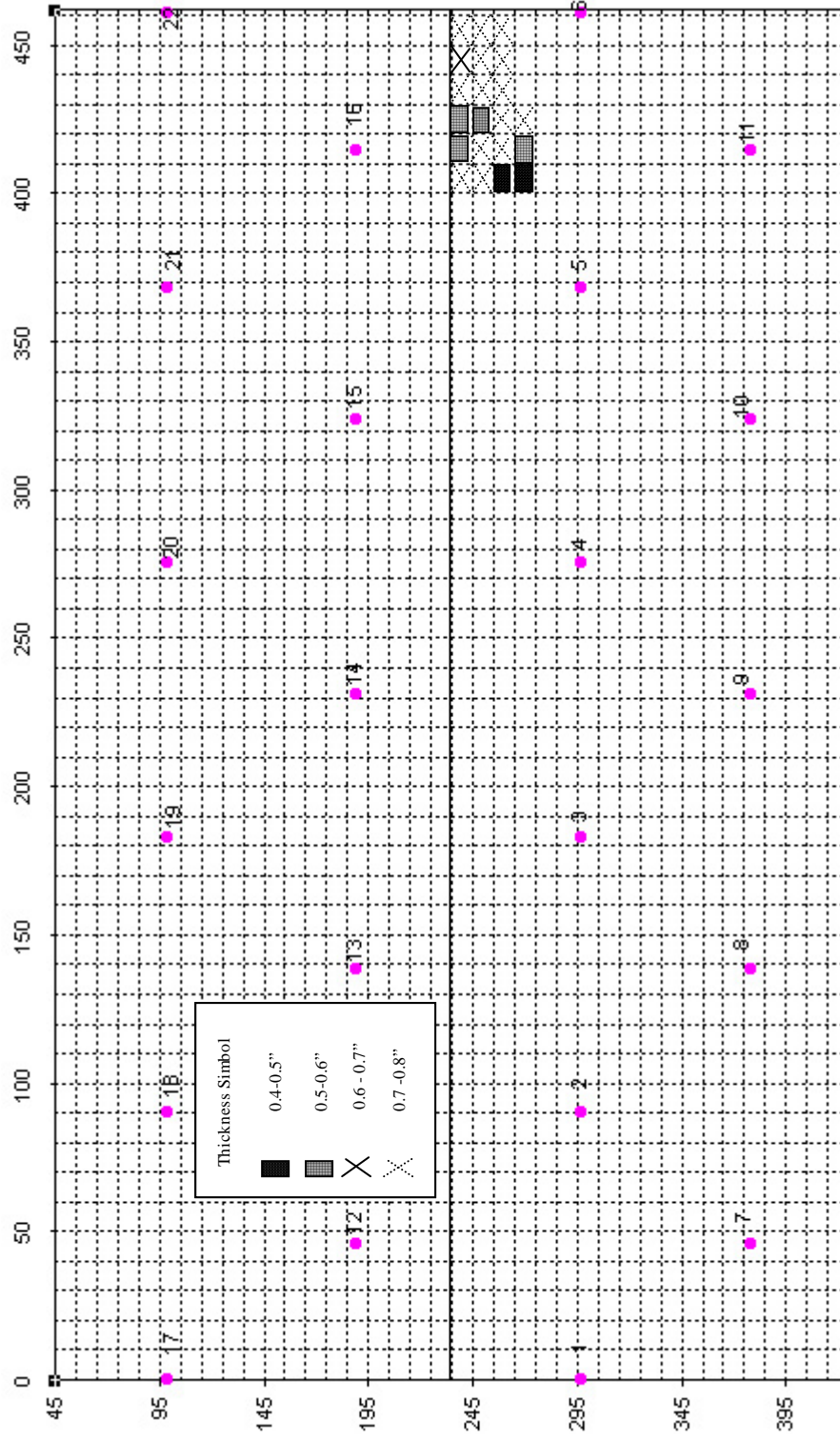


Figure 4.26 - Final Results



Figure 4.27 – Ultrasonic Testing on Top of the A End





Note: Nominal Thickness = 0.8125" Figure 4.28 - Results from Ultrasonic Inspection

## 4.6 TWIST BAR TEST

### 4.6.1 Test Procedure

A twist bar test is one of the standard tests in the AAR procedure. The objective of the twist bar test is to detect defects from the draft sill including the sill pad areas. To apply a torsional load to the bottom area of the tank car, a twist bar is positioned under the sill and a jack is used to apply an eccentric upward vertical load through the twist bar twisting. The test setup is shown in Figure 4.29.

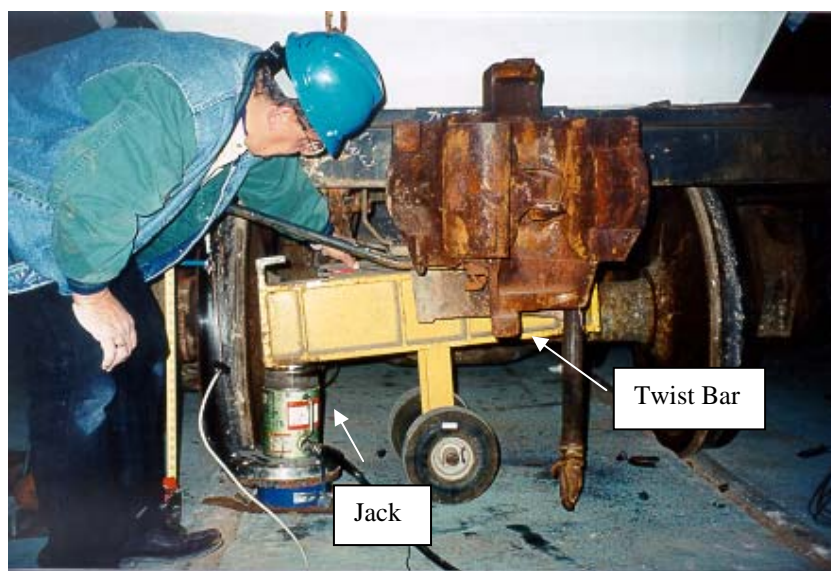


Figure 4.29 – Twist Bar Test

The typical loading schedule for the twist bar test is shown in Figure 4.30. At the beginning of the test, a background noise monitoring period is required to confirm there is no interference with the AE signals. Then the jack is lifted to 0.6” for a full tank car or 1.2 inches for an empty tank car. The load is held for 4 minutes at this deflection. For this test program, a load hold was conducted longer than 4 minutes to obtain as much emission as possible. As in the previous tests, emission was monitored during the load hold periods, but not during loading.

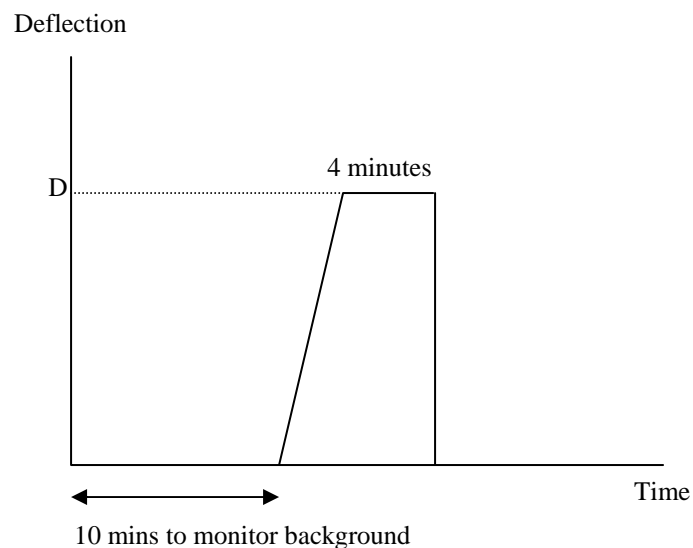


Figure 4.30 – Load Schedule for a Twist Bar Test

#### 4.6.2 Test Results

This section discusses test results from two twist bar tests. Both tests were conducted at the B end. The first test was with the jack positioned on the right

side of the sill. The second test was performed by moving the jack to the left side of the sill. After applying the twist load, another jack was used to raise the right bolster so as to provide more torsional load to the bottom area of the tank car.

- *Results from Twist Bar at BR*

In this test, a jack positioned on the right side of the sill was raised to one inch and the deformation was held for 45 minutes. AE monitoring was performed during that time. Unfortunately, in this test there was a random hardware error on 6 channels, which are channels 3, 4, 15, 16, 19 and 20. The error was a high frequency interference to signals from these six channels. Therefore, the source location analysis avoids using these six channels. Results from the combinations of three sensors are presented in Figure 4.31, while Figure 4.32 shows the final results. It is seen that most of the emissions came from the middle of the bottom of the tank car or from the known flaw at the top of the car. For the emissions at the bottom of the car, the results from combinations of three sensors in Figure 4.31 are more scattered. This is due to the hardware problem with channels 19 and 20, which are close to the defects. As noted above, the analysis did not include these two channels.

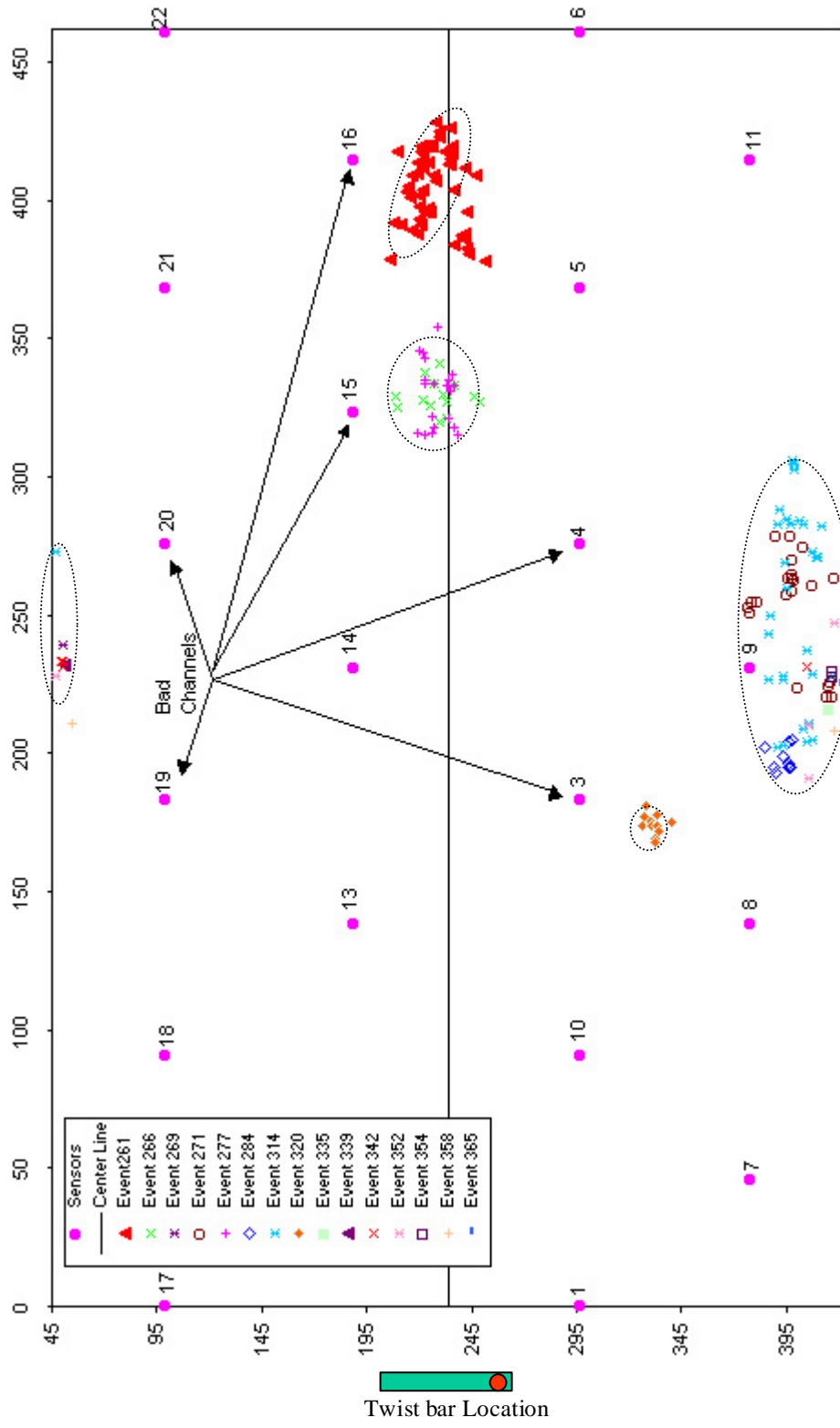


Figure 4.31 - Results from Combination of Three Sensors from the Twist Bar Test at BR

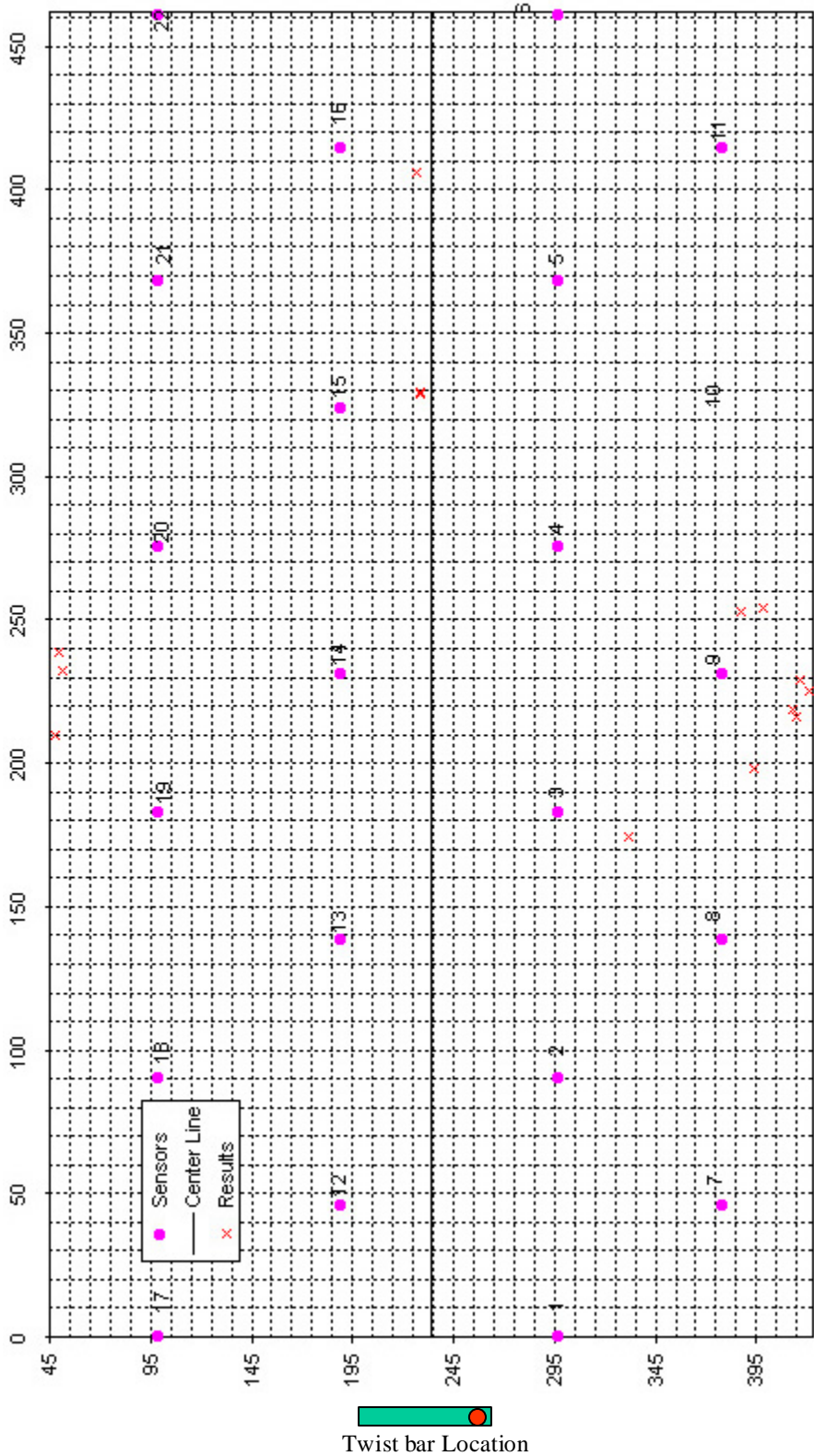


Figure 4.32 - Final Results from Twist Bar Test at BR

- *Results from Twist Bar at BL*

In this section, two tests were performed. First, a jack was positioned on the left side of the twist bar and the jack was raised to one inch and the deformation was held for an hour. AE monitoring was conducted during this load hold, unfortunately the data obtained suffers from the same hardware error that occurred in the previous test. Accordingly, it is difficult to analyze the data since the zone of defects was close to channels 19 and 20. The results for this part of the test are not discussed here.

Another jack was used to raise the right bolster on the same end while the load from the BL twist bar was still being applied. The bolster jack was raised to 1 inch and the load was held for 15 minutes. In this test, the hardware error was no longer a problem. The location results from the combinations of three sensors are shown in Figure 4.33 and the final results are presented in Figure 4.34.

The results from both twist bar tests show that most of the emission came from the middle of the bottom area of the tank. The results from the twist bar test at BL with a BR bolster jacking show that some emission also came from the area close to Sensor 6. The later area had had a bar welded to the tank car shell, which had been used in another test. The bar was removed before the jacking and twist bar tests, leaving a fractured weld on the tank. The location of the bar on the tank is shown in Figure 4.35. It is likely that the fractured weld created emission during the twist bar tests.

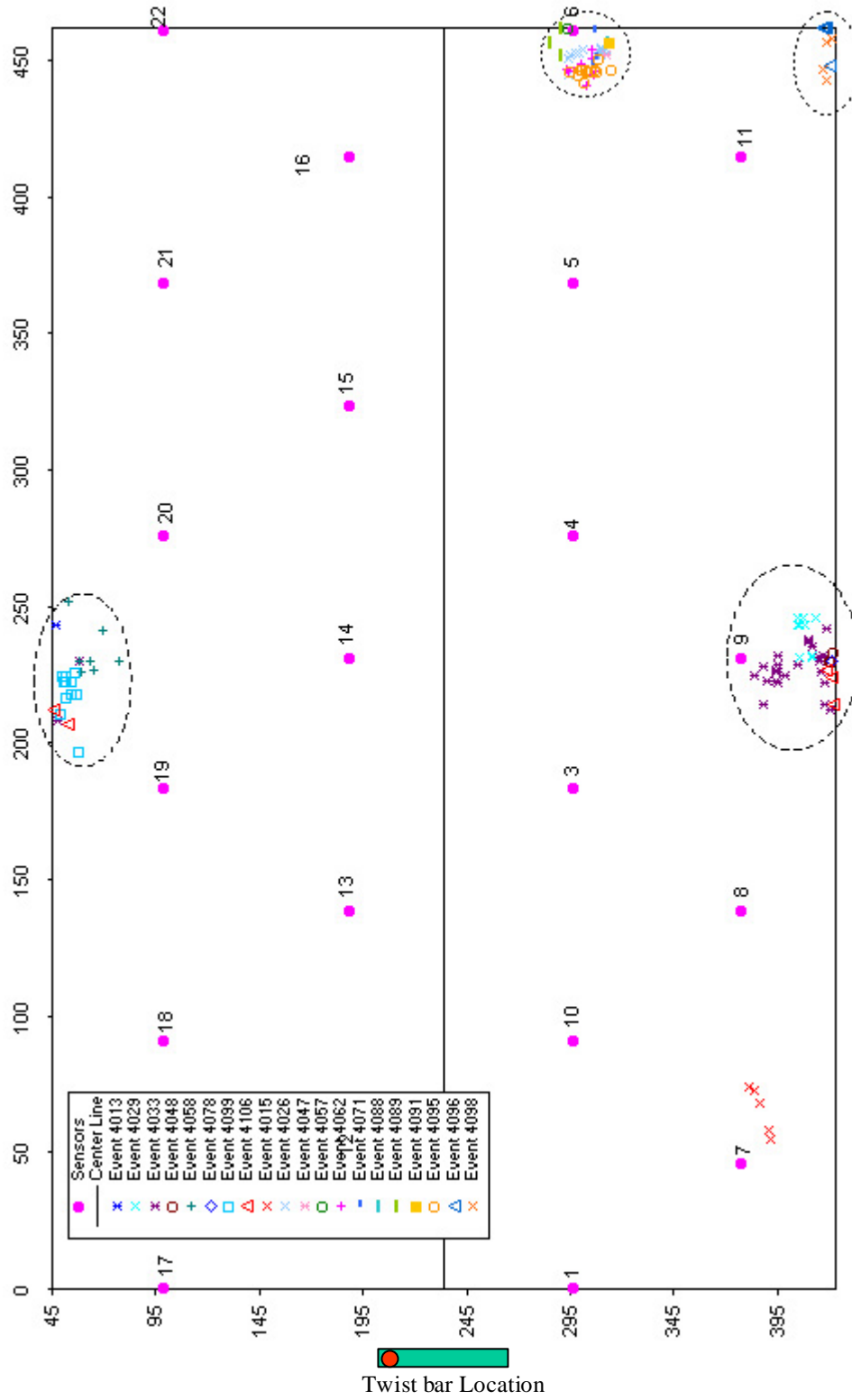


Figure 4.33 - Results from Combinations of Three Sensors from the Twist Bar Test



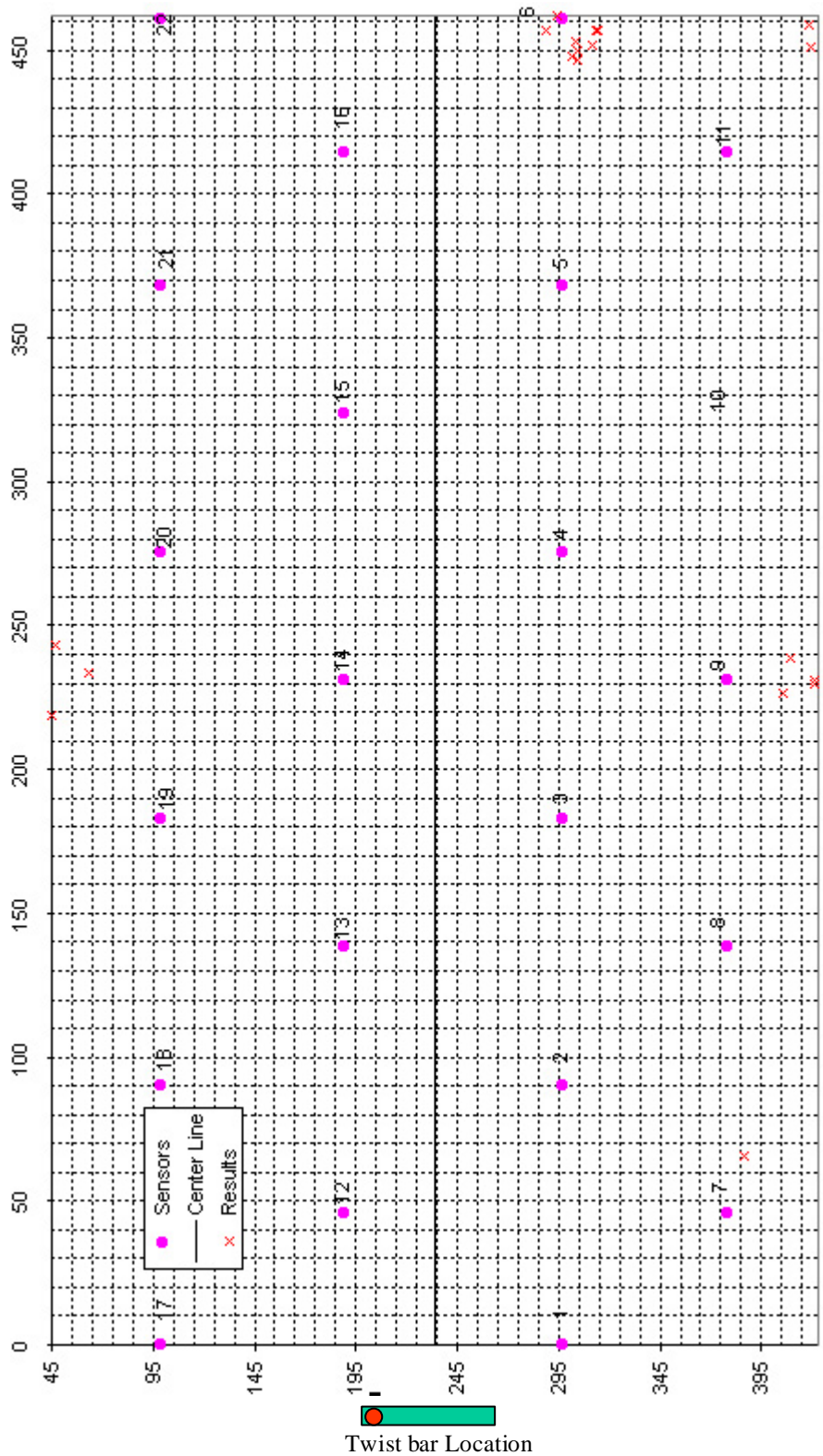


Figure 4.34 - Final Results from Twist Bar Test at BL and Jack at BR

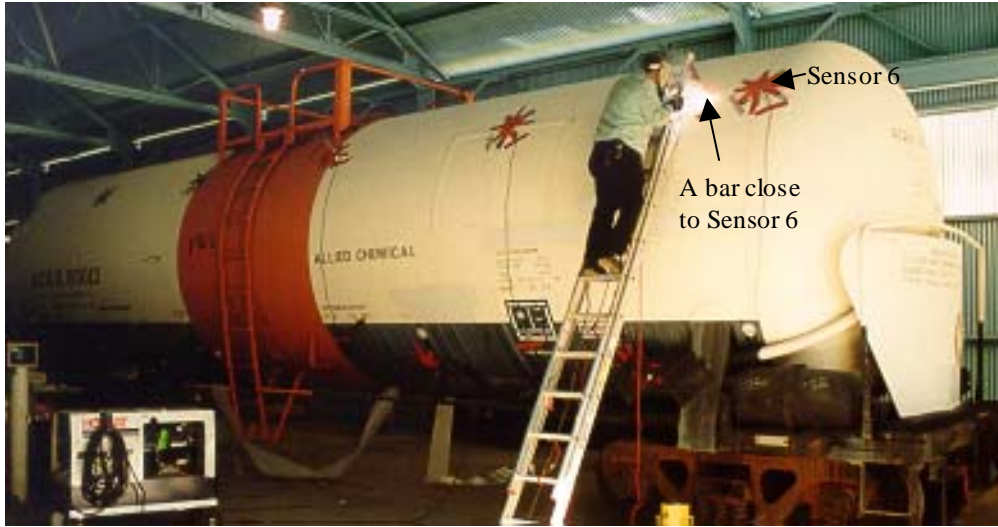


Figure 4.35 – Locations of the Bar

#### 4.7 SUMMARY

In this Chapter, a new search algorithm for a large cylindrical structure, and the use of the combinations of three sensors are developed. The procedure can be summarized below:

1. Select sensors used for source location analysis ( $N$  = number of sensors selected)
2. Calculate numbers of combinations of three sensors ( $n$ ):
$$n = \frac{N!}{(N-3)!3!}$$
3. Apply simplex optimization to each combination with four wave routes
4. Eliminate the answers with high Flag value

5. Eliminate the redundant paths
6. Eliminate the out of group answers coming from the sensors that do not cover the area of the source
7. The final result is the average of the grouped results from the right combinations of three sensors

Another benefit of the method is that the multiple-source problem is minimized. Every combination which includes the sensor receiving the signal from another source will yield an answer out of the group. That sensor can be removed the analysis.

Prior to this study, this tank car was inspected using other methods of nondestructive testing. The tank was found to be in very bad condition and had been removed from service. Cracks, blisters and internal corrosion were found inside the shell. This variation of shell thickness caused by corrosion and the delamination caused by blistering lead to wave mode conversion and variations in the wave velocity when filtered over a tight band frequency range. In this source location analysis, a constant velocity at the intersection of the group velocity of the first three modes for a 13/16 inches thick shell was used. This assumption leads to errors in the analysis, due to the variation in thickness. For this reason, the results from the simplex optimization calculations of the combinations of three sensors did not always give identical positions for the same source. In addition, the area of internal damage is relatively large and the results are grouped in this area, which makes it easier for the follow up inspection. Location results from the tests correspond well with the locations of a crack and of a fractured weld.

An interesting observation from the crack growth AE data is that it has different characteristic than the rest of the data. Data obtained from the BL

jacking test has high amplitude and long duration. This appears to be due to multiple hits registered as the same hit. This phenomenon is often referred to as overlapping hits. Once the data was band-pass filtered, it is difficult to define arrival time based on the peak. This is because there are many peaks in the wave package. It is also seen that this crack growth signal generated high energy in the lowest order symmetric mode, therefore the beginning of the wave can be seen clearly. Source location was performed successfully based on the initial portion of this wave mode.

## **CHAPTER 5**

### **PRELIMINARY STUDY OF SOURCE LOCATION ON WATER FILLED TANK CARS**

#### **5.1 INTRODUCTION**

The previous two chapters describe source location on an empty tank car. Promising results were obtained using an approach based on a narrow band frequency at the intersection point of the first three modes of the plate waves. This chapter reports experiments on liquid filled tank cars. In this case, water was used to fill the tank. The water inside the tank has a tremendous effect on the wave propagation. The use of pencil lead breaks to test a large area of the tank is almost impossible due to the low the energy generated by the source and the high attenuation caused by the liquid inside the tank. The bar bending technique described in Section 3.2 is an effective method of generating an artificial source, and is used in the study.

This chapter demonstrates that the same source location approach developed earlier for the empty tank cannot be applied to a liquid filled tank. A new source location approach using the low frequency signal was developed instead. The studies were performed on two tank cars, the 15/32" thick tank car located at the Ferguson Laboratory and the 13/16" thick tank car located at the Rescar facility in Orange, Texas. A new source location approach and the results from the bar bending are presented in this chapter.

## 5.2 ARTIFICIAL SOURCE

Two types of artificial sources were used for the preliminary wave propagation study on the tank car shell. The first is a center punch shown in Figure 5.1. The approximate overall length of the punch is 6 inches. The signal produced by this type of source has very high energy and is good for wave propagation studies in a highly attenuating specimen. An example of the AE signal generated by a center punch is shown in Figure 5.2. In the figure, the signal was captured by a R15I sensor 36 inches from the source. The amplitude of the signal is approximately 4.5 volts, which can be converted into 93 dB. It is seen that the signal generated by this type of source has high amplitude and energy.

The other type of artificial source used in the program was generated by the bar bending method described in Section 3.2.



Figure 5.1 - Center Punch

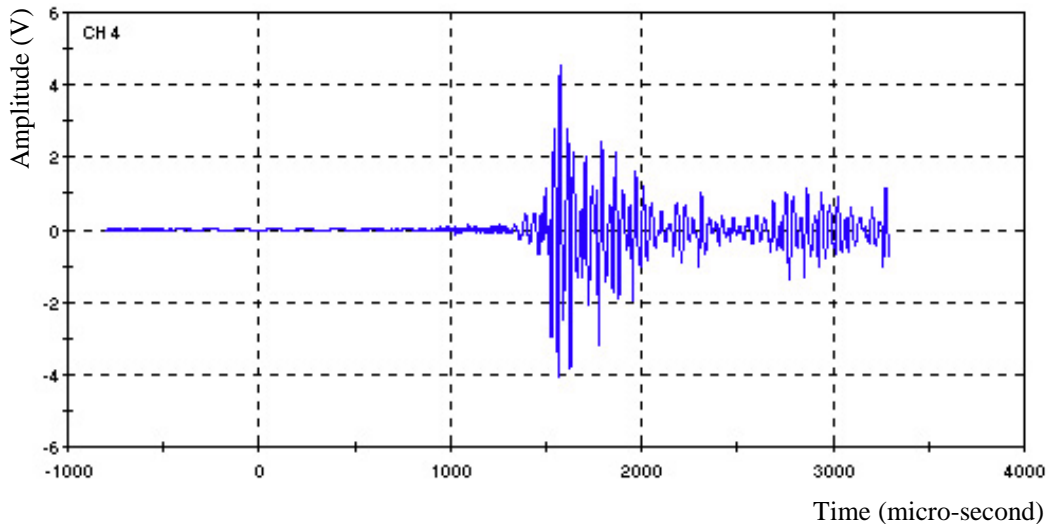


Figure 5.2 - Waveform from Center Punch Captured by R15I Sensor

### 5.3 SOURCE LOCATION STUDIES ON A TANK CAR WITH 15/32" INCH THICK WALL

#### 5.3.1 Instrument and Specimen

Except that the specimen was filled with water, the instrument and specimen used in this study are the same as these described previously in Section 3.3. The AE monitoring system was the MISTRAS system with wide band sensors. The coupling and attachment between the sensors and the tank shell were provided by vacuum grease and magnetic holdowns. The tank was in good condition, was located at the Ferguson Laboratory, and had a 15/32" thick wall.

### 5.3.2 Attenuation Test

An attenuation test was performed using a center punch. The test setup is shown in Figure 5.3. The first punch was performed one inch from the sensor and subsequent punches were performed every 9" except the 10<sup>th</sup> break is one inch from the previous break since it is the location of the vertical weld. In the test, both a wide band sensor and a R15I sensor were used.

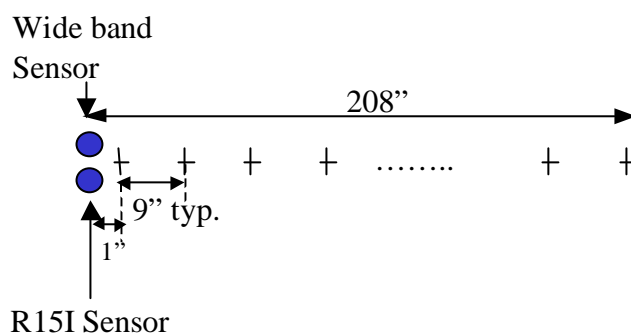


Figure 5.3 - Test Setup for Attenuation Test on Filled Tank

The attenuation results are plotted in Figure 5.4. It was found that the attenuation rate is much higher in the full tank compared to the empty tank (see Section 3.3.3). From the results shown in Figure 5.4, the attenuation curve is not smoothly decreasing and fluctuates as the source is moved further away. This might be from the effect of the water inside the tank. Additional studies of the effect of the signal traveling through the water will be reported later in this chapter.



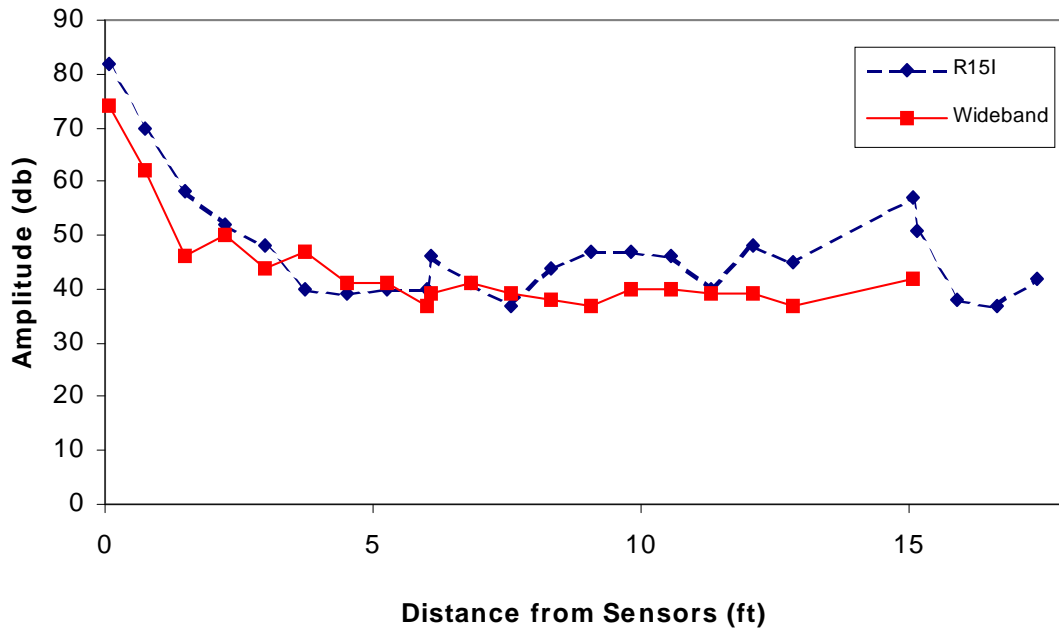


Figure 5.4 - Attenuation Curve for Water Filled Tank

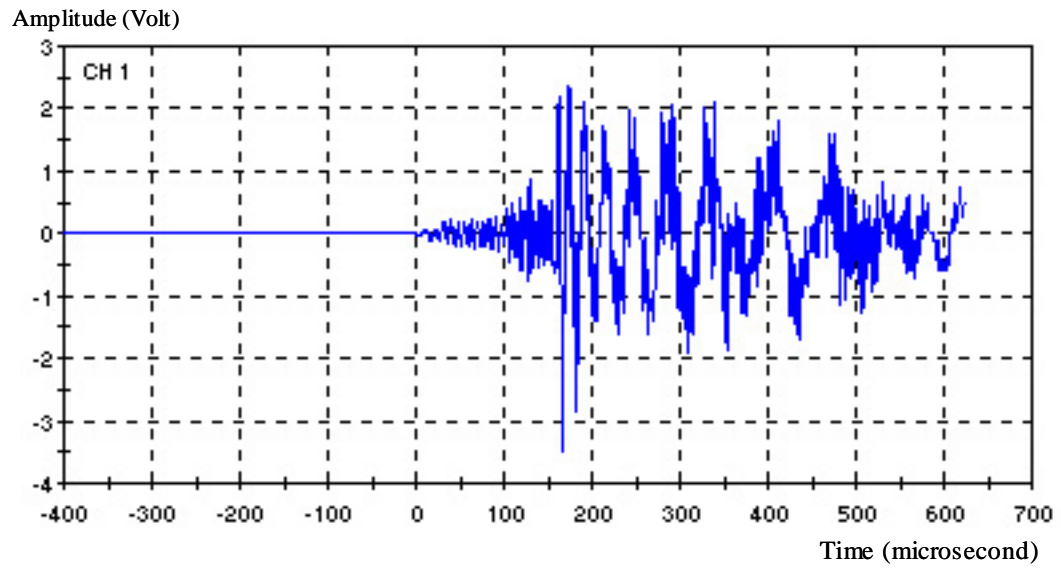
The attenuation results from Figure 5.4 show that when the source is less than 3 feet from the sensors, the resonant sensor is almost 10 dB more sensitive than the wide band sensor. At 3 to 7 feet, the wide band sensor is more sensitive than the resonant sensor. This is because high frequencies attenuate and only low frequencies can travel far through the shell. Wide band sensors can detect low frequency range waves whereas a hardware filter in the resonant sensor makes it impossible to capture low frequency range waves. Once the source is further away, the resonant sensor performs better. This could be because of the reflection of the water waves. More studies on the water borne wave are discussed later in the chapter.

### **5.3.3 Source Location Approach Using Narrow Band Frequency at the Intersection of the Group Velocity of the First Three Wave Modes**

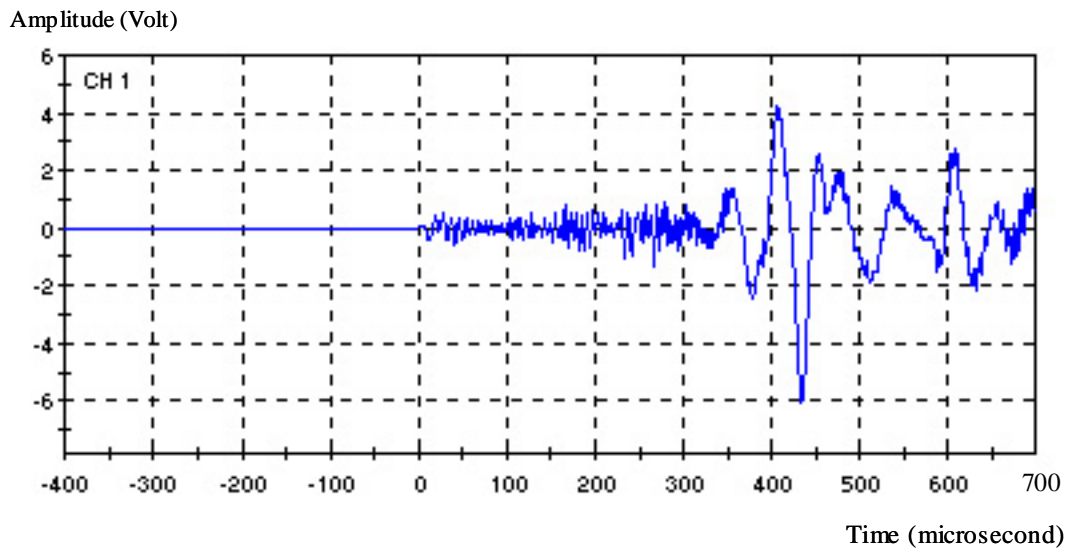
The first attempt to solve the source location problem on the liquid filled tank was the same approach used successfully with the empty tank. Figure 5.5a and Figure 5.5b show waveforms captured by wide band sensors on the empty and liquid filled tank. The signals were generated from bending a steel bar at the same location on the empty and full tank. In both cases, the sensors were placed 51” from the bars.

In Figure 5.5, the amplitude of the signal obtained from the empty tank is approximately 3.5 Volts, while the amplitude of the signal from the full tank is approximately 6.0 Volts. A Bessel type band-pass filter was applied to these waveforms over the frequency range of the intersection of the group velocity of the first three modes. In this case, a 145-155 kHz band-pass filter was used. The results are shown in Figure 5.6. It is seen that although the original signal on the water filled tank has higher amplitude, the extracted signal in the frequency range of 145-155 kHz has a much lower amplitude compared to the filtered signal from the empty tank. Also, there are three peaks in the wave package and it is confusing to define the arrival time of the peak or the beginning of the signal in the water filled tank.

In source location analysis, defining the arrival time corresponding to the wave velocity is the most important step. In the water filled tank, it is hard to define the arrival time since the 145-155 kHz signal range has low energy when the sensor is away from the source



a) Empty Tank



b) Water Filled Tank

Figure 5.5 – Waveform from Bar Bending

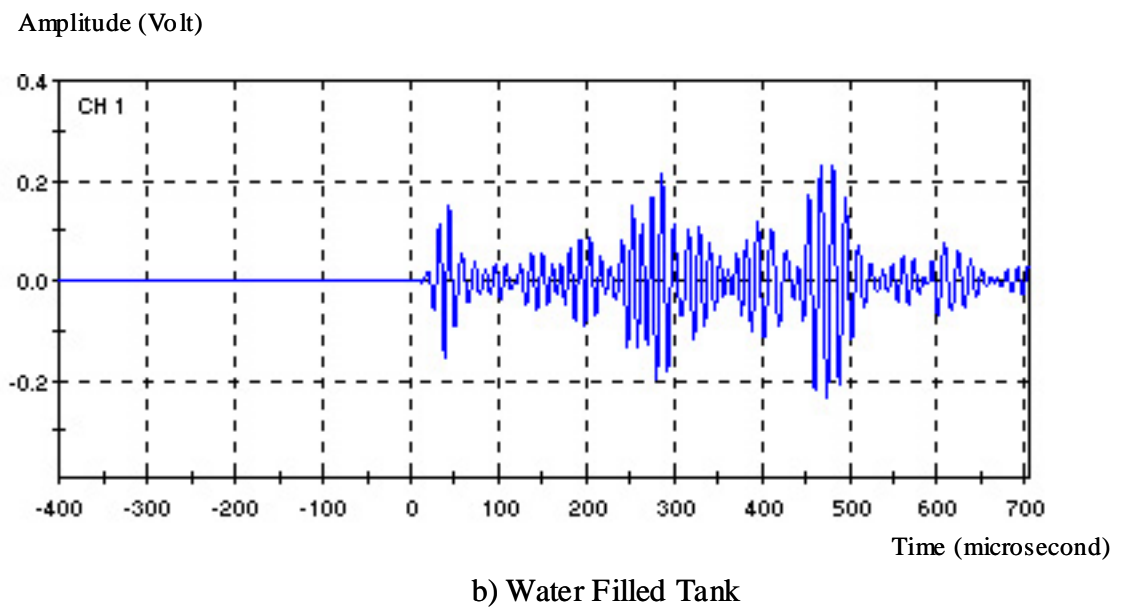
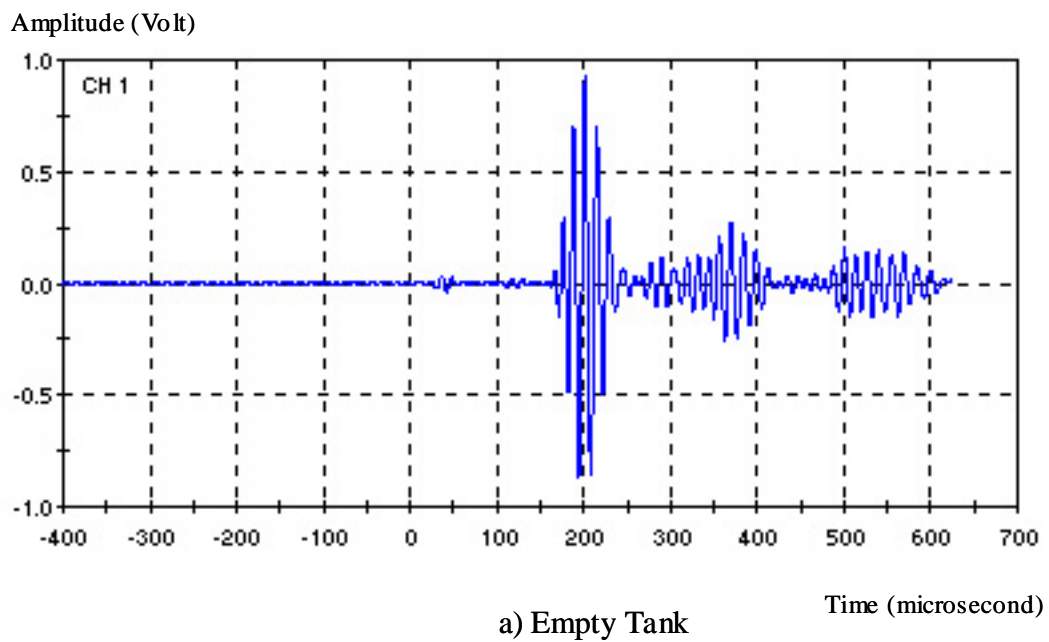


Figure 5.6 – Filtered Signal (145-155 kHz)

### 5.3.4 Source Location Approach for a Water Filled Tank car using Non Leaky Lamb Waves

#### 5.3.4.1 Background in Leaky/Non Leaky Lamb Waves

When a plate wave travels in a specimen, its energy always leaks out into the adjacent medium unless the specimen is tested in a vacuum. This phenomenon results in attenuation of the signal. In the previous study on an empty tank car, the tank shell was bounded by air, which has low impedance ( $Z$ ) compared to water. Table 5.1 shows the amount of energy transmitted through a boundary by a wave traveling in steel impinging on the interface with air or water.

Boundary Medium	Impedance ( $Z$ ) (lb/in <sup>2</sup> -sec)	Percentage of Energy Transmitted
Air	0.6	$6.6 \times 10^{-5}$
Water	2,382	24

Table 5.1 – Energy Transmitted through Air and Water Interfaces with Steel

The literature review in Chapter 2 (Section 2.2.5) shows that the angle of the leak energy ( $\theta_{leak}$ ) is dependent on the velocity in water and the phase velocity of plate waves in the tank shell. It shows that if the velocity in water is higher than the phase velocity in the steel, there is no energy transmitted into the water. This phenomenon can be used for modeling source location. Note that although, at the low frequency range, the Scholte-Stonley wave propagates along the surface between the water and the steel plate, an acoustic emission sensor is not able to detect this type of wave because the sensor is placed on the outer surface

of the tank shell [Cheeke, et all. 1998]. Therefore, the Scholte-Stoney waves are not included in the analysis.

The phase velocity of the first 3 modes for a 15/32” thick steel shell is shown in Figure 5.7. A detail of the phase velocity plot at low frequencies (0 to 100 khz) comparing the speed of the shell and water waves is presented in Figure 5.8.

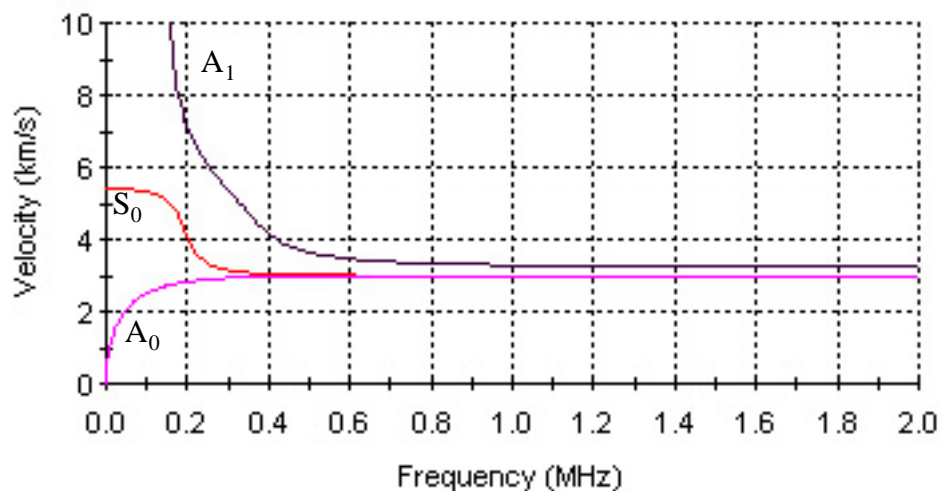


Figure 5.7 - Phase Velocity Dispersive Curve [PolyModal, 1998]

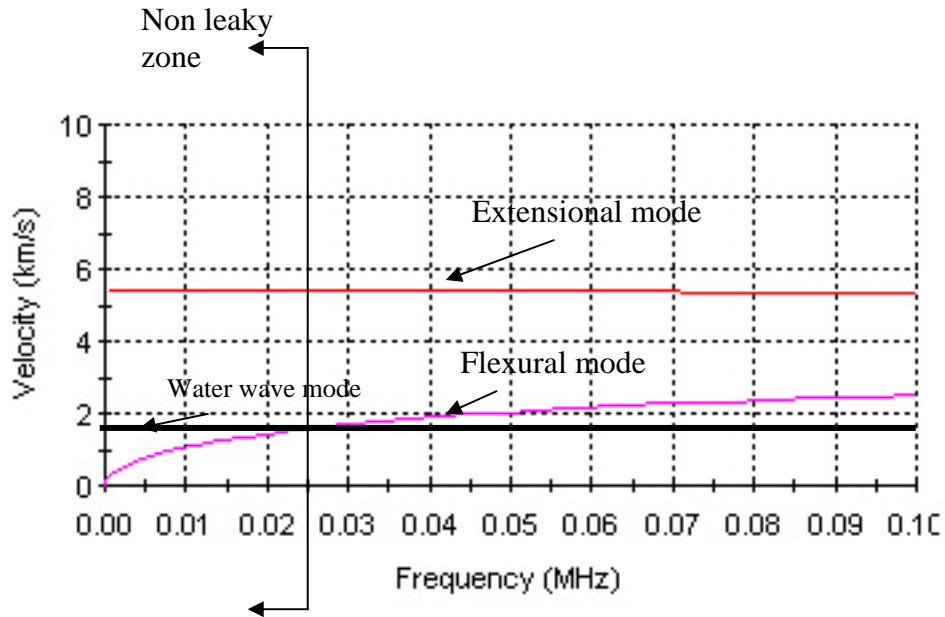


Figure 5.8 - Phase Velocity Dispersive Curve from 0 to 100 KHz Comparing Shell and Water Wave Velocity [PolyModal, 1998]

Since the motion of the lowest order symmetric mode is in the axial direction, very little energy leaks into the water from this mode. The water layer will have an impact on the lowest order anti-symmetric mode. In Figure 5.8, the velocity of the water wave is higher than the phase wave velocity of the plate below 25 kHz. The value is dependent on the type and thickness of the plate material. Below 25 kHz, the energy does not leak into the water. Therefore, this low frequency range can be used for source location.

#### 5.3.4.2 *Source Location Approach Based on Non-Leaky Part*

Section 5.3.3 shows that in the frequency range at the intersection of the group velocity of the first three modes (145-155 kHz) the waves have low energy at a relatively short distance from the source. This makes it difficult to be consistent in defining the arrival time of the filtered signal. The reason that the high frequency signal has low energy, is that most of the high frequency energy leaks into the water. Therefore, the source location approach outlined below focuses on a narrow band signal at a lower frequency which does not leak into the water.

From the dispersion curve in Figure 5.9 it is seen that at a very low frequencies (less than 50 kHz), the first mode, or lowest order symmetric mode, travels at a much higher speed than the second mode, or lowest order anti-symmetric mode. At this low frequency, the third mode does not exist. An example of the original signal detected by a wide band sensor and a filtered with a narrow band filter at 15-25 kHz is shown in Figure 5.10.

From Figure 5.10, it can be seen that at the low frequency, the first mode does exist but at a much lower energy. This helps define the time of arrival. Source location on the liquid filled tank can be performed based on the second mode at 15-25 kHz. The theoretical velocity at that frequency range is 2.1 km/sec (82,600 in/sec). The location algorithm used is the same one (simplex optimization) used in Chapter 3 to solve the problem on the empty tank.



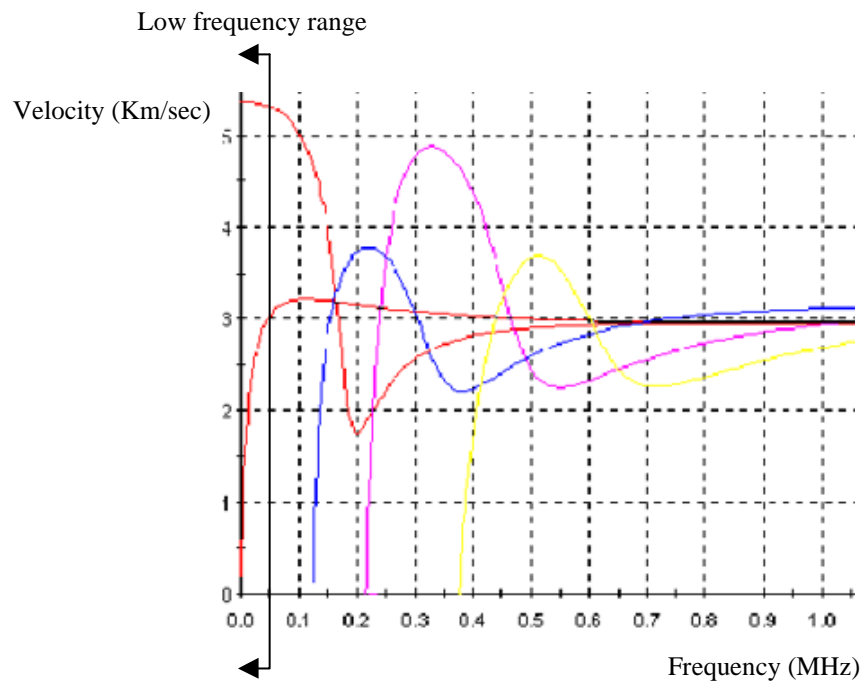
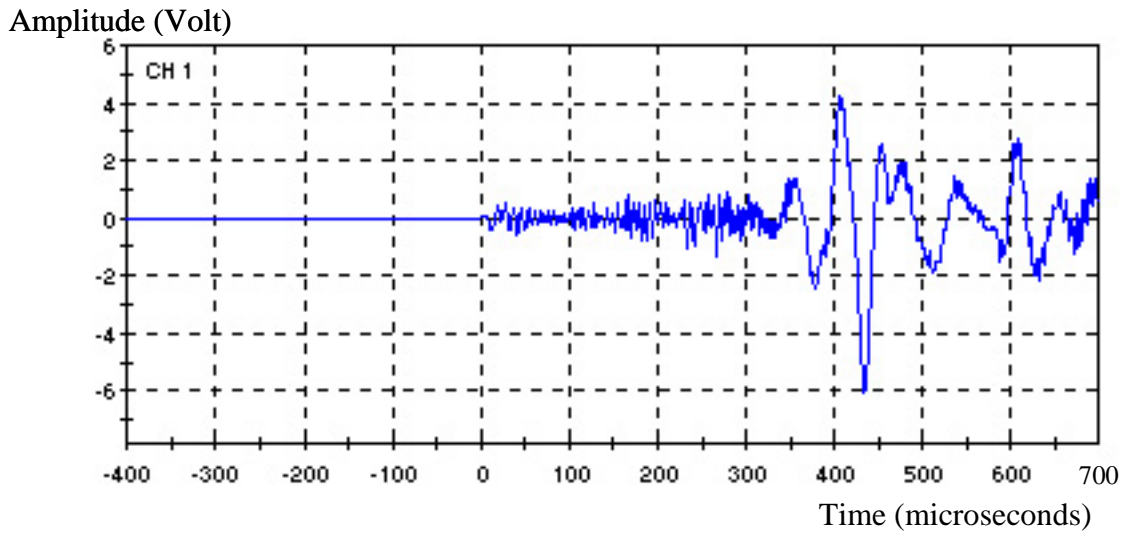
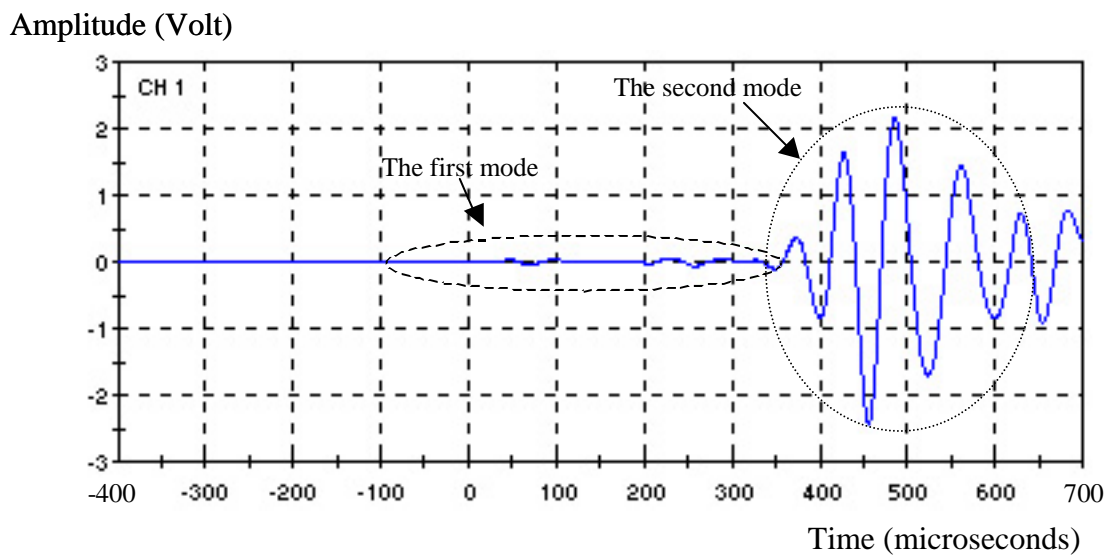


Figure 5.9 – Group Velocity Dispersive Curve



a) Original Signal from Wide Band Sensor



b) Signal with Narrow Band Pass Filter at 15-25Khz

Figure 5.10 – Signal from Bar Bending on the Full Tank

### 5.3.5 Velocity Measurement

Pencil lead breaks cannot be used as an effective artificial source on the water filled tank car due to high attenuation of the signal. A center punch was used as an artificial source to measure the velocity of the signal. Two wide band sensors were placed 4 inches apart and the center punch was applied every one inch away for 45 points. The test setup is shown in Figure 5.11.

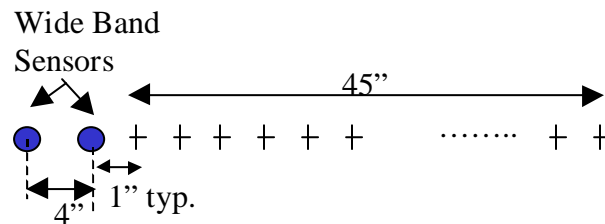


Figure 5.11 - Test Setup for Velocity

Two methods were used to calculate the wave velocity using the known distance between the two sensors. First, the wave velocity was calculated based on the first threshold crossing method. Second, a 15-25 kHz band-pass filter was applied to the signal. The arrival time of the filtered signal was determined as the median of the negative and positive peaks as discussed in Chapter 3.

The velocity results are shown in Figure 5.12. It can be seen that the velocities based on the first threshold crossing technique are not consistent compared to the ones calculated from the filtered narrow band signal. The average velocity of the 15-25 kHz signal is 82,638 inch/sec. This is very close to the theoretical value of 82,600 inch/sec (see Section 5.3.4.2). The velocity used in the source location calculation is the theoretical value of 82,600 inch/sec.

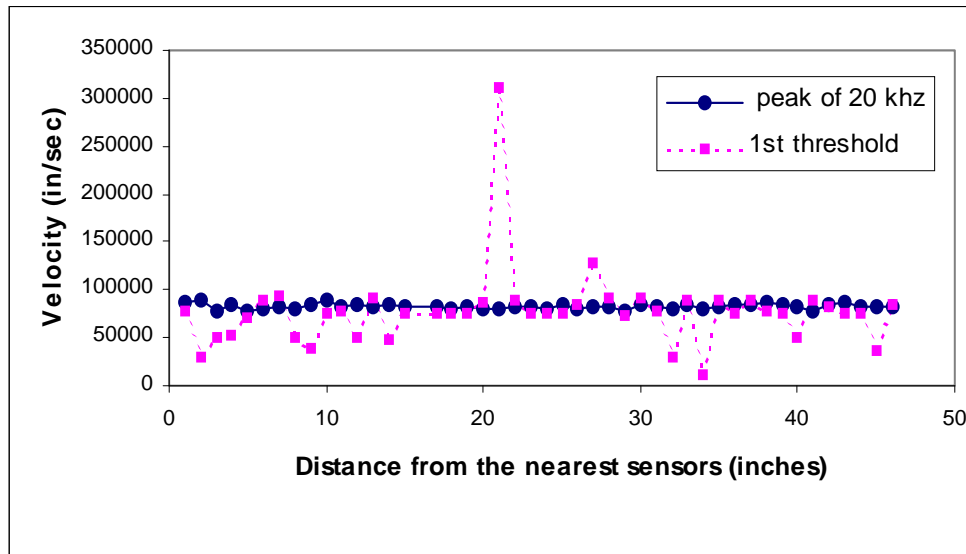


Figure 5.12 - Velocity Results of 15-25 KHz Signal on Water Filled Tank

The velocity results from the first threshold crossing technique yield lower value results than the results obtained from the empty tank (see Section 3.3.4.2.3). This is because the signal obtained from the full tank is comprised of low frequency waves since high frequency range attenuates into the water. The preset threshold defines the arrival time of the low frequency signal of the second wave mode. This results in a lower value of the velocity.

### 5.3.6 Results from Bar bending

Several bar bending tests were performed on the liquid filled tank in order to test the accuracy of the source location approach. The first test was performed on a small area (3ft x 3.75ft) with no discontinuities. The second test was monitored over a bigger area. The third, fourth, and fifth tests were performed on

an area with discontinuities. The last test was in the area that included the bolster. This section presents the results obtained from these tests

For the bar bending tests, the threshold was set at 45 dB and the sampling rate was set at 1 MHz. Data were recorded for a period of 1 millisecond. The delay time was set at 400 microseconds. For the source location analysis, the simplex optimization method was used with a step value of 0.1”.

- *Bar Bending in a Small Area*

Due to the concern about the severe attenuation with the full tank car, the first bar bending test was monitored over a small area (3 ft x 3.75 ft) with no discontinuity. The bar bending generated 830 hits. The amplitude of the hits ranged from 45 to 81 dB. The hits were grouped as 334 events. Most events did not strike all the sensors and only 4 were locatable. The results of the locatable events are presented in Figure 5.13. The maximum error from the test was 1.6” and the average error was 1.2”

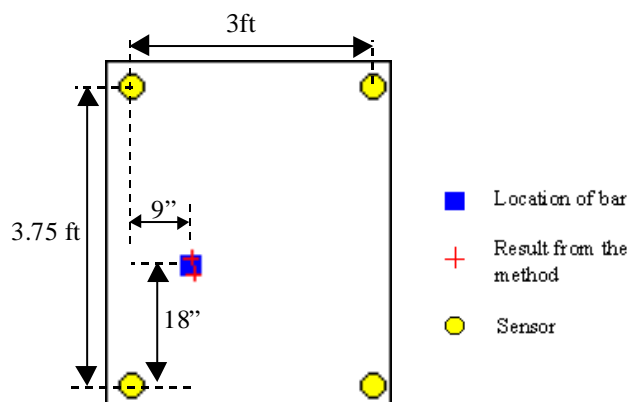


Figure 5.13 - Results from Bar Bending in a Small Area

From the test, few hits are locatable. This is an inherent problem with source location [Fowler, 1984] .

- *Bar Bending in an Area with no Discontinuity*

The second bar bending test was performed on a bigger area (6ft x 6ft) with no discontinuities. In this test, a bar was welded in the middle of the area enclosed by four sensors. A total of 942 hits were obtained. The amplitude of the hits ranged from 45 to 96 dB. The hits were grouped as 270 events, of which only 3 were locatable. The results of the locatable events are shown in Figure 5.14. The maximum error from the test was 1.8” and the average error was 1.5”

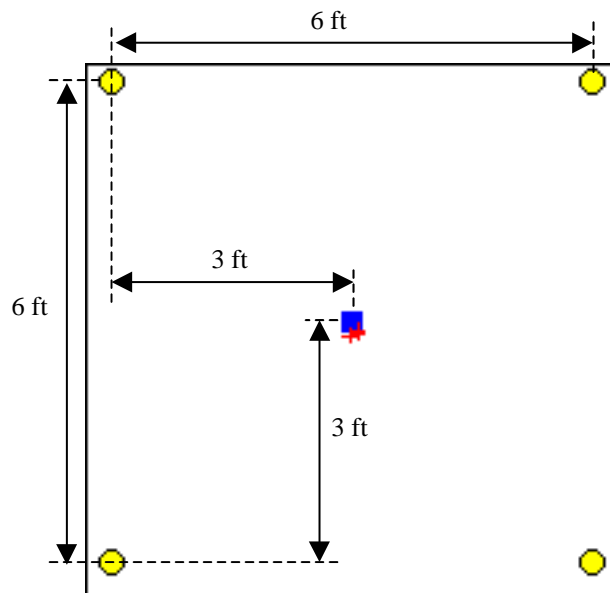


Figure 5.14 - Results from Bar Bending in an Area with no Discontinuities

- *Bar Bending in an Area with a Vertical Weld*

After obtaining good results from the area with no discontinuities, another bar bending test was performed in an area that included a vertical weld. The area bounded by the four wide band sensors was 6.83 ft x 6.75 ft.

In this test, a total of 348 hits were captured. The amplitude of the hits ranged from 45 to 70 dB. The hits were grouped as 77 events. Only 4 were locatable. The location results from the test are shown in Figure 5.15. The dotted line represents the vertical weld. The maximum error was 3.7" and the average error was 3.4".

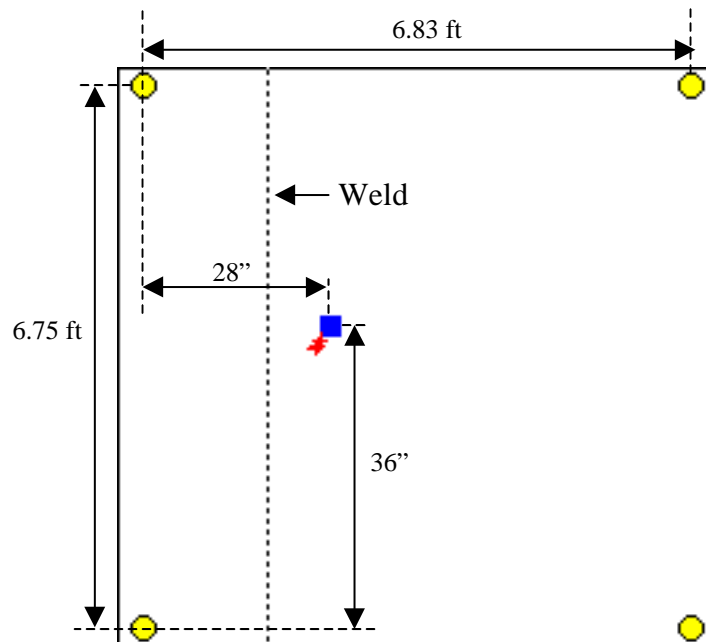


Figure 5.15 - Results from Bar Bending in an Area with a Vertical Weld

- *Bar Bending in an Area with Vertical and Horizontal Welds*

This test covered an area with vertical and horizontal welds. The area enclosed by the four sensors was 6.83 ft x 8.33 ft. A total of 219 hits were recorded. The amplitude of the hits ranged from 45 to 68 dB. The hits were grouped as 34 events, of which only 5 were locatable. The location results are shown in Figure 5.16. The maximum error was 1.22” and the average error was 0.9”

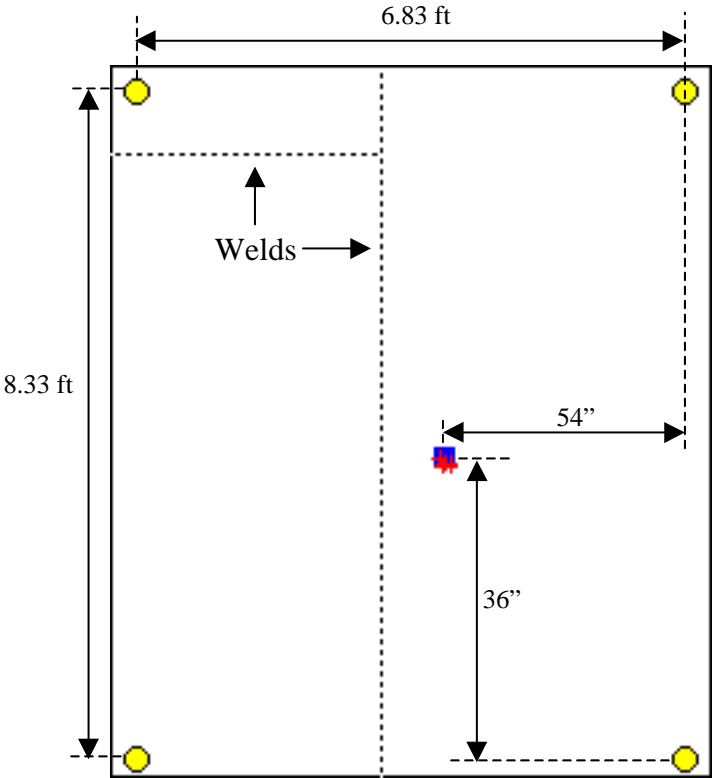


Figure 5.16 - Results from Bar Bending in an Area with Vertical and Horizontal Welds



- *Bar Bending in a Large Area*

Another bar bending test was performed in a large area on the tank body. The area included welded attachment clips for the ladder. The area covered by the sensors was 9ft x 9ft. A total of 562 hits were recorded and the amplitude of the hits ranged from 45 to 98 dB. The hits were grouped as 101 events, of which only three were locatable. The location results are presented in Figure 5.17. The maximum error was 4.3" and the average error was 2.2"

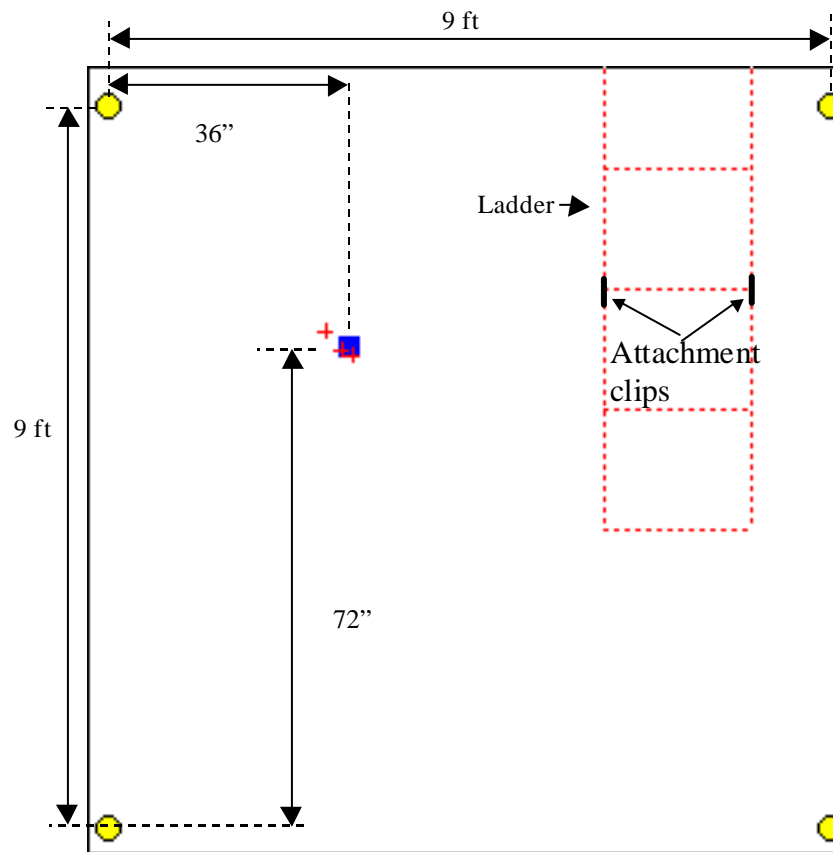


Figure 5.17 - Results from Bar Bending in a Large Area

- *Bar Bending in a Bolster Area*

The last bar bending test was carried out in one of the bolster areas. A bar was welded next to the bolster pad. The area bounded by the four sensors covered 3.75 ft x 5.25 ft. A total of 1783 hits were captured and the amplitude of the hits ranged from 45 to 92 dB. The hits were grouped into 371 events, of which 13 were locatable. The location results are shown in Figure 5.18. The maximum error was 3.8" and the average error was 3.3".

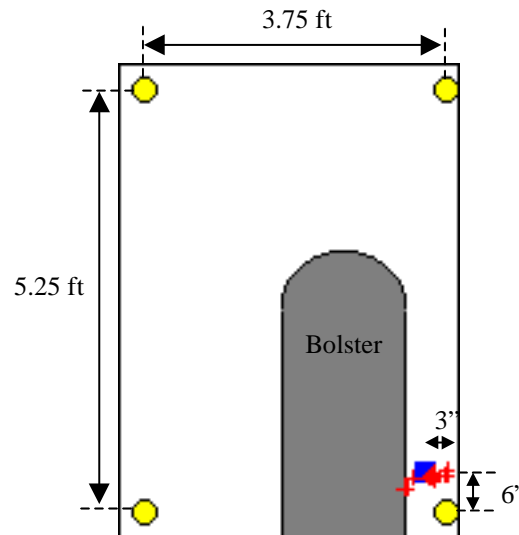


Figure 5.18 - Results from a Bar Bending in the Bolster Area

### 5.3.7 Conclusion

The research shows that water inside the tank car has a significant effect on plate wave propagation. It is important to mention again that the sensors used

in the tests are wide band. These sensors are capable of capturing signals at very low frequency but the sensitivity at higher frequency is not as good as with resonant sensors. Resonant sensors are unlikely to be used at the 15-25 kHz frequency. The lowest frequency resonant sensor sold by the principal supplier of acoustic emission equipment is 60 kHz. Below 60 kHz they use accelerometers. The problem with a resonant sensor is that it is too bulky at the low frequency. A wide band sensor is a damped resonant sensor. Accordingly it is relatively insensitive, as can be seen in Figure 2.2.

This work focuses on the low frequency signal, since the low frequency signals do not radiate the energy into the water. Also, due to high attenuation of high frequency signals, signals that are filtered in the range of the intersection of the group velocity are almost impossible to use since the signal has very low energy. This makes it very difficult to identify the peak amplitude for time of arrival determination. A complication with the signal in the low frequency range is that there are two different modes and they travel at different speeds. Fortunately, the first mode (lowest symmetry mode) travels much faster than the second (lowest anti-symmetry) and has a much lower energy content than the second mode. Therefore, it was possible to perform source location on the second mode in the low frequency range. The results from the bar bending sources are promising but the number of locatable hits is very low. The number of locatable events was as low as 1% of the total events. In no case, was it above 15%. The number of locatable hits would be higher if only three sensors were used in the analysis.

The drawback of using the low frequency signal is that there is likely to be interference from background noise in a real field test. This was not a problem in the bar bending tests performed in the Ferguson Laboratory since it is a controlled environment and there was no other load on the tank. Also, in order to capture

waves in this low frequency range, the transducers used in the tests were wide band sensors. In a field test it would be better to use an accelerometer which would provide greater sensitivity. Even though accelerometers are used for low frequency, such as micro-seismic applications, they cannot be used in tank car applications because the evaluation criteria are based in emission in the 100 to 200 kHz range.

## **5.4 SOURCE LOCATION STUDIES ON A TANK CAR WITH 13/16 INCH THICK WALL**

### **5.4.1 Introduction**

The tank car used in this study is the car described previously in Section 3.4. The tests on this tank car were performed as part of a field test in a tank car repair shop at Orange, Texas. The objective of the study is to develop a source location approach that can be used practically in field tests. A source location method based on the low frequency non-leaky wave was developed in the previous section. This method shows good accuracy, but for two reasons, the method is not practical to use in full scale field tests. First, there is likely to be interference from the background noise in the low frequency range. Second, the sensors that can capture a low frequency signal for source location and a higher frequency signal for structural evaluation are wide band sensors, which have low sensitivity compared to resonant sensors.

For the 15/32" thick tank discussed in Section 5.3 the first three wave modes have the same group velocity at 150 kHz. At this frequency the attenuation of the wave is large. In the thicker 13/16" thick tank discussed in this section the first three modes have the same group velocity at 100 kHz. At this lower frequency, the attenuation is not as great and it may be positive to use a 100 kHz resonant sensor. The purpose of this section is to explore that possibility.

Section 5.4.2 details the instrument used in these studies. Attenuation data for the full tank are shown in Section 5.4.3. A source location method using a higher range frequency is explored and the results from bar bending tests are reported in Section 5.4.4. A study of water borne waves and results from a bar

bending test used to illustrate the behavior of water borne waves are discussed in Section 5.4.5.

#### **5.4.2 Instrumentation**

A DISP 24 channel digital system was used for AE monitoring of jacking and bar twist tests. 24 R6I sensors were with 22 sensors mounted on the tank body and one on each head. All sensors were attached to the tank with duct tape and vacuum grease was used to provide coupling between the tank and the sensor.

#### **5.4.3 Attenuation Test**

An attenuation test, similar to that described in Section 5.3.2 was performed on this tank. For this test, only one sensor, an R6I, was used. A pencil lead break was performed at 4 inches from the sensor, followed by a lead break at 9 inches from the sensor and then in increments of 9 inches for a total of 13 breaks points. The results of amplitude versus distance of the source from the sensor are plotted in Figure 5.19.

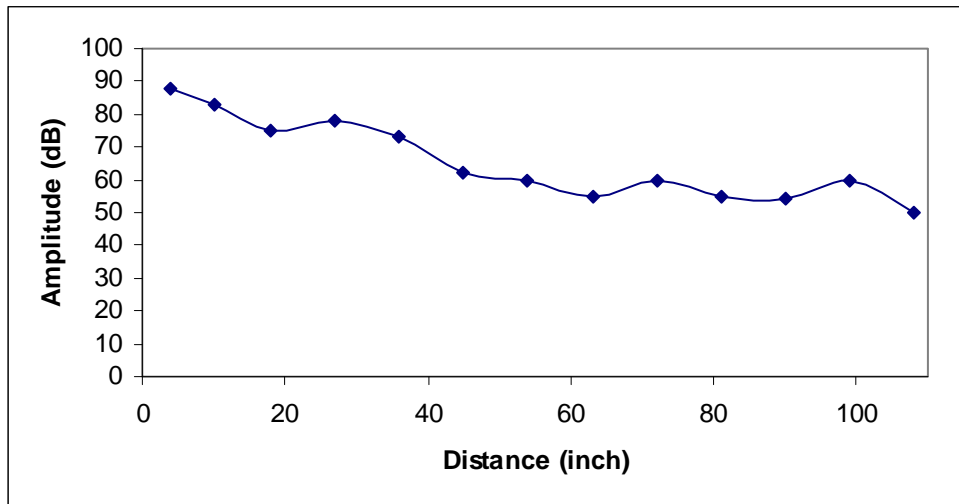


Figure 5.19 – Attenuation on a Water Filled Tank Car

#### 5.4.4 Source Location Analysis and Results from Bar Bending Approach

- *Source Location Analysis*

R6I sensors, which have their first resonance close to 100 kHz (see Figure 2.2) were used for this test. The source location approach based on low frequency waves that was described in Section 5.3 is not applicable for this test. Therefore, water borne waves become significant and the analysis of the source location problem is more complicated.

In this study, source location is approached through the shell paths. A frequency of 100 kHz is selected in the study since this frequency gives the same group velocity for the first three modes. This is shown in Figure 5.20. As was the case in Section 4.3, a velocity of 125,000 in/sec was used for the analysis. The three sensors technique (see Section 4.3) using simplex optimization with a step

value of 1" is used to locate the position of the source. With this method, the water borne signal is eliminated. The concept of eliminating the water borne signal is the one used in example #2 in Section 4.3.2 for minimizing the multiple source problem. An important feature of this approach is the use of a resonant sensor which has higher sensitivity than a wide band sensor. Therefore, the resonant sensor is able to capture the higher frequency component with higher amplitude.

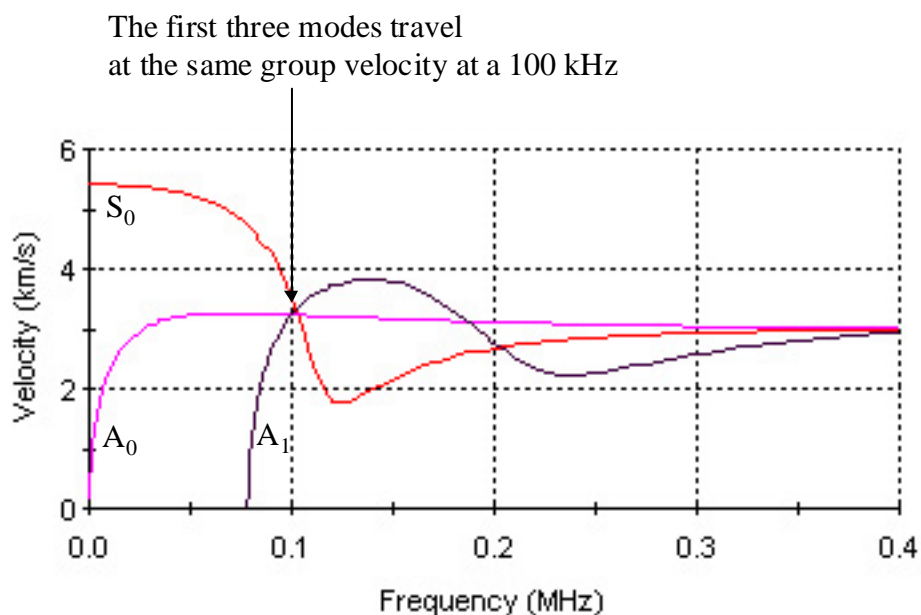
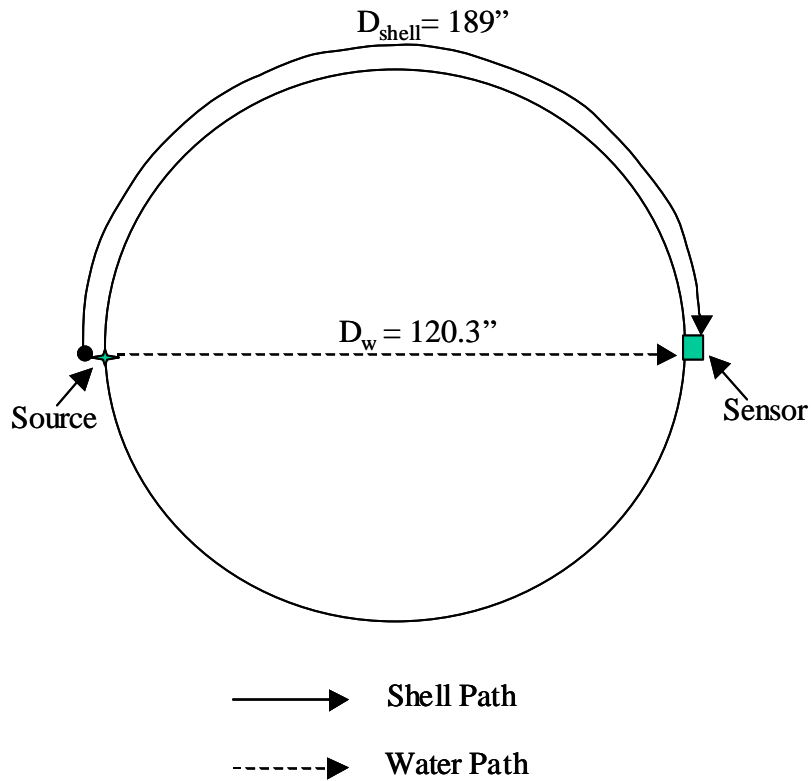


Figure 5.20 – Group Velocity of 13/16" Thick Tank Car Shell

As mentioned before, the frequency value used in the analysis is 100 kHz. At this frequency, the wave travels at 125,000 in/sec. Water waves travel at a speed of 60,000 in/sec. Therefore, if attenuation is not a problem, the first waves to arrive at a sensor will always be through the shell path rather than



through the water. A simple calculation for wave propagation through the shell and water is shown in Figure 5.21. Note that the diameter of the tank is 120.3”.



$$\text{Time the source takes to propagate through the shell} = \frac{189}{125,000} = 0.001512 \text{ Sec.}$$

$$\text{Time the source takes to propagate through water} = \frac{120.3}{60,000} = 0.002005 \text{ Sec.}$$

Figure 5.21 – Wave Propagation Time Through Shell and Water

- *Results from Bar Bending Approach*

Five bar bending tests were performed on the water filled tank. The locations of the bars, labeled A through E and the sensors are shown in Figure 5.22. The bar bending results in high energy signals and, even though part of the signal leaks into the water as it propagates in the shell, the amplitude is still above the threshold when it reaches many of the sensors. Thus the first wave reaching the sensor will travel along the shell path.

The first bar was welded at location A (see Figure 5.22). Sensor 9 was placed next to the bar to capture the arrival time at the source. This sensor is not used in the source location analysis. It is, however, used to study the water borne wave as discussed in Section 5.4.5. In this test, the bar was difficult to break resulting in more AE events than previous bar bending tests. A total of 13,133 hits were obtained from bending the bar. These hits were grouped as 753 events of which 33 were locatable using the shell path analysis. The results from the test are presented in Figure 5.23. The maximum error was 15" and the average error was 8".

The second bar was welded at location B (see Figure 5.22). A total of 4,708 hits were obtained from bending the bar. These hits were grouped as 184 events of which 6 were locatable. The results from the test are presented in Figure 5.24. The maximum error was 10" and the average error was 4".

The third bar was welded at location C (see Figure 5.22). A total of 3,689 hits were obtained from bending the bar. These hits were grouped as 133 events of which 8 were locatable. The results from the test are presented in Figure 5.25. The maximum error was 7" and the average error was 5".

The fourth bar was welded at location D (see Figure 5.22). A total of 4,049 hits were obtained from bending the bar. These hits were grouped as 146

events of which only 3 were locatable. The results from the test are presented in Figure 5.26. The maximum error was 6" and the average error was 5".

The last bar was welded at location E (see Figure 5.22) next to a bolster. A total of 13,613 hits were obtained from bending the bar. These hits were grouped as 835 events of which 12 were locatable. The results from the test are presented in Figure 5.27. The maximum error from the results was 7" and the average error was 5".

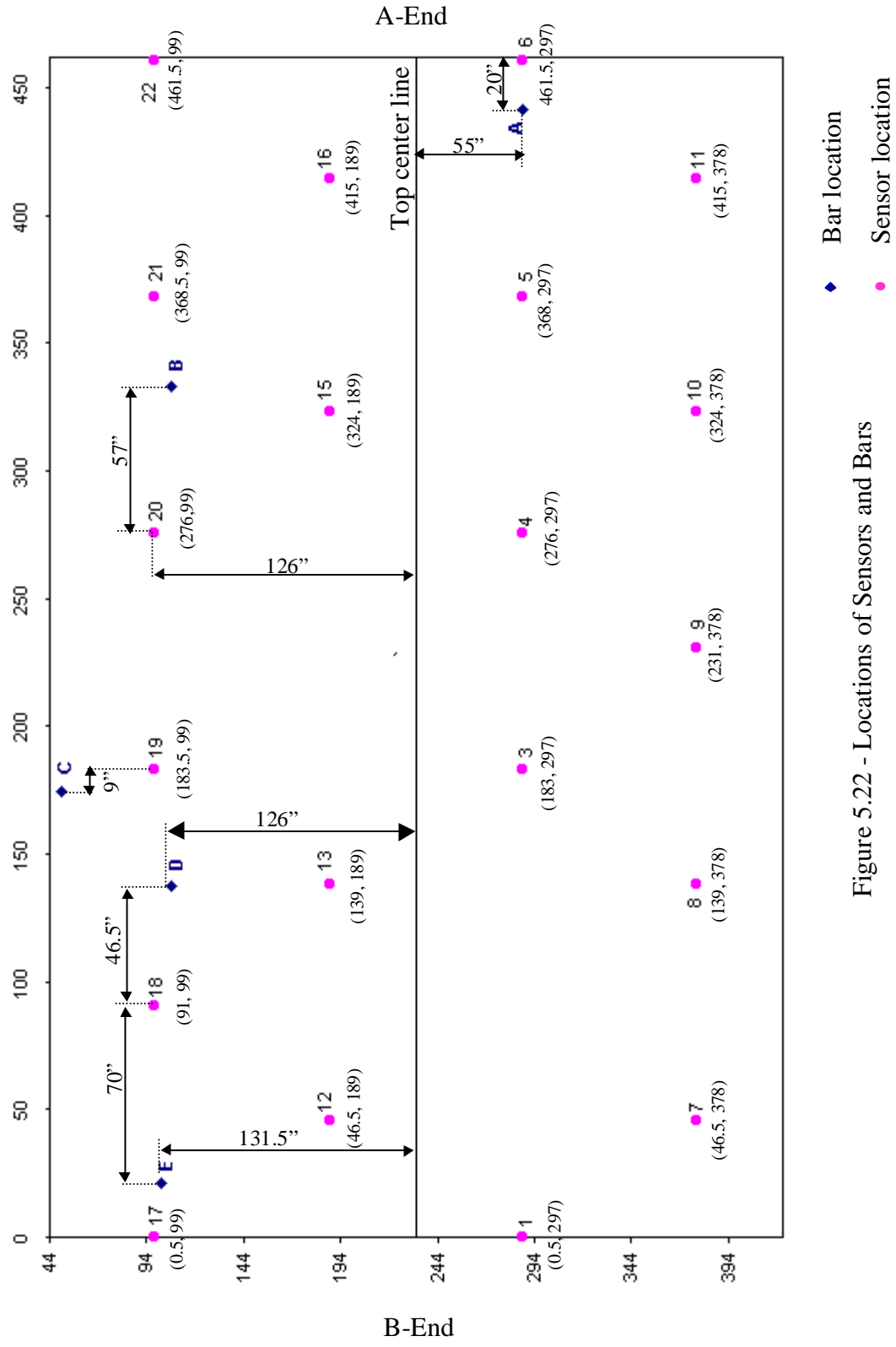


Figure 5.22 - Locations of Sensors and Bars

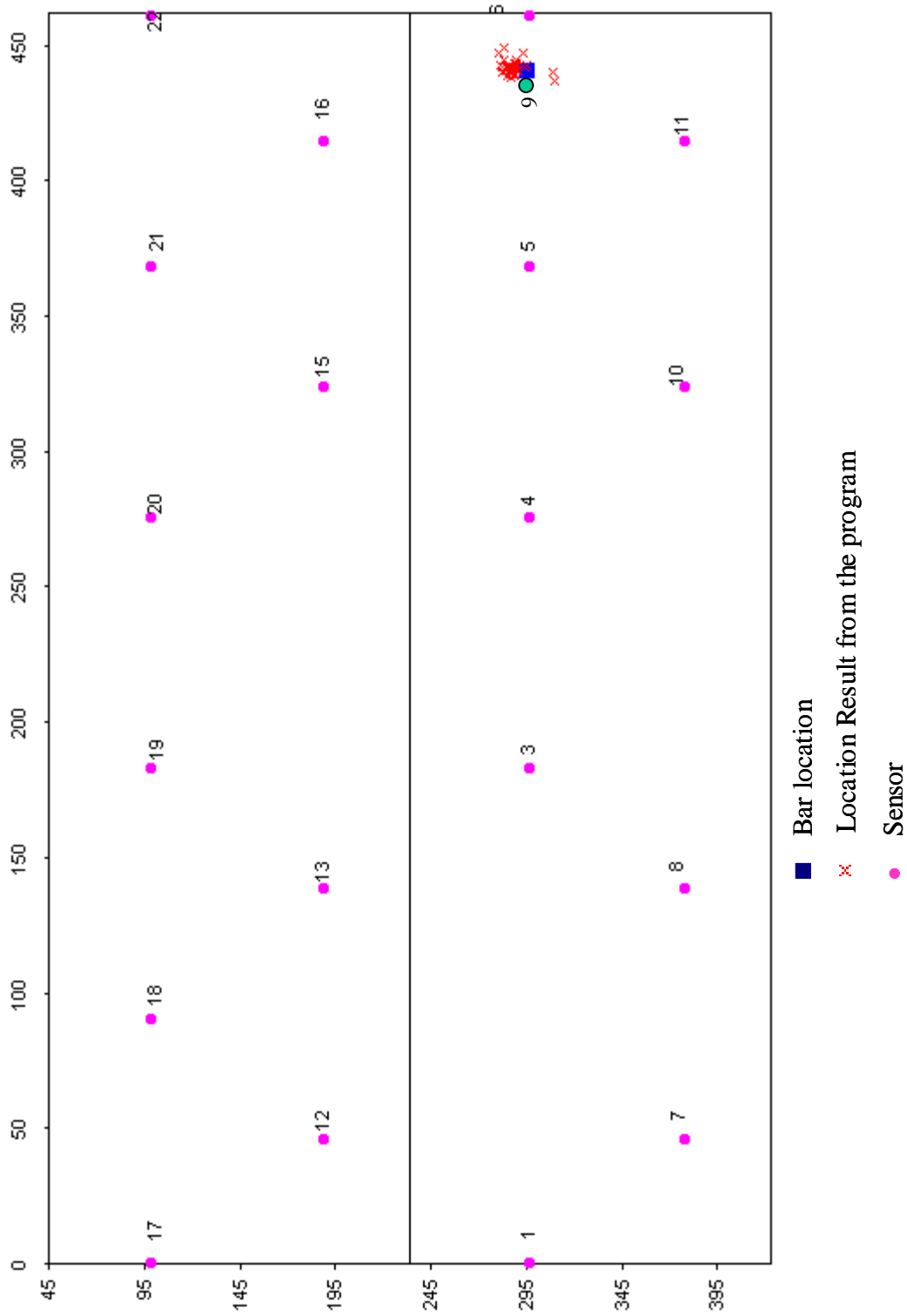


Figure 5.23 - Results from a Bar Bending Test at Location-A

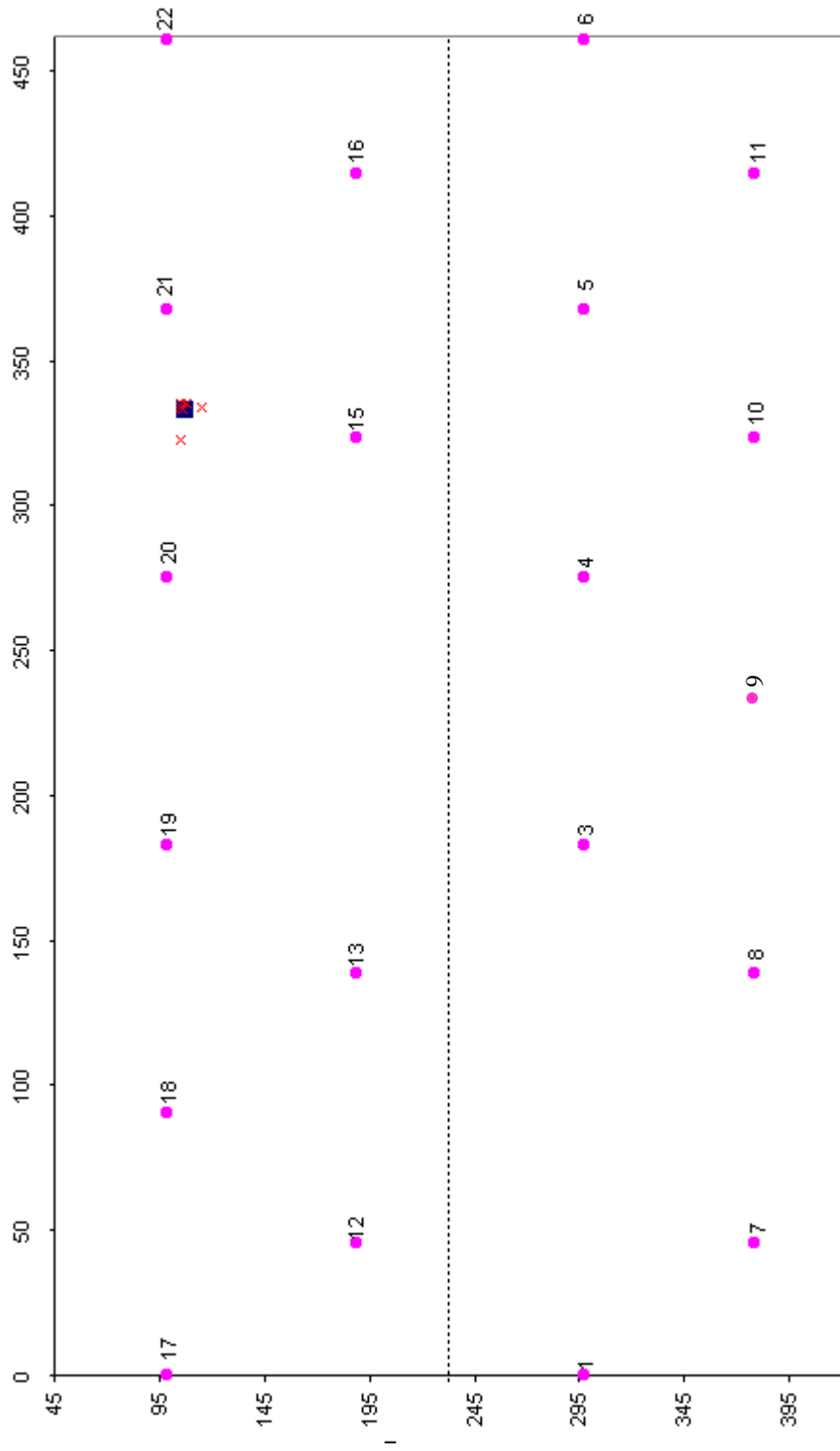


Figure 5.24 - Results from a Bar Bending Test at Location B

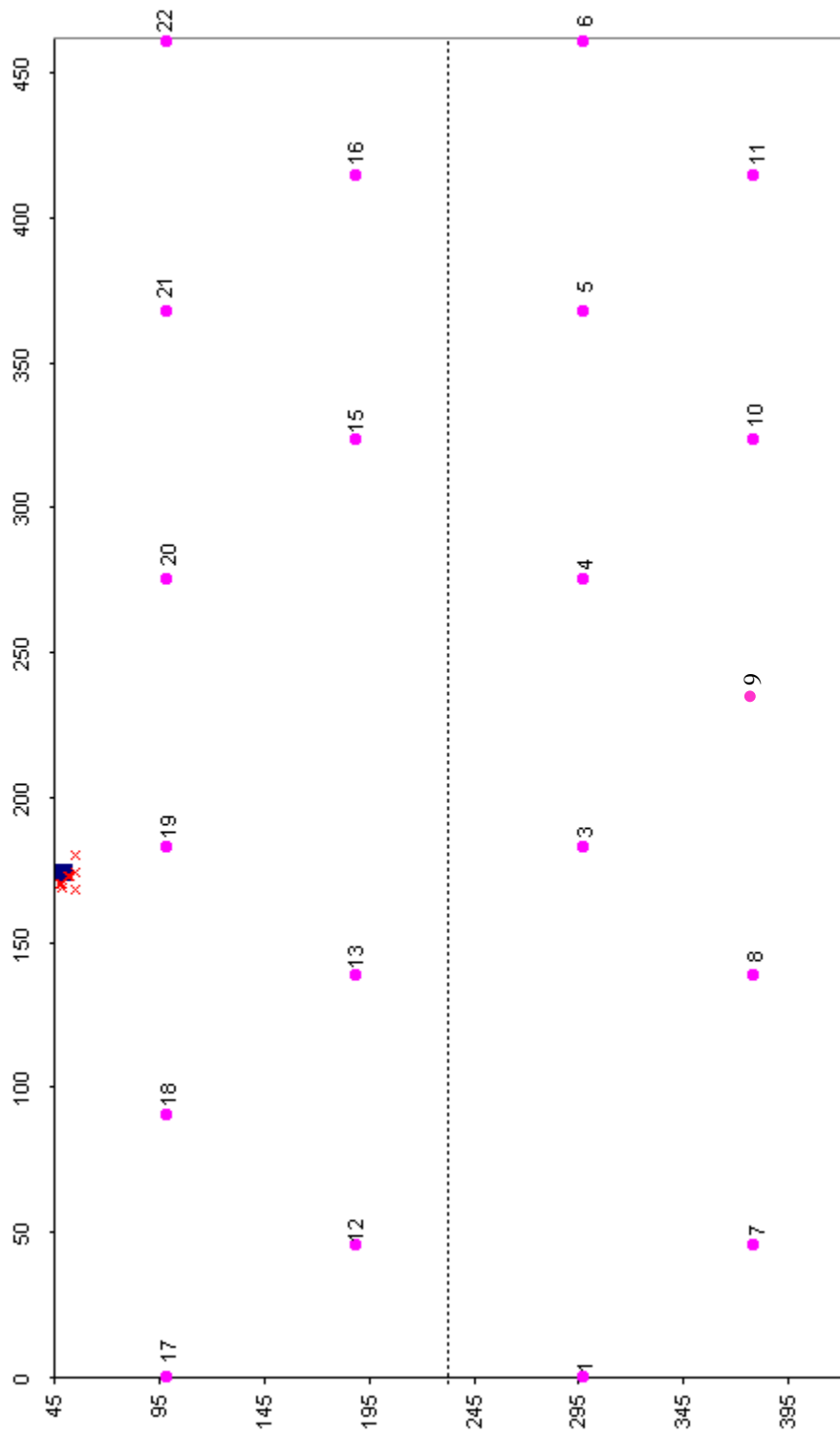


Figure 5.25 - Location Results from a Bar Bending Test at Location C

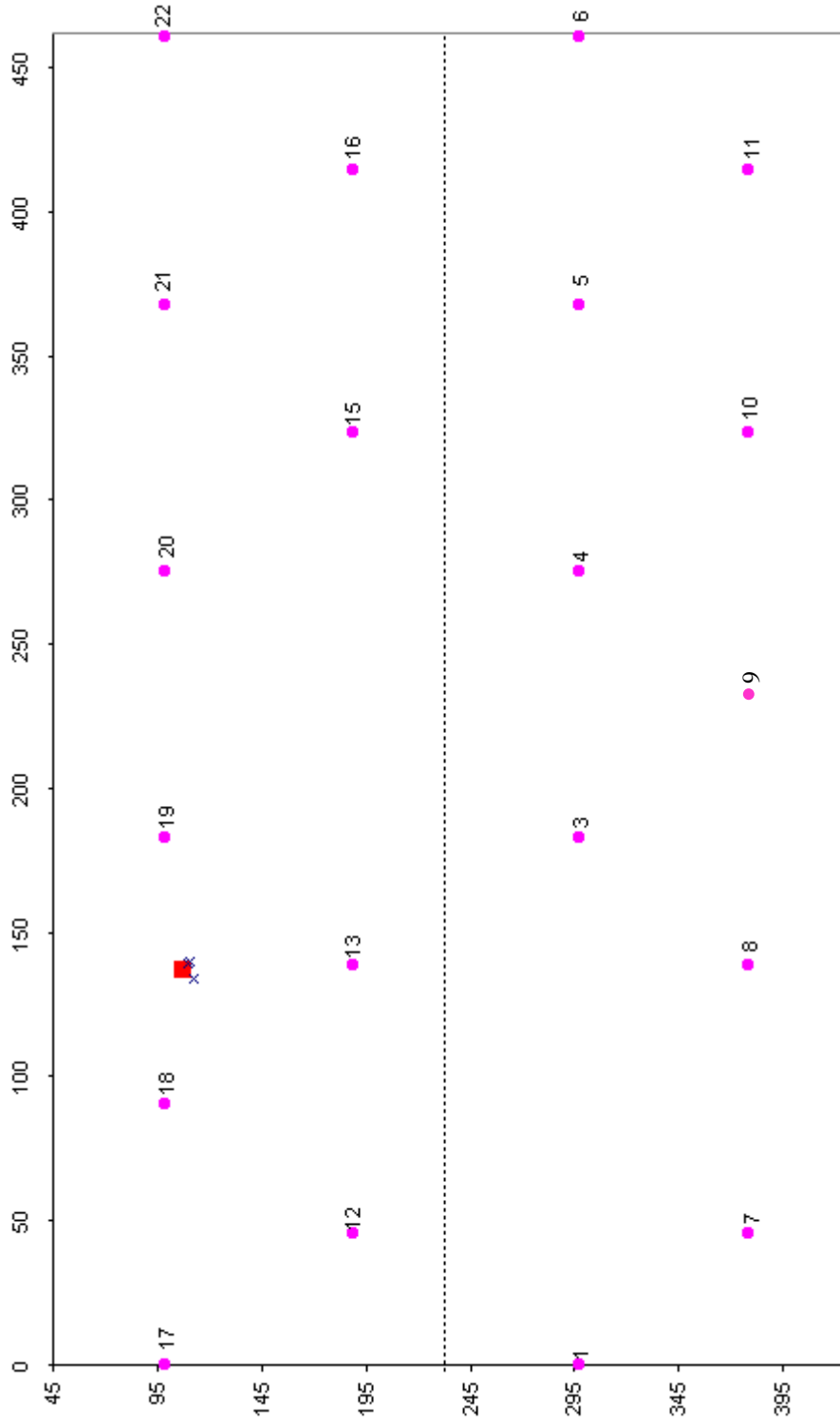


Figure 5.26 - Location Results from a Bar Bending Test at Location D



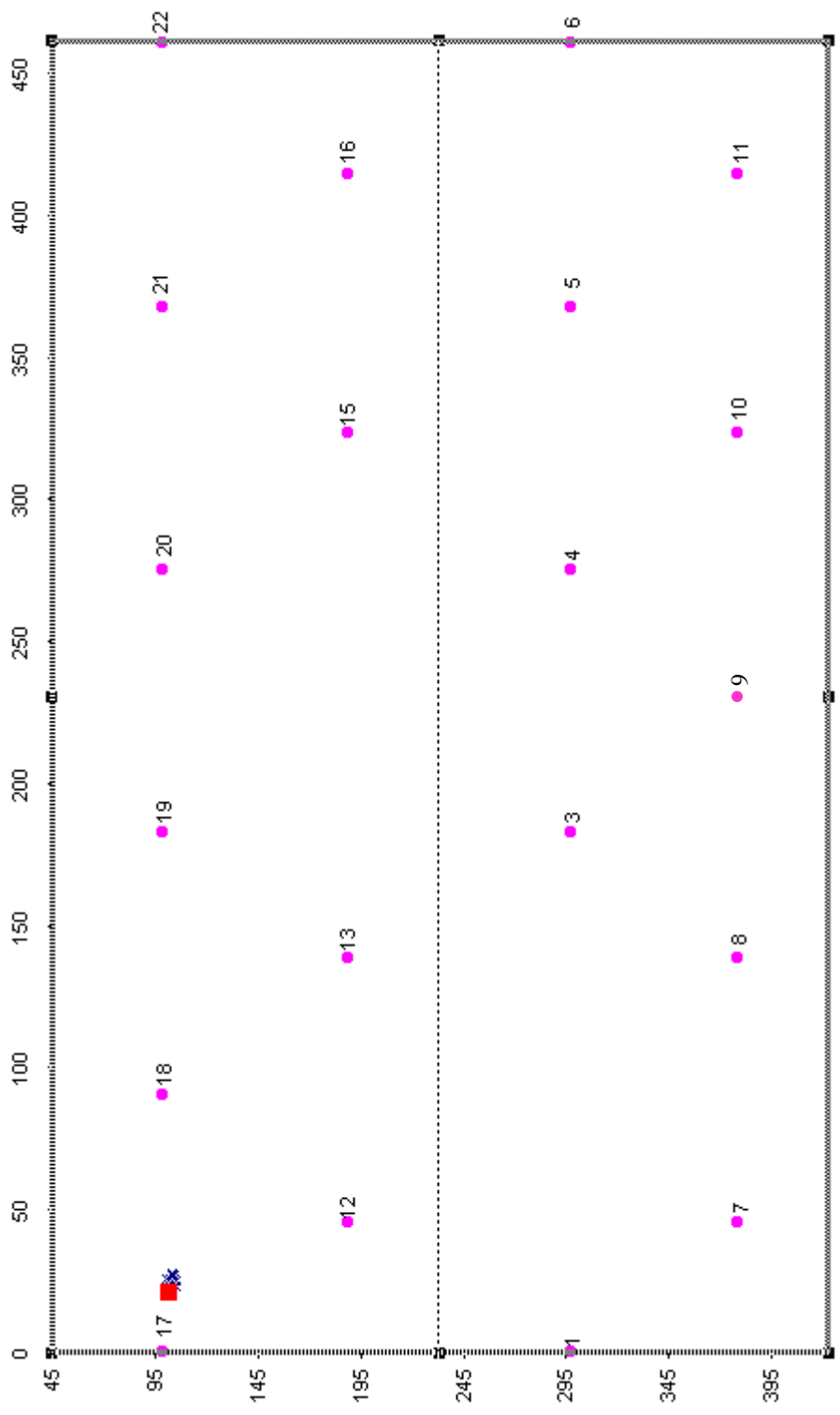


Figure 5.27 - Location Results from a Bar Bending Test at Location E

- *Discussion of the Results from Bar Bending Tests*

The results from the bar bending tests reported in the previous section show good promise that the method could be used in practice. It forms the basis for a field source location method. The method is applied to the data from the internal pressure test in Chapter 6. Data generated from the bar bending has high energy, therefore the filtered signal contains enough energy to identify the modes of the waves. It will be interesting to see how the method performs with the low to medium energy data which will be the range obtained from a tank car test.

#### **5.4.5 A Study of Water Borne Waves**

Once a wave is generated in the tank car shell, it can radiate into the water. This section studies the wave propagation into and through the water. There are three types of waves radiating into the water. The first one is the portion that leaks from the plate waves. It is called a leaky Lamb wave. The second wave is the low frequency signal that cannot leak into the water. Instead, it is trapped between the surface layer of the water and the tank shell. This wave is called a Scholte-Stonely wave and was discussed earlier in Section 5.3.4.1. The third wave is directly transmitted from the source into the water.

#### 5.4.5.1 Water Borne Waves

- *Leaky Lamb Waves*

Section 5.3.4 briefly described the leaky Lamb wave theory but focused only on the non-leaky part. This section provides additional information about the leaky portion of the wave and describes how it leaks into the water.

As discussed in Section 2.2.5 the leakage angle is a function of the ratio of the water wave velocity to the phase velocity of the wave traveling in the steel. Except at low frequency (see Section 5.4.2), the phase velocity is a function of the frequency. Accordingly, each frequency transmits into the water with a different angle.

A phase velocity dispersion curve for 13/16" thick steel plate is shown in Figure 5.28. A more detailed plot between 0 and 100 kHz is shown in Figure 5.29. Since the symmetric mode does not have significant leakage into the water because of the axial motion of the waves, the following calculation focuses on the anti-symmetric mode. In Figure 5.29, it is seen that a 100 kHz frequency travels at a speed of 2.8 km/sec or 110,236.2 in/sec. Note that 1 km/sec = 39370.1 inch/sec.

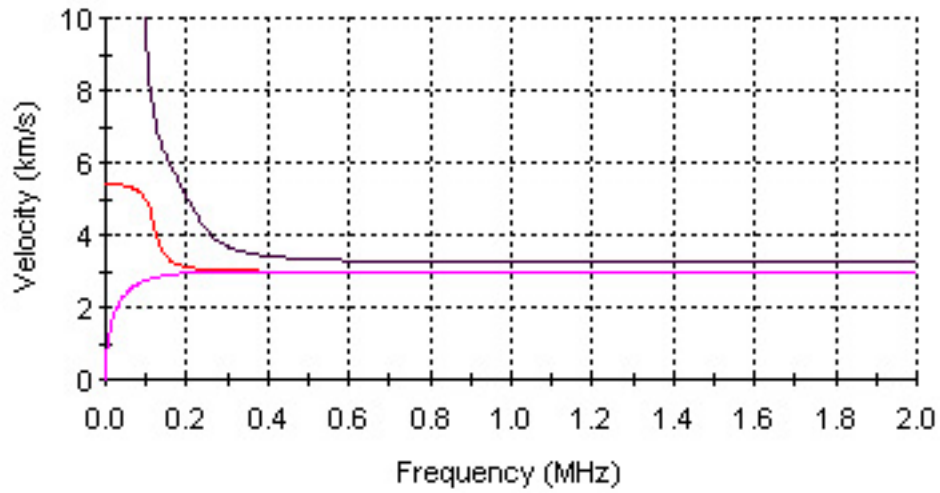


Figure 5.28 – Phase Velocity of 13/16” Thick Steel Plate

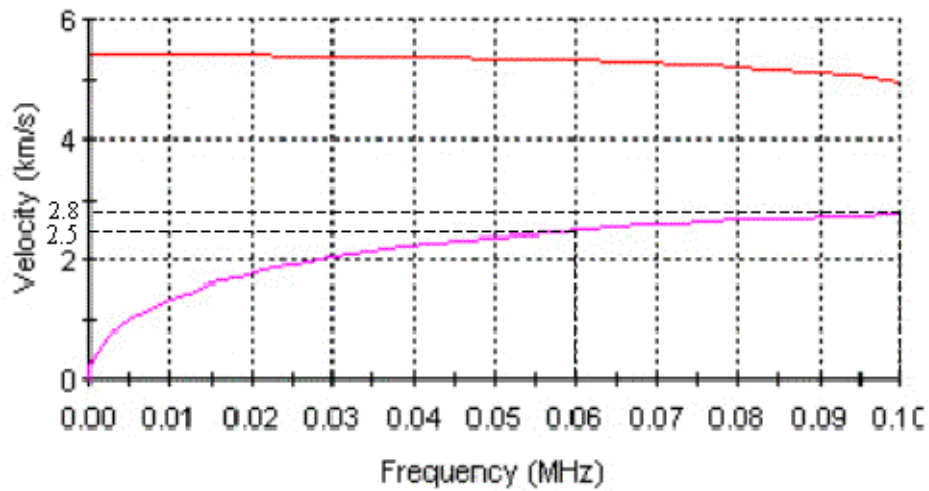
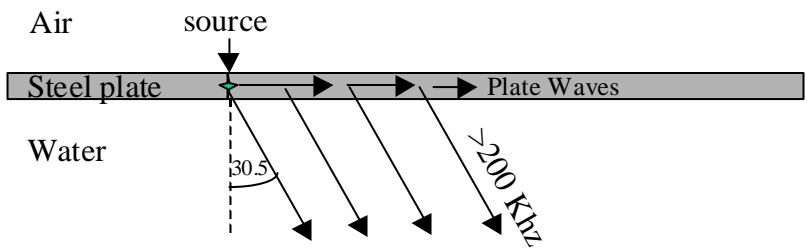


Figure 5.29 – Phase Velocity from 0 to 100 kHz of 13/16” Thick Steel Plate

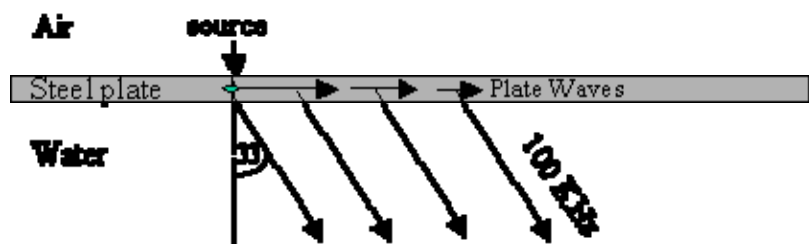
The velocity of the water wave is 60,000 in/sec. Using equation 2.13, the leak angle of the 100 kHz component is:

$$\theta_{leak} = \sin^{-1}\left(\frac{V_{water}}{V_{ph}}\right) = \sin^{-1}\left(\frac{60,000}{110236.2}\right) = 33^\circ$$

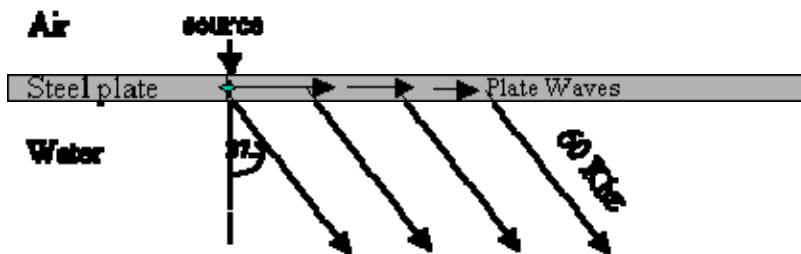
For a 60 kHz content, the phase velocity is 2.5 km/sec or 98,425.2 inch/sec. The leak angle is 37.5°. From the phase velocity chart in Figure 5.29, it can be seen that higher frequency range (> 200 kHz) approaches the Rayleigh velocity which is 3.0 km/sec or 118,110.24 inch/sec in this case. These higher frequency ranges have the same angle leakage angle of 30.5°. These calculations are summarized in Figure 5.30 for three different frequencies. Figure 5.31 shows the leakage waves for all three frequencies.



a) Leakage for Frequencies Higher than 200 kHz



b) Leakage wave for 100 kHz Wave



c) Leakage Wave for a 60 kHz Wave

Figure 5.30 – Leakage Angle of Different Frequencies Transmitted into the Water

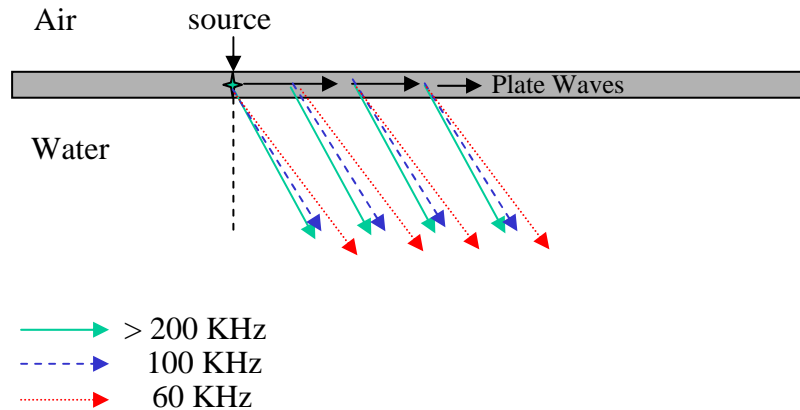


Figure 5.31 – Leakage Waves for Three Frequency Components

- *Scholte-Stonely Waves*

Scholte-Stonely waves are discussed in Section 2.2.5. At a very low frequency, the plate wave velocity is less than the wave velocity in water. Accordingly, this low frequency wave does not radiate into the water. Instead, it is trapped and propagates between the surface layer of the water and the steel. This wave is not detectable by AE sensors because the sensors are placed on the outside of the shell. For this reason, Scholte-Stonely waves are not discussed in the analysis.

- *Direct Transmitted Wave*

If a bar is welded perpendicular to the shell of a water filled tank car and bent, the emission goes along two paths. The first path is the plate waves

propagating along the shell and the second path is the waves transmitted directly into the water. This is shown in Figure 5.32. The previous sections discussed plate waves radiating their energy into the water. This section discusses the wave that is directly transmitted into the water.

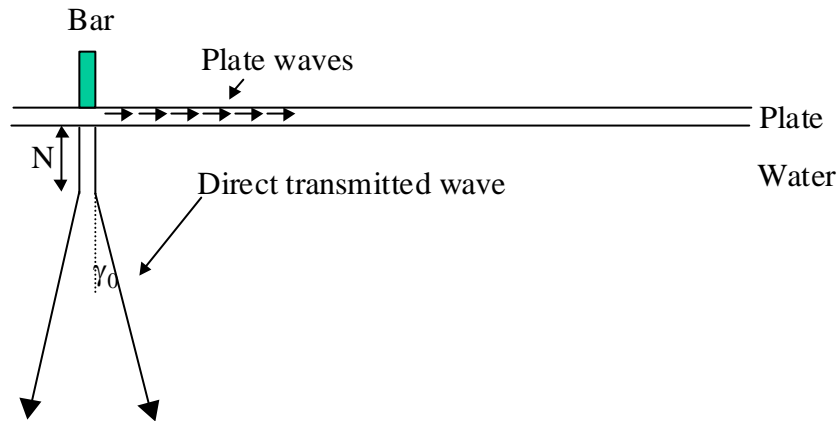


Figure 5.32 – AE generated by Bar Bending on a Full Tank

In order to illustrate this behavior, a bar was tag welded to the tank car wall. The size of the weld was approximately ¼". When sound passes into the water, the wave in the near field travels as a parallel beam for a distance N and then diverges with the angle  $\gamma_0$  [Krautkramer, 1969]. For a small ratio of  $\lambda/D$ , where D is the size of the weld and  $\lambda$  is the wavelength of the wave, N and  $\gamma_0$  can be calculated by:

$$N = \frac{D^2 - \lambda^2}{4\lambda} \dots\dots\dots(4.1)$$



$$\gamma_0 = \sin^{-1}\left(\frac{1.2\lambda}{D}\right) \dots\dots\dots(4.2)$$

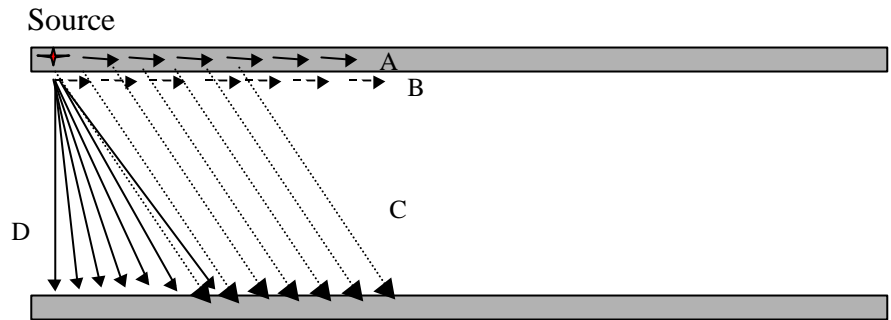
The size of the weld is ¼”. The wavelength of the longitudinal wave in water at a 100 kHz is 0.6”. For a λ/D of 0.833, the theory gives an angle of divergence of 90°. In this case, the ratio λ/D is 2.4 and sin(γ<sub>0</sub>) is greater than 1. The physical interpretation of this is that the sound wave travels in every direction in the water.

- *Summary of Four Possible Wave Propagation Routes in a Liquid Filled Tank Car*

This section summarizes different types of water borne waves. Figure 5.33 illustrates possible wave propagation paths in a liquid filled tank car. In Figure 5.33, it is seen that emission from a source can propagate through the tank car shell as Lamb waves. This is marked as A. The low frequency components do not radiate energy into the water, instead, they become trapped at the interface between the steel and water forming a Scholte-Stoneley waves. This is marked as B. Since AE sensors are attached at the outer shell of the tank car, they do not detect the Scholte-Stonley wave.

At higher frequencies, the lamb waves leak into the water. This is shown as C in Figure 5.33. The figure shows only one frequency component of the water borne waves. However, different frequency components of the Lamb wave leak into the water at different angles.

Wave propagation in a liquid filled tank car becomes even more complicated when waves traveling in the water strike the tank car wall on the other side. This topic is discussed in Section 5.4.5.2.

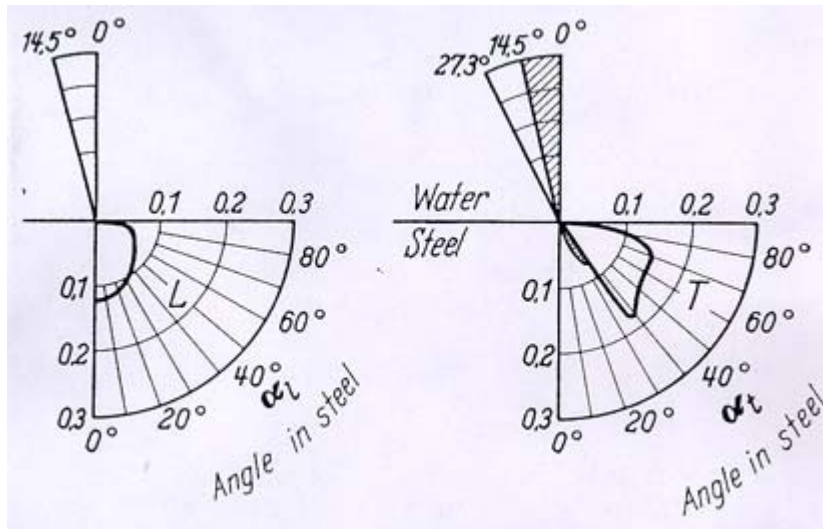


- → A = Lamb waves from the source
- - - -> B = Scholte-Stoneley Waves
- .....> C = Water Borne P-Wave or Leaky Waves from A
- > D = Direct Transmitted Wave from the Source

Figure 5.33 – Possible Waves in a Tank Car

#### 5.4.5.2 Waves at Interfaces with Oblique Incidence

As discussed earlier in Section 2.2.2, when a wave strikes an interface between two layers and part of the energy reflects back into the incident material, part of the energy transmits into the new layer. Figure 5.34 shows the ratio of the energy of the incident wave traveling in the water to the ratio of the energy transmitted into the steel at a water/steel interface.



a) Transmitted Longitudinal Wave      b) Transmitted Transverse Wave

Figure 5.34 – Energy Transmitted at a Water/Steel Interface [Krautkramer, 1969]

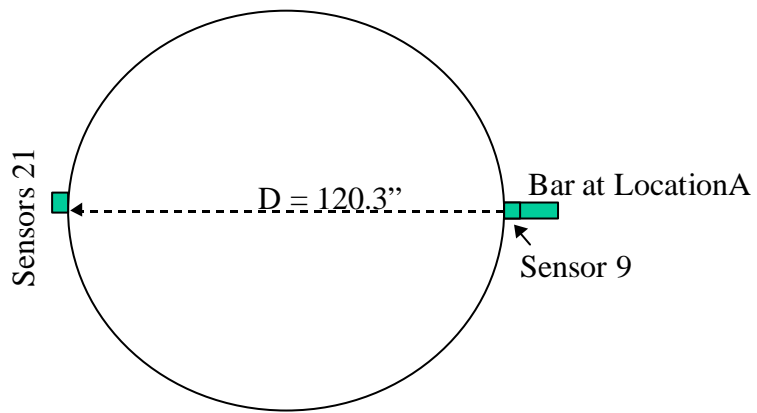
Figure 5.34a shows that for water/steel interface, a transmitted longitudinal wave occurs if the angle of incidence is below 14.5°. The transmitted wave can contain up to 11% of the incident waves energy. Figure 5.34b shows that a transmitted transverse wave occurs at the same time. This wave has a transmitted energy of up to 8%. At angles of incidence between 14.5° and 27.3°, a transmitted transverse wave is obtained with energy values approaching 20%. For incident angles above 27.3° the wave is not transmitted into the shell.

### *5.4.5.3 Results from Water Borne Studies*

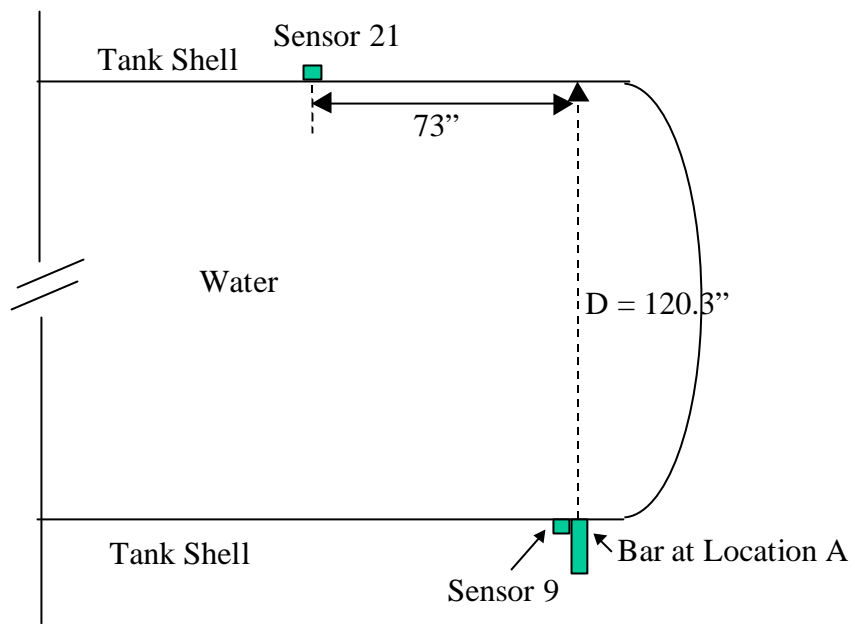
This section studies the water borne wave from a bar bending test discussed previously. The bar was at location A (Section 5.4.4 and Figure 5.22). In this test, a sensor was placed next to the location of the bar. This sensor serves as a trigger sensor to measure the approximate time of the emission at the source. In this test, source location analysis was performed through the shell path with Sensors 5, 6, 11, and 16. Sensor 21 was on the opposite side of the tank car as shown in Figure 5.35. Figure 5.35a shows the end view of the tank and Figure 5.35b shows the top view.

The analysis was performed using the waves in the 100 kHz frequency range. Data from sensors 9 and 21 were band-pass filtered with a 95-105 kHz band-pass filter. The arrival time of the signal was defined by the median of the negative and positive peaks of the filtered signal.

28 events were included in the analysis. Figure 5.36 shows the difference in the arrival time between sensors 9 and 21 compared to the amplitude measured at sensor 9. For low amplitude hits, the average time the signal took to propagate between the sensors was 0.00245 seconds. For high amplitude hits, the average propagation time was 0.00162 sec.



a) End View



b) Top View

Figure 5.35 – Bar A and Sensor Locations on the Tank Car

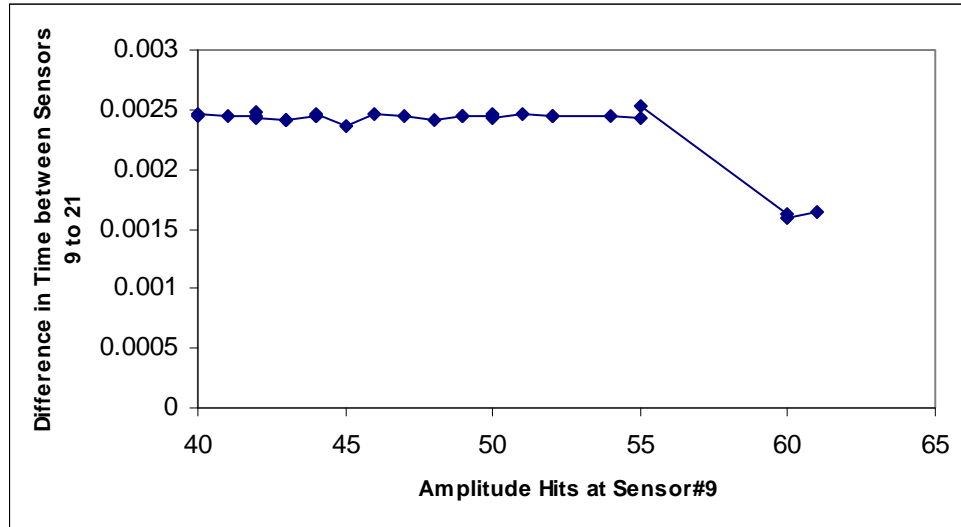


Figure 5.36 – Measured Wave Propagation Time between Sensors 9 and 21

A possible propagation path for the directly transmitted wave through the water and transmitted along the plate is shown in Figure 5.37.

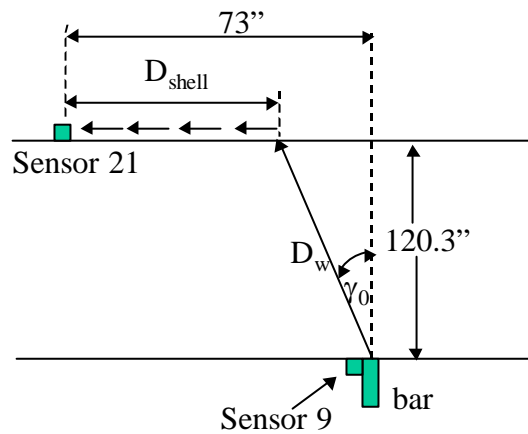


Figure 5.37 – Propagation Path between source and Sensor 21 for Directly Transmitted Water Borne Wave

From the figure,  $D_w$  is the distance the wave propagates through the water and  $D_{shell}$  is the distance the wave travels through the shell. In term of  $\gamma_0$ :

$$D_w = \frac{120.3}{\sin(\gamma_0)}$$

$$D_{shell} = 73 - D_w \cos(\gamma_0)$$

The velocity of the water wave is 60,000 in/sec. The propagation time ( $t_w$ ) of the water borne wave is given by:

$$t_w = \frac{D_w}{60,000}$$

The velocity of the plate waves at a 100 kHz is 125,000 in/sec. The time ( $t_{shell}$ ) that the plate waves take to propagate to sensor 21 is calculated by:

$$t_{shell} = \frac{D_{shell}}{125,000}$$

The total time the wave takes to propagate from the source to sensor 21 is  $t_w + t_{shell}$ . This value is calculated in term of  $\gamma_0$  and plotted in Figure 5.38.

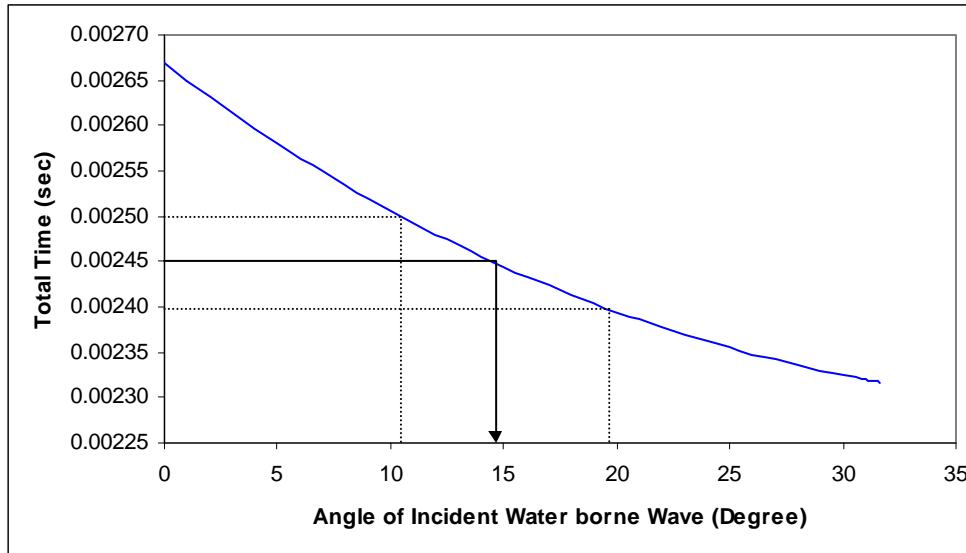


Figure 5.38 – Calculated Time for the Wave to Propagate from the Source to Sensor 21 Versus the Angle of the Incident Water Borne Wave

For the low amplitude data, the measured difference in the arrival times between sensors 9 and 21 varied between 0.00240 to 0.00250. This range of data corresponds to a range of angles for the incident water born wave of 10 to 20 degrees. The average of the measured difference in the arrival times is 0.00245 and this value corresponds to an angle of slightly less than 15 degrees. Note that this angle generates the highest energy in the transverse mode.

For high amplitude data, the measured wave propagation times between Sensors 9 and 21 are a lot less than for the low amplitude data. The propagation times are between 0.00159 to 0.00165 seconds. This is because the wave travels through the shell and high amplitude data survives from the attenuation and reaches sensor 21 on the other side of the tank. The shell distance from the bar to



Sensor 21 is 203.5". Assuming a plate wave velocity of 125,000 in/sec, the theoretical travel time through the shell from the bar to sensor 21 is 0.001628 sec.

#### *5.4.5.4 Discussion of Water Borne Waves*

If the amplitude of the wave is high enough, the signal always arrives at the sensors through the shell path first. If the wave is low amplitude, it attenuates along the shell path because the plate waves leak their energy into the water. In this case, the shell path wave does not reach the sensors on the other side and they detect the water borne signals.

As discussed earlier, there are three types of waves generated in the water. The first one is the leaky lamb waves. This wave radiates into the water at an angle between  $30^\circ$  and  $37.5^\circ$  for frequency components above 60 kHz. When the wave strikes the other side of the shell, it does not transmit into the shell because the angle is greater than  $27.3^\circ$ . However, the water borne leaky Lamb waves may be transmitted into the head of the tank. The most important effect of the leaky Lamb wave is that they decrease the energy of the Lamb waves propagating in the shell. This results in high attenuation of the wave.

The second type of wave is Scholte-Stonley wave. This wave is not detectable by the AE sensor because the sensor is placed at the outer surface shell and the waves travel along the interface between the water and steel. The last type of wave is the directly transmitted wave from the source into the water. This wave diffracts in many directions depending on the size of the source.

Section 5.4.5.2 shows that at small incident angles from 0 to 14.5 degrees, the transmitted longitudinal waves are generated with an energy of up to 11% of the incident wave. The transmitted transverse waves are generated at angles

between 14.5 to 27.3 degrees with an energy that can approach 20% of the incident wave.

The results from Section 5.4.5.3 show that the near and far field sensors detect the wave incident at the interface at slightly less than 15 degrees. This angle generates the highest energy transmitted transverse waves.

## **5.5 SUMMARY**

This chapter focuses on source location on a water filled tank car. The concept of the work is based on a tight band frequency to minimize the dispersion problem. First, the source location was performed based on the low non-leaky frequency range. Wide band sensors were used in the tests and make it possible to capture the low frequency data. The location results from this method showed good accuracy. There are two disadvantages of using the low frequency range. First, the frequency range is likely to have interference from the background noise. Second, in order to capture the low frequency wave, an accelerometer or a wide band sensor must be used. The accelerometer is insensitive to high frequency waves used for structural evaluation, and the wide band sensor is also insensitive.

For the thicker tank car tested in Orange, Texas, resonant sensors (R6I) were used. This sensor has higher sensitivity compared to the wide band but it does not respond well in the low frequency range. Therefore, the source location method focused on a higher frequency range. In this work, the 100 kHz frequency range was used. Unfortunately, this frequency component leaks energy into the water and attenuation and water borne waves are problems.

The water bypass problem was solved with a software algorithm that uses combinations of three sensors to locate the position of the source. If one of the

sensors included in the analysis detects the water borne wave instead of the plate wave, the combinations including that sensor will give results that do not fit the group. For this method to work well, more than three sensors are required to detect the shell path signal.

Source location analysis using the shell path and data from the bar bending show good promise. A disadvantage of this approach is that a lot of information from the water borne wave is thrown away.

The water borne wave was also studied. It was found that three types of waves can be generated in the water. Only two types of wave are considered here. First, the Leaky lamb wave and second, the directly transmitted wave. The study shows that as the plate wave propagates through the shell, it leaks out part of its energy into the water. This results in high attenuation of the wave. This leaky wave does not transmit into the shell when it strikes the other side of the tank car. The wave that is transmitted into the shell opposite to the source is the directly transmitted wave.

The results from the bar bending in Section 5.4.5.3 shows that the near and far field sensors detect the plate waves at the incident angle of slightly less than 15 degree. This angle is the angle that has the highest energy of the transverse mode can be generated from the incident water borne wave.

## **CHAPTER 6**

### **INTERNAL PRESSURE TEST OF A TANK CAR**

#### **6.1 INTRODUCTION**

This chapter describes the source location results from an internal pressure test conducted on a steel tank car. The tank car used in the test is the one located at Rescar facility in Orange, TX. An internal pressure test is one of the most commonly used acoustic emission tests on tank cars and pressure vessels. The purpose of the test is to detect defects such as corrosion, bad welds, and cracks in the tank and lining. In this research test, a pressure test was conducted on a tank car that has been removed from service due to severe internal corrosion and blistering. The objective of the test was to obtain acoustic emission from a tank car with known defects and to apply the source location approach developed earlier in Chapter 5 to pinpoint flaw locations. The service history and sources of emission associated with this car are discussed in Section 4.2.3.

#### **6.2 EXPERIMENTAL SETUP**

##### **6.2.1 Instrumentation and Sensor Location**

In the pressure test, water was used to pressurize the tank car. A DISP digital acoustic emission system with 24 channels was used to monitor the emission. 24 R6I sensors were used and their locations on the tank are shown in Figure 6.1. Note that the two heads and two sensors, each head, are not shown in the figure. In Figure 6.1, the tank is shown as a top view opened up from the bottom. Twenty-two sensors were located on the tank body and one in the middle

of each head. Vacuum grease and duct tape were used to couple and attach the sensors to the tank car shell.

The AE data recorded by the instrument includes the parametric information such as amplitude, duration, and arrival time and a complete waveform of the signal. The threshold was set at 45 db. This was higher than that normally used for a tank car pressure so as to eliminate noise that originated from rust on the car. The AE acquisition system was set at a sampling rate of 1 MHz and data were recorded for 1024 sampling points. A pre-trigger time or time delay of 200 microseconds was set to capture the beginning part of the waveform that arrives before the threshold. The nominal time span recorded for each waveform was 1 microsecond.

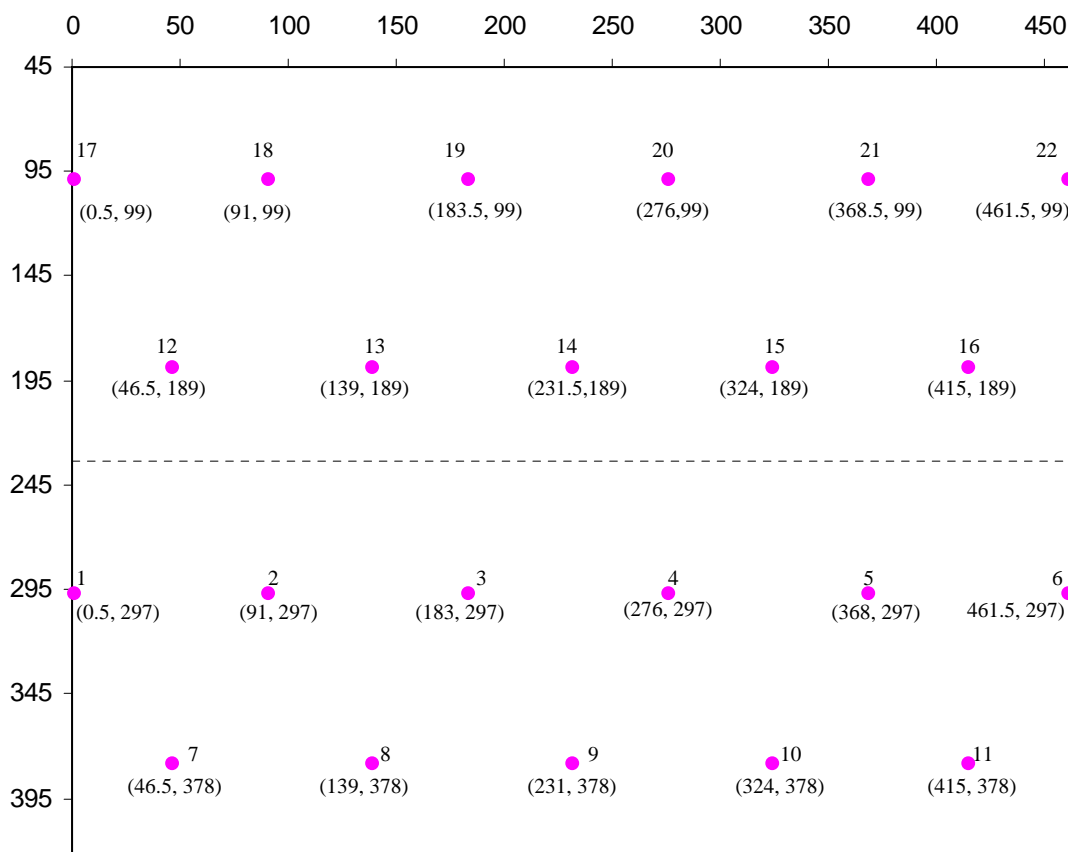


Figure 6.1 – Sensor Locations

## 6.2.2 Loading Sequence

The tank car was in bad condition. Accordingly, a stepped loading sequence was selected for the AE test. The relief valve of the tank was set at 300 psi, as specified in the AAR test procedure [AAR]. The maximum test pressure was 270 psi, which is 90% of the relief valve pressure. Stepped load increments of 20 psi were used up to the last increment of 10 psi. Load holds between increments were 3 minutes except at the 140 psi load hold and the final load hold. The 140 psi load hold was for 10 minutes and the one at the maximum load was for 30 minutes. The loading sequence is shown in Figure 6.2. AE was only recorded during the load hold periods.

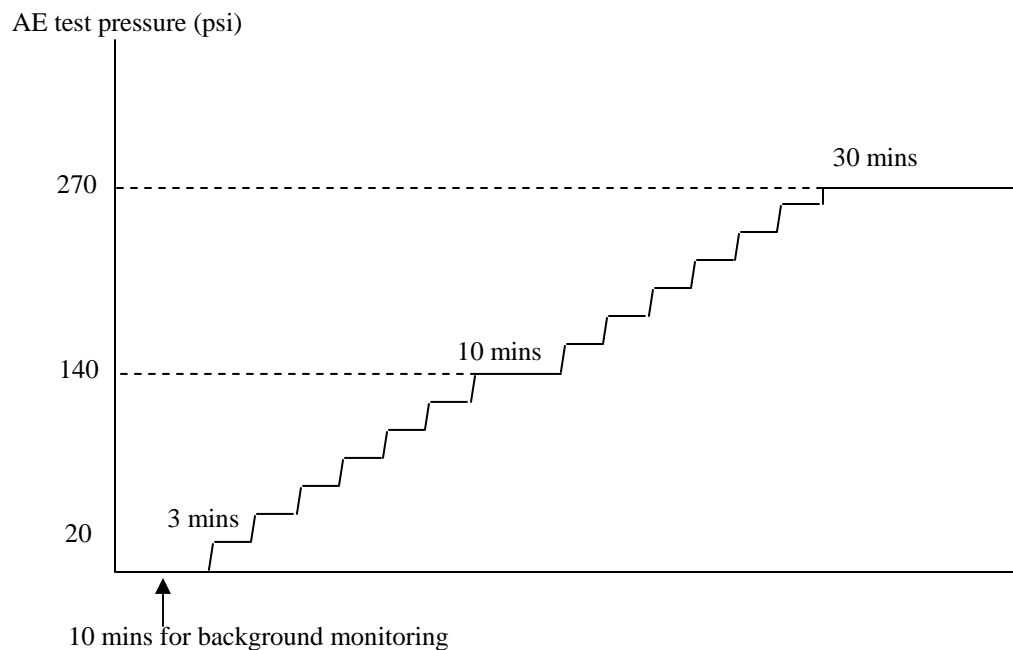


Figure 6.2 – Load Sequence for the Pressure Test

## **6.3 SOURCE LOCATION ANALYSIS**

### **6.3.1 Source Location Method using Higher Frequency**

In this section, the source location method used to analyze the data from the internal pressure test was the same method used earlier in Section 5.4.4. The method uses the frequency range where the first three modes intersect. For a 13/16" thick shell, that range occurs at a 100 kHz. The method is also similar to the one used for an empty tank (see Chapter 3 and 4). A combination of three sensors and the simplex optimization technique were used to eliminate the water borne wave. The underlying concept is similar to the approach used to minimize multiple sources. The technique is discussed in the second example given in Section 4.3.3. The method locates the position of the source by using the wave traveling through the shell. A step value of 1" was used in the simplex optimization.

### **6.3.2 Results from the Pressure Test**

For the entire test, a total hits of 15,193 hits were recorded during load holds. These hits were grouped as 3,161 events. The maximum amplitude hit was 99 dB. This section discusses the results from the load holds from 100 psi to 270 psi. These data were grouped as 2,352 events. The results are divided into eight groups as shown in Figures 6.3 to 6.18. The groups are separated by defect location.

Figure 6.3 presents the results from the first group. In the figure, the plotted locations are from the combinations of three sensors. The plot presents all possible locations for all three sensor combinations for each event. Accordingly,

more than one point is plotted for each event. Figure 6.4 shows the final locations. The plot presents only one point for each event, and that point is the location of the source using the method outlined in Section 5.3.3. Twenty nine AE events show that the defects are at the bottom of the car approximately 270 inches from the B end. The results from the first group are used for water borne wave studies in Section 6.4.

The results from the second group are shown in Figures 6.5 and 6.6. Figure 6.5 shows the locations from the combinations of three sensors. Figure 6.6 shows the final locations. Note that because the plot is a view of the tank car opened up from the bottom, the locations at the top and bottom of the figure are actually close to each other. This group of events are located at the bottom of the tank car, close to the events from the first group. The difference is that this group are more scattered and will not be used in the water borne study in Section 6.4. The source location results from the second group are located at the bottom of the car approximately 240 to 290 inches from the B end.

The results from the third group are shown in Figures 6.7 and 6.8. Figure 6.7 shows the locations from the combinations of three sensors. Figure 6.8 shows the final locations. The source location results from this group are located at the bottom of the tank approximately 360 inches from the B end. In this group, the events struck only three sensors; sensors 10, 11, and 21. Accordingly, the final result is the same as the results from the sensor combinations.

The results from the fourth group are shown in Figures 6.9 and 6.10. Figure 6.9 shows the locations from the combinations of three sensors and Figure 6.10 shows the final locations. The results from this group are located at the bottom of the tank approximately 230 inches from the B end. This location corresponds to the location where a bar was welded to the tank. The bar had been removed from the tank as a part of the study reported in Chapter 5.



Figure 6.11 presents the results from several groups of defects located along the bottom of the tank car. Figure 6.12 shows the final source locations. It should be noted that none of the location areas were covered in the first four groups.

The results from the sixth group are shown in Figures 6.13 and 6.14. Figure 6.13 shows the locations from the combinations of three sensors. Figure 6.14 shows the final locations. The source location results from this group are located at the top of the tank along the center line. The defects toward the A end correspond to the severe corrosion and blistering confirmed by ultrasonic testing (Figure 4.28).

The results from the seventh group are shown in Figures 6.15 and 6.16. Figure 6.15 shows the locations from the combinations of three sensors. Figure 6.16 shows the final locations. The sources detected in this group are located on the side of the car between sensors 14 and 20.

The results from the last group are shown in Figures 6.17 and 6.18. Figure 6.17 shows the locations from the combinations of three sensors. Figure 6.18 shows the final locations. The sources in this group are located on the side of the car between sensors 15 and 20.

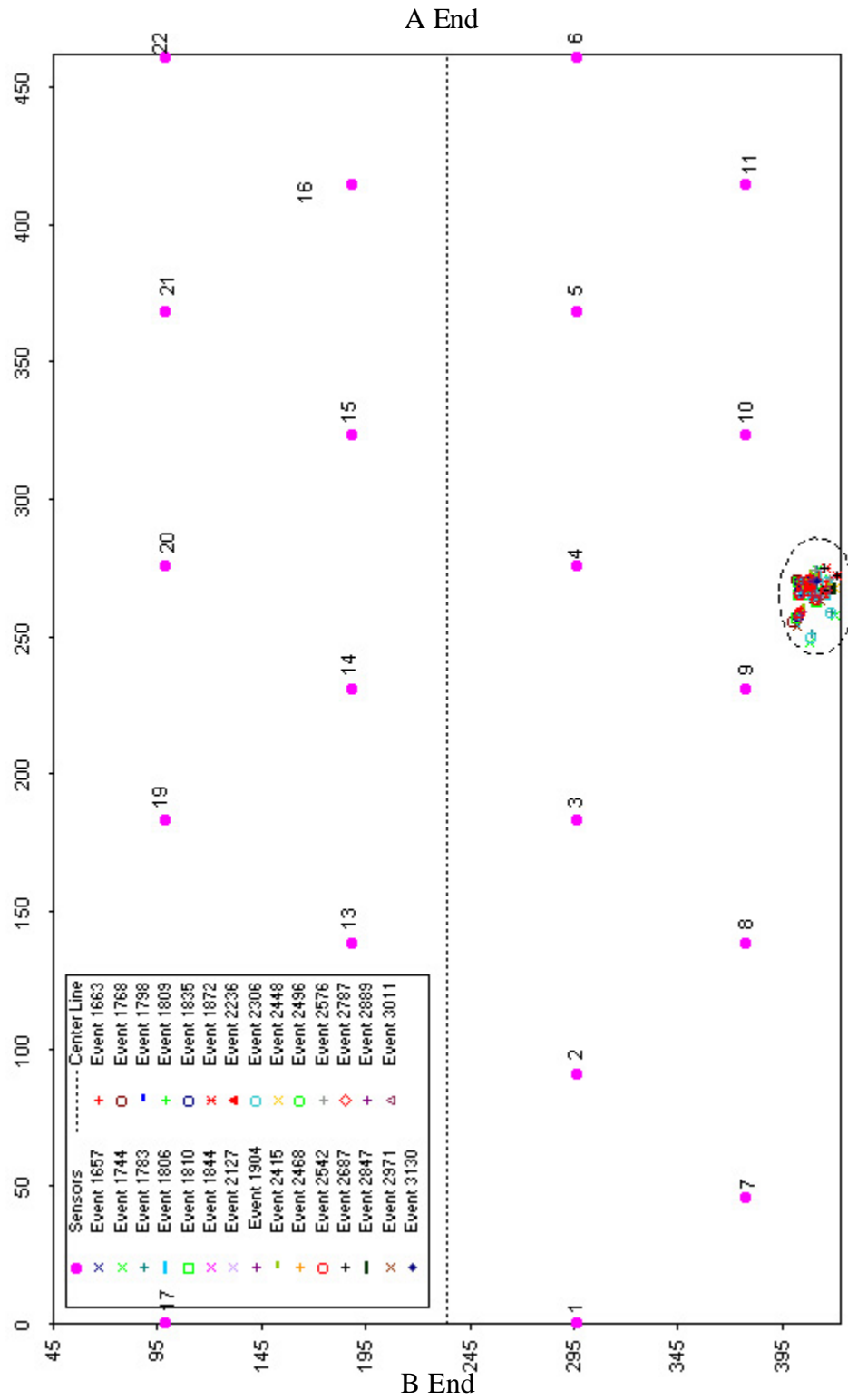


Figure 6.3 - Results from Combinations of Three Sensors from the First Group

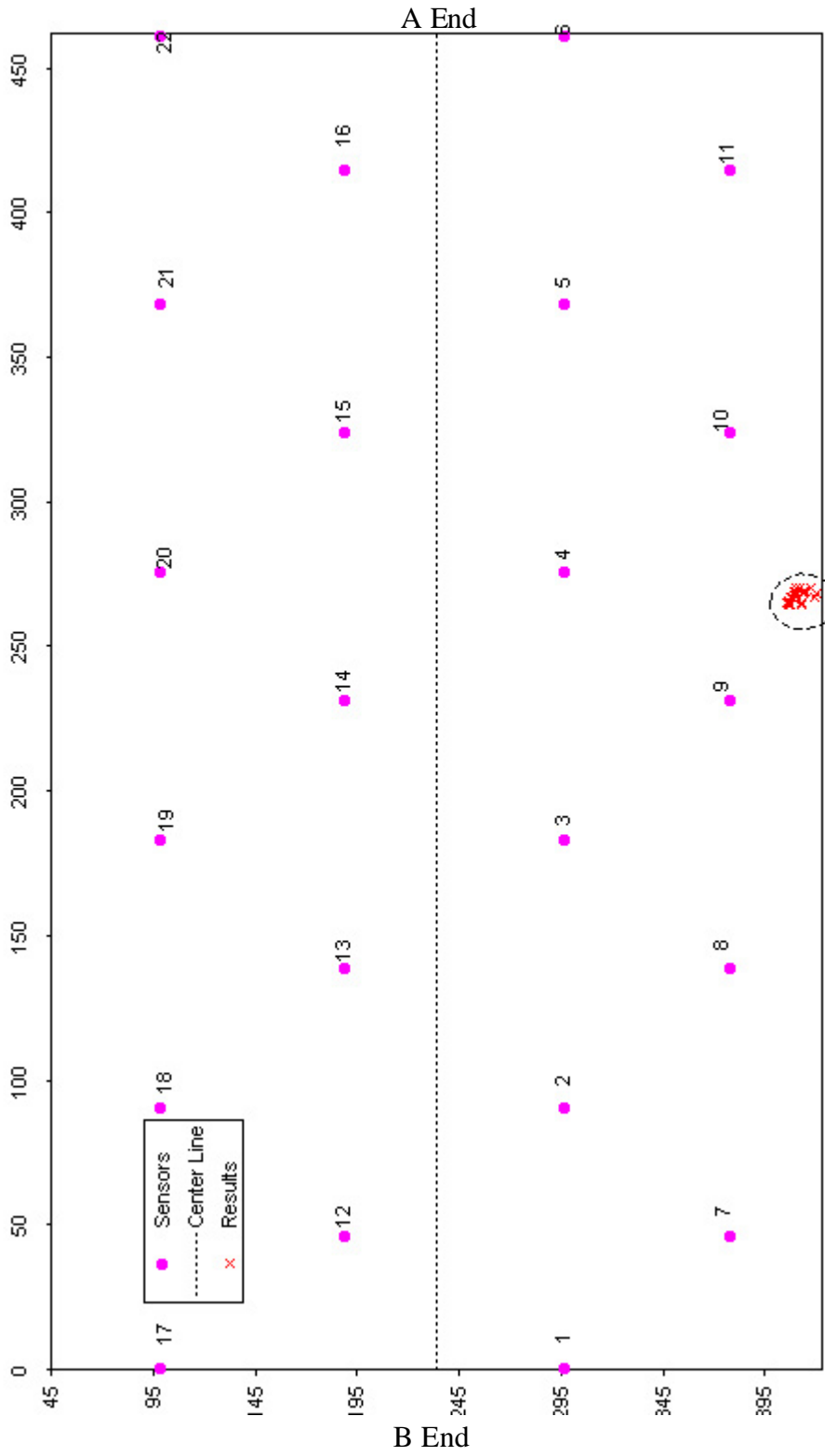


Figure 6.4 - Final Results for Data from the First Group

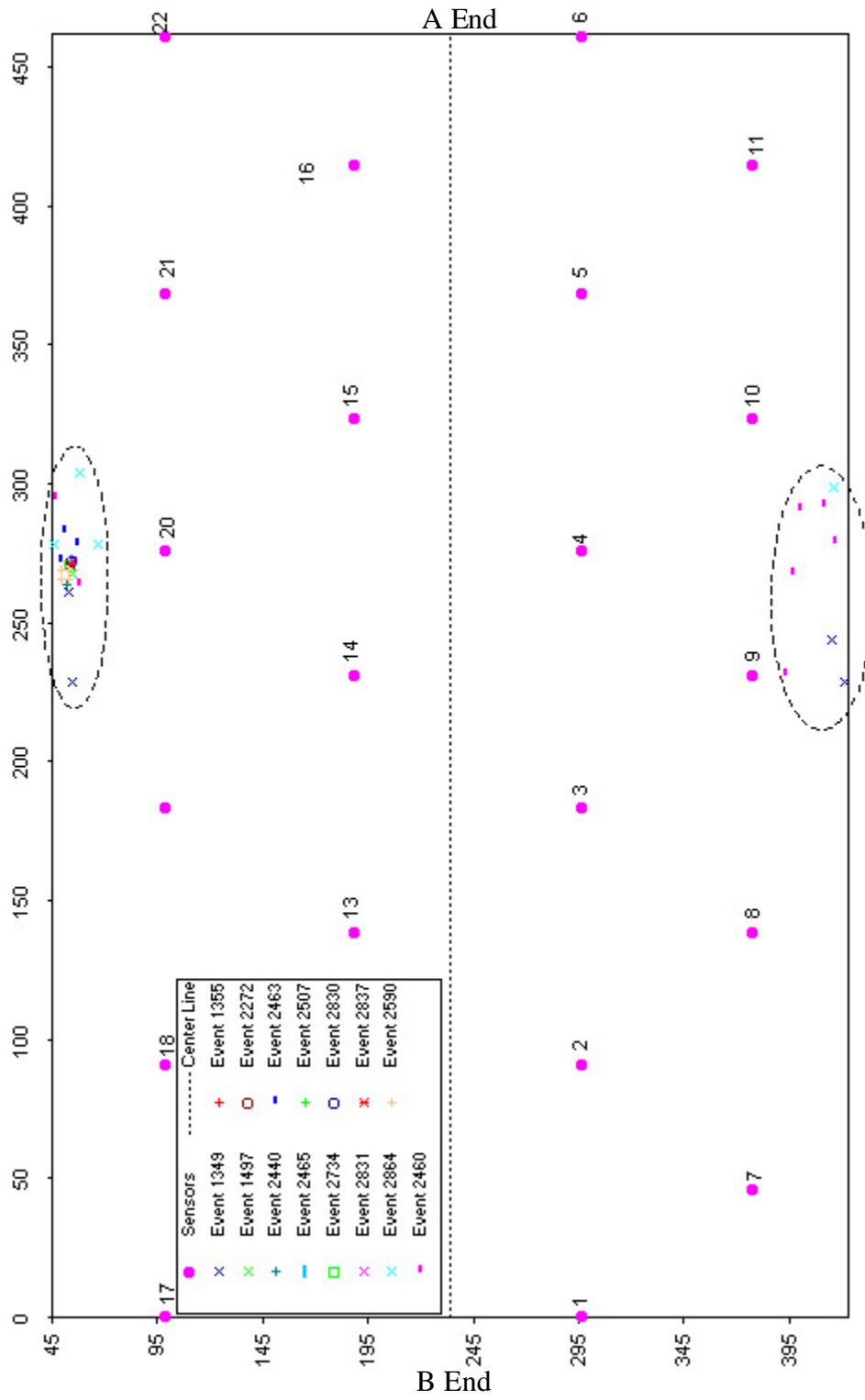


Figure 6.5 - Results from Combinations of Three Sensors from the Second Group

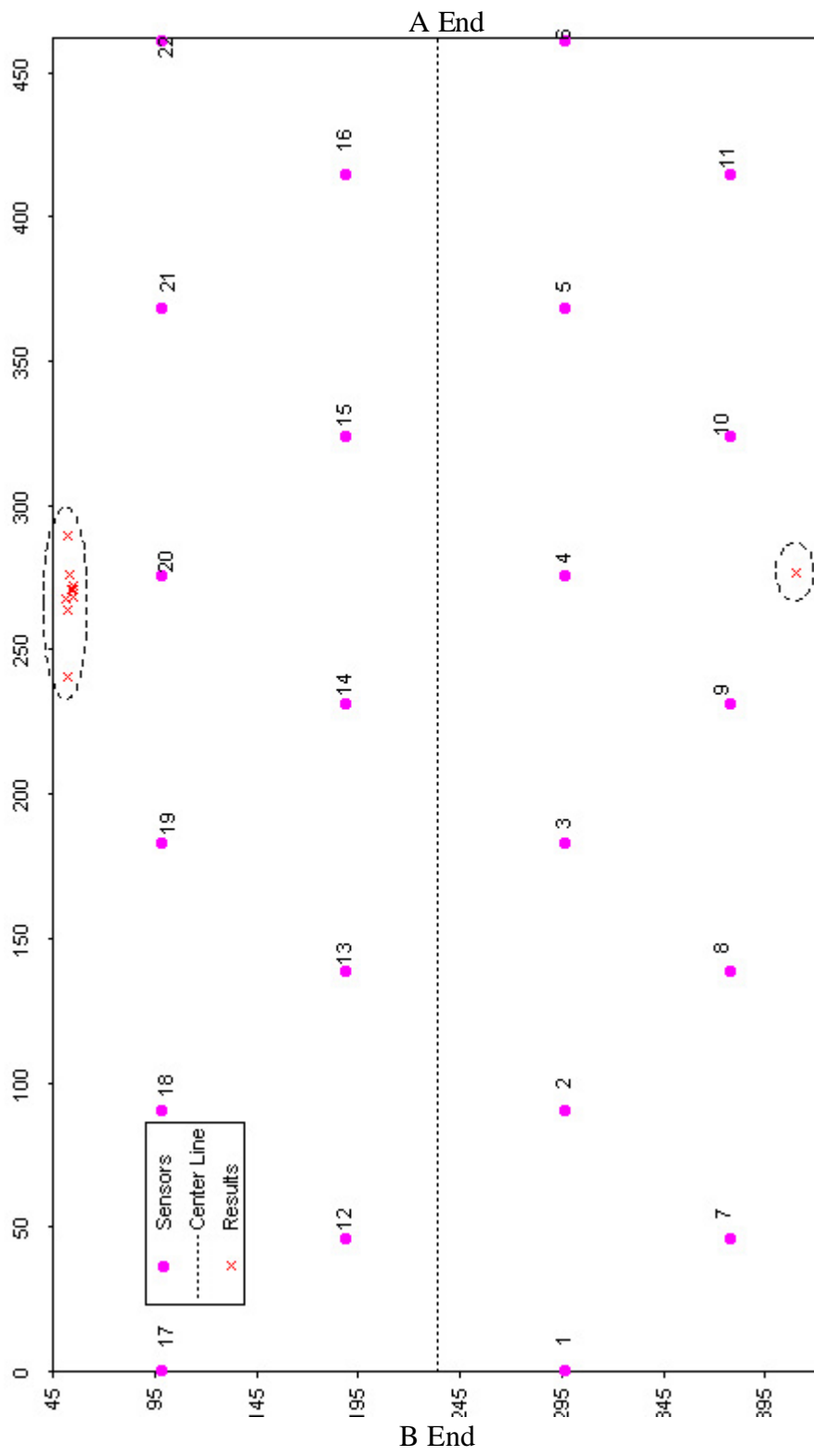


Figure 6.6 - Final Results for Data from the Second Group

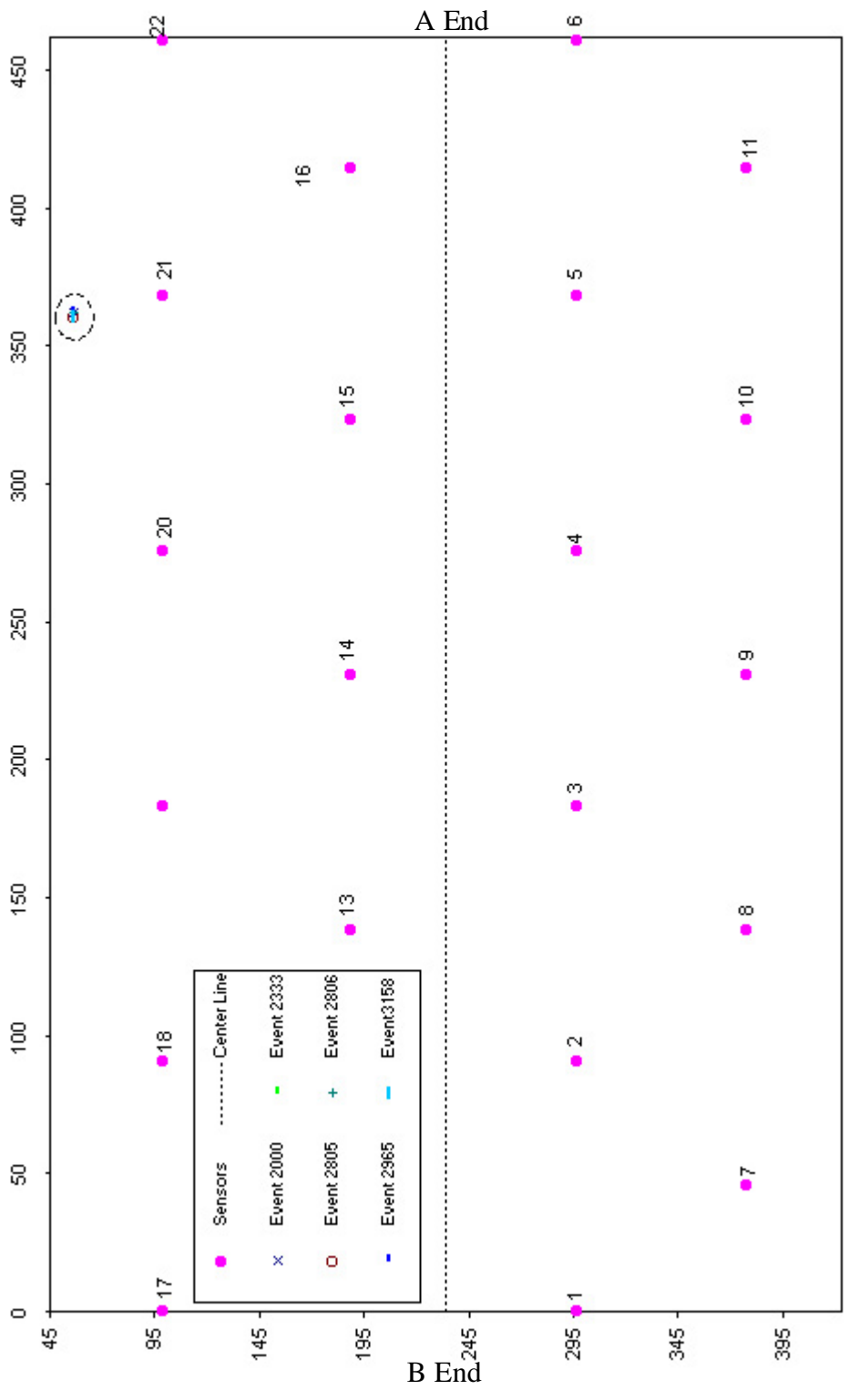


Figure 6.7 - Results from Combinations of Three Sensors from the Third Group

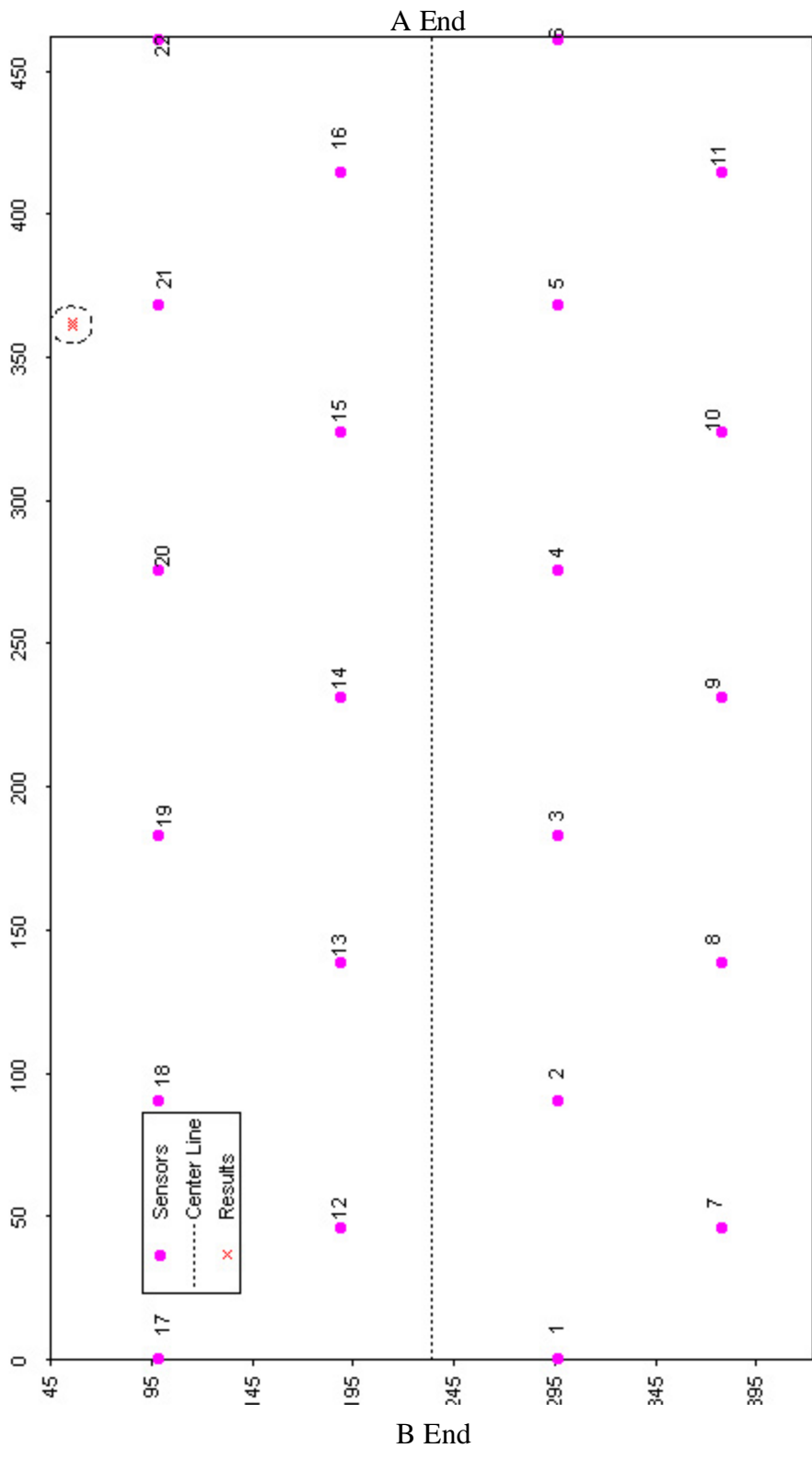


Figure 6.8 - Final Results from the Third Group

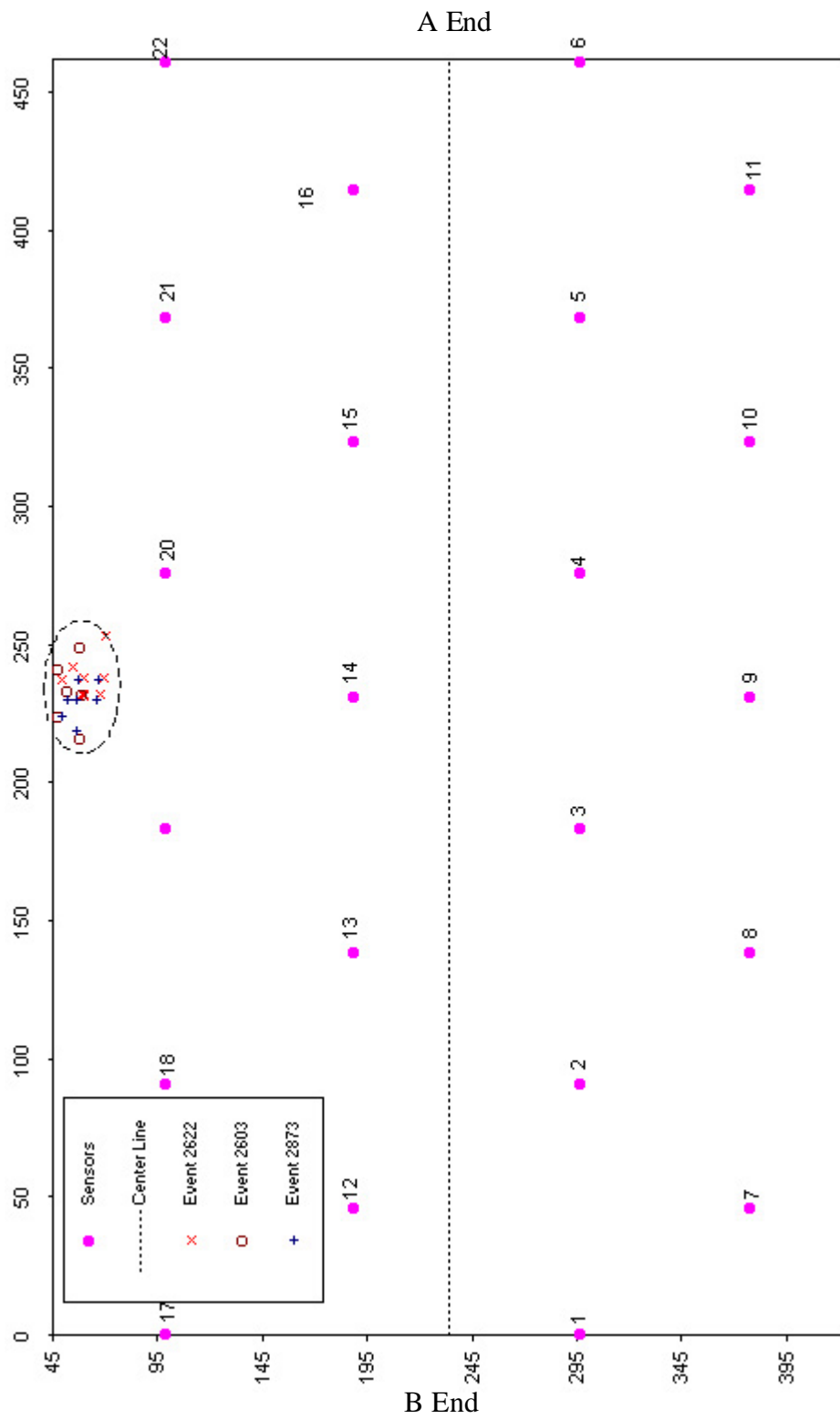


Figure 6.9 - Results from Combinations of Three Sensors from the Fourth Group



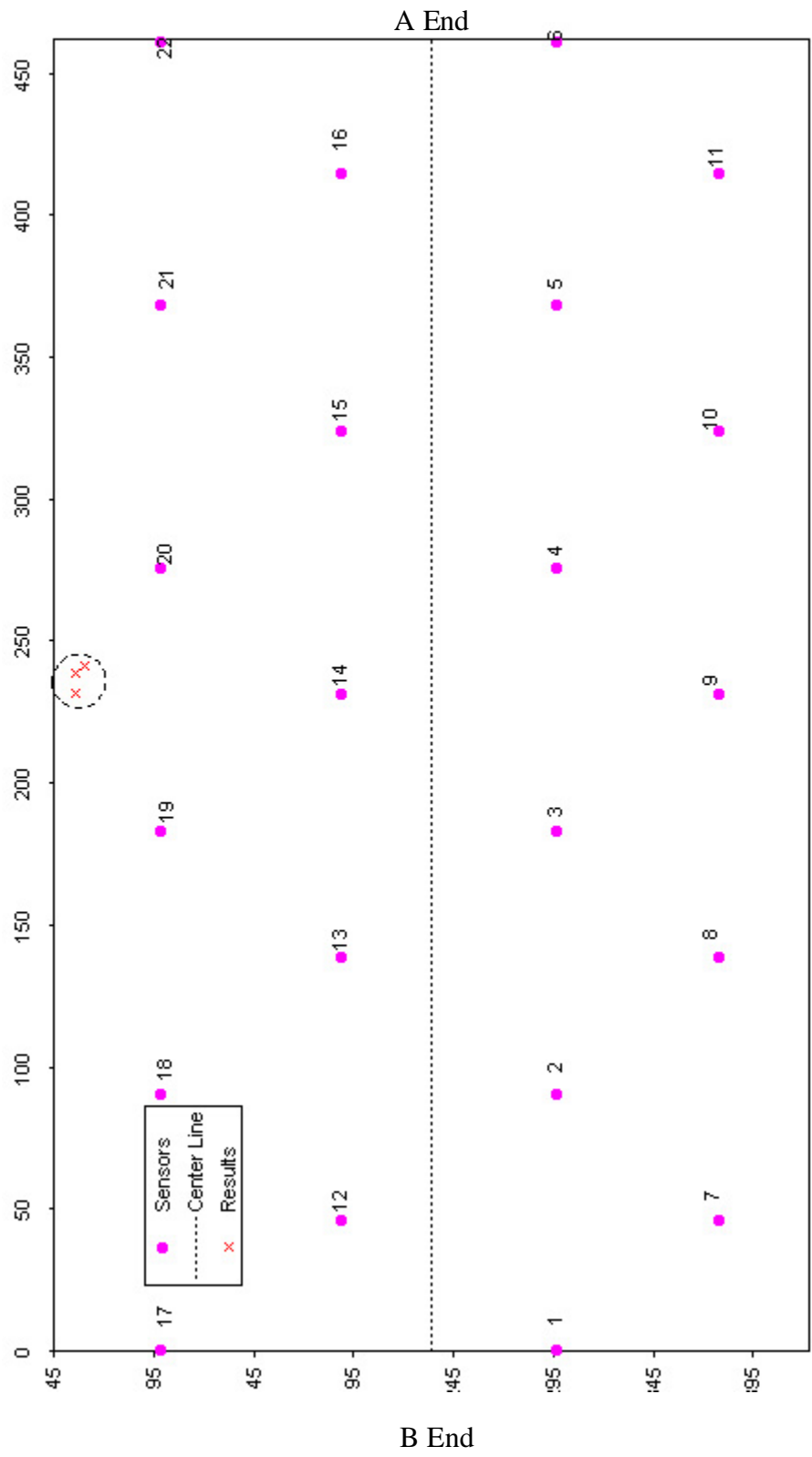


Figure 6.10 - Final Results for Data from the Fourth Group

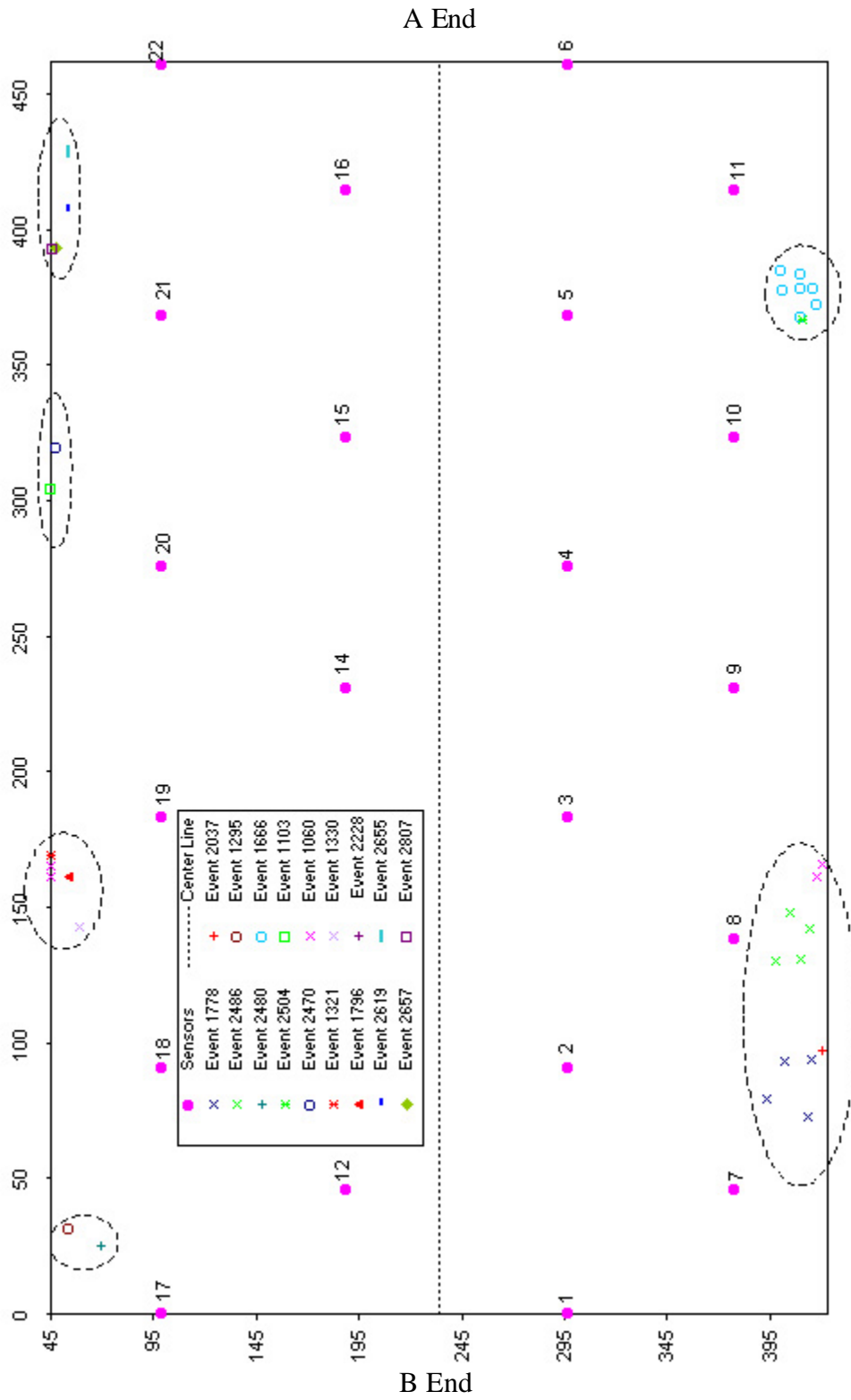


Figure 6.11 - Results from Combinations of Three Sensors from the Fifth Group

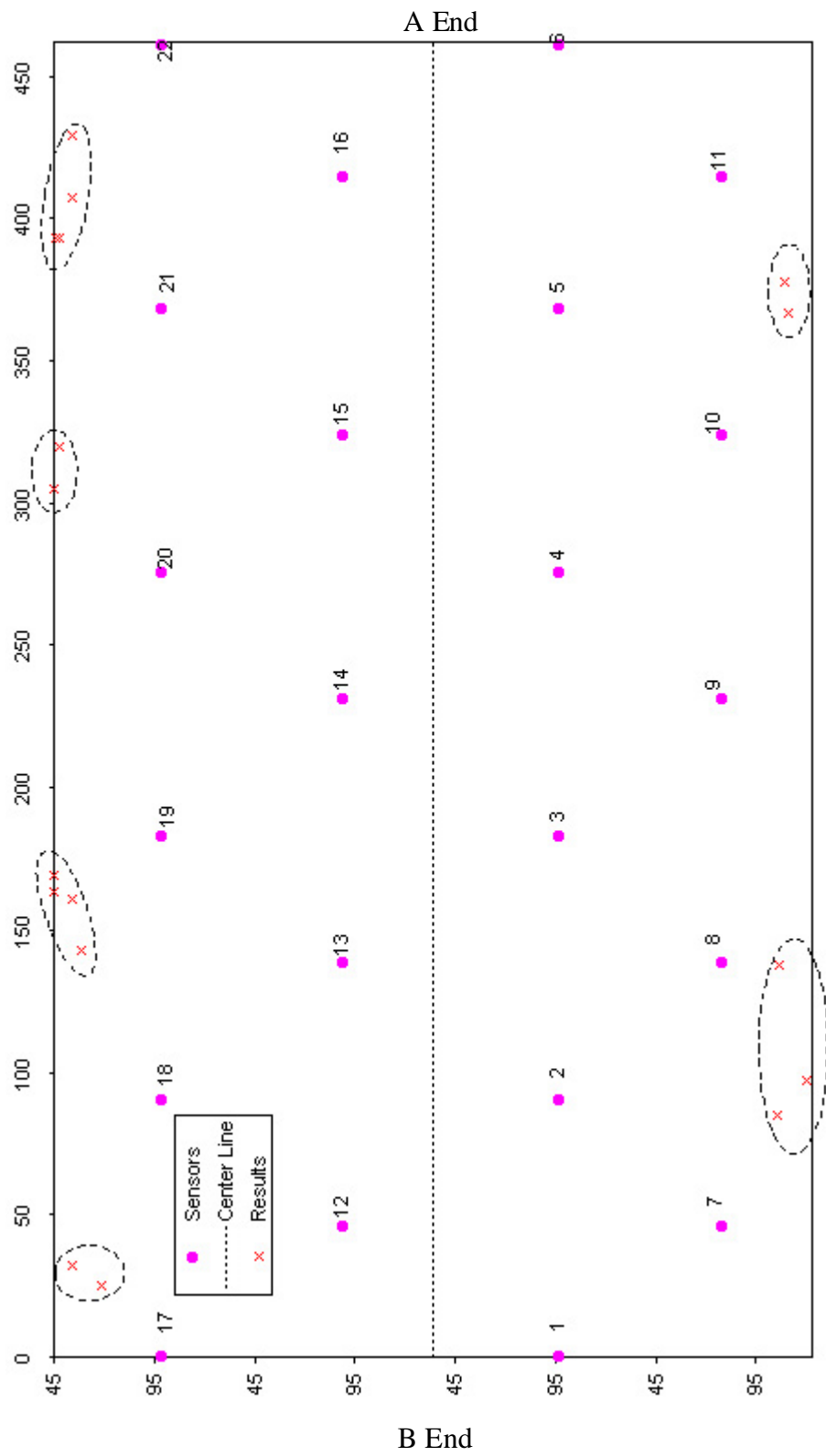


Figure 6.12 - Final Results for Data from the Fifth Group

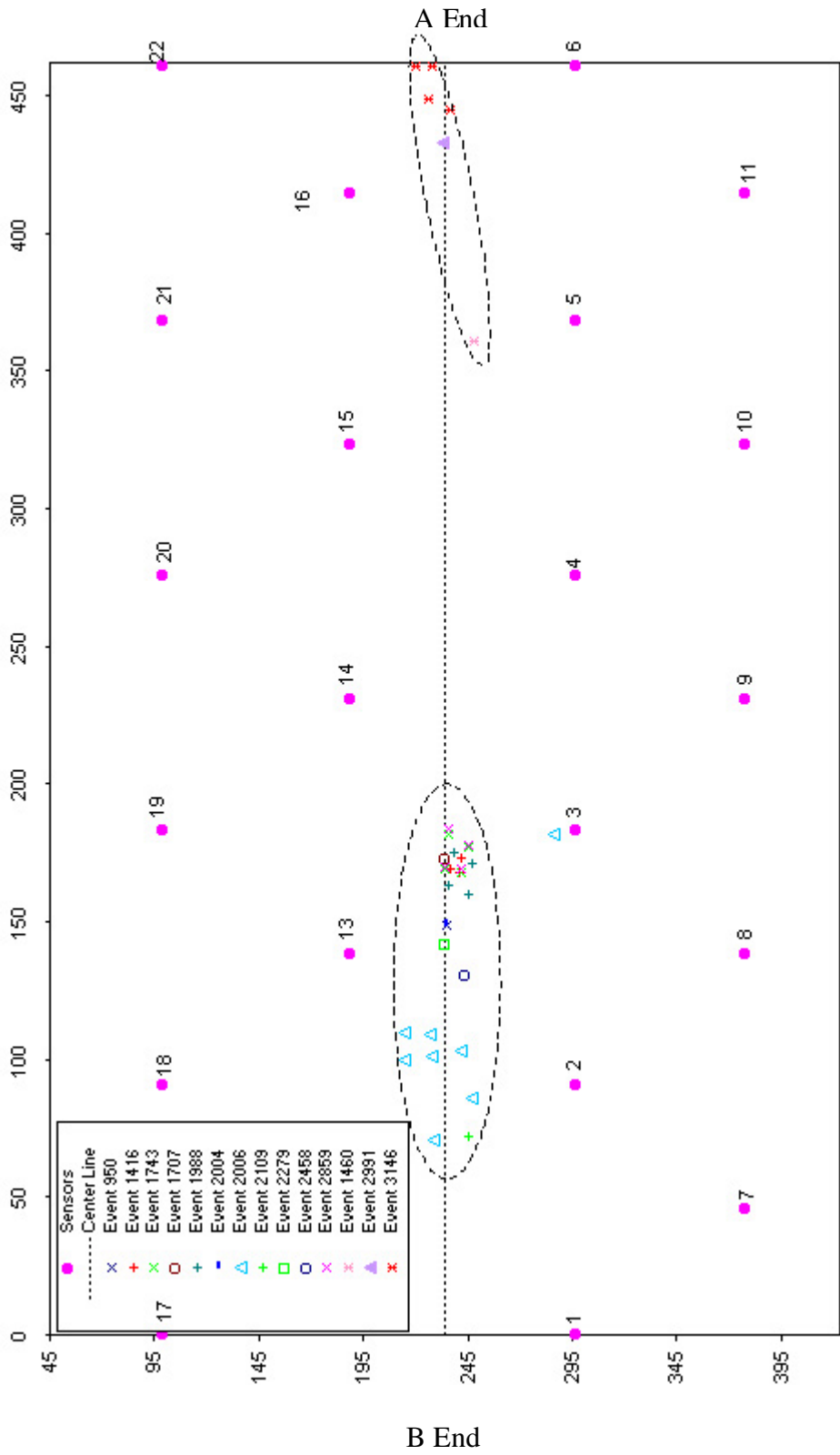


Figure 6.13 - Results from Combinations of Three Sensors from the Sixth Group

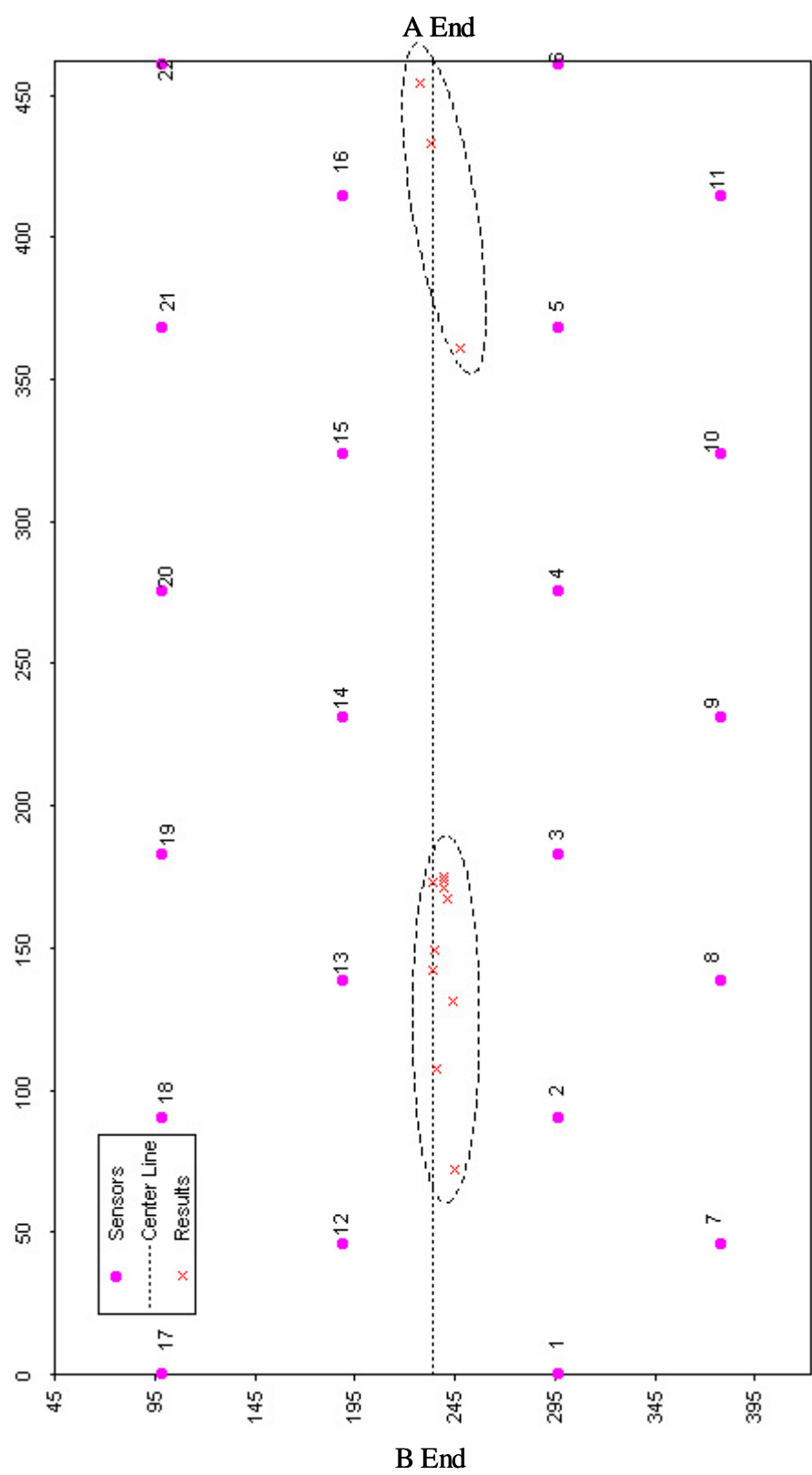


Figure 6.14 - Final Results for Data from the Sixth Group

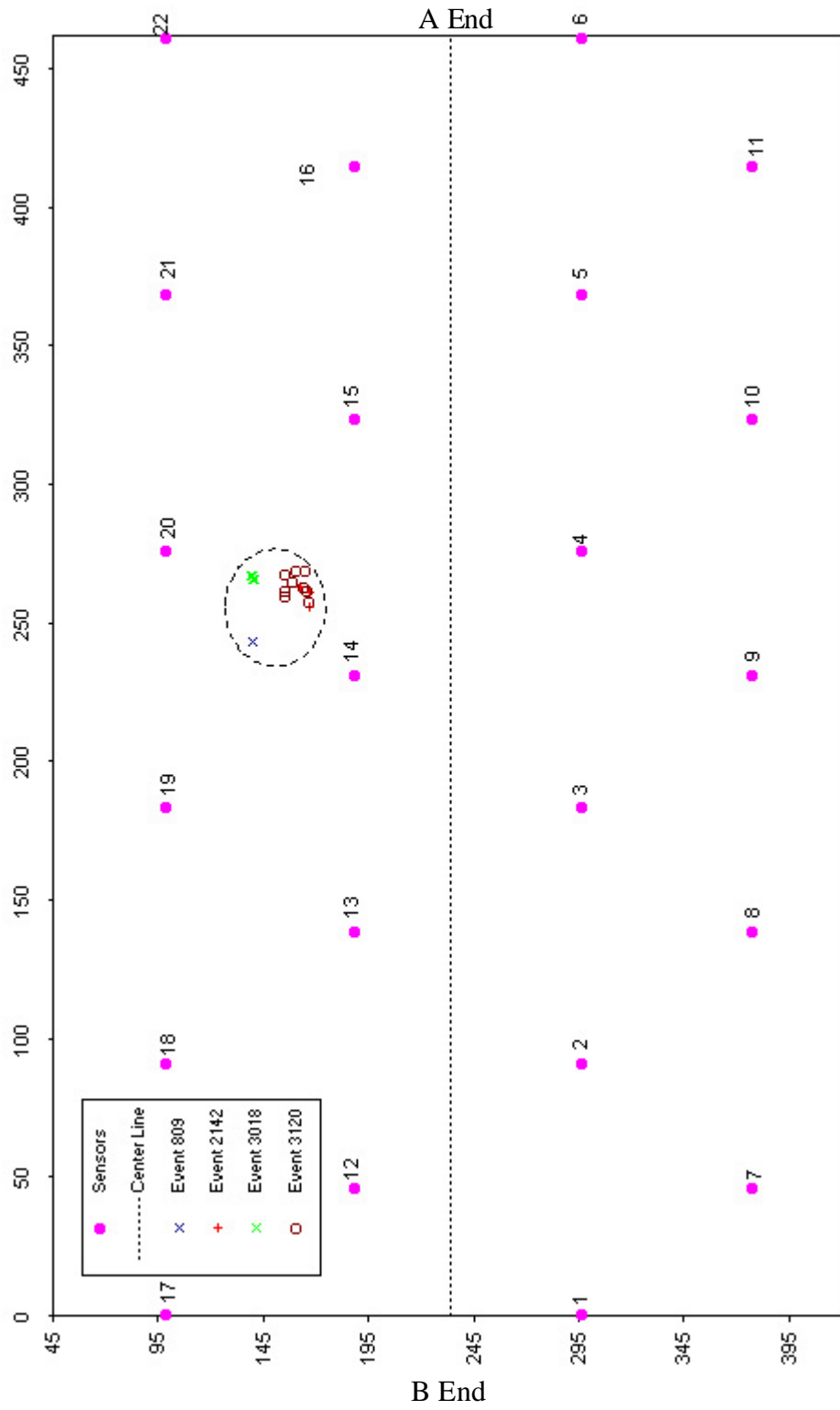


Figure 6.15 - Results from Combinations of Three Sensors from the Seventh Group

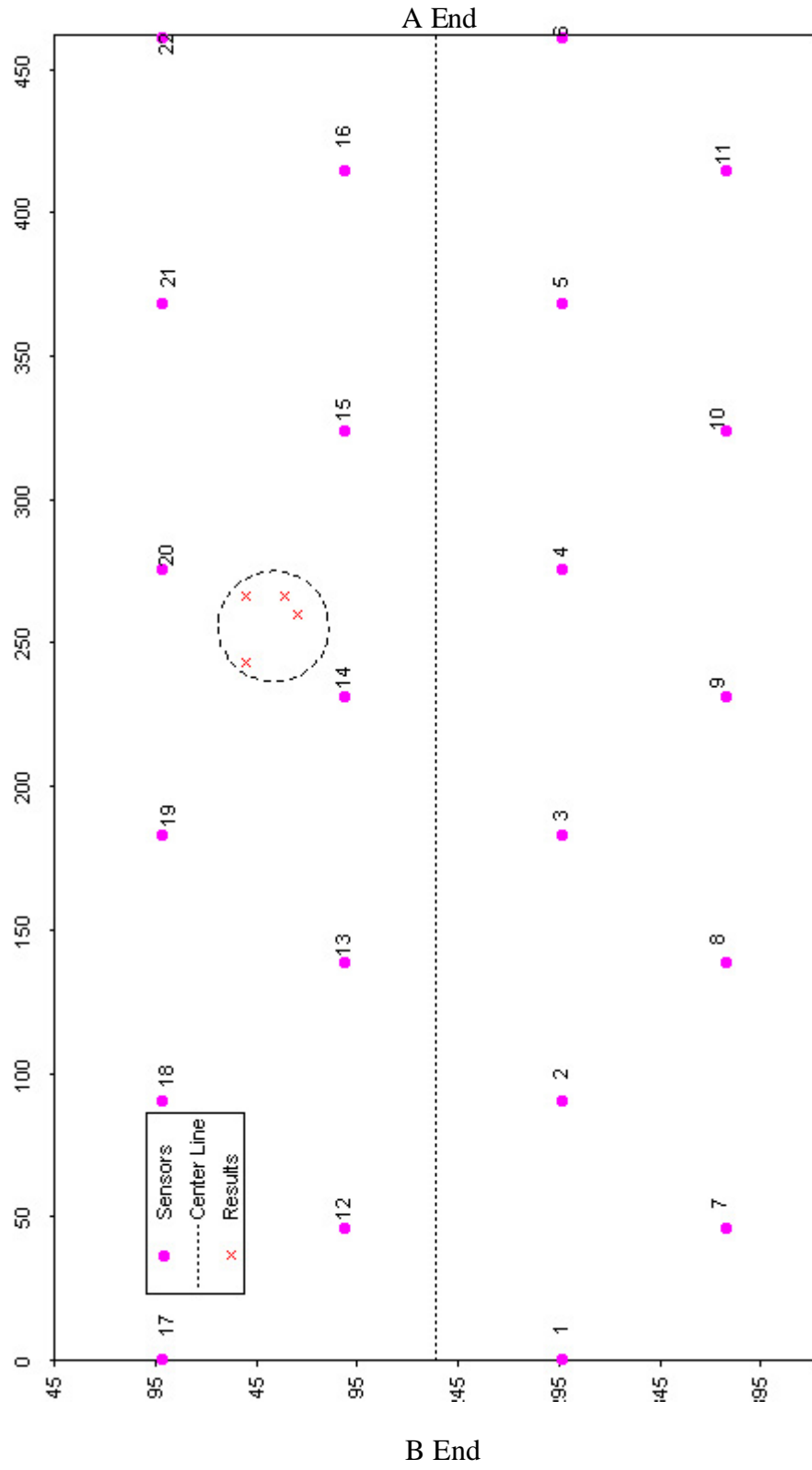


Figure 6.16 - Final Results for Data from the Seventh Group

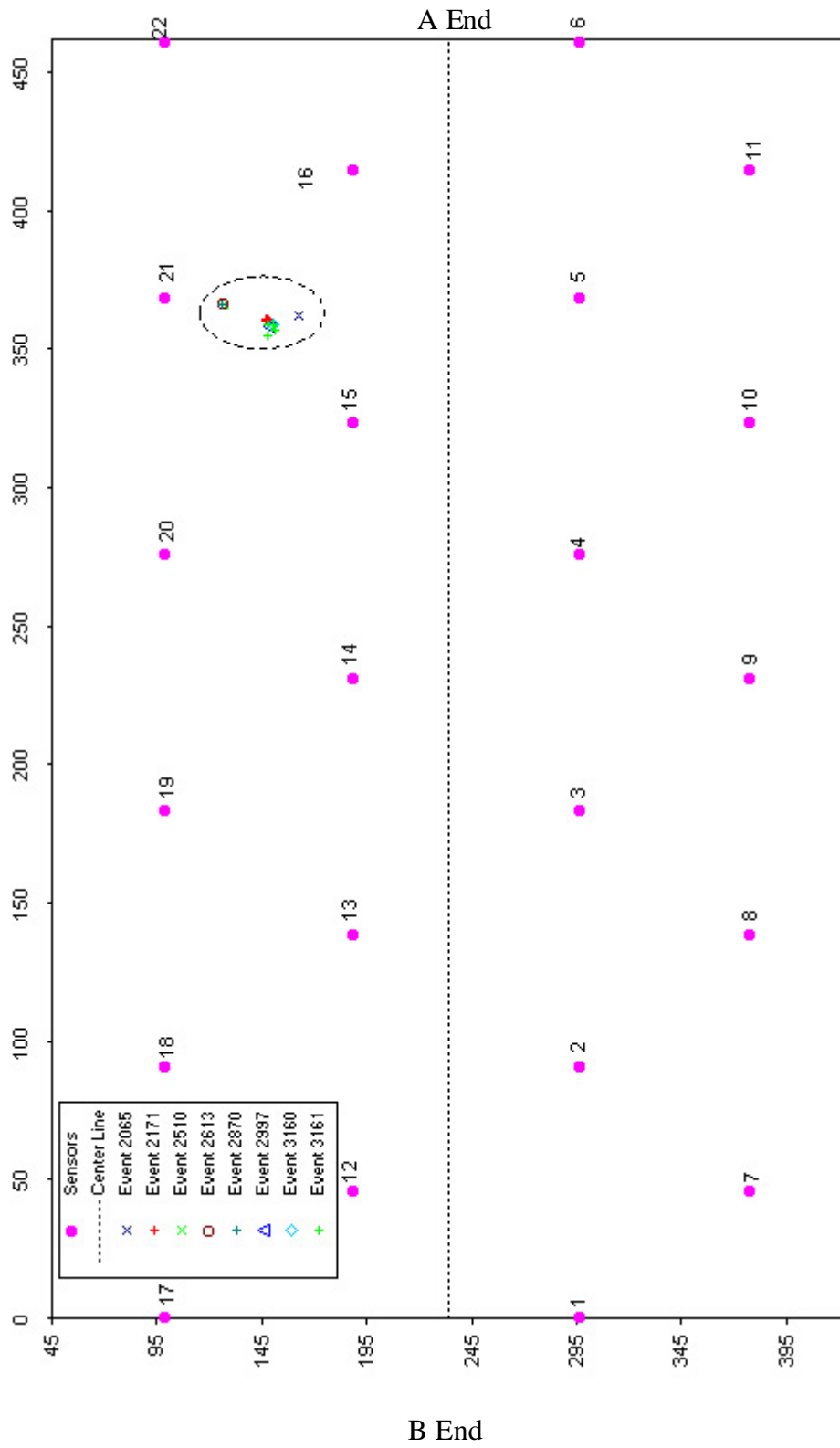


Figure 6.17 - Results from Combinations of Three Sensors from the Last Group



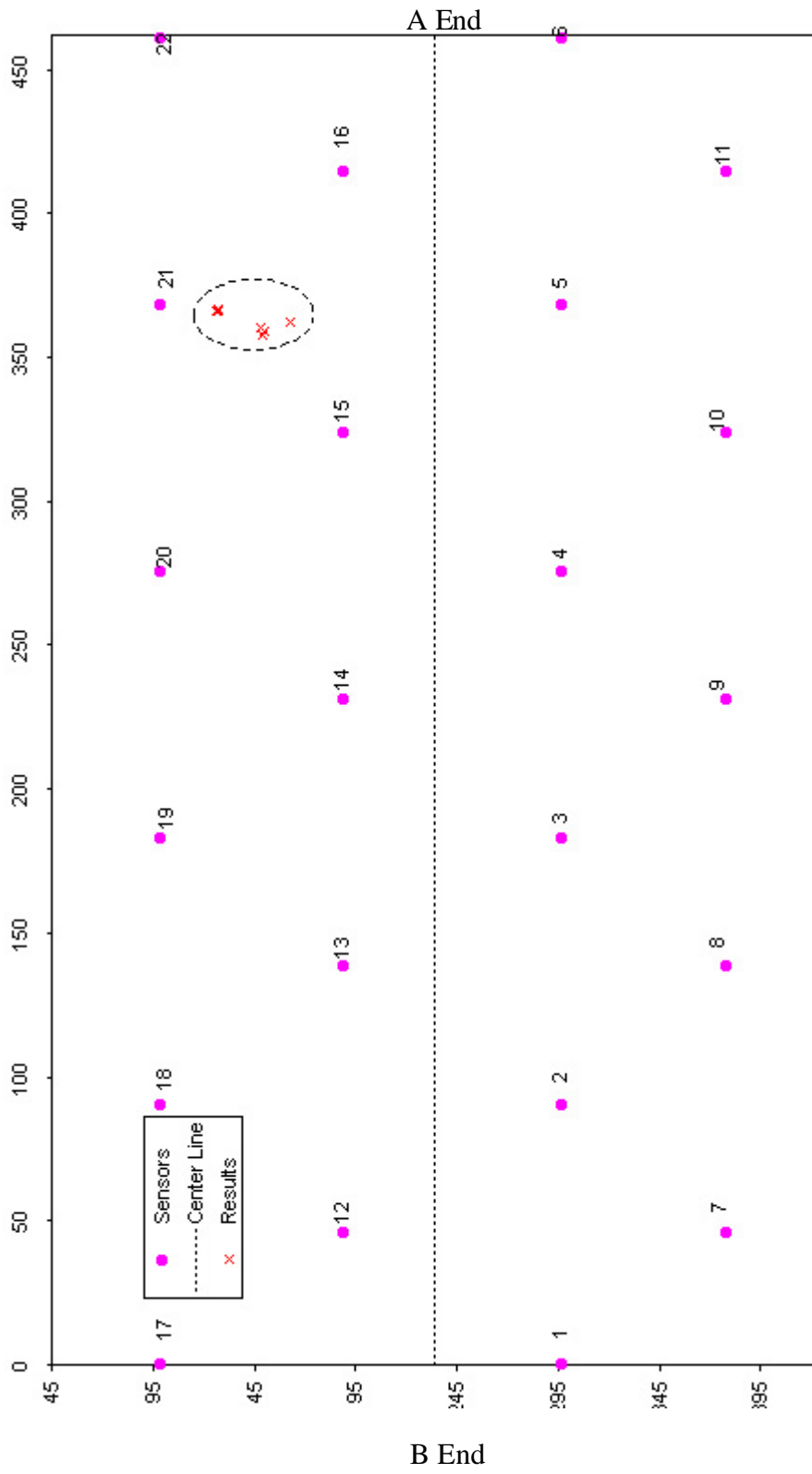


Figure 6.18 - Final Results for Data from the Last Group

### 6.3.2 Discussion of the Source Location Method and Results

In this test, R6I resonant sensors were used, therefore the source location method based on the non-leaky part or the low frequency range is not applicable. The method used in the preceding section still focuses on a tight frequency band to minimize the dispersion problem. The frequency band is chosen so that it included the intersection of the first three waves modes. This point occurs at 100 kHz for a 13/16" thick shell. At the intersection point, the first three modes travel at the same speed of 125,000 in/sec (3.2 km/sec).

Unfortunately, the tank car has severe internal corrosion and blistering resulting in variations in the thickness. The ultrasonic test performed on a local area of the tank reported that the thickness of the shell varied from 0.4" to 0.8" (see Figure 4.28). The group velocity dispersive curve for the nominal thickness of the car (13/16") and for the shell with 0.4" thickness are shown in Figures 6.19 and 6.20.

It is seen that the intersection point of the first three modes moves from 100 kHz to 210 kHz when the thickness decreases from 13/16" to 0.4". Since the source location method works on a tight band frequency at 100 kHz, the filtered waveform obtained from a 0.4" thick area contains two wave modes. The first mode travels much faster than the second mode. The group velocity of the second mode at a 100 kHz is almost the same as the group velocity of the first three modes for a 13/16" thick area. For this reason, it is desirable to base the arrival time on the second mode. Generally, the energy of the first mode ( $S_0$ ) is very low compared to the energy of the second mode ( $A_0$ ), which means that close to the sensor, the velocity of the second mode will normally determine the hit arrival time.

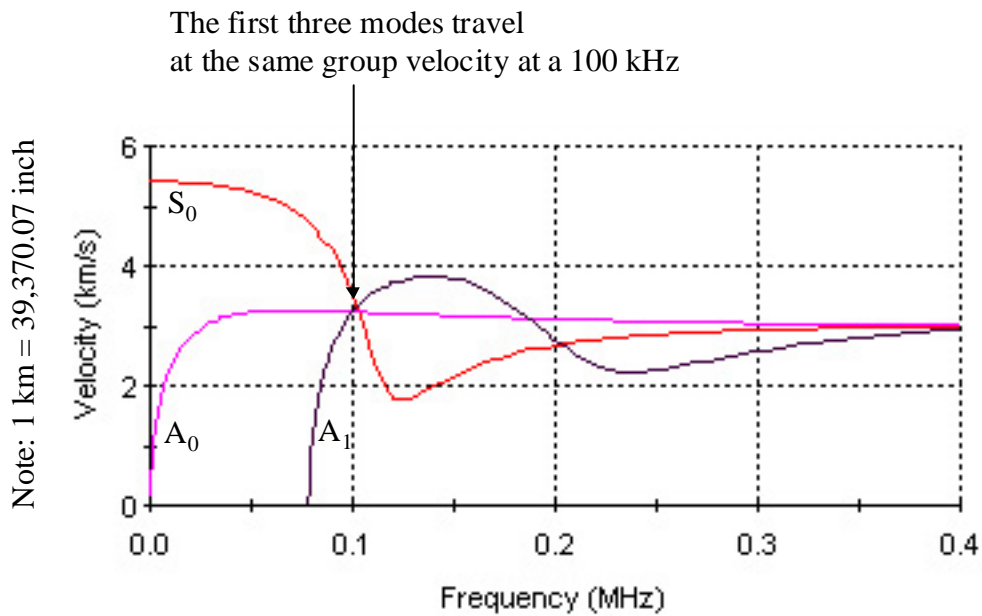


Figure 6.19 - Group Velocity of 13/16" Thick Tank Car Shell

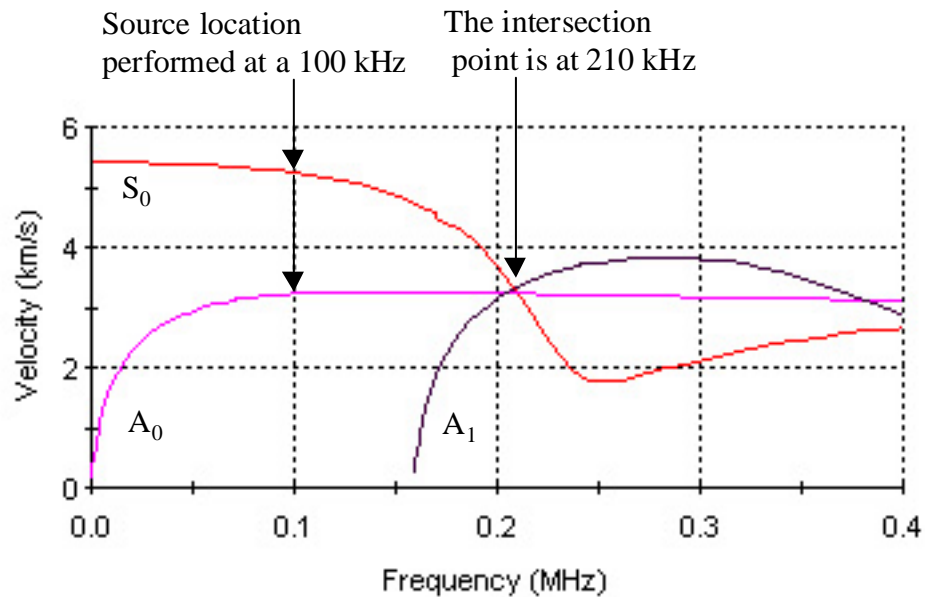
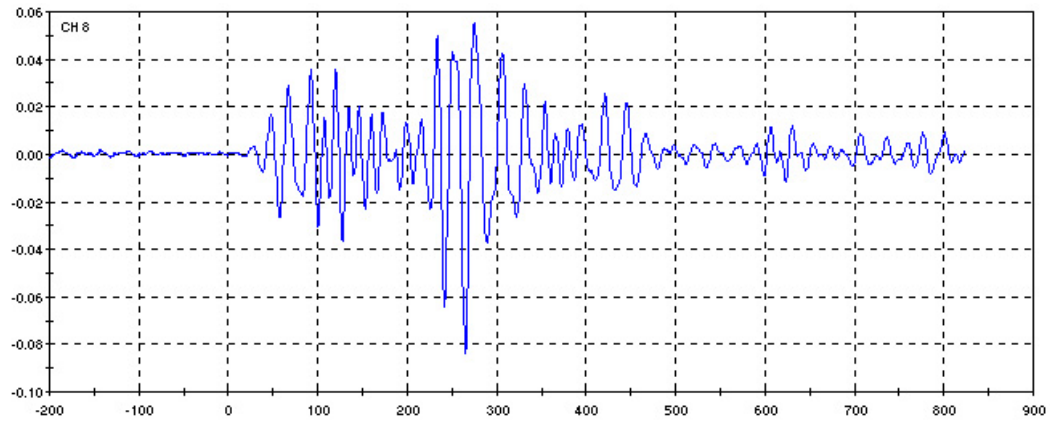


Figure 6.20 - Group Velocity of 0.4" Thick Tank Car Shell

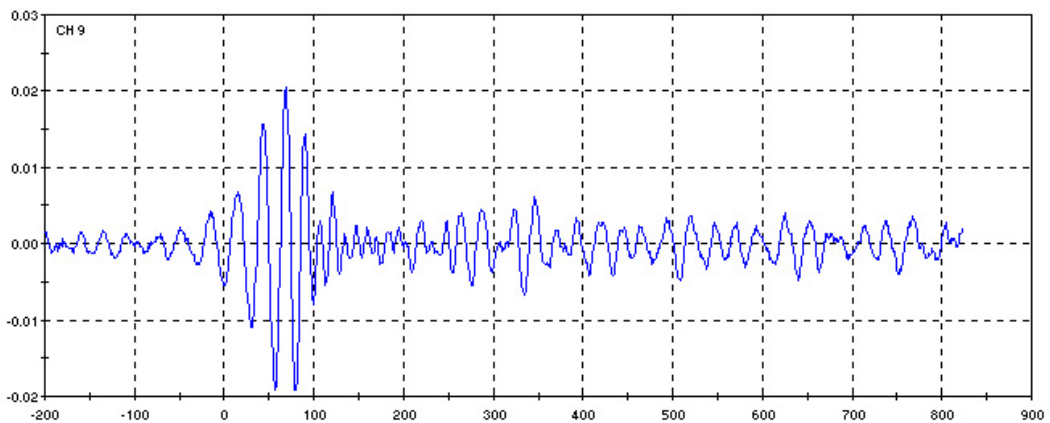
The motion of the first mode is along the direction of travel, whereas, the motion of the second mode is perpendicular to the direction of propagation. Therefore, in a water filled tank car, the second mode radiates energy into the water more than the first mode. This makes it difficult to define the mode from the size of the energy. An example of this problem is illustrated in Figures 6.21 to 6.22. The data are from event 1321 from the internal pressure test. The source was located 134” from sensor 8 and 171” from sensor 9 (see Figure 6.11). Figure 6.21 shows the original waveform and Figure 6.22 shows the waveform filtered at 100 kHz. From the filtered waveform in Figure 6.22, it is seen that the second mode at sensor 9 has less amplitude than the first mode. This is a factor that makes it difficult to select the arrival time based on the second mode which for the thin area of the tank has approximately the same velocity as the first three modes in the original thickness area.

In the analysis, the approach of using combinations of three sensors and simplex optimization was used to eliminate the water borne wave. With this technique, at least three or more sensors must detect the signal through the shell path. Unless this occurs, the water borne hit cannot be separated from the group. Partly because of this limitation, more than 50% of the events cannot be located.

Most of the source locations presented in the previous section are located at the bottom of the tank car. The first group of events discussed in Section 6.3.2 is used in the following section to study water borne waves.

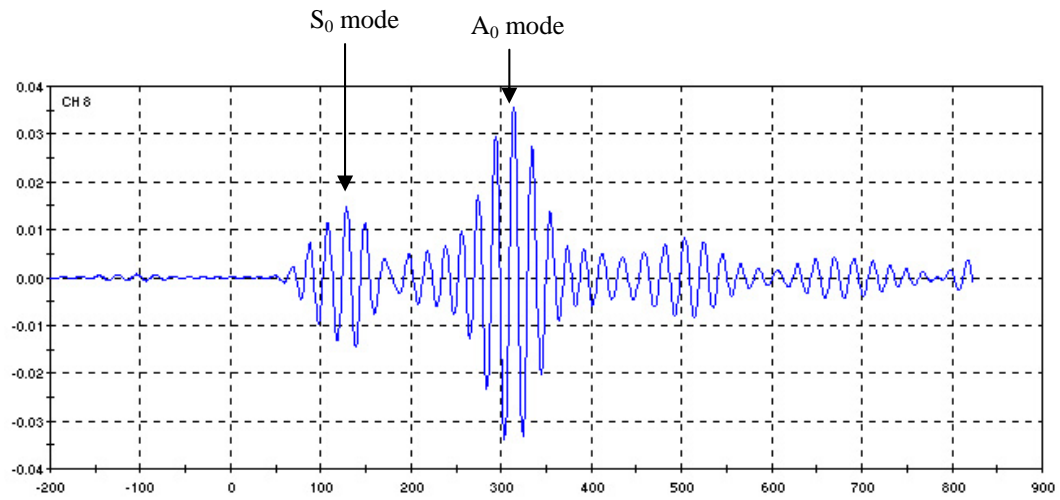


a) Original Waveform from Sensor 8

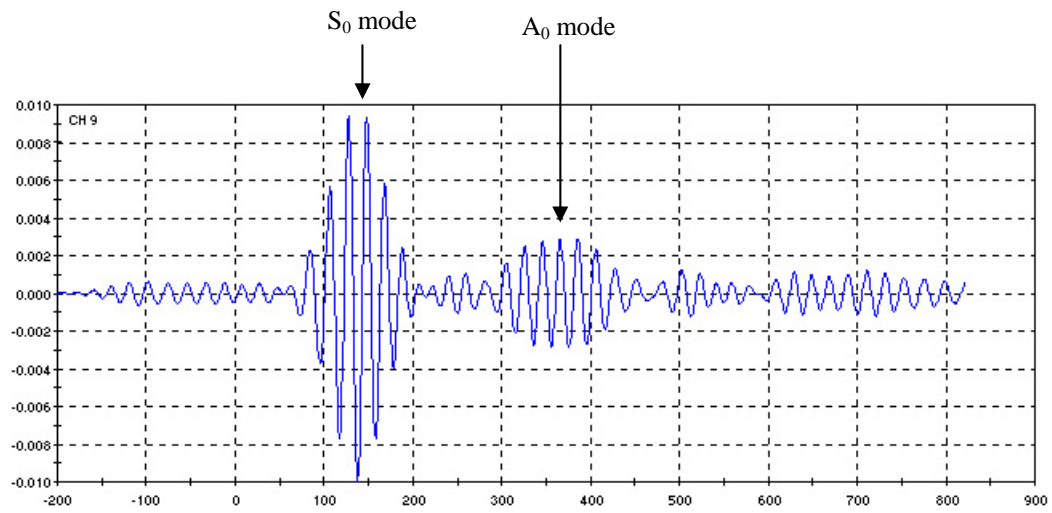


b) Original Waveform from Sensor 9

Figure 6.21 - Original Event 1321 Waveform



a) Filtered Waveform from Sensor 8



b) Filtered Waveform from Sensor 9

Figure 6.22 - Filtered Event 1321 Waveform at a 100 kHz

## 6.4 WATER BORNE WAVE STUDY

The results from the internal pressure test presented in Section 6.3.1 show that most of the emission came from the bottom of the tank car. The sources of the first group of events are grouped in one area at the bottom of the tank, approximately 270 inches from the B end. In this section, this group of data is used to study water borne waves.

There are 29 events in the first group. In two out of 29 events, two sensors detected water borne waves. This section analyzes the data from one of these events. The data were bandpass filtered at 100 kHz and the median of the negative and positive peaks was used to define the arrival time.

Figure 6.23 shows the results from Event 1744 using combinations of 3 sensors from the six sensors that received hits. These sensors with hits are 9, 10, 19, 20, 21, and 13. The number of analysis sets for every combination of three sensors is 35 sets. The plot shows only the results with a low Flag value. It is seen that every sensor combination that includes sensor 13, yields results out of the group. This means the either sensor 13 detects another source (multiple source problem) or a water borne wave from the other side of the tank. In this study, it is assumed that sensor 13 detects the water borne signal. Therefore, source location was calculated using the shell path and Sensors 9, 10, 19, 20, and 21. The time of the original event ( $t_0$ ) was calculated from the five sensors used for the source location. The difference between  $t_0$  and the arrival time at sensors receiving the water borne signals are calculated. These data are used to in the following analyses.

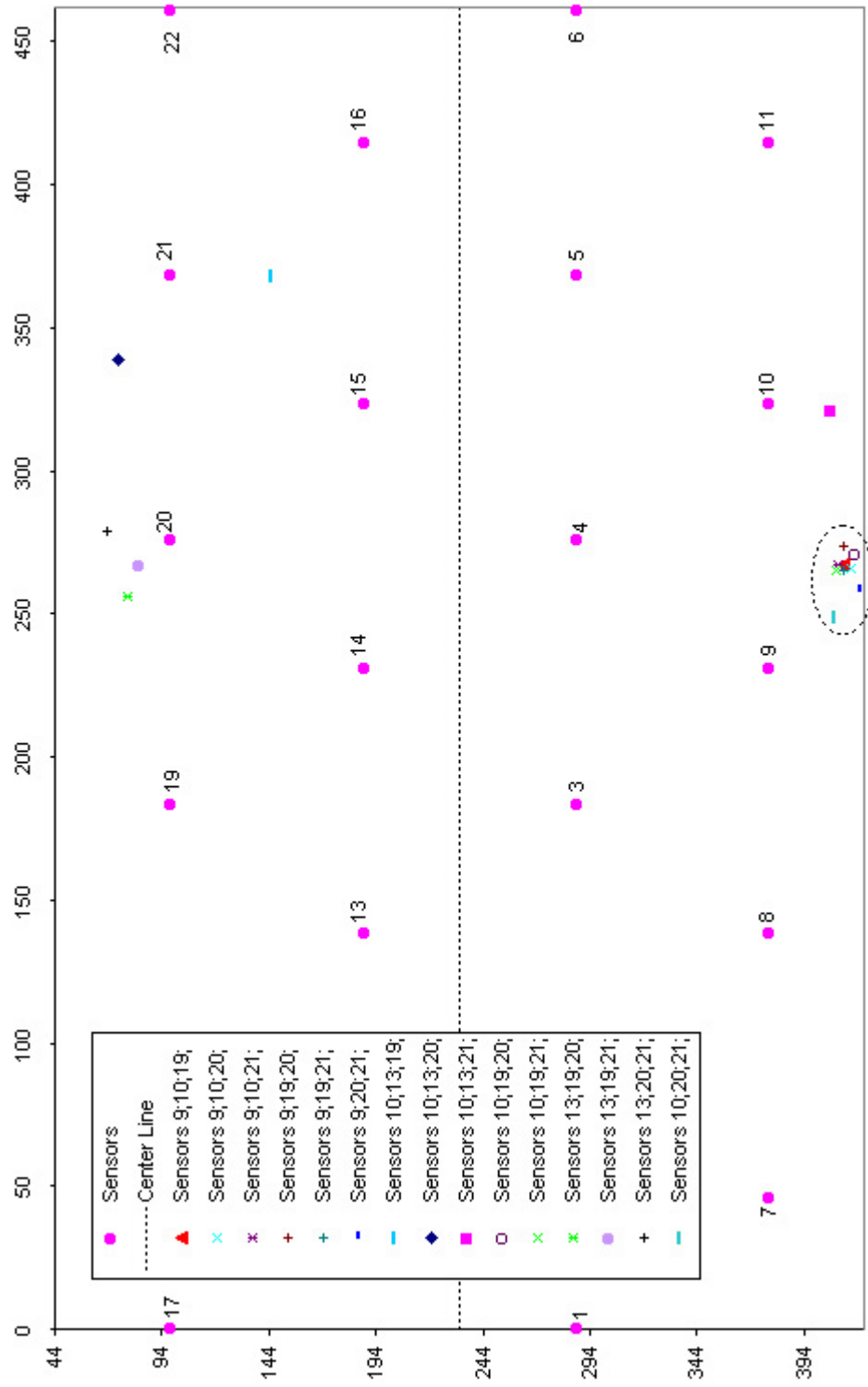


Figure 6.23 - Source Location Results for Event 1744 Including Water Borne Wave



- *Measured Data*

Seven sensors detected the signal from this event. Five sensors (sensors 9, 10, 19, 20, and 21) detected the signal from the shell path and the other two (sensors 13 and 15) detected the water borne signal. The position of the source was calculated using the sensors that received the signal through the shell. The source has coordinates 264, 413. The times of the original event ( $t_0$ ) were calculated from Sensors 9, 10, 19, 20, and 21 assuming a wave velocity of 125,000 in/sec. The differences between  $t_0$  and the arrival time at sensors 13 and 15 are shown in Table 6.1.

Sensor used for calculating $t_0$	Difference in the arrival time between Sensor 13 and $t_0$ (Sec)	Difference in the arrival time between Sensor 15 and $t_0$ (Sec)
9	0.00290675	0.00258125
10	0.00294705	0.00262155
19	0.00289035	0.00256485
20	0.00297185	0.00264635
21	0.00291185	0.00258635
Average	<b>0.00292557</b>	<b>0.00260007</b>

Table 6.1 – Measured Differences in the Arrival Time between  $t_0$  and Sensors 13 and 15.

- *Theoretical Model*

The average event location from Sensors 9, 10, 19, 20, and 21 is shown in Figure 6.24. The source was located at the coordinate 264, 413 and the point opposite to the source is marked as “O”, which has the coordinate 264, 224.

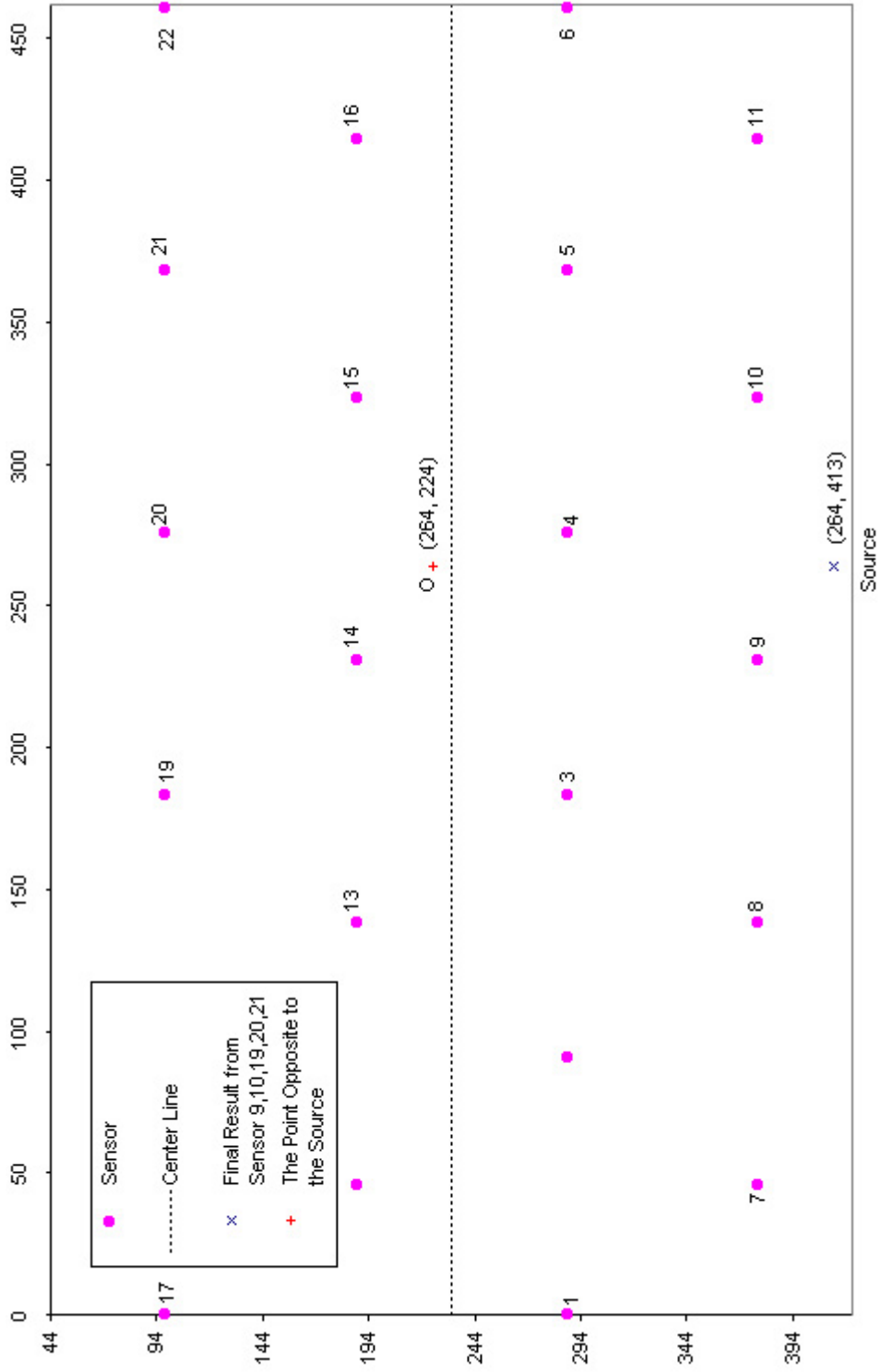


Figure 6.24 - Event 1744 Final Results

From the water borne study in Chapter 5, it is known that the wave propagates from the source in every direction but in order for the wave to enter the steel on the opposite side of the tank it must strike on the angle between  $0^\circ$  and  $27.3^\circ$ . This section calculates the time for the wave to propagate through the water, into the shell, and then propagate to sensors 13 and 15. Figure 6.25 shows the top view of the shell showing the position of sensors relative to the point on the shell (O) directly opposite the source. Line BC is the line along the length of the tank car passing through point O. Line AA is the line along the circumference passing point O. Line A'A' is the line parallel to line AA located X inches from line AA.

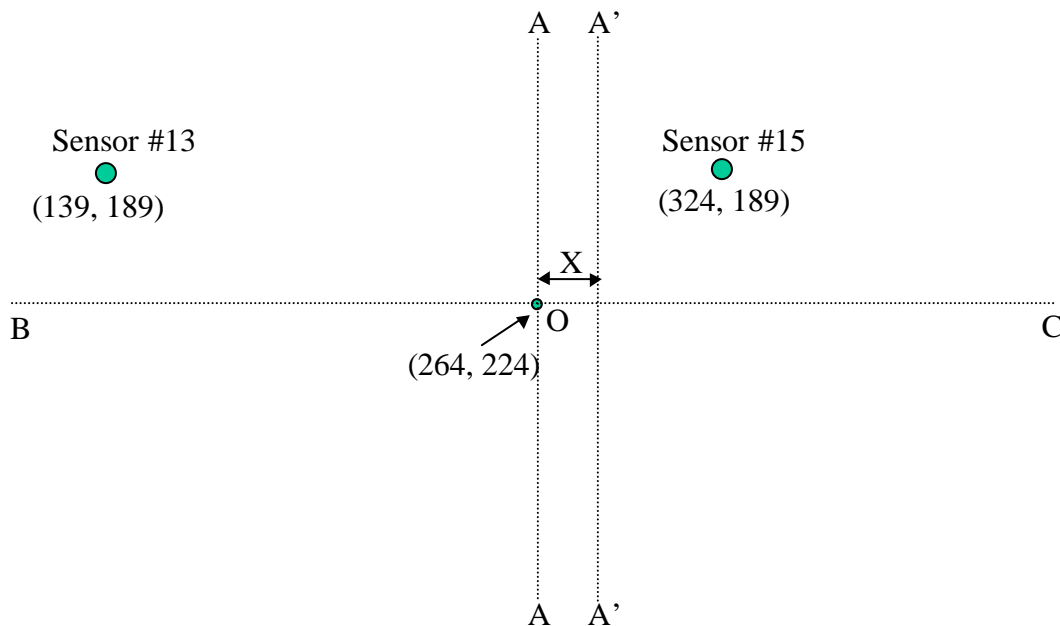


Figure 6.25 – Top View of Shell Showing Position of Sensors Relative to Point on Shell (O) Directly Opposite Source

Since the tank car is cylinder, the incident points with the same angle at different lines (BC, AA, and A'A') are not located the same distance from the position O. Figure 6.26 shows the water borne wave path that forms the basis of the calculations for the incident angle on line BC.

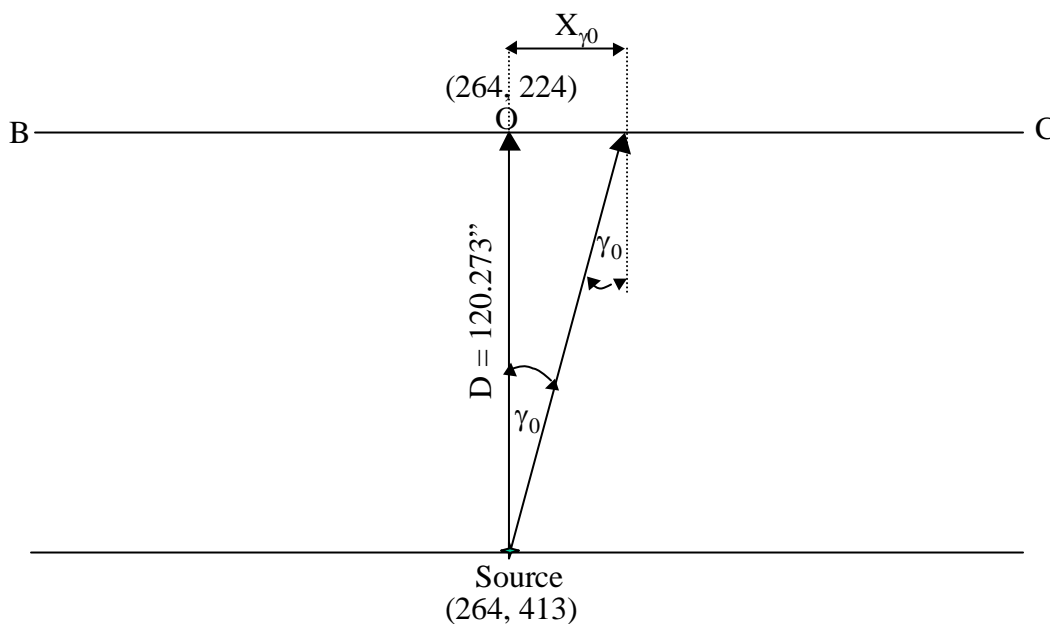


Figure 6.26- Side View of the Tank Showing the Point the Incident Water Borne Wave Strikes on Line BC with Angle  $\gamma_0$

$X_{\gamma_0}$  for any incident angle  $\gamma_0$  at line BC is calculated by:

$$X_{\gamma_0} = 120.273 \tan (\gamma_0) \dots \dots \dots (6.1)$$

Figures 6.27 and 6.28 show the water borne wave paths that form the basis of the calculations for the incident angle on line AA and A'A'. Note that line A'A' is X inches from line AA.

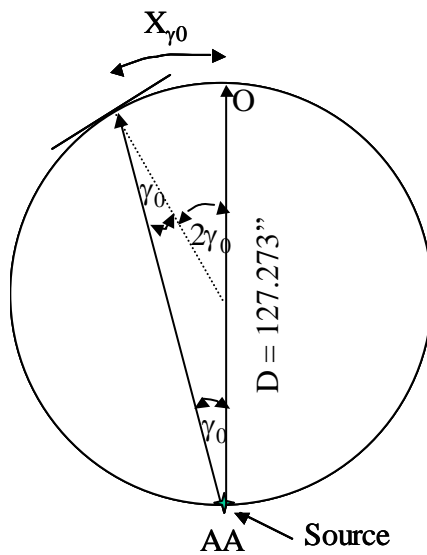


Figure 6.27 – Section AA Showing Wave Propagation Through Water with Incident Angle  $\gamma_0$

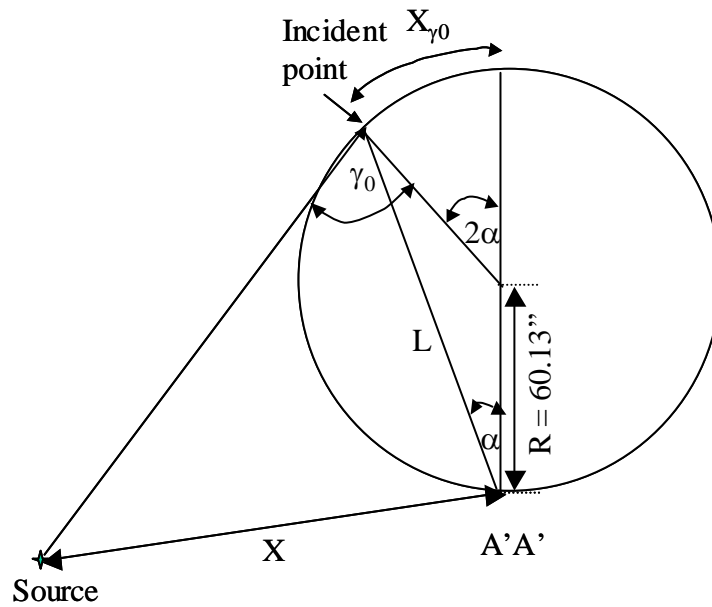


Figure 6.28 – Section A'A' Located X inches from Section AA Showing Wave Propagation Through Water with Incident Angle  $\gamma_0$

$X_{\gamma_0}$  for the incident angle  $\gamma_0$  at section AA is calculated by:

$$X_{\gamma_0} = \frac{2(\gamma_0)\pi D}{360} \dots\dots\dots(6.2)$$

The calculation for  $X_{\gamma_0}$  for the incident angle  $\gamma_0$  at section A'A' is more complicated. From the triangle inside the circle, L can be computed by:

$$L = 2R \cos(\alpha) \dots\dots\dots(6.3)$$

For the triangle from source to the incident point and to point A', L can be computed by:

$$L = (\sqrt{L^2 + X^2}) \sin(90 + \gamma_0 + \alpha) \dots\dots\dots(6.4)$$

Substituting L from equation 6.3 in equation 6.4 and for a given value of the incident angle  $\gamma_0$ , the angle  $\alpha$  can be calculated. This process is carried out by trial and error procedure for different values of  $\gamma_0$ . The calculation for  $X_{\gamma_0}$  (Figure 6.28) for the incident angle  $\gamma_0$  at section A'A' can be calculated by:

$$X_{\gamma_0} = \frac{2(\alpha)\pi D}{360} \dots\dots\dots(6.5)$$

The incident angles of  $-15^\circ$ ,  $-7^\circ$ ,  $0^\circ$ ,  $+7^\circ$ , and  $+15^\circ$  are calculated and the contours of these incident angles are plotted in Figure 6.29.

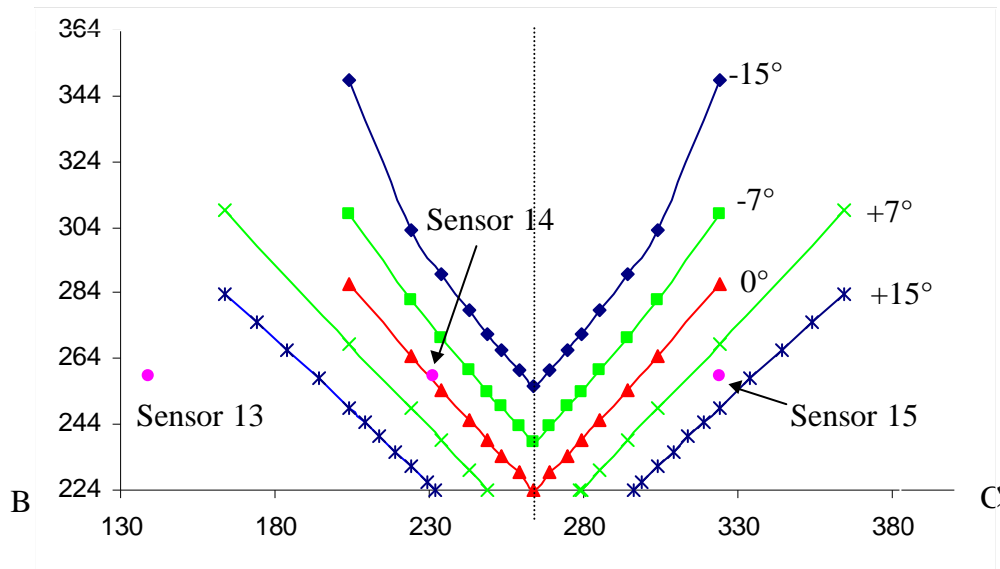


Figure 6.30 – Top View of the Tank Showing Incident Angle Contour Plots of 0, 7, and 15 Degrees

For incident angles that are positive, the transmitted waves propagate outward from point O. For negative angles the waves propagate back towards point O.

The path that the wave takes to reach sensor 13 through the water with an incident angle of 15 degrees is shown in Figure 6.31. The calculated time is 0.002890 seconds. This compares with the measured time of 0.00291 seconds.

Sensor 14 did not detect the signal. This is because sensor 14 was located in the negative angle zone in the position that only extensional wave could reach it. When the wave incidents at the negative angle, it propagates back toward point O.

The plot of the total time that the wave takes to reach sensor 15 as a function of the incident angle of the water borne wave is shown in Figure 6.32.

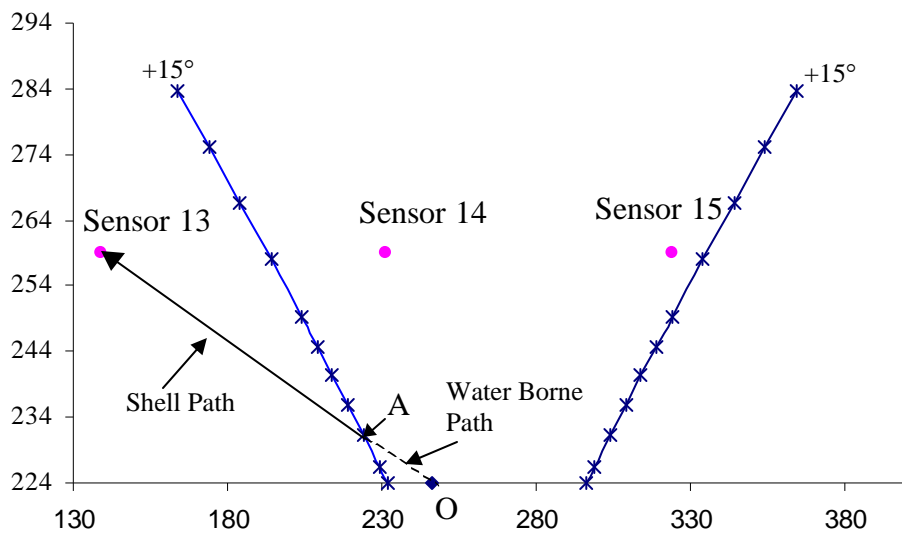


Figure 6.31 – Source Propagates through Water and Incident at Point A and Propagate along the Shell to Sensor 13

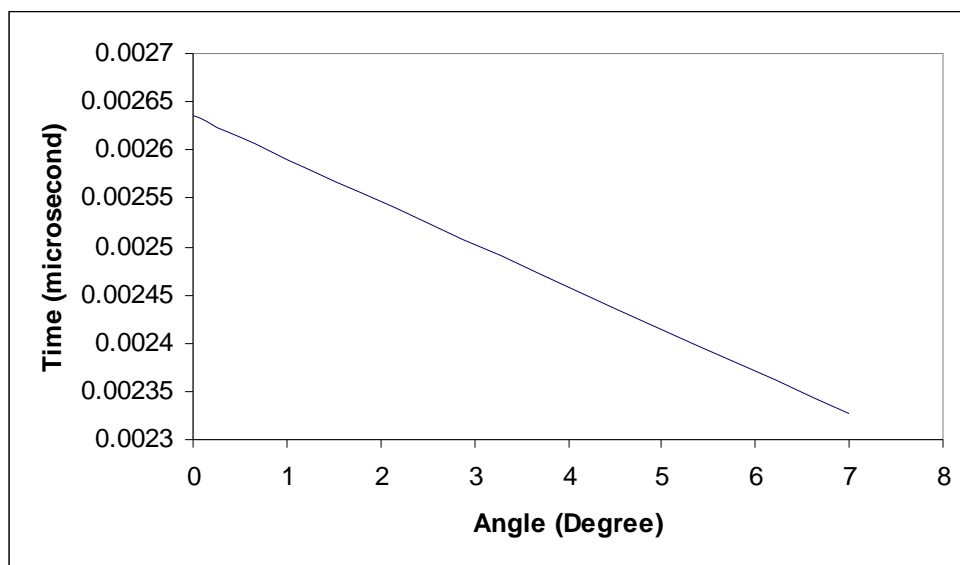


Figure 6.32 - Calculated Time for the Wave to Propagate from the Source to Sensor 15 Versus the Angle of the Incident Water Borne Wave



- *Discussion*

The average measured time for the wave to propagate to sensor 13 is 0.00292 microseconds (see Table 6.1). The time calculation for the wave to propagate to sensor 13 with an incident angle of 15 degree is 0.002890. In this case, the result is in agreement with the results reported in Section 5.4.5.3. This is close to the angle that generates the transverse mode with the most energy. At this angle, approximately 20% of the energy in the incident wave is transmitted into the shell.

The average measured time for the source to propagate to sensor 15 is 0.00260 microseconds (see Table 6.1). From the incident contour in Figure 6.30, it is seen that the wave can not reach the sensor when it is incident at +15 degree. From Figure 6.32, the value matches the incident angle of between 0 and 1 degree. This is the angle that generates the longitudinal mode with the most energy. At this angle, approximately 11% of the energy in the incident wave is transmitted into shell.

## **6.5 SUMMARY**

This chapter reports the source location results from an internal pressure test. The source location approach uses a tight band-pass frequency filter at a 100 kHz. The median of the negative and positive peaks are used to define the arrival time. With the algorithm based on combinations of three sensors, the water borne waves are eliminated from the analysis. The results show that most of the defects were in the bottom of the tank car.

The locations of the flaws analyzed as the first group are in a very small area. The data from this group are used for the study of water borne waves. The

analysis of the water borne waves in this chapter shows good agreement with the study of the water borne waves from a bar bending, which were reported in Chapter 5. The studies show that although the water borne wave diffracts in different direction, only oblique incident angles are able to transmit the energy into the tank car shell. At an incident angle of  $14.5^\circ$ , the transverse component that is produced in the shell has the highest energy content. The experimental data shows that a water borne wave striking the shell at an angle of 15 degree is consistent with the time of arrival of the wave at a sensor on the tank wall opposite the source.

## **Chapter 7**

### **Exploratory Source Location Studies in Composites**

#### **7.1 INTRODUCTION**

The purpose of the research reported in this chapter is to explore alternative methods of approaching the source location problem in composites. The studies were performed on a fiber reinforced composite pipe. Details of the specimen are discussed in Section 7.2. The study first focused on the difference in the arrival time source location technique that was applied successfully to an empty and full tank car (see Chapters 3 to 6). Therefore, the work started from measurement of wave velocities in different directions. The results are presented in Section 7.3. As shown in Chapter 2, the theoretical analysis of wave propagation is considerably more difficult in composites than in a homogeneous material. The experimental results from Section 7.3 confirmed the complications of wave propagation paths and speeds, factors which make it more difficult to use the conventional source location method. In order to address these problems, a neural network approach using multi-layer perceptron (MLP) with error back propagation is introduced in this chapter as discussed in Section 7.4. Section 7.5 discusses the experimental program and results obtained from the neural network approach. Finally, conclusion and recommendation for the future research are presented in Section 7.6.

## 7.2 SPECIMEN AND INSTRUMENTS

The specimen used in the study is a fiber reinforced epoxy pipe made by the filament winding process. The reinforcement is E-Glass with 60% content by weight and a winding angle of  $\pm 56$  degrees. The pipe is 3 feet long, 5.95" diameter and 0.37" wall thickness. The pipe has a tapered overwrap at each end. The clear length of the pipe between the overwraps is 20 inches. The pipe is shown in Figure 7.1. Note that the pipe selected in this study is only one of many different types of fiberglass composites. The results from the study of this pipe might be very different for other types of composites such as mat construction and woven roving.



Figure 7.1 – Glass Fiber Reinforced Epoxy Pipe

The six channel MISTRAS digital acoustic emission monitoring system was used with wide band sensors (S9208). Vacuum grease was used as couplant and duct tape was used to attach the sensors to the surface of the pipe.

### **7.3 PRELIMINARY STUDY OF CONVENTIONAL TIME OF ARRIVAL SOURCE LOCATION THE METHOD**

As mentioned earlier, source location in composites was first approached by the conventional method using the arrival time. The studies of the tank cars discussed in Chapters 3 through 6 show that source location can be performed successfully using a tight band-pass filter at the intersection of the group velocity of first three wave modes. However, composites behave very differently from steel and this study began by using experiment and analysis to determine if conventional source location methods are applicable to composites.

In the time of arrival method, the main factor is the wave velocity. Therefore, this section focuses on measurement of the wave velocity in the pipe.

#### **7.3.1 Wave Velocity on Composites**

Conventional source location techniques based on time of arrival have been widely used in homogeneous materials with no discontinuities. In the previous study on a tank car, since the first part of the waveform, or the lowest order symmetric mode (or the first mode), has a severe attenuation problem, the study was focused on the use of the lowest order anti-symmetric mode (or the second mode) instead. The work reported in Chapter 3 to 6 have shown that the difference in time of arrival approach can be used successfully if the dispersive wave is used with a tight band frequency range.

In this work, the velocities were measured based on the first mode, which is the fastest mode, and the first threshold crossing. Generally, the first mode suffers from the attenuation problem and is below the threshold. Therefore, it is difficult to determine. In this case, however, the size of the pipe is small enough that visual inspection of the waveform can be used to determine the correct arrival time of the beginning of the wave mode. This technique requires that each waveform be visually inspected to locate the most likely time of arrival of the first mode. In contrast, the threshold technique usually detects the second mode. The visual inspection technique is subjective, depending on the discretion of the researcher.

- *Wave Velocity in Axial Direction*

Velocity in the axial direction was measured by breaking pencil lead (0.3 mm 2H) every 1 inch away from the first sensor for 12 inches. Two wide band sensors were placed 4 inches apart to capture the waveform. The measurement scheme is depicted in Figure 7.2. The crosses in the figure are the locations of pencil lead breaks.

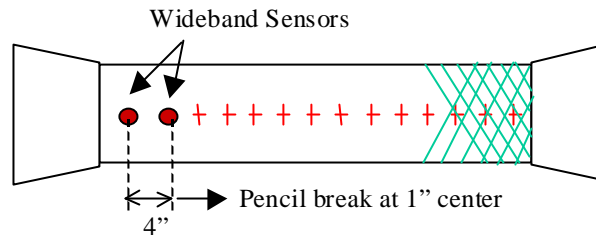
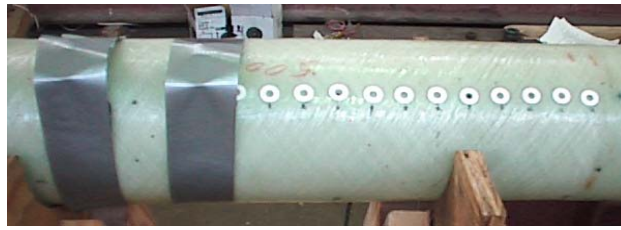


Figure 7.2 – Measurement of Velocity in Axial Direction

With two sensors and the known locations of the sources, the velocity can be determined. The velocity for each pencil break was determined using visual inspection to determine the beginning of the first mode and the first threshold crossing technique. The results of the wave velocities travelling in the axial direction are plotted in Figure 7.3. In the plot, the distance is measured from the source to the midpoint between the two sensors.

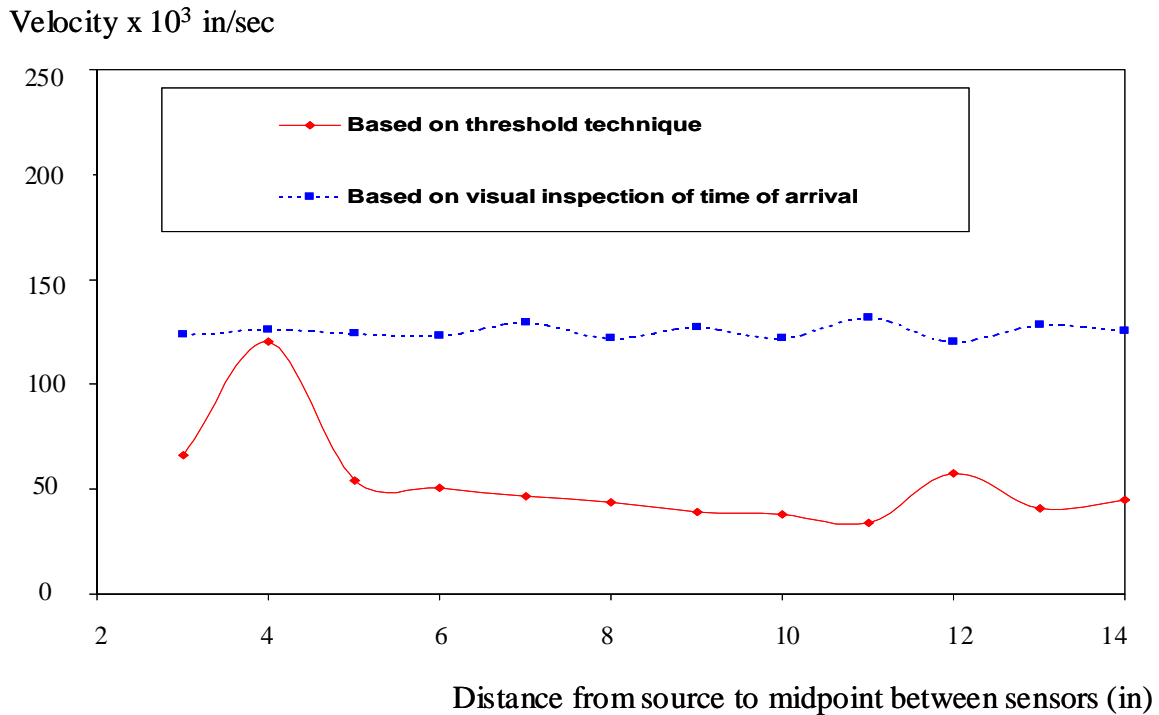


Figure 7.3 – Wave Velocity in Axial Direction

From the plot, the threshold crossing technique seems to be unreliable. When the source is close to the sensors (0"-4"), the method yields a higher velocity compared to the rest. This is because the method detects the arrival time from the first mode, which has higher velocity than the second mode. From 5" to 11", the results seem to be more reliable. The results in this range are lower and slightly decreasing when the source is further away. This is because the threshold crossing technique defines the arrival time from the second mode which travels slower. Attenuation makes the method detect the time at a later phase point as the source travels is moved further away from the sensors resulting in a slight decrease. The velocity based on visual inspection of the wave to determine the



arrival time yielded more reliable results. The average velocity in the axial direction of the fiber reinforced pipes is 125,400 in/sec based on visual inspection of the beginning of the first mode.

- *Wave Velocity in Hoop Direction*

The velocity of travel in the hoop direction was also measured. Sensors were placed two inches apart and pencil lead breaks were performed every one inch away from the sensor for six inches. The measurement scheme is depicted in Figure 7.4.

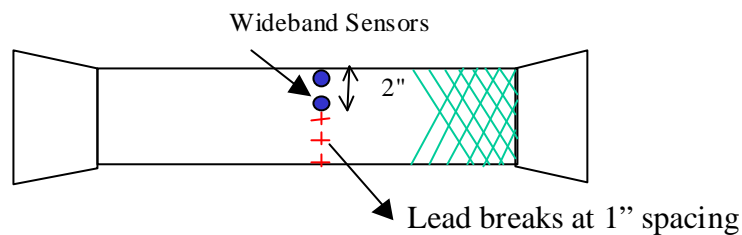


Figure 7.4 – Measurement of Velocity in Hoop Direction

The velocity results are plotted in Figure 7.5. The results from the first threshold crossing show considerable variation. When the source is closer to the sensors, the method detects the arrival time of the first mode resulting in higher velocity. When the source is further, the method detects the time of the second mode which travels slower. The velocity based on the visual inspection of the arrival time shows better consistency. The average wave velocity based on the beginning of the first mode propagating in the hoop direction is 146,500 in/sec.

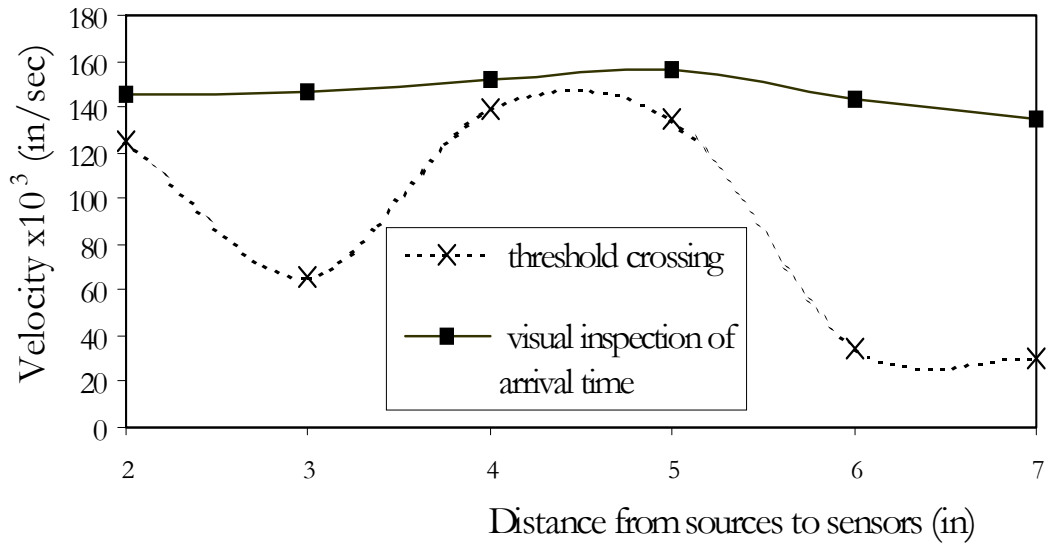


Figure 7.5 – Wave Velocity in Hoop Direction

- *Wave Velocity in Fiber Direction*

Finally, wave velocities travelling along the fiber direction were measured. The measurement scheme is shown in Figure 7.6. Two wide-band sensors were placed two inches apart and pencil lead breaks were performed every one inch away for 6 inches from the sensor. The results are shown in Figure 7.7.

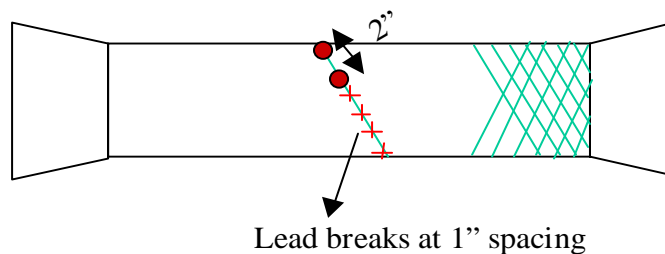


Figure 7.6 – Measurement of Velocity along Fiber Direction

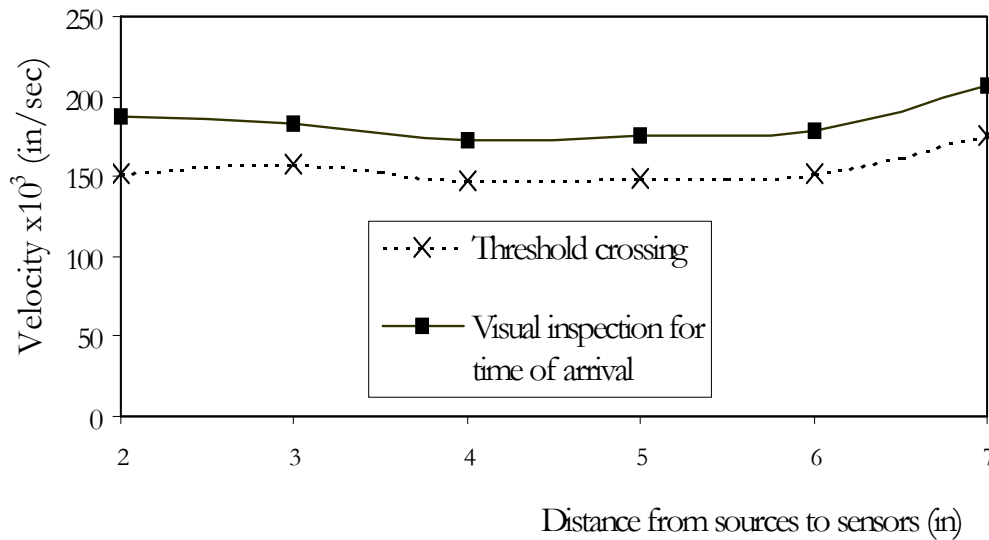


Figure 7.7 – Wave Velocity along Fiber Direction

In this case, the velocities from the threshold crossing method and the beginning of the first mode show reliable results. The average velocity from the visual inspection of the beginning of the first mode is 183,900 in/sec, while the first threshold crossing yields the average velocity of 155,000 in/sec. In this case, the first threshold crossing detects the arrival time from the first mode but not at the beginning of the mode, while the visual inspection defines the arrival time at the beginning of the first mode. Since the waves are dispersive, defining the arrival time at different phase points results in different value of velocity. It is interesting to notice that the results from the first threshold crossing are consistent. That means the first threshold crossing technique was able to detect the time at relatively the same point. This is probably because the waves do not attenuate very much in this direction.

### 7.3.2 Discussion

There are two interesting points in the previous data. First, the waves travel at different speeds in different directions. Second, it is seen in Figure 7.7 that the threshold crossing method yielded consistent velocity results along the fiber direction. Since the threshold crossing was able to define the arrival time at the same points, the attenuation might be less along the fiber direction.

Figure 7.8 shows the attenuation in three directions (axial, hoop, along fiber). From the attenuation plots, it is seen that attenuation along the fiber direction is less severe compared to the other two directions. With the low attenuation along the fibers, the signal can propagate along the fibers and may reach the sensor by the spiral route shown in Figure 7.9, rather than by the direct route.

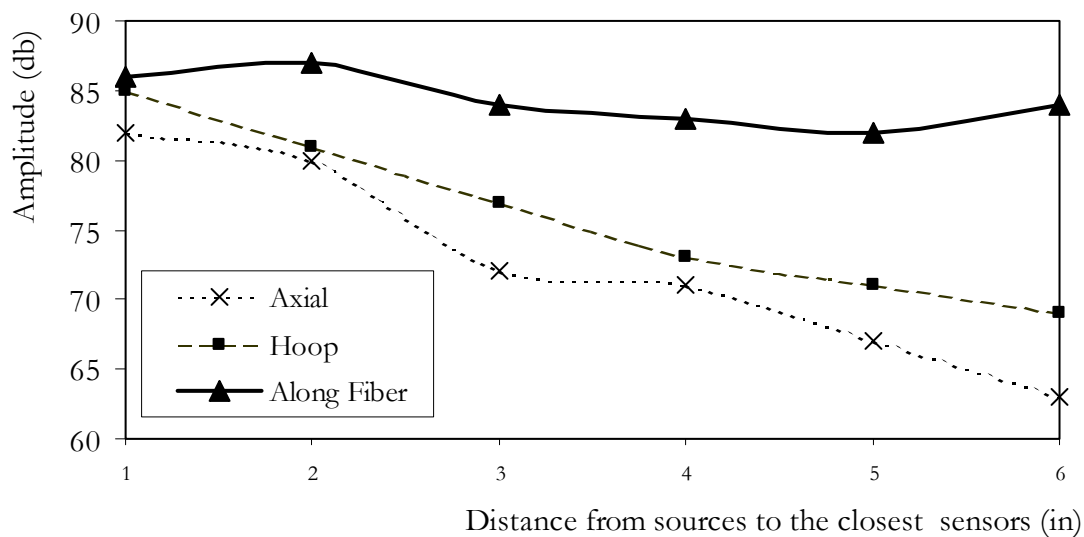


Figure 7.8 – Attenuation in Different Directions

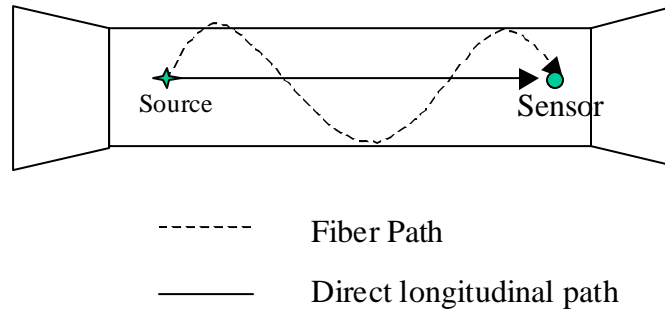


Figure 7.9 – Possible Wave Paths

The attempt to define the group velocity in the composite was not pursued in this work because of two reasons. First, it is a lot harder to calculate the dispersive group velocity in composites since the modulus of the fibers and resin are very different. Second, the previous studies show that the approach using difference in time of arrival seems to be not practical for source location due to:

1. Different velocities in different directions
2. High attenuation in some directions
3. Alternative paths in continuous fiber composites

Therefore, there is no need for an effort to explore the group velocity technique. Since the source location approach based on time of arrival is not appropriate for composite materials, a new approach using a multi-layer perceptron neural network is explored.

## 7.4 SOURCE LOCATION WITH A NEURAL NETWORK APPROACH

### 7.4.1 Introduction to MLP Neural Network

The network used in this program is generally called multi-layer perceptron (MLP). This type of network is known as a universal approximator. The model was developed using MatLab [MatLab student version, 1998] with NetLab toolbox. The MLP network is comprised of three layers, the input, hidden, and output layers. The network topology is depicted in Figure 7.10.

In designing the network, the good input parameter combination needs to be determined. Good input parameters are those that affect a change in the output values. For the hidden layer, it is necessary to determine the number of hidden units. For this layer, there is no design rule of thumb. The only way to obtain an optimal number of hidden units is by trial and error.

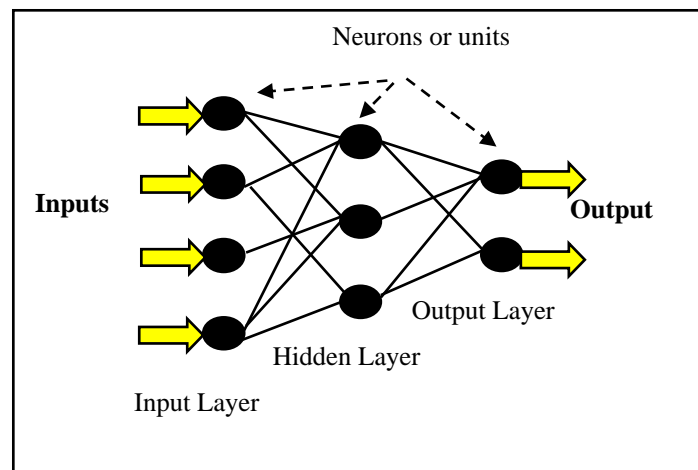


Figure 7.10 – MLP Neural Network

Each layer is connected by weighting functions. The role of a weighting function is to control the contribution of the input. Weighting functions are random numbers for the network. With training data, the network learns to adjust the weighting value to yield a correct output. Since the network learns from training data, this data is very important in obtaining a good network.

In this section, training and testing data were obtained from artificial excitations using pencil lead breaks at known locations. The MLP network was trained and tested using this set of data.

#### **7.4.2 Training Data**

The pipe was divided into 6 sections around the circumference and 4 sections along the length as shown in Figure 7.11. This yields 24 zones of output. The scheme called 1 of N coding was used to assign output functions for the network. 0 and 1 were used to identify each output. For example, there are 4 sections along the length. Section one was assigned as “1,0,0,0” and section two was “0,1,0,0” etc.

A good network requires a lot of training data points. As it would be impractical and costly to apply real damage to the specimen in order to obtain the training data, an artificial excitation using pencil lead breaks was used. Lead breaks were performed at 1100 different locations on the pipe; 900 data points for training purposes and 200 data points for testing the network. In this test, three wide band sensors were used. The locations of the sensors are shown in Figure 7.11.

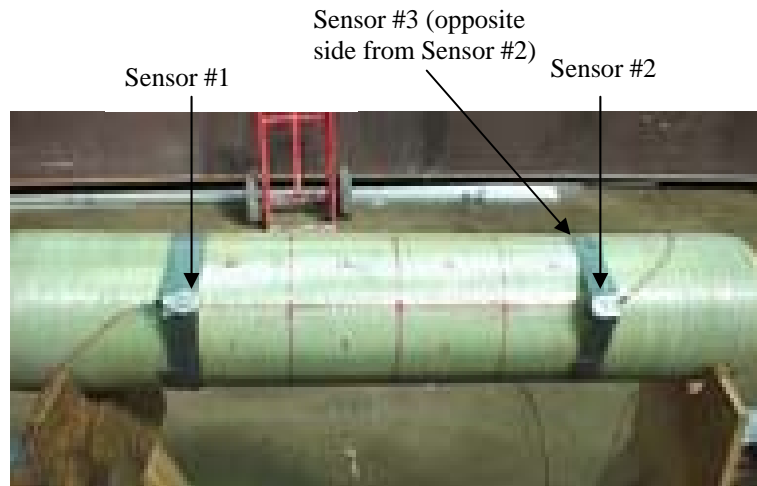


Figure 7.11 – Output Zones on the Pipe

### 7.4.3 Network Model

The first network model was trained with time of arrival, amplitude, duration, average frequency, rise time, and signal strength. The model used these inputs from 3 sensors. This requires a total of 18 inputs. As noted previously, the output was divided into 24 zones, and 900 data points were obtained for training the network. Due to a limitation in array size for the version of MatLab used in this study, this model could not work, and it was necessary to reduce the size of the network. Instead of having one big network with 24 outputs, the network was divided into 2 networks. One yielded output in term of longitudinal sections (4 outputs) and the other gave answers in term of the circumferential sections (6 outputs). The output zones are shown in Figure 7.12.



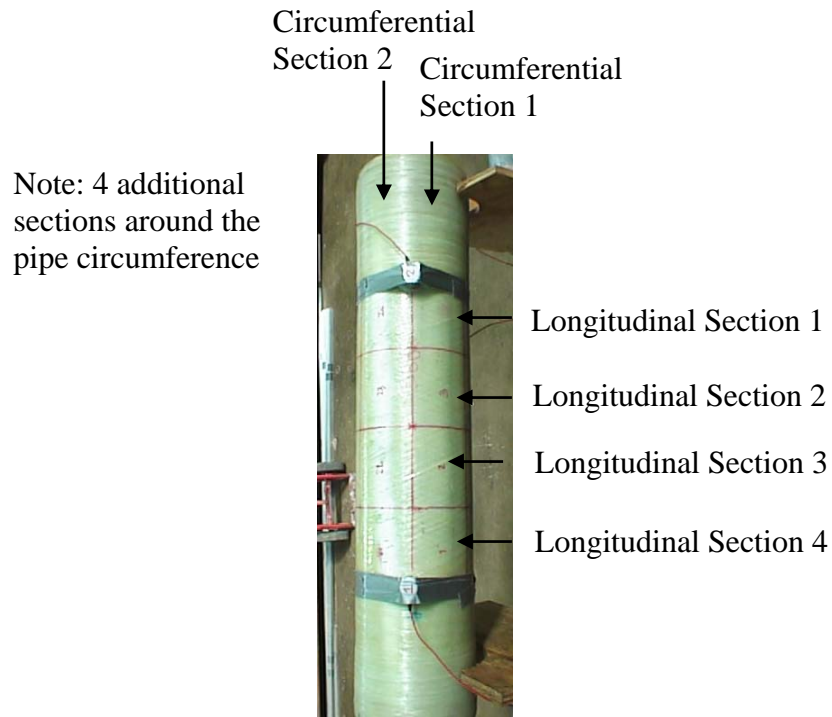


Figure 7.12 – Output Zones

#### 7.4.4 Feature Extraction

In this step, four input combinations were used to run the network. The network was trained with 100 epoch (or iterations) and 12 units in the hidden layers using 900 training data points. The first combination used is the difference between the arrival time ( $\Delta T$ ) and difference between the amplitude ( $\Delta \text{Amplitude}$ ) from 3 sensors. The second combination uses the difference between the time of arrival from three sensors. The third combination uses the parameters from only

one sensor. The last combination uses the amplitude, duration, and rise time from 3 sensors. The errors when using different combinations are shown in Table 7.1.

Input Combinations	Missclassification Error	
	Circumferential Section	Sections along the length
- $\Delta T$ and $\Delta$ Amplitude (6 inputs)	5%	55%
- $\Delta T$ only (3 inputs)	6%	40%
- All input from 1 sensor (arrival time, amplitude, duration, rise time, avg. freq., and signal strength)	25%	60%
- Amplitude, duration, rise time (9 inputs)	3%	38%

Table 7.1 – Feature Extraction

Table 7.1 shows that for both networks, the input combination of amplitude, rise time and duration from all 3 sensors seems to be the best combination to predict the location. It is also interesting to note that this input combination describes the shape of the waveform. As discussed in Chapter 2, research shows that the shape of the waveform changes as the wave travels further.

For the prediction of circumferential sections, the last input combination of amplitude, duration, and rise time yields good accuracy (3% missclassification rate). In the other hand, the network prediction of longitudinal sections gives very poor results for all input combinations. This is due to symmetry of the pipe and the choice of sensor locations.

### 7.4.5 Network Optimization

In this section, the network that focuses on the axial sections is examined in greater detail. Networks with varying numbers of hidden units were trained and the accuracy of each network was evaluated. First, the network was trained with 30 iterations on 800 data points. The number of hidden units was varied from 1 to 18. A plot of misclassification error is shown in Figure 7.13. The plot shows that increasing the number of hidden units above 6 has only a small effect on the error.

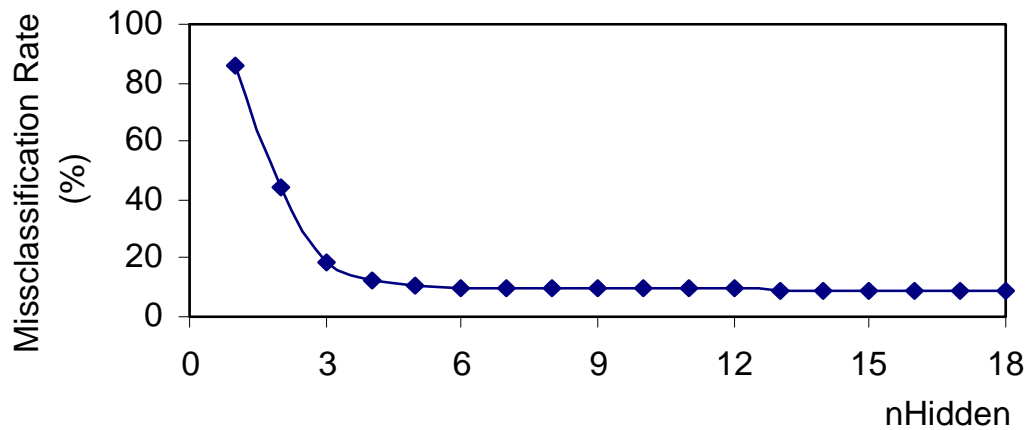


Figure 7.13 – Simulations of Hidden Units

### 7.4.6 RESULTS FROM THE FINAL NETWORK

The final network has the input combination of amplitude, duration, and rise time from 3 sensors (9 inputs). The 4 axial section outputs with 12 hidden units are used. The results from training and testing this network are shown in

Table 7.2. The reader is reminded that the training and testing data at this step are from artificial sources (pencil lead breaks).

Type Of Data	Misclassification Rate
Training data (900 points)	4%
Testing data (200 points)	6%

Table 7.2 – Training and Testing Results

## **7.5 EXPERIMENTAL PROGRAM**

### **7.5.1 Introduction**

The potential of using a MLP neural network for source location on composites was studied in the previous section. The proposed network was trained with pencil lead breaks and showed promising results. To experimentally verify the approach, impact testing and internal pressure testing were performed on the same type of pipe. Source location was performed by the network model developed in the previous section.

## 7.5.2 Test Setup

In order to check the network with genuine emission, the pipe was subjected to a pendulum impact test. Figure 7.14 shows the impact test frame along with the AE acquisition system. The sharp end of the pendulum was used and the impact location was in the exact middle of the pipe.

A MISTRAS AE monitoring system with three wide band sensors (S9208) was used to capture the emission from the impact. Sensor locations were the same as the ones in the previous study. The threshold was set to 40 dB, with a gain of 40 dB in the pre-amplifier and a pretrigger time of 100  $\mu$ sec. The pre-trigger allowed the system to capture the complete waveform.

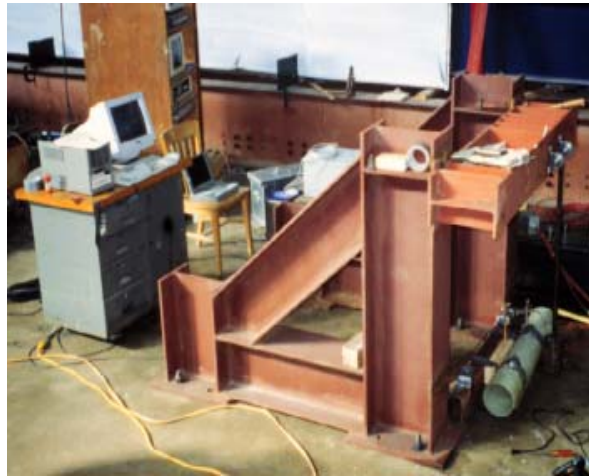


Figure 7.14 – Impact Testing Frame

### 7.5.3 Final Neural Network Model

The network used is the multi-layer perceptron (MLP) using error back propagation discussed in Section 7.4. A schematic diagram of the final network model is shown in Figure 7.15.

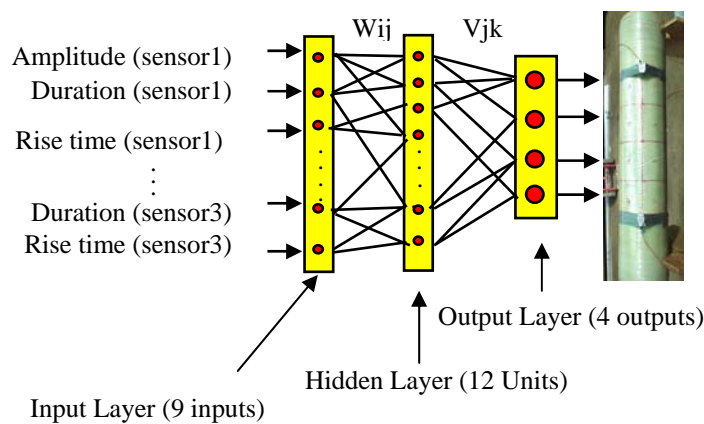


Figure 7.15 – Final Network

The network was composed of nine inputs from three sensors. Input combinations of amplitude, duration, and rise time from each sensor showed good sensitivity to the change of outputs. Twelve hidden units were used with four nodes of output in terms of axial sections. Note that the output value is a Boolean function with a result of either 1 or 0. The output value of 1 means that node (or section) is the correct answer. In order to obtain a correct value of the weighting functions ( $W_{ij}$  and  $V_{ij}$ ), the process required training data with known outputs (also called supervised training). First, the weighting function was randomized by a computer, after the network was trained, the error generated by the network was

compared to the real output. Then, this error was back propagated through the network to adjust the weighting values in order to obtain a corrected output. This process is known as error back propagation.

#### 7.5.4 Experimental Results

From the impact test, damage was located exactly between sections 2 and 3. This is shown in Figure 7.16. Forty-five data points (events) were obtained from this test. AE emissions are fiber breakage and matrix cracking, and vibration noise. Most of the noise came from the vibration of the pipe immediately following impact. Since wide band sensors were used in the test, it is not difficult to tell the difference between genuine emissions and vibration noise. After filtering out the noise events, there were five genuine data points left. These were input into the trained network. The results for these five data points are shown in Table 7.3.

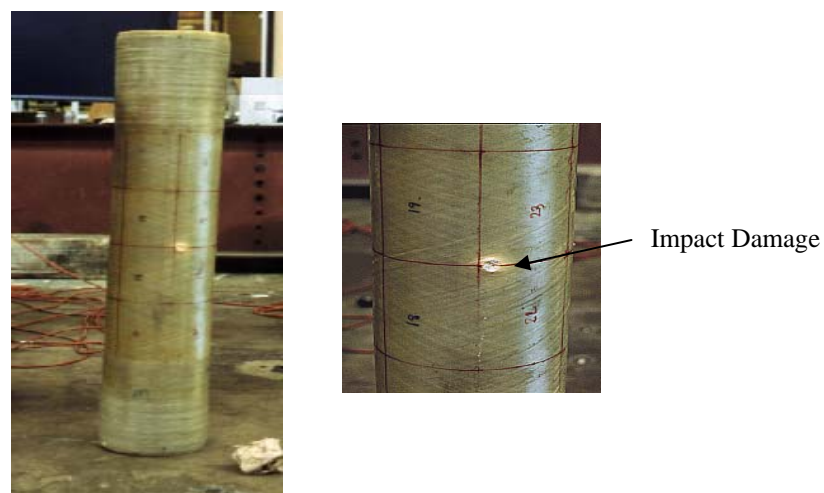


Figure 7.16 – Damage Location

DATA POINT	OUTPUT FROM NETWORK	ROUNDED OUTPUT
1	0.04, 0.87, 0.89, 0.00	0, 1, 1, 0
2	0.02, 0.93, 0.86, 0.01	0, 1, 1, 0
3	0.12, 0.85, 0.79, 0.00	0, 1, 1, 0
4	0.13, 0.83, 0.87, 0.09	0, 1, 1, 0
5	0.16, 0.87, 0.89, 0.12	0, 1, 1, 0

Table 7.3 – Output in Terms of Section

Table 7.3 shows that the raw outputs from sections 2 and 3 are close. Based on the rounded integer output, the network indicate that all damage locations are in Sections 2 and 3. This is corresponding to the damage location in Figure 7.16.

## 7.6 SUMMARY AND FUTURE RESEARCH

Three factors make the conventional differences in time of arrival source location approach very difficult to apply. First, waves travel at the highest speed along the fiber direction and at a greatly reduced speed in other directions. Second, the attenuation rate along the fiber direction is very small compared to the other directions. This means that the signal might not reach sensors through a direct path, but a wave traveling an indirect route along fibers may reach the sensor.

A new source location technique using a MLP neural network with error back propagation was introduced in this chapter. After several trials of input



combinations and network parameters, the final network used an input combination of amplitude, duration, and rise time from 3 sensors. 12 hidden units, and 4 outputs completed the network. The results from pencil lead breaks are promising.

The network was then experimentally verified with real emission data from impact testing of the pipe. It yielded correct location results. This study shows that there is a potential for use of neural network to solve source location problem in composites.

## **CHAPTER 8**

### **SUMMARY AND CONCLUSIONS**

#### **8.1 SUMMARY**

The objective of the research program reported in this dissertation was development of reliable techniques for acoustic emission source location. The study consisted of two parts. First, the research focused on development of source location methods for homogeneous plates. The specimens used in the program were steel railroad tank cars. The second part of the research was an exploratory study of source location in fiber reinforced composites.

The first part of the study comprised four different steps. The research program began with preliminary studies of wave propagation in an empty tank. Artificial sources were used to generate emission in the tank car shell. Conventional source location methods such as zonal, and difference in time of arrival were explored. These studies gave an understanding of the problems with conventional source location methods. An improved method of source location, using a tight band frequency filter, was suggested. Preliminary experiments with this method showed promise.

In the second step, the source location method using the tight band frequency filter was applied to data obtained from jacking and bar twist tests on an empty tank car. In this step, a software algorithm based on simplex optimization and combinations of three sensors was used. This method was extended to minimize the multiple source problem. Experimental studies confirmed that the method was able to locate cracks, corrosion, rust, and blistering in a tank car.

In the third step, source location was studied on a tank car filled with water. A preliminary study of wave propagation in a water filled tank car using artificial sources provided valuable information. In this step, both wide band and resonant sensors were studied. Two source location approaches were developed. One using the very low frequency non-leaky Lamb wave zone, and the other using a tight band frequency filter at higher frequencies. Both methods located the position of the sources using the waves traveling along the shell. The algorithm using combinations of three sensors developed in the second step was applied to eliminate problems caused by the water borne waves. The water borne wave propagation route was also studied.

The last step of this part of the research utilized the source location method and software algorithm developed in the third step to analyze data from an internal pressure test.

The second part of the research studied the possibility of using a neural network based source location method for fiber reinforced composites. The specimen used in the test was a continuous glass fiber filament wound reinforced epoxy pipe. A neural network model was developed for the pipe. The network was trained with data from an artificial source and tested against data from the pipe which had been deliberately damaged by impact.

## **8.2 CONCLUSIONS**

The conclusions listed in Section 8.2.1 and 8.2.2 below are believed to apply to acoustic emission source location on any metal plate structure. However, the research supporting the conclusions and reported in this dissertation was performed on steel tank cars. Accordingly, the conclusions in this section are stated in terms of steel tank cars.

### 8.2.1 Source Location on an Empty Tank Car

The following contribute to unreliable source location results in an empty tank car:

1. *Dispersion.* A tank car is a thin plate structure. Acoustic emission waves propagating in this type of structure are dispersive plate waves. The term dispersive means that the velocity of the wave depends on the frequency and thickness of the material. This phenomenon also results in a changing waveform shape as the wave propagates.
2. *Attenuation.* Attenuation results in a loss of energy and decrease in amplitude as a wave travels through a medium. As a result, not enough sensors detect the signal. This is a very common problem in commercial field testing. If the amplitude of the signal is below the preset channel threshold, the hit will not be recorded. Attenuation also results in inaccuracies in time of arrival determination due to the stress wave being measured at different points on different channels.
3. *Multiple Sources.* It is possible that two or more defects will emit at the same time. When this occurs, it is difficult to separate the data for each source.

The advantages and disadvantages of current source location techniques are summarized as follows.

1. The zonal method with an open sensor arrangement gives satisfactory results but has very poor resolution. The method is robust and is not adversely affected by the attenuation problem. In many cases, attenuation improves the robustness of the method.
2. The zonal method with a close sensor arrangement is very difficult to apply and can give erroneous results. For the method to work well, all the sensors are required to have identical sensitivity. This is not practical with currently available sensor technology.
3. The difference in time of arrival method using a preset threshold to define the arrival time yields poor results. This method is hurt by the attenuation and dispersion problem listed above.

A significant improvement in the accuracy and reliability of source location can be achieved by use if the following:

1. A signal filtered with a tight band-pass filter centered on the intersection of the group velocities of the first three wave modes. In this way, the dispersion problem is minimized, and a constant velocity can be used for the source location calculations.

2. Resonant sensors having a frequency range consistent with the intersection point of the group velocities.
3. The signal arrival time based on the median of the negative and positive peaks of the band-pass filtered signal. The decrease in the amplitude of the signal that results from normal attenuation does not have an effect on the arrival time measured in this manner.
4. Simplex optimization to determine the position of the source. The step increment should be consistent with the desired accuracy of the location.
5. Utilize combinations of three sensors to find the position of the source. This method minimizes the multiple source problem. If a combination includes a signal from another source, it will give a location that is very different from the other calculated locations. With this technique, at least four sensors are required to detect the signal from the source of interest.

### **8.2.2 Source Location on Liquid Filled Tank Car**

Source location on a liquid filled tank car has the same source location problems as an empty car. It is further complicated by leakage of the wave energy into the liquid and misleading results caused by liquid borne signals. Leakage of the wave energy into the liquid results in a large increase in attenuation. Two source location approaches can be considered for water filled tank cars.

The first method uses very low frequency waves which are non-leaky. The method addresses the dispersion, attenuation, and water borne problems. The key issues with this method are:

1. *Dispersion and Attenuation.* As with the empty tank, the method focuses on a tight frequency band and uses the median of the negative and positive peaks to define the arrival time.
2. *Water Borne Waves.* The method works in a very low frequency range. In this range, the energy of the plate waves does not radiate into the water. Therefore, the water borne waves are eliminated.
3. *Field Use.* The method is not practical for field test use since there will be interference from background noise in the very low frequency range. Another serious problem is the insensitivity of the accelerometers and wide band sensors that must be used to capture low frequency signals. These sensors are too insensitive to adequately capture signals at the higher frequencies which are used for structural evaluation.

The second method is similar to the method used for empty tank cars and uses high frequency waves centered on the intersection of the group velocities of the first three wave modes. This method has the following advantages and disadvantages.

1. Attenuation in a liquid filled tank becomes increasingly severe at higher frequencies. Accordingly, it is not possible to use this

method on thin wall tank cars, such as the one tested at the Ferguson Laboratory. This tank car is 15/32" thick and the frequency at the intersection of the group velocities is 150 kHz.

2. Use of resonant sensors at 100 kHz makes it possible to detect the data needed for source location on thicker tanks, such as the 13/16" tank car tested at Orange, Texas.
3. At the higher frequencies used in this test, energy is radiated into the water and results in water borne signals. To overcome this problem, the method based on combinations of three sensors was found to be effective.

Additional conclusion concerning water borne wave propagation are as follows:

1. Three types of waves can enter the water:
  - a. Leaky Lamb Waves
  - b. Scholte-Stonley Waves
  - c. Direct Transmitted Waves
2. A water borne wave that is detectable by an acoustic emission sensor on the opposite side of a cylindrical tank enters the water as a direct transmitted wave.



3. Incident angles between 0 and 27.3 degrees transmit waves from the water into the tank car shell. An incident wave at 14.5° transmits the maximum energy into the tank wall.

### **8.2.3 Source Location in Fiber Reinforced Composites**

Source location in a continuous glass fiber reinforced epoxy pipe is difficult using time of arrival based methods. Three factors contribute to the problem:

1. Different wave velocities occur in different directions
2. Attenuation is always large and is different in different directions
3. The signal can propagate along the fibers in a spiral path. Waves that travel this route are less attenuated than waves traveling across the fibers. As a result, waves traveling along the spiral route may travel further along the pipe.

Use of neural networks for source location in composites shows promise and should be researched further.

### **8.3 FUTURE DIRECTION**

The source location methods and software algorithms developed as part of in this research program gave promising results and should be pursued.

It is believed that the results of the work on metal plate structures are suitable for implementation into field test acoustic emission applications. As a first step towards integrating the technology into practice, the results of the work

should be shared with individuals that utilize acoustic emission in an established field test application. Potential applications that could utilize this research to their economic benefit include aircraft structures, pressure vessels and tanks, and bulk liquid transport vehicles such as tank cars and tank trucks.

It is recommended that additional source location research include methods for fiber reinforced composites. The preliminary study into the use of a neural network shows promise. Use of the technique on larger specimens and different types of construction is suggested.

## Appendix A

### Triangulation with Four Sensors

This section presents the derivations for source location solutions using four sensors. The derivation was presented by Hsu [1975] as a part of NSF research for error analysis for flow source location.

Let the four sensors 0, 1, 2, and 3 be located at  $(0, 0)$ ,  $(x_1, y_1)$ ,  $(x_2, y_2)$ , and  $(x_3, y_3)$  as shown in Figure A1. Let and AE source be at  $(x, y)$  and travel at a constant speed  $V$ . The time durations required for the source to travel to sensors 0, 1, 2, and 3 are  $t$ ,  $t+t_1$ ,  $t+t_2$ ,  $t+t_3$ , respectively.

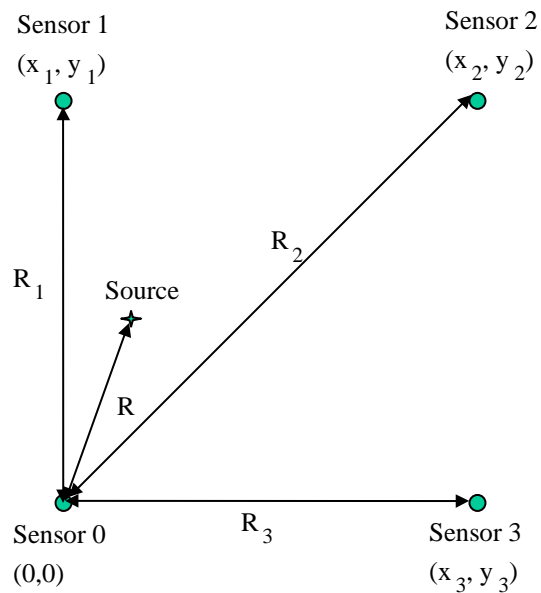


Figure A1 – Four Sensor Arrangement

The relationship between the velocity and time can be given in:

$$x^2 + y^2 = V^2 t^2 \dots\dots\dots(A1)$$

$$(x - x_1)^2 + (y - y_1)^2 = V^2 (t + t_1)^2 \dots\dots\dots(A2)$$

$$(x - x_2)^2 + (y - y_2)^2 = V^2 (t + t_2)^2 \dots\dots\dots(A3)$$

$$(x - x_3)^2 + (y - y_3)^2 = V^2 (t + t_3)^2 \dots\dots\dots(A4)$$

Subtracting Equation A1 from Equations A2 through A4 yields:

$$2x_1x + 2y_1y + 2Vt_1R = R_1^2 - V^2 t_1^2 \dots\dots\dots(A5)$$

$$2x_2x + 2y_2y + 2Vt_2R = R_2^2 - V^2 t_2^2 \dots\dots\dots(A6)$$

$$2x_3x + 2y_3y + 2Vt_3R = R_3^2 - V^2 t_3^2 \dots\dots\dots(A7)$$

where  $R = \sqrt{x^2 + y^2}$ ,  $R_1 = \sqrt{x_1^2 + y_1^2}$ ,  $R_2 = \sqrt{x_2^2 + y_2^2}$ , AND  $R_3 = \sqrt{x_3^2 + y_3^2}$

Since Equations A5, A6, and A7 are linear in x, y, and R, the solutions for x, y, and R in terms of known geometric parameters, speed of propagation, and arrival times can be solved. The solutions are:

$$x = \frac{D_x}{D} \dots\dots\dots(A8)$$

$$y = \frac{D_y}{D} \dots\dots\dots(A9)$$

$$R = \frac{D_R}{D} \dots\dots\dots(A10)$$

and

$$D = \begin{vmatrix} 2x_1 & 2y_1 & 2Vt_1 \\ 2x_2 & 2y_2 & 2Vt_2 \\ 2x_3 & 2y_3 & 2Vt_3 \end{vmatrix} \dots\dots\dots(A11)$$

$$D_x = \begin{vmatrix} R_1^2 - V^2 t_1^2 & 2y_1 & 2Vt_1 \\ R_2^2 - V^2 t_2^2 & 2y_2 & 2Vt_2 \\ R_3^2 - V^2 t_3^2 & 2y_3 & 2Vt_3 \end{vmatrix} \dots\dots\dots(A12)$$

$$D_y = \begin{vmatrix} 2x_1 & R_1^2 - V^2 t_1^2 & 2Vt_1 \\ 2x_2 & R_2^2 - V^2 t_2^2 & 2Vt_2 \\ 2x_3 & R_3^2 - V^2 t_3^2 & 2Vt_3 \end{vmatrix} \dots\dots\dots(A13)$$

$$D_R = \begin{vmatrix} 2x_1 & 2y_1 & R_1^2 - V^2 t_1^2 \\ 2x_2 & 2y_2 & R_2^2 - V^2 t_2^2 \\ 2x_3 & 2y_3 & R_3^2 - V^2 t_3^2 \end{vmatrix} \dots\dots\dots(A14)$$

The final solutions for x, y, and R are:

$$x = \frac{[(R_1^2 - V^2 t_1^2)(y_2 t_3 - y_3 t_2) + (R_2^2 - V^2 t_2^2)(y_3 t_1 - y_1 t_3) + (R_3^2 - V^2 t_3^2)(y_1 t_2 - y_2 t_1)]}{2[(t_1(x_2 y_3 - x_3 y_2) + t_2(x_3 y_1 - x_1 y_3) + t_3(x_1 y_2 - x_2 y_1)]V}$$

$$y = \frac{[(R_1^2 - V^2 t_1^2)(x_3 t_2 - x_2 t_3) + (R_2^2 - V^2 t_2^2)(x_1 t_3 - x_3 t_1) + (R_3^2 - V^2 t_3^2)(x_2 t_1 - x_1 t_2)]}{2[(t_1(x_2 y_3 - x_3 y_2) + t_2(x_3 y_1 - x_1 y_3) + t_3(x_1 y_2 - x_2 y_1)]V}$$

$$R = \frac{[(R_1^2 - V^2 t_1^2)(x_2 y_3 - x_3 y_2) + (R_2^2 - V^2 t_2^2)(x_3 y_1 - x_1 y_3) + (R_3^2 - V^2 t_3^2)(x_1 y_2 - x_2 y_1)]}{2[(t_1(x_2 y_3 - x_3 y_2) + t_2(x_3 y_1 - x_1 y_3) + t_3(x_1 y_2 - x_2 y_1))V}$$

## References

- 1 Association of American Railroads (AAR), "procedure for Acoustic Emission Evaluation of Tank Cars and IM101 Tanks", Issue 8, October 1999.
- 2 ASTM, Annual Book of ASTM Standards, vol. 03.03, Nondestructive Testing Designation E976-94.
- 3 Standard Terminology for Nondestructive Examinations (ASTM E 1316).
- 4 Bao, X. L., Franklin, H., Uberall, H. and Poncelet, O., "Fluid Borne and Lamb-Type Waves on Elastic Plates in Contact with Two Different Fluids", Acta Acustica (Stuttgart), vol. 84, no. 5, Sept-Oct 1998, S. Hirzel Verlag GmbH & Co Stuttgart, Germany, pp. 823-829.
- 5 Barga, R. S., Friesel, M. A. and Meador, J. L., "Source Location of Acoustic Emissions from Atmospheric Leakage using Neural Networks", Proceedings of SPIE – The International Society for Optical Engineering Applications of Artificial Neural Networks II, April 2-5 1991, vol. 1469, 1991, pp. 602-611.
- 6 Beattie, A. G., "Acoustic Emission Principles and Instrumentation", Journal of Acoustic Emission, vol. 2, no. 1-2, 1983, pp. 95-192.
- 7 Bedford, A. and Drumheller, D. S., "Introduction to Elastic Wave Propagation", John Willey & Son, 1993.

- 8 Bishop, C. M., "Neural Networks for Pattern Recognition", Clarendon Press, Oxford, 1995.
- 9 Bray, D. E. and Stanley, R. K., "Nondestructive Evaluation: A Tool in Design, Manufacturing, and Service", Revised Edition, CRC Press, 1997.
- 10 Calibration sheet for R6I Sensor by Physical Acoustic Corporation, 2000
- 11 Cheeke, J. D. N., li, X. and Wang, Z., "Observation of Flexural Lamb Waves ( $A_0$  Mode) on Water-Filled Cylindrical Shells", Journal of the Acoustical Society of America, vol.104, no. 6, Dec 1998, pp. 3678-3680.
- 12 Cheeke, J. D. N., Shannon, K. and Wang, Z., "Loading Effect on  $A_0$  Lamb-like Waves in Full and Partially filled Thin-Walled Tubes", Sensors and Actuators, B: Chemical proceedings of the POLCAP'98 conference on pollution Sensors Dec7-Jan 9, 1998, vol. 59, no. 2, 1999, pp. 180-183.
- 13 Diachok, O. I., "Ultrasonic Scattering from polycrystalline Solids and Plates", Journal of the Acoustical Society of America, vol.53, no. 3, Mar 1973. pp. 946-949.
- 14 El Hajjar, R. "Structural Response of Railroad Tank Cars during Acoustic Emission Testing" Master Thesis, University of Texas at Austin, may 2000.
- 15 Ensminger, D., "Ultrasonics: Fundamentals, Technology, Applications", Revised Edition, Marcel Dekker, Inc, New York and Basel, 1988.



- 16 Feynman, R. P., Leighton, R. B., and Sand, M., "The Feynman Lectures on Physics", vol. 2, Addison-Wesley publishing Company, 1964.
- 17 Fowler, T. J., "Acoustic Emission of Fiber Reinforced Plastics", Journal of the Technical Councils of ASCE, vol. 105, December 1979, ASCE, New York.
- 18 Fowler, T. J., "Acoustic Emission Testing of Chemical Process Industry Vessel", The 7<sup>th</sup> International Acoustic Emission Symposium, October 23-26<sup>th</sup>, 1984.
- 19 Fowler, T. J., Crump, T. N., and Barnes, C. A., "Crack Size Detection Capability of Acoustic Emission", Review of Progress in Quantitative Nondestructive Evaluation, vol. 15B, 1996
- 20 Gorman, M. R., "New Technology for Wave Based Acoustic Emission and Acousto-Ultrasonics", AMD vol 188, Wave Propagation and Emerging Technologies, ASME 1994.
- 21 Gorman, M. R., "Plate Wave Acoustic Emission", Journal of the Acoustical Society of America, vol. 90, no. 2, July 1991, pp. 358-364.
- 22 Gorman, M. R., "Wave Propagation and Signal Analysis", Short Course, 38<sup>th</sup> AEWG meeting, May 1995, NASA Langley Research Center.
- 23 Gorman, M. R., and Ziola, S. M., "Plate Waves Produced by Transverse Matrix Cracking", Ultrasonics.

- 24 Graff, K. F., "Wave Motion in Elastic Solids", Clarendon Press, Oxford, 1975.
- 25 Halmshaw, R., "Non-Destructive Testing", Second Edition, Edward Arnold, 1991.
- 26 Heiple and Carpenter, "Acoustic Emission Produced by Deformation of Metals and Alloys – A Review: Part I", Journal of Acoustic Emission, vol. 6, no. 4, 1987
- 27 Heiple and Carpenter, "Acoustic Emission Produced by Deformation of Metals and Alloys – Part II", Journal of Acoustic Emission, vol. 6, no. 3, 1987
- 28 Hsu, N. N., "Acoustic Emission – Error Analysis for Flaw Source Location", Report no. IG75ER-0123, Lockheed-Georgia Company, August 1975.
- 29 Hsu, N. N. "Acoustic Emission Simulator", U.S. Patent 4,018,084, April 19, 1977
- 30 Hutton, P. H., Jolly, W. D., and Vetrano, J. B., "Acoustic Emission for Periodic and Continuous Flaw Detection in Pressure Vesels", U.S. – Japan Joint Symposium on Acoustic Emission, Tokyo, Japan 1972

- 31 Innovative Acoustic Source Location and Identification Methods for Railroad Tank Car Testing, Phase I final Report to U.S Department of Transportation, April 1998 by Physical Acoustics Cooperation.
- 32 Kettani, M. C. L., Pareige, P., Luppe, F. and Ripoche, J., “Experimental Study of the conversion of Lamb Waves at the End of an Immersed Plate”, *Acta Acustica*, vol. 82, no. 2, Mar-April 1996, S. Hirzel Verlag GmbH & Co Stuttgart, Germany, pp. 251-259.
- 33 Kinra, V. K. and Iyer, V. R., “Ultrasonic Measurement of the Thickness, Phase Velocity, Density or Attenuation of a Thin Viscoelastic Plate, Part I: the Forward Problem”, *Ultrasonics*, vol. 33, no. 2, Mar 1995, pp. 95-109.
- 34 Kraukramer, J., “Ultrasonic Testing of Materials”, Springer-Verlag, New York, 1969
- 35 Lamb, H., “On Waves in an Elastic Plate”, *Proc. R. Soc. London Ser. A.* vol 93, 1917, pp. 114-128.
- 36 Mindlin, R. D., “Waves and Vibrations in Isotropic Elastic Plates, Structural Mechanics”, edited by J. N. Goodier and N. J. Hoff, Pergamon, New York, 1960.
- 37 MONPAC Technology Package on AE data analysis, “Report DA3 Jolly-Stuart’s Location Construction”

- 38 Motegi, K. and Toda, K., "Interaction between Two Leaky Lamb Wave Modes Propagating in a Water-Loaded Bilayer Consisting of a Piezoelectric Ceramic Plate and a Glass Plate", *Ultrasonics*, vol. 37, no. 2, Feb 1999, pp. 141-147.
- 39 *Nondestructive Testing Handbook*, 2<sup>nd</sup> edition, vol. 5 Acoustic Emission Testing.
- 40 Ohshio, Y., Yamamoto, S., Tsukikawa, T., Ueyama, H., Watanabe, J., Ohnishi, K., Saikudo, R. and Iwadate, T., "Acoustic Emission Testing of Pressure Vessels Made of 2 1/4 Cr-1mo Steel", *Advance in Acoustic Emission proceedings of International Conference on Acoustic Emission American Society for Nondestructive Testing*, Dunhart, 1981, pp. 274-289.
- 41 Ohtsu, M., "Determination of Crack Orientation by Acoustic Emission", *Materials Evaluation*, vol. 45, Sept 1987, pp. 1070-1075.
- 42 Ohtsu, M., "Mathematical Theory of Acoustic Emission and Moment Tensor", *Journal of the Society of Materials Science, Japan*, vol. 36, no. 408, Sept 1987, pp.1025-1031.
- 43 Ohtsu, M., Okamoto, T. and Yayuma, S., "Moment Tensor Analysis of Acoustic Emission for Cracking Mechanisms in Concrete", *ACI Structural Journal*, March-April 1998, pp. 87-95.
- 44 Osborne, M. F. M. and Hart, S. D., "Transmission, Reflection, and Guiding of an Exponential Pulse by a Steel Plate in Water I (Theory)",

Journal of the Acoustical Society of America, vol.17, no. 1, July 1945, pp. 1-17.

- 45 Pareige, P., Luppe, F. and Ripoche, J., “Scattering of Lamb Waves at the Edge of a Semi-Infinite Plate Embedded in Water”, Journal of the Acoustical Society of America, vol. 92, no. 2, Aug 1992, pp. 1056-1847.
- 46 Pavlakovic, B. N., “Leaky guided Ultrasonic Waves in NDT”, PhD thesis, University of London, October 1998.
- 47 PolyModal Software Manual by physical Acoustic Corporation, 1998
- 48 Prosser, W. H. and Gorman, M. R., “Plate Mode Velocities in Graphite/Epoxy Plates”, Journal of the Acoustical Society of America, vol. 96, August 1994, pp. 902-907.
- 49 Prosser, W. H. and Gorman, M. R., “Plate Mode Velocities in Graphite/Epoxy Plates”, Journal of the Acoustical Society of America, vol. 96, no. 2, August 1994, pp. 902-907.
- 50 Prosser, W. H., Dorigi, J. and Gorman, M. R., “Extensional and Flexural Waves in a Thin – Walled Graphite/Epoxy Tube”, journal of Composite Materials, vol. 26, no. 14, 1992, pp. 2016-2027.
- 51 Prosser, W. H., Jackson, K. E. and Kellas, S., “Advanced Waveform-Based Acoustic Emission detection of Matrix Cracking in Composites”, Materials Evaluation, vol. 53, Sept 1995, pp. 1052-1058

- 52 Queheillalt, D. T., Lu, Y., Wadley, H. N., “Laser Ultrasonic Studies of Solid-Liquid interface”, Journal of the Acoustical Society of America, vol. 101, no. 2, February 1997, pp. 843-853.
- 53 Ramirez, G., “Monitoring and Prediction of Damage in Filament Wound Composite Pipes under Pressure Loading”, PhD Dissertation, Department of Civil Engineering, University of Texas at Austin, May 1999.
- 54 Redfern, F. R. and Munson, R. D., “Acoustic Emission Source Location – A mathematical Analysis”, 1982.
- 55 Reese, R. T. and Kawahara, W. A., “Hanbook on Structural Testing”, The Fair Press, Inc, 1993.
- 56 Sawaguchi, A. and Toda, K., “Lamb Waves Propagation Characteristics on Water-Loaded  $\text{LiNbO}_3$  Thin Plates”, Japanese Journal of Applied Physics, Part1: Regular Papers & Short Notes & Review Papers Proceedings of the 13<sup>th</sup> Symposium on Ultrasonics, vol. 32, no. 5B, May 1993, pp. 2388-2391.
- 57 Schmidt, H. and Jensen, F. B., “A Full Wave Solution for Propagation in Multilayered Viscoelastic Media with Application to gaussian Beam Reflection at Fluid-Solid Interface”, Journal of the Acoustical Society of America, vol. 77, no. 3, March 1985, pp. 813-825.

- 58 Shiotani, T, Sakaino, N, Shigeishi, M, Ohtsu, M, Asai, Y, and Hayashi, T. “AE Characteristics of Full-Scale Concrete-Piles Under Bending and Shear Load”
- 59 Smirnov, V. N. and Lin’kov, E. M., “On a Source of High-Frequency Seismic Disturbances and Flexural Gravitational Waves in the Antarctic”, *Izvestia, Earth Physics*, vol. 8, 1967, pp. 88-92.
- 60 Stulen, F. B., “Improved Accuracy and Reliability of Estimates of Defect Locations by Detailed Analysis of Acoustic Emission Waveforms”, *Nondestructive Evaluation: NDE Planning and Application*, vol. 5, 1989 pp. 121-127.
- 61 Sullivan, R. W., Balasubramaniam, K. and Bennett, G., “Plate Wave Flow Patterns for Ply Orientation Imaging in fiber Reinforced Composites”, *Materials Evaluation*, vol. 54, no. 4, April 1996, pp. 518-523.
- 62 Tiede, D. A. and Eller E. E., “Sources of Error in AE location Calculations’, *Dunegan/Endevco Report*, San Juan Capistrano, CA 1982
- 63 Viktorov, I. A., “Rayleigh and Lamb Waves”, *Plenum Press*, New York, 1967.
- 64 Wilcox, P. D., “Lamb Wave Inspection of Large Structures Using Permanently Attached Transducers”, *PhD Thesis*, Imperial College of Science, University of London, March 1998.

- 65 Yamany, S., "Multilayer Neural Network",  
<http://cairo.spd.Louisville.edu/~yamany/annie/node8.html>.
- 66 Yopez Roca Luis Octavio, "Acoustic Emission Examination of High Strength Prestressed Concrete Girders" Thesis presented to The University of Texas at Austin, August 1997
- 67 Ying, S.P., Hamlin, D.R. and Tanneberger D., "A Multi-channel Acoustic Emission Monitoring System with Simultaneous Multiple Event Data Analyses.", *Journal of the Acoustical Society of America*, vol. 55, no. 2 February 1974
- 68 Yoon, D. J., Kim, Y. H. and Kwon, O. Y. "Algorithm for Acoustic Emission Source Location in Cylindrical Structures", *Journal of Acoustic Emission*, vol. 9, no. 4, 1990, pp. 237-242.
- 69 Yuyama, S., Okamoto, T., Shigeiski, M., Ohtsu, M. "Acoustic Emission Generated in Corners of Reinforced Concrete Rigid Frame Under Cyclic Loading", *Materials Evaluation*, March 1995 pp 409-412
- 70 Zhu, Q. G., Ruf, H. J., and Mayer, W. G., "Lamb Wave Radiation from Plate Termination in Liquid", *Ultrasonics*, vol. 29, no. 6, Nov 1991, pp. 459-463.
- 71 Ziola, S. M. and Gorman, M. R., "Source Location in Thin Plates using Cross Correlation", *Journal of the Acoustical Society of America*, vol. 90, Nov 1991, pp. 2551-2556.





## VITA

Yajai Promboon was born in Bangkok, Thailand on January 10, 1973, the daughter of Seubsak and Yenchit Promboon. She received the degree of Bachelor of Engineering in 1993 from King Monguth Institute Technology at Lardkrabang. In September 1994, she entered the graduate school of the University of Texas at Austin where she received the degree of Master of Science in Engineering in August 1996. After graduation, she attended the graduate school of the University of Texas at Austin in September 1996 for her Doctoral degree.

Permanent address: 70/622 Soi 8 Prachanives II Prachacheun Rd. T.Tacye A. Maung, Nonthaburi, 11000 Thailand

This dissertation was typed by the author